Monte Carlo simulations for system modeling in emission tomography

Monte-Carlosimulaties voor systeemmodellering in emissietomografie

Steven Staelens

Promotoren: Prof. dr. I. Lemahieu
Prof. dr. ir. R. Van de Walle

Proefschrift ingediend tot het behalen van de graad van
Doctor in de Toegepaste Wetenschappen

Vakgroep Elektronica en Informatiesystemen
Voorzitter: Prof. dr. ir. J. Van Campenhout
Faculteit Toegepaste Wetenschappen
Academiejaar 2004 – 2005

UNIVERSITEIT GENT

Acknowledgement

It would be totally unfair to state that this dissertation is an individual merit. On the contrary, this work is the result of an excellent collaboration between researchers within Medisip who were supported in their efforts by the worldwide OpenGATE collaboration to reach the specific aims described in this work. Therefore I would like to express my gratitude to those that were indispensable for my PhD project.

When I joined the Medisip research group in 2001, prof. dr. I. Lemahieu told me that I would be given the opportunity to travel around the world on a search for knowledge and collaborators. At first instance I thought this was an overstatement. Three years and many international conferences, meetings and workshops later I sincerely believe it was an understatement. Ignace, thank you very much for all these possibilities who enhanced my knowledge of the field to a very large extent. Reading textbooks on the topic in order to achieve the same level would have taken me many more years. Prof. dr. ir. R. Van de Walle taught me that achieving nice figures, beautiful results and impressive computer code is not the ultimate goal of a researcher. A scientific project can only be succesful if you communicate with experts by publishing your data. Thanks to him I am now aware that international publications are the ultimate way to achieve even better data. Many groups do theoretical work in Nuclear Medicine, others work on the clinical and practical aspects. Thanks to prof. dr. R. Dierckx I was able to do both. As the head of the Nuclear Medicine department of the University Hospital he gave me and my colleagues full and unconditional access to all cameras and their components. Rudi, thanks for your confidence in our possibilities.

Although I would very much like to, it would take up too much space to thank every individual member of the OpenGATE collaboration. Prof. dr. C. Morel introduced me within GATE only 2 months after the beginning of the project. That allowed me to collaborate very closely with dr. D. Strul and dr. G. Santin from the very start of GATE until today and hopefully for many more years to follow. Christian, Giovanni, Daniel, Sebastien thanks a lot for all those nice GATE meetings.

For three years long I worked together on the Nuclear Medicine subtopic with three great colleagues with a scientific and collaborative spirit: dr. M. Koole, dr. S. Vandenberghe and dr. ir. Y. D'Asseler. They deserve explicit credits: chapter 5 of this work is done together with Michel, chapter 6 together with Yves and chapter 7 together with Stefaan. They are no longer colleagues, they have become my friends. I also wish our new lab-coworkers: Jan, Jeroen, Stijn and Roel good luck with their research these next years. Also thanks to our former system administrator ing. E. Nolf and to mevr. Rita Breems, our secretary.

Next to all those collaborators I would like to thank my parents. My mother for her beloved concern and my father for teaching me that it is important to be pragmatic, even in science. The most important person in all this however is my girlfriend Katrijn. Countless are the weekends and the nights she had to spend alone because I was working on yet another deadline or was abroad for some meeting or conference. She beared everything with a smile, moreover she supported and encouraged me to do even better. I can best express her share in this PhD thesis by using the following quote of a colleague: ’damned, Steven, for you it’s easy to achieve all your results, it is the only thing you need to do in life, Katrijn takes care of all the rest.’ I could not have said it any better....

Thanks to all.

ir. S. Staelens
August 16th 2004

Content

List of Figures

List of Tables

Hoofdstuk 0

Nederlandstalige Samenvatting

0.1 Inleiding

Niet-invasieve diagnostische beeldvorming kan uitgevoerd worden door middel van verschillende technieken: technieken die anatomische informatie geven, zoals bijvoorbeeld magnetische-resonantiebeeldvorming (MRI) en gecomputerizeerde tomografie (CT), en technieken die functionele informatie opleveren, onder andere SPECT (Eng.: Single Photon Emission Tomography) en PET (Eng.: Positron Emission Tomography). Recente toestellen combineren twee modaliteiten (SPECT/CT-PET/CT) om hardwarematig anatomische en functionele beeldfusie te verkrijgen. Nucleaire geneeskunde heeft een grote maatschappelijke impact gezien men in de oncologie steeds meer geïnteresseerd is in een diagnostisch middel dat kwaadaardige aandoeningen in een vroeg stadium kan ontdekken en dat kan gebruikt worden voor classificatie van de ziekte. Bij onderzoeken in de nucleaire geneeskunde wordt een radiofarmaceutisch produkt ingespoten bij de patiënt. De gegenereerde fotonen worden gedetecteerd en de verkregen data worden achteraf gereconstrueerd om een driedimensionale verdeling van de radioactieve speurstof in de patiënt te verkrijgen. Optimalisatie, evaluatie en herontwerp van de elementen in deze beeldvormingsketen wordt meestal gedaan door gebruik te maken van Monte-Carlosimulaties. Monte-Carlomethoden zijn numerieke berekeningsmethoden gebaseerd op willekeurige bemonstering van de variabele. Von Neumann [78] verwees bijgevolg in de naamgeving naar het beroemd gokcentrum in Monaco. Deze methoden zijn heel geschikt voor de medische fysica gezien de stochastische aard van de stralingsemissie, het deeltjestransport en de detectieprocessen. De doorbraak voor Monte-Carlomethoden in dit domein kwam er met de paper van Raeside [86] in 1976, maar de methode bereikte niet zijn volledig potentieel ten gevolge van computerbeperkingen. Door de opkomst van betaalbare mini-clusters is er de laatste 3 tot 5 jaar een hernieuwde interesse ontstaan, wat nu resulteert in meer dan 1600 wetenschappelijke artikels per jaar [142]. Onderliggende doctoraatsthesis probeert in te spelen op deze nieuwe tendensen. Sectie 0.2 geeft eerst een kort overzicht van de nucleaire geneeskunde, introduceert de GATE software en bespreekt de belangrijkste toepassingsgebieden waarin simulaties een belangrijk voordeel kunnen opleveren. Sectie 0.3 valideert en verifieert het GATE simulatieplatform versus metingen met een commerciële scanopstelling. Simulaties kunnen ook het inzicht in bestaande systemen verbeteren, zoals aangetoond wordt in sectie 0.4. Sectie 0.5 beschrijft het gebruik van simulaties als ondersteuning bij het ontwerp van een nieuw toestel voor kleine proefdieren dat een hogere spatiale resolutie nastreeft en in sectie 0.6 wordt een theoretisch model afgeleid voor de respons van een scintillatiedetector in gammacamera-PET toepassingen. De resultaten van secties 0.4 en 0.6 vereisten een Monte-Carlogebaseerde benadering om de verkregen data te reconstrueren, wat besproken wordt in sectie 0.7.

0.2 Monte-Carlosimulaties in emissietomografie

0.2.1 Nucleaire geneeskunde

Nucleaire medische beeldvorming houdt het gebruik in van speurstoffen, radioactief gemerkte farmaceutische produkten, om aandoeningen van het menselijk lichaam te diagnosticeren. Plaatsgevoelige detectoren worden gebruikt om de straling uitgestuurd door het farmaceutisch produkt te detecteren, waardoor de verdeling van de speurstof in het lichaam kan bepaald worden. Moderne nucleaire medische beeldvorming bestaat uit twee hoofdtakken: éénfotonige beeldvorming, en fotonbeeldvorming door positronannihilatie, waarbij twee fotonen gelijktijdig gedetecteerd worden.

SPECT, PET en gammacamera-PET

Eénfotonige beeldvorming vereist tenminste één detector op een vaste positie om een tweedimensionale projectie van de driedimensionale verdeling van het radiofarmaceutisch produkt te verkrijgen. Hiervoor wordt typisch een gammacamera gebruikt die opgebouwd is uit een collimator, een scintillatiekristal, een lichtgeleider, fotovermenigvuldigerbuizen (PMT, Eng.: PhotoMultiplierTube) en elektronica die de positie en de energie codeert (figuur 1). Beeldvorming door een enkele projectie kan verbeterd worden door de gammacamera eenvou-

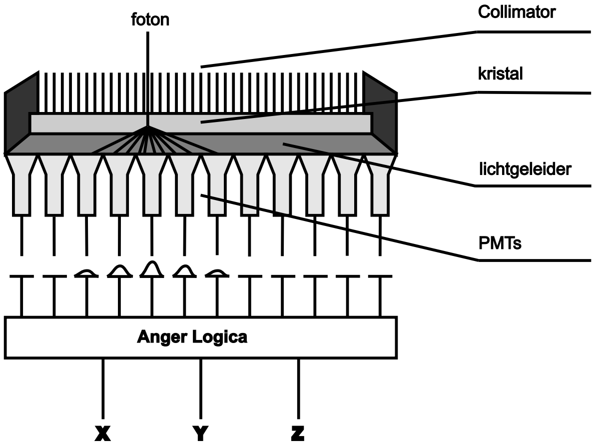

Figuur 1: Gammacamera : technisch schema.

digweg te draaien rond de patiënt om zo een reeks van tweedimensionale projecties te verkrijgen wat diepteinformatie oplevert. Deze tomografische techniek wordt met de noemer SPECT aangeduid. De meeste systemen bestaan uit twee of drie camera's die op een toestel gemonteerd zijn, waardoor de spatiale en temporele resolutie verbetert. Het meest gebruikte radionuclide in SPECT is ^{99m}Tc, met een halfleven van 6.03 h. De bij het verval uitgestuurde fotonen hebben een energie van 140.5 keV.

In tegenstelling tot SPECT, waar de speurstof gemerkt wordt met een fotonemitter, wordt bij PET een positronemitter aangewend. Bij het radioactief verval wordt een positron, het antideeltje van een elektron, uitgezonden dat na een korte weg te hebben afgelegd, annihileert tijdens de botsing met een elektron om daarbij twee fotonen van 511 keV uit te zenden in dezelfde richting met tegenovergestelde zin. Deze twee fotonen worden vervolgens simultaan gedetecteerd en daaruit kan men afleiden dat de interactie heeft plaatsgevonden langs de aldus gedefinieerde interactielijn (LOR, Eng.: Line of Response). Aangezien de detectie van twee fotonen voldoende is om de spatiale informatie te bepalen, heeft een systeem met positronannihilatie zoals PET het voordeel dat er geen fysische collimatie nodig is, waardoor de sensitiviteit veel groter is. Een PET-camera bestaat uit een serie van ringdetectoren, met gescheiden kristallen, gekoppeld aan PMT's. Afhankelijk van de gewenste sensitiviteit kunnen de individuele detectoren in coïncidentie werken met andere tegenoverliggende detectoren in dezelfde ring of ook met detectoren in andere ringen. Het produceren van een speurstof voor PET-toepassingen vereist de aanwezig-

(a) (b)

Figuur 2: (a) SPECT/CT: Siemens TruePoint, (b) PET/CT: Philips Gemini

heid van een cyclotron om instabiel ^{18}F te genereren alvorens dit gekoppeld wordt aan fluorodeoxyglucose (FDG). Dit maakt de PET-techniek duurder in uitbating dan SPECT. Daarnaast is een typische PET-camera ook een grootte-orde duurder dan een SPECT-toestel door de grote hoeveelheid kristalmateriaal dat vereist is in de ring. Een alternatief voor de geometrie van de ringscanner is de draaiende planaire detectorgeometrie. Eerder dan de patiënt te omsluiten met detectoren, worden tegenovergestelde detectoren geroteerd, wat goedkoper is maar dit ten koste van sensitiviteit. Sommige producenten hebben hun SPECT-gammacamera's dan ook uitgerust met coïncidentie-opnamemodules en dikkere kristallen om ze te gebruiken als gammacamera-PET-toestel. Dit zal besproken worden in sectie 0.4.

Hybride toestellen

De softwarematige fusie van anatomische en functionele beelden is over het algemeen succesvol voor de hersenen, maar levert vaak moeilijkheden op voor de rest van het lichaam, bijvoorbeeld door beweging van de patiënt tussen de twee scans door. Een alternatief hiervoor is de beeldtechnologieën te combineren in één scanner, die dan anatomische en functionele beelden nauwkeurig kan aligneren in dezelfde scansessie (Figuur 2). Een bijkomend voordeel van zo een SPECT/CT en PET/CT is dat de CT-beelden omgeschaald kunnen worden naar de gepaste energie en gebruikt kunnen worden om een attenuatiecorrectie uit te voeren, wat de nood voor een afzonderlijke tijdrovende transmissiescan elimineert. Sectie 0.4 zal een methode voorstellen om de transmissiescan eveneens simultaan uit te voeren bij gammacamera-PET.

Beeldvorming van kleine proefdieren

Deze nieuwe beeldvormingssystemen laten onderzoekers toe om proefdieren op een niet-invasieve wijze te onderzoeken op mutaties of pathologieën, om de progressie van de ziekte vast te stellen en om de reactie op therapie weer te geven. Op die manier kunnen nieuwe technologieën en geneesmiddelen onderzocht worden op potentiële humane toepassingen. Verschillende modaliteiten zijn reeds gevalideerd en beschikbaar voor onderzoeksdoelen zoals microCT, microPET, microSPECT (enkel- en meervoudige kegelgatcollimator, spleetcollimator, vlakkencollimator) en optische beeldvorming.

Reconstructie

Beeldreconstructie van projectiedata verkregen onder verschillende hoeken kan op verschillende manieren uitgevoerd worden: analytische reconstructie, deterministische iteratieve reconstructie en statistische iteratieve reconstructie. Een deterministisch model wordt verkregen wanneer de systeemkarakteristieken in rekening gebracht zijn. Dit systeem kan dan algebraïsch opgelost worden. Het reconstructieprobleem kan ook statistisch voorgesteld worden met als grote voordeel dat een kleinere variantie verkregen wordt als de geschikte modellen, zoals een Poissonmodel voor radioactief verval, en een Gaussiaans model voor detectorrespons, gebruikt worden. Iteratieve reconstructietechnieken zijn in staat om beelddegraderende effecten in het reconstructiealgoritme in te bouwen om de resulterende kwaliteit van het gereconstrueerde beeld te verbeteren. Het succes van een iteratief algoritme hangt grotendeels af van de juistheid waarmee de systeemmatrix gemodelleerd wordt. De meest realistische oplossing maakt gebruik van een Monte-Carlogesimuleerde driedimensionele projector. Dit wordt in meer detail besproken in sectie 0.7

0.2.2 GATE, een simulatieplatform voor SPECT en PET

Er was nood aan een Monte-Carlocode die in staat is om complexe PET-, en SPECT-geometrieën alsook andere beeldvormingsconfiguraties op een gebruiksvriendelijke manier te implementeren, rekening houdend met tijdssynchronisatie, en waarbij de uitgebreide en accurate fysische modelleringsmogelijkheden van algemene simulatiepakketten behouden blijven. Zo een simulatieplatform werd ontwikkeld binnen het OpenGATE-samenwerkingsverband.

OpenGATE collaboratie: geschiedenis en doelstellingen

De oorsprong van GATE loopt terug tot een werkvergadering georganiseerd in juli 2001 in Parijs, waar de aandacht uitging naar de toekomst van Monte-

Carlosimulaties in de nucleaire geneeskunde. De consensus was om de Geant4-simulatietoolkit ontwikkeld in C++ te kiezen als vertrekpunt, en om langetermijn ondersteuning en in onderhoud te voorzien door de ontwikkeling van de code te verdelen over meerdere onderzoeksgroepen. De onderzoeksgroepen betrokken bij de initiële ontwikkeling van de GATE-software, UNIL te Lausanne, ELIS te Gent en LPC te Clermont-Ferrand, besloten in januari 2002 een OpenGATE-samenwerkingsverband op te starten. De basisimplementatie en validatie van GATE werd door deze onderzoeksgroepen uitgevoerd en resulteerde in 4 publicaties over de grondslagen van GATE [73,92,107,111]. Nadien groeide het samenwerkingsverband heel snel tot het 21 leden uit Europa, Noord-Amerika en Azië telde. Er werd ook een grote inspanning gedaan om GATE voldoende flexibiliteit mee te geven met als doel het gemakkelijk modelleren van nieuwe detectiesystemen [104] zodanig dat het platform onafhankelijk is van zijn conceptietijdstip, wat veelal niet het geval is met specifieke PET- en SPECT-simulatiepakketten. Een praktisch voorbeeld zal toegelicht worden in sectie 0.5. Na een initiële validatie, die in sectie 0.3 besproken zal worden, werden meer inspanningen gedaan om te verifiëren of het GATE-simulatieplatform nuttig zou zijn in klinische toepassingen [106]. Dit zal het geval blijken te zijn in sectie 0.4. Momenteel wordt geconcentreerd op verdere verbetering van de digitalisator om het rekenproces nauwkeuriger te maken [91, 97, 103]. Sectie 0.6 zal een accuraat theoretisch model voor de spatiale resolutie in continue detector PET voorstellen dat kan geïncorporeerd worden als een nauwkeurige resolutiemodule in de digitalisator. Op de “Satellite Workshop” over GATE (MIC 2003, Portland USA) kondigde het OpenGATE-samenwerkingsverband de eerste openbare vrijgave van GATE aan, die plaatsvond op 7 mei 2004. De ultieme doelstelling van het OpenGATE-samenwerkingsverband is om GATE verder te ontwikkelen en te valideren, zodat het een gouden standaard wordt voor Monte-Carlosimulaties in de nucleaire geneeskunde [4, 68].

Onderliggend manuscript heeft in eerste instantie bijgedragen tot de ontwikkeling en validatie voor SPECT vanaf de beginfase. In een later stadium heeft dit onderzoek de ontwikkeling van PET-digitalisatormodules opgeleverd naast uitbreidingen voor Monte-Carlogebaseerde reconstructies. Bovendien heeft deze doctoraatsthesis het gebruik van gevoxelizeerde patiëntdata mogelijk gemaakt.

GATE: basiseigenschappen

Softwarearchitectuur: de softwarecomponenten van GATE moeten algemeen genoeg zijn om herbruikt te kunnen worden van de ene context naar de andere en een modulaire opbouw moet ervoor zorgen dat GATE in staat is om te evolueren wanneer innovatieve toepassingen in zicht komen. Daarom werd een gelaagde softwarestructuur geïmplementeerd met een kernlaag, een toepassingslaag en een gebruikerslaag. De kernlaag bevat alle klasses die vereist zijn in Geant4-gebaseerde simulaties: gebeurtenisgeneratie, interactiefysica,... en bovendien ook klasses die specifiek zijn voor GATE-simulaties zoals het virtueel klokobject dat alle processen synchroniseert. De kernlaag bestaat daarnaast ook uit basisklasses, dit zijn klasses die een groep componenten bepalen met een set gemeenschappelijke eigenschappen. Met andere woorden, de kernlaag omvat dus de basismechanismen die in GATE beschikbaar zijn voor geometriebepaling, tijdsbeheer, bronbepaling, digitalisatie en data-uitvoer. De toepassingslaag daarentegen bestaat uit klasses die afgeleid zijn van de basisklasses om specifieke processen of objecten te modelleren zoals bijvoorbeeld translaties afgeleid van de bewegingsbasisklasse. Elke GATE-klasse voorziet in een aanvulling die de opdracht vertaalt, zodat de functionaliteit van de klasse beschikbaar is door middel van tekstcommando's die op hun beurt de gebruikerslaag vormen. Een compleet simulatiescript kan in acht stappen omschreven worden: (1) camerageometrie, (2) fantoomgeometrie, (3) acquisitiesysteem, (4) tijdsparameters, (5) formaat van de data-uitvoer, (6) fysische processen, (7) radioactieve bron(nen) en (8) commentaarniveau. Voor elke stap kan een specifieke macro gedefinieerd worden, opgebouwd uit standaard GATE-commandolijnen.

De fysica: de elektromagnetische interacties gebruikt in GATE, zijn afgeleid van Geant4. Zoals in Geant4, kan ook GATE twee verschillende pakketten gebruiken om elektromagnetische processen te simuleren: het standaardenergiepakket en het lage-energiepakket. Voor biomedische toepassingen levert het lage-energiepakket een nauwkeuriger model van de interacties, maar dit ten koste van een toegenomen rekentijd. GATE omvat ook twee specifieke modules voor PET. De eerste module gebruikt het von Neumannalgoritme [133] om een analytisch β^+ spectrum te bemonsteren, en in de tweede module wordt de intrinsieke niet-collineariteit van de twee annihilatiefotonen geïncorporeerd, wat immers niet in rekening gebracht wordt bij Geant4. GATE erft de mogelijkheid van Geant4 om grenzen te stellen aan de productie van secundaire elektronen, X-stralen en deltastralen. Ook worden alle boven de grens gegenereerde deeltjes gevolgd tot het einde van hun bereik, dit in tegenstelling tot andere Monte-Carlocodes.

Geometrie: het volume van de “wereld” is de top van de volumehiërarchie en bepaalt het referentiekader van de simulatie. Het kan een of meerdere sub-volumes bevatten, dochtervolumes genoemd. Zoals in Geant4 gebruikt ook GATE erfelijkheid tussen klassen om die bijzondere volumehiërarchie af te leiden. Een logisch volume wordt bepaald door al zijn eigenschappen (naam, vorm, grootte en materiaalsamenstelling) behalve zijn positie in de wereld. Toegang tot een materiaaldatabasebestand is de methode om materiaaleigenschappen toe te kennen aan volumes en om hun werkzame doorsnedes te kennen. Wanneer logische volumes op bepaalde posities geplaatst worden, vormen ze fysische volumes. Dit laatste kan gebeuren door elementaire geometrische transformaties die logische volumes in meerdere posities en oriëntaties repliceren en plaatsen om aldus fysische volumes te vormen.

Een van de kerneigenschappen van GATE is de mogelijkheid om hits te lokaliseren in individuele detectoren en vervolgens pulsen te creëren. De bepaling van de posities van de individuele detectoren in een scanner is echter een belangrijke en moeilijke taak in het genereren van de uitvoer. Om het modelleringsproces te vereenvoudigen en om in een toegewijde hiërarchische uitvoer te voorzien, worden voorgedefinieerde globale systemen gebruikt. De meeste van de geometrische concepten zijn immers gemeenschappelijk aan verschillende beeldvormingssystemen. Een PET scanner bijvoorbeeld bestaat typisch uit één of meerdere ringen die opgebouwd zijn uit blokken, onderverdeeld in individuele kristallen. Die opbouw is bijgevolg ondergebracht in een systeem dat bestaat uit een groep van geometrieën dat compatibel is met een of meerdere formaten van data-uitvoer. Het gebruik van systemen bij het modelleren van nieuwe acquisitieopstellingen zal aangewend worden in sectie 0.5.

Brondefinities: de ruimtelijke verdeling van een GPS-bron (Eng.: General Particle Source) kan gespecificeerd worden door gebruik te maken van vijf tweedimensionale vormen (cirkel, annulus, ellips, vierkant en rechthoek) en vier driedimensionale vormen (bol, ellipsoïde, cilinder en parallellepipedum). Een GPS kan bovendien gelimiteerd worden tot een willekeurig element van de geometrie. De emissiesectoren kunnen afgelijnd worden door middel van een azimuthale en een polaire hoek. Positronbereik en gamma-acollineariteit kan aan de brondefinitie toegevoegd worden voor PET-toepassingen. Een belangrijke klinische uitbreiding zijn de gevoxelizeerde, niet-homogene, antropomorfe bronnen, gebaseerd op ingelezen digitale fantoom- of patiëntdata [105]. Naast de bronverdeling kan ook de patiëntgeometrie als gevoxelizeerde attenuatiemap ingelezen worden om de meest realistische simulaties te kunnen nastreven.

GATE: tijdsbeheer

Een van de kenmerkende eigenschappen van GATE is het beheer van de tijdsafhankelijke verschijnselen, zoals beweging van een detector of de kinetiek van het bronverval. De synchronisatie van de bronkinetiek met de beweging van de geometrie laat toe om realistische acquisities te simuleren, met inbegrip van beweging, ademhaling en hartritmes van de patiënt, rotatie van de scanner of veranderingen van de activiteitsverdeling in de tijd. Vanuit het oogpunt van tijdsbeheer kan de simulatie ingedeeld worden in: (a) bepaling van de bewegingen geassocieerd met de fysische volumes die de detector en het fantoom of de patiënt beschrijven; (b) beschrijving van de radioactieve bronnen, en (c) specificatie van de start- en stoptijden van de acquisitie. Een correcte en accurate synchronisatie van gebeurtenissen laat de modellering toe van tijdsafhankelijke processen zoals telkadans, toevallige coïncidenties, opeenhoping van pulsen, dode tijd in de detector en simultane emissie/transmissiestudies, hetgeen besproken zal worden in sectie 0.4.

GATE: digitalisatie

De digitalisatie is het proces waarbij de elektronicarespons van een detector gesimuleerd wordt. Dit houdt de omzetting in van de deeltjesinteracties naar energiebins, detectieposities en naar coïncidenties bij PET. Dit is een sleuteleigenschap in GATE die het nauwkeurig simuleren van het gedrag van realistische scanners toelaat. Om dit te doen zijn delen van de geometrie ontworpen als sensitieve detectoren, die deeltjesinteracties (hierna hits genoemd) in die welbepaalde fysische volumes registreren en opslaan. Informatie over interacties in niet-sensitieve volumes wordt niet bijgehouden. In GATE zijn twee types sensitieve detectoren gedefinieerd: de kristalsensitieve detector (kristalSD) en de fantoomsensitieve detector (fantoomSD). De kristalSD wordt gebruikt om hits (interacties), die in de detectoronderdelen van de scanner voorkomen, te genereren. De fantoomSD wordt gebruikt om Compton- en Rayleighinteracties, die voorkomen in het gezichtsveld (FOV, Eng.: Field of View) van de scanner, te detecteren en te tellen. De bedoeling van de digitalisatieketen is het reproduceren van een realistisch waarnemingsproces door de relevante fysische waarneembare grootheden uit de hits af te leiden. De digitalisator bestaat uit een keten van verwerkingsmodules (Figuur 3) die een lijst van hits aannemen van de sensitieve detectoren en deze transformeert in pulsen, tellen genoemd. De sleutelelementen van deze keten worden hierna kort besproken.

Hittoevoeger: een deeltje dat een sensitieve detector binnendringt kan meerdere hits genereren (ten gevolge van meerdere Comptoninteracties bijvoor-

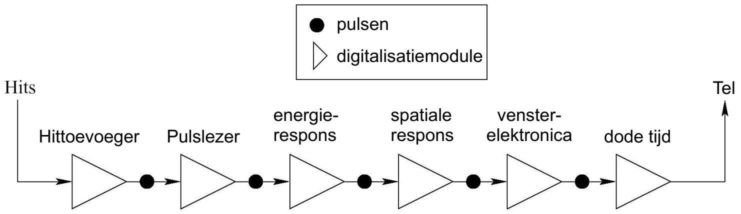

Figuur 3: De digitalisator bestaat uit een keten van verwerkingsmodules die een lijst van hits aannemen en verwerken tot een tel die een fysisch waarneembare grootheid is.

beeld). De hittoevoeger voegt de afgestane energie van deze hits samen per sensitieve detector om een puls te verkrijgen. De positie van die puls wordt bepaald als de energie-gewogen centroïdepositie van de constituerende hits. Als een deeltje interageert in verschillende sensitieve detectoren zal de hittoevoeger een lijst van pulsen genereren, één voor elke sensitieve detector.

Pulslezer: scanners (met uitzondering van deze met een één-op-één uitleesschema) hebben gewoonlijk een uitleessegmentatie die verschillend is van de detectorsegmentatie. Om dit te simuleren voegt een pulslezermodule de pulsen samen in een door de gebruiker gedefinieerde groep van sensitieve detectoren. Dit resulteert in een grotere puls met als positie die sensitieve detector waar de meeste energie werd afgezet (winnaar krijgt alles-paradigma).

Gebruikersmodules: de overige modules van de digitalisatieketen transformeren deze pulsen in de fysische waarneembare grootheden van de scanner, de tellen. Deze modules zijn energieresolutie, energiebereik, spatiale resolutie, tijdsresolutie, dode tijd en een coïncidentiesorteerder voor PET. Andere door de gebruiker gedefinieerde modules kunnen individueel toegevoegd worden om meer specifieke eigenschappen te modelleren. Het gebruik van een geschikte digitalisatieketen maakt het mogelijk om nauwlettend de elektronicarespons van de detector te reproduceren.

DigiGATE: voor de optimalisatie van de parameters van de digitalisator is het aangewezen om de resultaten van verschillende digitalisatieparameters te vergelijken met metingen. Om deze specifieke taak uit te voeren beschikt GATE over een bewerkingsprocedure die DigiGATE genoemd wordt. In deze procedure worden hits gelezen uit een gesimuleerde databestand en onmiddellijk doorgegeven aan de digitalisator. Alle condities zijn identiek, met inbegrip van de tijdsafhankelijkheid zodanig dat nieuwe tijdsrovende simulaties vermeden worden bij het evalueren van de digitalisatorparameters.

Rekentijd

Een typische PET-simulatie genereert en volgt 852 gebeurtenissen per seconde op een 1 GHz computer. Dit resulteert typisch in 16 coïncidenties per seconde voor de GATE testopstelling die bestaat uit een hypothetische PET-scanner. Voor de SPECT-testopstelling worden 417 gebeurtenissen gegenereerd en gevolgd wat slechts resulteert in 0.83 detecties per seconde. Er zijn vier oorzaken voor de hoge rekentijd bij de simulaties met collimator. Het totaal aantal geregistreerde tellen in SPECT is minder dan 0.02 % van de gegenereerde gebeurtenissen, omdat de collimator voor het kristal de meeste van de inkomende fotonen stopt en daarbij alle optredende processen registreert. Een tweede oorzaak is dat GATE elk foton doorheen elk object van het experiment volgt. Ten derde werden tot nu toe geen variantiereductiemethoden gebruikt, maar daarop wordt onderzoek uitgevoerd binnen onze groep [34]. Tenslotte werd de emissiehoek niet beperkt tot een vast bereik om de verstrooiingsprocessen in de fantomen of de terugverstrooiing van de tweede detectorkop niet te beïnvloeden.

0.2.3 Belang van nauwkeurige Monte-Carlomodellering in nucleaire geneeskunde

Monte Carlo is de enige mogelijke benadering voor alle toepassingen waar metingen niet uitvoerbaar zijn en waar analytische modellen niet beschikbaar zijn ten gevolge van de complexe aard van het probleem [2, 76]. De vier hoofdtoepassingsgebieden van Monte-Carlomodellering in de nucleaire medische beeldvorming worden hieronder in detail besproken.

Correctietechnieken voor attenuatie en verstrooiing

De aanwezigheid van verstrooiing en attenuatie in nucleaire medische beelden beperkt de nauwkeurigheid van de activiteitskwantificatie. Verstrooiing brengt geen belangrijke artefacten teweeg, in tegenstelling tot attenuatie, maar vermindert het contrast door laagfrequente vaagheid toe te voegen in het beeld. Monte-Carloberekeningen zijn krachtige instrumenten in attenuatie- en verstrooiingscorrectie, aangezien de gebruiker de mogelijkheid heeft om de gedetecteerde fotonen op te delen in hun componenten of naargelang hun interactiegeschiedenis. Monte-Carlomodellering laat dus een gedetailleerd onderzoek toe van de ruimtelijke- en de energieverdeling van Comptonverstrooiing:

energiespectra, puntspreidingsfuncties en verstrooiingsfracties kunnen gesimuleerd worden. Heel wat onderzoek en ontwikkeling werd geconcentreerd op verstrooiingscompensatie voor kwantitatieve SPECT [6, 8, 9, 11]. Vooral in gevallen waar simultaan een transmissie- en een emissiescan wordt opgenomen blijken Monte-Carlosimulaties onmisbaar. Dit zal geïllustreerd worden in sectie 0.4. In PET zijn enkele basisbenaderingen gevolgd voor verstrooiingscorrectie [58]. Hier zijn Monte-Carlosimulaties vooral belangrijk om de invloed van de verstrooiingsorde en de verhouding tussen object- en detectorverstrooiing te kunnen inschatten, om er vervolgens op een afdoende manier voor te kunnen corrigeren in een iteratief algoritme. Dit zal eveneens toegelicht worden in sectie 0.4.

Afbeeldingssystemen en ontwerp van collimatoren

Modellering van beeldformatie is een van de belangrijkste redenen van het bestaan van Monte-Carlosimulaties in de nucleaire geneeskunde. Monte-Carlomethodes kunnen belangrijke bijdragen leveren tot de ontwikkeling van nieuwe collimatorontwerpen, nieuwe detectorconstructie, nieuwe elektronica en geoptimaliseerde camerabewegingen [137]. In sectie 0.5 zullen de simulaties toegelicht worden voor een nieuw SPECT-ontwerp dat een hogere resolutie beoogt. Het bestaat uit een vaste-stof-strookdetector gekoppeld aan een roterende-vlakkencollimator. De laatste jaren werden Monte-Carlosimulaties in systeemontwerp ook vaak gebruikt om potentiële ontwerpen van positrontomografen voor kleine proefdieren te bestuderen [56, 97].

Modellering van de detector

Monte-Carlosimulaties van detectorresponsen en -efficiënties zijn uitermate belangrijk aangezien het scintillatiekristal de kritieke component is in emissietomografie. Een belangrijk interesseveld is resolutieherstel bij PET. De penetratie van annihilatiefotonen in het detectormateriaal voor de interactie, is een statistisch proces dat leidt tot aanzienlijke verplaatsing en anisotropie van de puntspreidingsfunctie [60, 103]. Compensatie voor kristalpenetratie is dus de belangrijkste uitdaging om de spatiale resolutie bij PET te verbeteren. Theoretische modellen voor die anisotrope spatiale resolutie kunnen alleen geverifieerd worden door Monte-Carlosimulaties aangezien deze experimenten afhangen van de interactiediepte, wat heel moeilijk empirisch te bepalen is met de huidige toestellen. Dit zal uitgebreid besproken worden in sectie 0.6. Monte-Carlosimulaties bewijzen ook hun nut bij het ontwerp van TOF (Eng.: Time Of Flight) PET, waar verschillende detectorkristallen getest kunnen worden en waar de invloed van tijdsresolutie op variantiereductie kan gesimuleerd worden [15, 80, 112].

Algoritmen voor beeldreconstructie

Monte-Carlosimulaties zijn heel nuttig gebleken voor validatie en vergelijkende evaluatie van beeldreconstructietechnieken, aangezien het mogelijk is om een referentiebeeld te verkrijgen waarmee de gereconstrueerde beelden vergeleken dienen te worden. Een ander onderzoeksdomein is de Monte-Carlogebaseerde reconstructie. In parallelle-bundel-SPECT gebeurt de reconstructie meestal als een verzameling van 2D analytische of iteratieve reconstructies. Om expliciet rekening te houden met het 3D karakter van het beeldvormingsproces, kan een gesimuleerde 3D projector, die de 3D fotonspreiding modelleert en ook alle andere beelddegraderende effecten in rekening brengt, gebruikt worden in een volledig 3D reconstructiealgoritme. Bij PET is de hoofddoelstelling het resolutieherstel door incorporatie van detectorresponsfuncties in de reconstructie. Sectie 0.7 zal het incorporeren in de reconstructie van gesimuleerde responsfuncties bespreken daar sectie 0.4 en sectie 0.6 zullen aantonen dat interkristalverstrooiing en kristalpenetratie belangrijke beelddegraderende effecten zijn. De detectorrespons simuleren vermijdt dat deze analytisch berekend moet worden.

Toepassingen in andere domeinen

Monte-Carlosimulaties worden in radionuclidebehandelingen, brachytherapie, hadrontherapie en radiotherapieonderzoek in grote mate gebruikt voor dosimetrische doeleinden. Hybride toestellen zoals SPECT/CT en PET/CT zullen in radiotherapeutische behandelingen toelaten om het geplande doelvolume op CT beter af te lijnen. Nauwkeurige Monte-Carlosimulaties moeten overeenkomstig gebruikt worden in het virtuele planningsysteem van de behandeling om de meest precieze schattingen van de dosis te handhaven [25]. De SPECT/CT- of PET/CT-beelden samen met de precisie van de dosimetrische Monte-Carlosimulaties zullen dus rechtstreeks de accuraatheid van de bestralingen beïnvloeden en de colaterale schade aan functionele organen verminderen.

0.2.4 Besluit en originele bijdragen

In deze sectie werd een kort overzicht gegeven van nucleaire geneeskunde en bijhorende instrumentatie om de doelstellingen van onderliggend proefschrift te situeren. De GATE-implementatie waartoe dit proefschrift bijgedragen heeft, resulteerde in twee samenwerkingsartikels [4, 68]. Daarnaast werd de klinische aanvulling besproken die ervoor zorgt dat digitale patiëntendata kunnen ingelezen worden door de simulator als een bronverdeling of als een attenuatiegeometrie [105]. Tenslotte werd een grondige literatuurstudie voorgesteld in deze sectie waaruit vier hoofdtoepassingen van Monte-Carlomethodes in nucleaire medische beeldvorming blijken. Deze worden in het vervolg van dit hoofdstuk in afzonderlijke secties besproken na de GATE-validatie die bediscussieerd wordt in de volgende sectie.

0.3 Validatie

0.3.1 Inleiding

In deze sectie tonen we validatieresultaten van GATE gebaseerd op de vergelijking van simulaties versus experimentele data, verkregen met een standaard SPECT-camera. Fotoelektrisch effect, Compton- en Rayleigh-verstrooiing zijn inbegrepen in de simulaties van het gammatransportproces. De belangrijkste componenten van de scintillatiecamera werden gemodelleerd. Meer specifiek werden een lage-energie en hoge-resolutie (LEHR, Eng.: Low Energy High Resolution) parallelle-bundelcollimator en een medium-energie en algemeen-gebruik (MEGP, Eng.: Medium Energy General Purpose) parallelle-bundelcollimator gemodelleerd, zo accuraat mogelijk gelijkend op de reële vorm. In deze validatiestudie vergeleken we de gesimuleerde en gemeten energiespectra van verschillende isotopen: ^{99m}Tc, ^{22}Na, ^{57}Co en ^{67}Ga. De sensitiviteit werd geëvalueerd door gebruik te maken van bronnen op variërende afstanden tot het detectoroppervlak. Onderzoek van de verstrooiingscomponent werd uitgevoerd in verschillende energievensters bij verschillende afstanden tot de detector en voor verschillende attenuatiegeometrieën. Spatiale resolutie werd geëvalueerd door gebruik te maken van een^{99m}Tc bron op variërende afstanden.

0.3.2 Modellering van de basisgeometrie

De camera die gebruikt werd voor de validatie is een tweekoppige AXIS-camera, gefabriceerd door Philips Medical Systems. Elke detectorkop bevat een 54 cm (transaxiaal) op 38 cm (axiaal) NaI-kristal met een dikte van 0.95 cm. De uitlezing gebeurt door PMT's en in optimale condities is de energieresolutie 9.5 $\%$ bij 140.5 keV en is de intrinsieke spatiale resolutie 0.33 cm. Het gedetailleerd simulatiemodel van de geometrie van de detectorkop vertrekt van de collimator, dan het kristal in zijn verpakking, de lichtgeleider, de PMT's en de compressieplaat, de luchtisolatie, de loden sluiting tot de beschermkap.

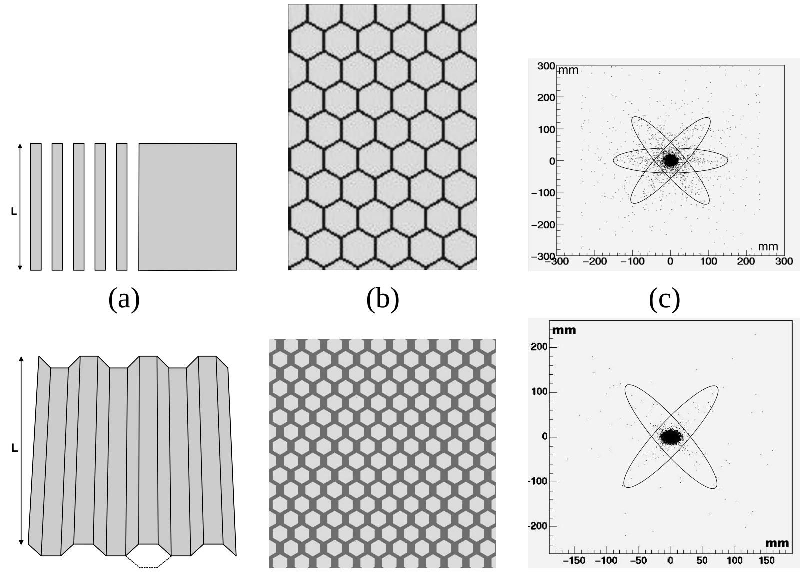

(a) (b) (c)

(d) (e) (f)

Figuur 4: Simulatie van de septale penetratie van een puntbron voor twee types van collimatoren: (a) detail gegoten collimator (lengte L); (b) transversaal beeld van een gegoten collimator; (c) gegoten collimatorpenetratie; (d) detail collimatorplaat; (e) transversaal beeld van een geplooide collimator; (f) geplooide collimatorpenetratie.

Om nauwkeurige modellen van LEHR- en MEGP-collimatoren te verkrijgen, moeten de luchtopeningen overeenkomstig de technische specificaties (diameter van de opening en de septale dikte) gemodelleerd worden. De loden collimator is gemodelleerd door het periodiek herhalen van een hexagonale luchtopening in een rechthoekige matrix. Deze matrix werd dan opgevuld met een verschoven duplicaat om een hexagonale dichtste stapeling te verkrijgen. In realiteit kan een collimator op twee verschillende manieren vervaardigd worden: door het gieten in een vorm of door het plooien van platen (Figuur 4). In het eerste geval zullen de schotten dezelfde dikte hebben in alle richtingen, in het tweede geval zal de septale dikte in de ene richting het dubbele zijn van de dikte in de andere richtingen. Men ziet bij geplooide collimatoren vier streepartefacten (figuur 4(f)) in plaats van zes (figuur 4(c)) en er is in het spectrum minder bijdrage rond de X-stralenpiek van lood. De constructiewijze heeft een belangrijke invloed op het energiespectrum, de sensitiviteit en de spatiale resolutie. Na het nemen van radiografische opnames van de collimator konden we concluderen dat we met een geplooid collimatorontwerp te maken hadden.

0.3.3 Evaluatie van de energiespectra

Energieresolutiemodule

Het scintillatieproces en optisch fotonentransport werden niet gemodelleerd voor SPECT, maar in de plaats daarvan werd een energievervager gebruikt. We implementeerden de energiemodule om een energieafhankelijke spectrale resolutie te verkrijgen volgens $\sim 1/\sqrt{E}$ (sectie 0.2.2 [99]) met een resolutie van 9.5 $\%$ bij 140.5 keV, zoals opgegeven door de producent van de detector. In figuur 5(a) worden het gesimuleerde spectrum en het opgemeten spectrum van een ^{99m}Tc-bron in lucht op 15 cm van de detector vergeleken. Er werd een goede overeenkomst gevonden wat betreft de energie en hoogte van de fotopiek en van de lood X-stralenpiek. Men kan concluderen uit de algemene gelijkheid van de vorm dat de camera goed gemodelleerd is en dat de verstrooiingsprocessen in de detector nauwgezet gesimuleerd worden. Figuur 5(b) visualiseert het spectrum van de ^{99m}Tc-bron in een attenuatie- en verstrooiingsmedium op 10 cm van de detector. De simulatie en het experiment komen volledig overeen wat betreft de toegenomen bijdrage bij lagere energieën, veroorzaakt door fotonen die verstrooid werden in het met water gevulde fantoom.

Vorm van de energiespectra bij verschillende isotopen

We hebben ook een evaluatie uitgevoerd voor verschillende andere isotopen. De energieresolutiemodule beschreven in de vorige sectie werd aangepast om de juiste energieresolutie bij de gepaste belangrijkste fotopiekenergie voor elk isotoop toe te laten (sectie 0.2.2). De validatie-experimenten werden uitgevoerd zonder een collimator, met de bron van elk isotoop op 20 cm van de detectorkop geplaatst. Voor ^{22}Na, ^{57}Co en ^{67}Ga, die verschillende energiedistributies en fotopiekenergieën hebben, worden de experimentele spectrale distributies perfect gereproduceerd door de simulaties, hetgeen bewijst dat de energievervager een breed energiebereik bestrijkt.

0.3.4 Sensitiviteitsvalidatie

We hebben ook de absolute sensitiviteit (in cps/MBq) van het GATE-model van onze detector geëvalueerd, gebruik makend van een ^{57}Co-bron van 9.3 MBq $\pm$ 3 $\%$. We voerden een planaire acquisitie van deze bron uit gedurende 600 s en registreerden het totaal aantal tellen. We simuleerden hetzelfde experiment met GATE. De absolute sensitiviteit gemeten met de ^{57}Co-bron was 231 $\pm$ 17 cps/MBq, de gesimuleerde absolute sensitiviteit 246 $\pm$ 16 cps/MBq, een verschil van slechts 6.1 $\%$ met de experimentele waarde. Deze discrepantie is waarschijnlijk te wijten aan het gebrek aan kennis over het

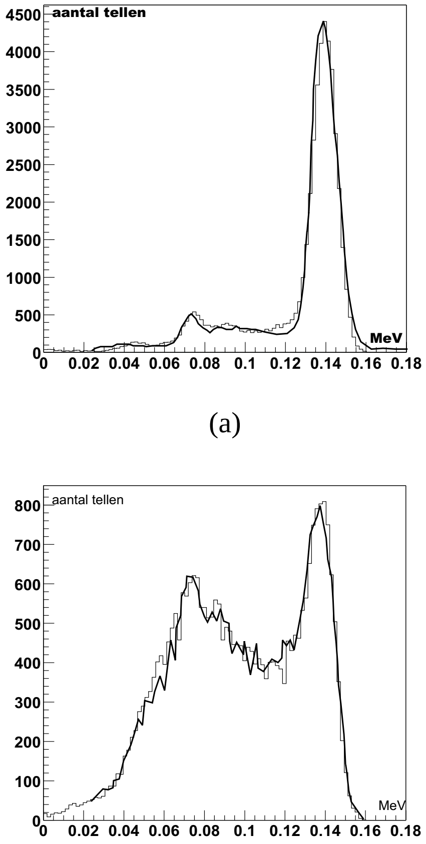

(a)

(b)

Figuur 5: Vergelijking van het gesimuleerde en gemeten ^{99m}Tc-spectrum: (a) bron in lucht; (b) met $H_2 0$-verstrooiingsmedium. Zwarte lijn: meting, grijze lijn: simulatieresultaten in histogramvorm.

gedrag van de camera beneden 40 keV in de meting. In dit experiment werden geen energievensters opgelegd, en de mogelijkheid bestaat dus dat processen werden overschat in één energiebereik en onderschat in een ander. Daarom hebben we de sensitiviteit bijkomend geëvalueerd in twee afzonderlijke energiebereiken om zeker te zijn dat er geen additionele effecten aanwezig waren in de simulaties. In het eerste experiment voerden we een statische scan (met de LEHR-collimator) uit van een puntbron op verschillende afstanden van de detector. We namen data op in het fotopiekbereik en in het Comptonbereik. We startten overeenkomstige simulaties voor elk experiment en vergeleken de gesimuleerde en experimentele sensitiviteiten. In figuur 6(a) zien we een goede overeenkomst tussen beide. We herhaalden een gelijkaardig experiment met de MEGP-collimator waarbij dezelfde bron gebruikt werd. De experimenten werden opnieuw gereproduceerd door gebruik te maken van GATE. De resultaten zijn afgebeeld in figuur 6(b) waar de sensitiviteit in beide energiebereiken is weergegeven, en waarbij we opnieuw een goede overeenkomst zien tussen simulaties en realiteit. Deze goede overeenkomsten, die binnen de foutenmarge liggen, sluiten de mogelijkheid van inter-bereik compensatiefouten uit en bevestigen een positieve sensitiviteitsvalidatie. Bovendien bleef de sensitiviteit constant met de afstand zoals theoretisch bewezen werd voor parallelle-bundelcollimatoren. Toepassing van een van de dode-tijdmodellen van GATE in de simulaties was overbodig in al deze lage telstudies.

0.3.5 Verstrooiingsprofielen

We breidden de validatie uit door verstrooiingsprofielen op verschillende afstanden van de detector op te meten, met en zonder attenuatie, in het Compton- en in het fotopiekbereik. In het eerste experiment voerden we een statische scan uit van een puntbron in lucht, op verschillende afstanden van de detector met de LEHR-collimator. Dit werd opgemeten voor het fotopiekbereik en voor het Comptonbereik. De afstand had effect op de breedte op halve hoogte (FWHM, Eng.: Full Width at Half Maximum) in het fotopiekbereik zoals verwacht voor een parallelle-bundelcollimator. De goede overeenkomst tussen de gesimuleerde en gemeten verstrooiingsprofielen in het Comptonbereik bevestigen de accurate simulatie van de verstrooiingsinteracties in de collimator en in de andere delen van de detectorkop wat reeds bleek uit de goede sensitiviteitsovereenkomst in een gelijkaardig experiment (zonder attenuerend medium), besproken in de vorige sectie. In een tweede experiment werd de puntbron vervangen door een lijnbron geplaatst in een met water gevuld cilindrisch fantoom van 22.3 cm diameter op 10 cm van de detectorkoppen, in dit geval uitgerust met de LEHR-collimatoren. Ook hier konden we besluiten dat de verstrooi-

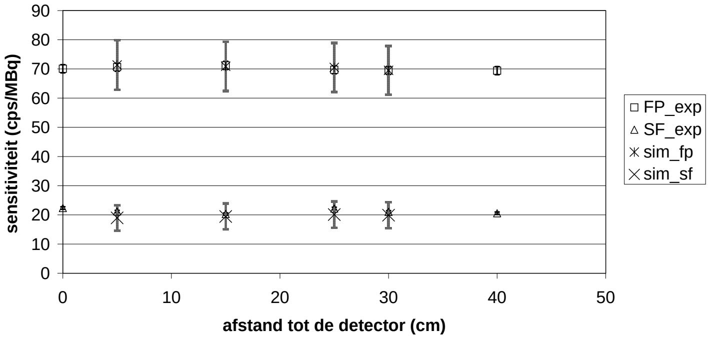

(a)

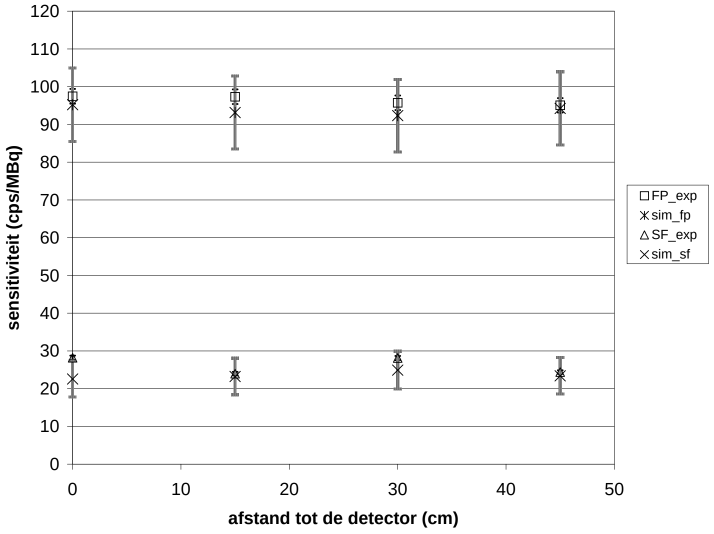

(b)

Figuur 6: Sensitiviteit: (a) LEHR-collimator; (b) MEGP-collimator. FP = fotopiekvenster (129-151 keV), SF = verstrooiing in het bereik 92-126 keV (Comptonbereik).

ingsprocessen in het fantoom gepast gemodelleerd zijn voor alle gevallen en dat de FWHM, zoals verwacht, toeneemt met de diepte van de lijnbron in het fantoom.

0.3.6 Vergelijking van de spatiale resolutie

Er werd een “spatiale vervager”-module gecreëerd om de intrinsieke spatiale resolutie, veroorzaakt door de kristalverstrooiing en door uitlezing van het signaal, te modelleren, terwijl de extrinsieke resolutie (veroorzaakt door alle andere delen van de detector) gesimuleerd werd. De spatiale vervager-module vervangt de opgenomen positie van elke tel in het kristal door een Gaussiaans vervaagde positie. De werkelijke waarde van de intrinsieke resolutie werd in de simulaties gelijkgesteld aan de waarde opgegeven door de producent (0.33 cm). De bijdrage van de collimator aan de spatiale resolutie werd volledig gesimuleerd. Om de validiteit van de spatiale vervager voor de intrinsieke resolutie en het collimatormodel te onderzoeken, werden de simulaties geverifieerd aan de hand van additionele experimenten. Figuur 7 toont de resultaten van deze experimenten, waarbij de gesimuleerde FWHM’s vergeleken worden met de gemeten FWHM’s van lijnbronnen op verschillende afstanden in lucht. Er is een goede overeenstemming bereikt binnen de foutenmarges, zowel voor de LEHR- als voor de MEGP-collimator. Tenslotte werd de experimentele setup voor de LEHR collimator verruimd door de lijnbron in het centrum van een met water gevuld fantoom in te brengen. Het fantoom werd op 10 cm van de detectorkop geplaatst zodat de lijnbron op 21 cm van de detector stond. We vonden een FWHM van 1.3 cm ± 0.1 cm bij de reële data, en 1.36 cm ± 0.02 cm in de simulatie, hetgeen bevestigt dat de spatiale resolutie nauwkeurig gesimuleerd wordt, ook in de aanwezigheid van een attenuerend medium.

0.3.7 Besluit en originele bijdragen

In deze sectie hebben we de softwareuitbreidingen besproken die geïmplementeerd werden om GATE tot een nauwkeurig simulatieplatform voor SPECT-beeldvorming te maken. De resultaten van dit validatieproces waren nauwkeurig en veelbelovend voor toekomstige toepassingen. We hebben kunnen aantonen dat GATE heel weinig benaderingen nodig heeft wanneer echte cameraontwerpen gesimuleerd worden, wat het simulatieplatform heel flexibel maakt. Het werk beschreven in deze sectie resulteerde in de eerste tijdschriftpublicatie wereldwijd over GATE-validatie [107]. Sindsdien hebben andere onderzoeksgroepen de validatie uitgebreid naar andere SPECT camera’s, naar PET-acquisitieopstellingen en naar beeldvormingssystemen voor

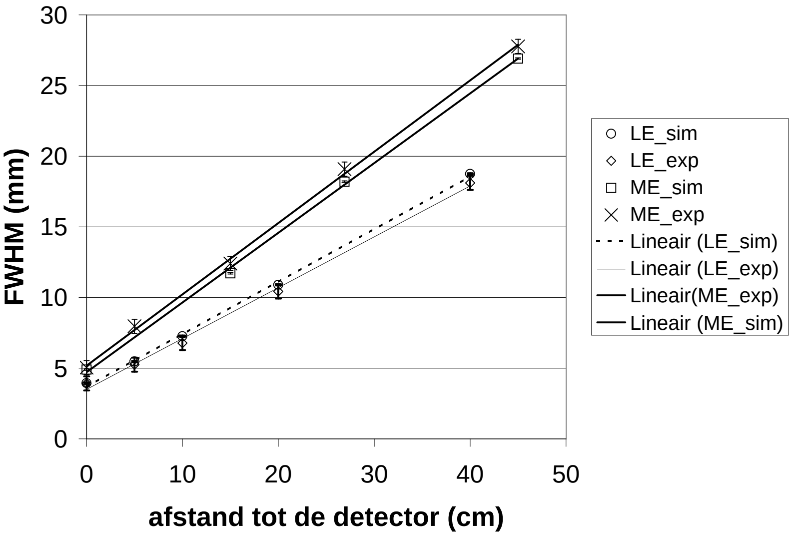

Figuur 7: Vergelijking van de spatiale resolutie voor een LEHR- en voor een MEGP-collimator (LE = lage energie, ME = medium energie, sim = gesimuleerde waarden, exp = experimentele waarden): LEsim toont de gesimuleerde spatiale resolutie, LEexp de verkregen spatiale resolutie voor de LEHR-collimator, terwijl MEsim en MEexp gesimuleerde en verkregen spatiale resolutie voor de MEGP-collimator illustreren; er werd een lineaire curve gefit aan elke dataplot.

kleine proefdieren. Het OpenGATE samenwerkingsverband concentreert zich in verder onderzoek op de validatie van GATE voor dosimetrische applicaties.

0.4 Correctietechnieken voor attenuatie en verstrooiing

0.4.1 Inleiding

Monte-Carlosimulaties laten toe om gedetecteerde fotonen op te splitsen in hun componenten of in hun gebeurtenislokatie. Een toepassing daarvan in SPECT en gammacamera-PET is simultane emissie- en transmissiebeeldvorming. Simulaties zullen in deze sectie gebruikt worden om richtlijnen inzake protocoloptimalisatie voor te stellen. Bij volledige-ring-PET hebben Monte-Carlosimulaties onder andere een meerwaarde bij het verifiëren welke verstrooiingsorde het meest bijdraagt tot de beelddegradatie. Ook de relatie tussen objectverstrooiing en kristalverstrooiing is relevant om zo optimaal mogelijk te corrigeren voor verstrooiing in een reconstructiealgoritme. Deze twee aspecten zullen in dit hoofdstuk besproken worden door de gelijktijdige emissie- en transmissiescans met Beacon te behandelen en door het relatief belang van hogere-orde-patiëntverstrooiing in PET-beelden te onderzoeken.

0.4.2 Beacon-attenuatiecorrectie voor gammacamera-PET en SPECT

Niet-uniforme patiëntattenuatiemappen verkregen met transmissiescans zijn een belangrijk middel om de kwaliteit van SPECT- en PET-beelden te verbeteren. In sommige gevallen wordt dit gedaan door gebruik te maken van een axiaal bewegende puntbron met een hoge-energie-isotoop die een waaier van fotonen uitzendt (figuur 8), wat resulteert in een asymmetrische waaierbundel-beeldvormingsgeometrie [148]. Transmissiescans worden dikwijls simultaan opgenomen met de emissiestudie om de scantijd van de patiënt te verlagen en om de efficiëntie te verhogen. Verschillende methodes werden al voorgesteld om een onderscheid te kunnen maken tussen fotonen afkomstig van een emissiebron en fotonen afkomstig van een transmissiebron [10, 42, 117]. In gammacamera-PET en in SPECT echter blijft er nog een intervenstercontaminatie bestaan: van de emissiebron in het attenuatievenster voor gammacamera-PET en van de attenuatiebron in het emissievenster voor SPECT. De meeste fabrikanten raden een additionele tijdsrovende correctiescan aan. Door middel van simulaties onderzoeken we de protocoloptimalisatie wat intervenstercontaminatie betreft. Het Beacon^{TM}(Philips)-toestel werd gebruikt om onze

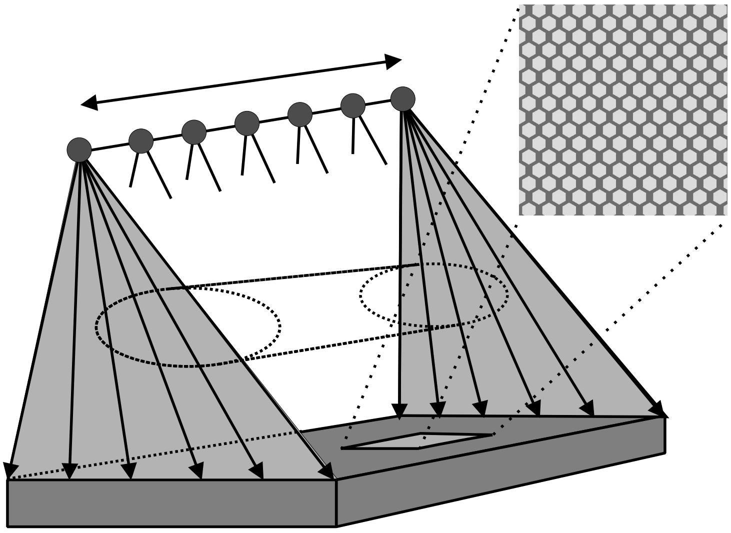

Figuur 8: Beacon^{TM} acquisitiesetup: ^{133}Ba-fotonen worden uitgezonden door een bewegende puntbron die de tegenoverliggende detector bestraalt: asymmetrische beeldvorming met stralen in waaiervorm.

simulaties te evalueren. Het bestaat uit twee bewegende ^{133}Ba-bronnen van 10 mCi met fotonemissies van 356 keV. Wanneer het Beacontoestel gebruikt wordt in gammacamera-PET-mode zijn er geen vrijheidsgraden voor kristal en collimator. De intervenstercontaminatie werd in detail onderzocht voor deze opstelling om de kritieke onderdelen op te sporen. Voor Beacon-SPECT daarentegen werden verschillende simulatiestudies met variërende kristaldikte en wisselende collimator uitgevoerd om de diverse vrijheidsgraden te evalueren om diezelfde intervenstercontaminatie te onderzoeken.

Methoden

De metingen werden uitgevoerd op een driekoppige Philips IRIX scintillatiecamera. Het Beacontoestel kan echter ook gekoppeld worden aan de AXIS-camera die tweekoppig is. Beide camera's werden gesimuleerd door gebruik te maken van GATE, waarbij alle processen in de collimator meegerekend werden. De GATE simulaties werden vooreerst gevalideerd voor AXIS, IRIX en Beacon [107, 109]. Door middel van een centraal virtueel klokobject is het mogelijk tijdsafhankelijke processen te simuleren en hen gesynchroniseerd te houden. Ook bewegende bronnen kunnen geïncludeerd worden, in dit geval door een translatiesnelheid te geven aan elementen van de brongeometrie. Dit wordt gedemonstreerd in figuur 9, waar de detectoren van een tweekoppige AXIS-camera afgebeeld zijn, gelijktijdig draaiend met de lineaire beweging van de ^{133}Ba-puntbronnen. Daarnaast wordt ook het verval van emissie- en transmissiebronnen gesynchroniseerd. De krachtige ROOT [18] data-analysemodules van GATE maken het mogelijk om een onderscheid te maken tussen de gedetecteerde gebeurtenissen, afkomstig van de emissiebronnen enerzijds en de geregistreerde fotonen gegenereerd door de Beacon attenuatiebronnen anderzijds, zodat een emissiebeeld en een transmissiebeeld gereconstrueerd kunnen worden wanneer de simulatie beëindigd is.

Gammacamera-PET

Eerst werden gammacamera-PET-simulaties uitgevoerd om te evalueren welke parameters belangrijk zijn voor de neerwaartse verstrooiing van de^{18}F fotonemissies (511 keV) in het ^{133}Ba-attenuatie-energiebereik. Figuur 10 toont een intrinsieke contaminatie van het emissievenster voor deze gammacamera-PET toepassing, en ook een neerwaartse contaminatie van het emissie-isotoop in het attenuatiebereik. Figuur 11 toont de bijdragen in de verstrooiingsorde en duidt het relatief belang van elk deel van de opstelling aan. Als we de nietverstrooide fotonen en de intrinsieke verstrooiingsgebeurtenissen van het fantoom weglaten, is er te zien dat de grootste degradatie veroorzaakt wordt door de openframe filterlagen en door de einddelen van de detector. In toekomstige studies moet dus een herontwerp van deze cameraonderdelen nagestreefd worden voor simultane emissie- en transmissie-gammacamera-PET toepassingen.

Beacon-SPECT

Voor Beacon-SPECT werden drie types simulaties uitgevoerd, gezien er twee additionele vrijheidsgraden zijn in deze toepassing: collimator en kristaldikte. Het opnemen van de attenuatiemap van een koud, met water gevuld, cilindrisch fantoom werd gesimuleerd door gebruik te maken van het GATE-model van de IRIX-camera (1.905 cm kristal), met de LEHR-collimatoren (0.061 cm straal en 0.0203 cm septale dikte) en het Beacontoestel. Dit werd voor dezelfde camera herhaald met een dun kristal van 0.9525 cm en met dezelfde LEHR-collimatoren. Tot slot werden de simulaties overgedaan met de MEGP-collimatoren (0.170 cm straal en 0.0864 cm septale dikte) vastgemaakt aan de originele 1.905 cm-dikke kristaldetectoren. Deze opstelling wordt immers klinisch toegepast in vele medium-energiestudies. In de volgende paragrafen worden deze drie opstellingen vergeleken om de neerwaartse verstrooiing van de attenuatiebron in het emissievenster te kunnen kwalificeren. Figuur 12 toont

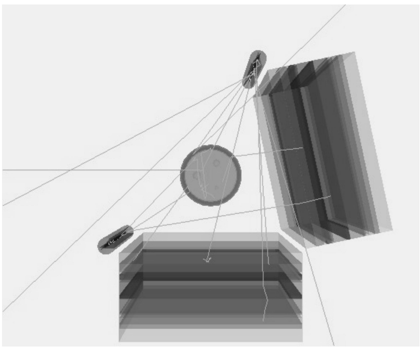

(a)

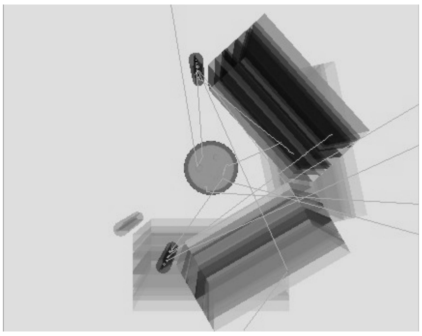

(b)

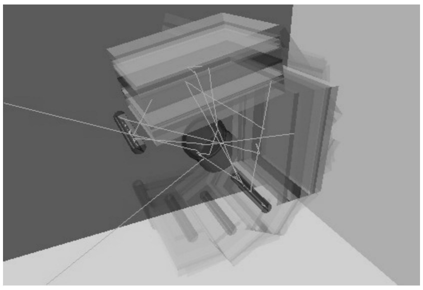

(c)

Figuur 9: Gesimuleerd model van een tweekoppige AXIS-camera: collimator, kristal in zijn aluminium verpakking, lichtgeleider, PMT's, compressieplaat, luchtisolatie en loden afsluiter zijn afgebeeld voor elke detectorkop. Een watergevuld cilindrisch fantoom werd gemodelleerd in het centrum van de FOV: (a) detail van de fotonemissies van de bewegende ^{133}Ba puntbronnen, (b) rotatie van de detector; (c) idem.

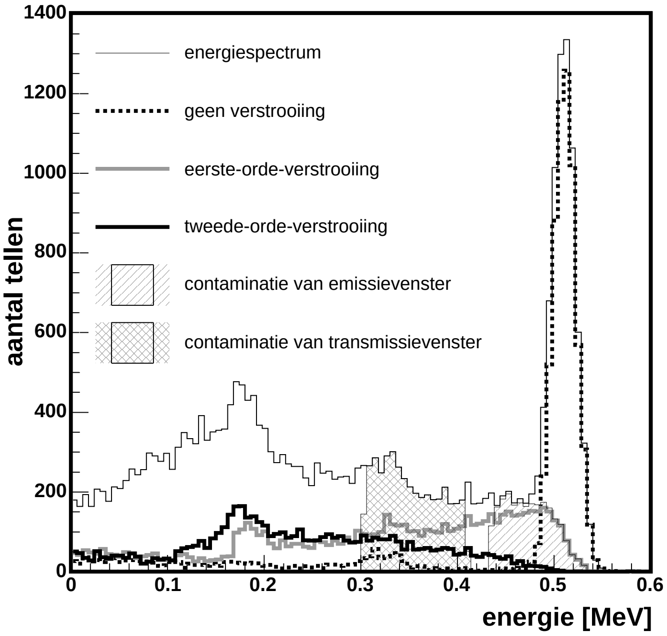

Figuur 10: ^{18}F-spectrum van een gammacamera-PET-opstelling: intrinsieke verstrooiingscontaminatie van ^{18}F in het emissievenster (30% rond 511 keV) en neerwaartse verstrooiingscontaminatie van ^{18}F in het ^{133}Ba-transmissie-energiebereik (45% rond 356 keV) werden gearceerd, eerste- en tweede-orde-verstrooiingsbijdragen van de 511 keV emissiefotonen werden afgebeeld.

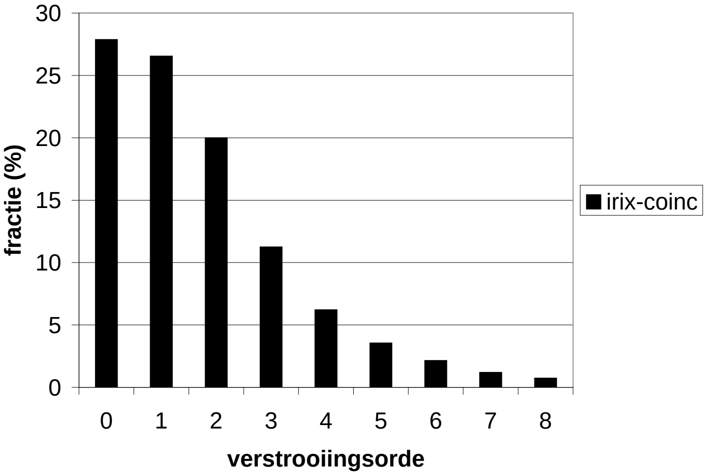

(a)

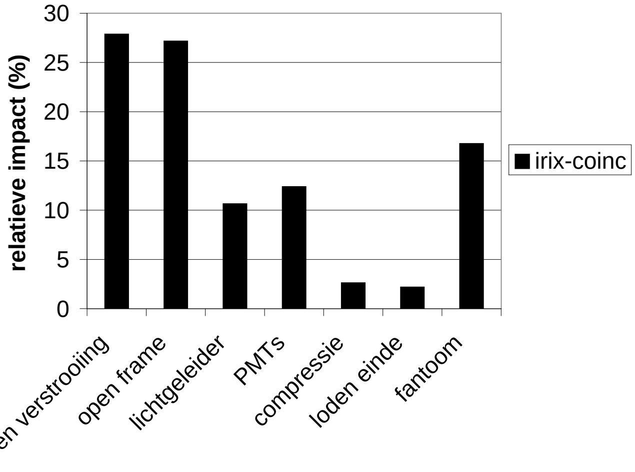

(b)

Figuur 11: Opstelling van gammacamera-PET : dik kristal, openframecollimatoren: (a) verstrooiingsclassificatie en (b) relatief belang van elk detectoronderdeel.

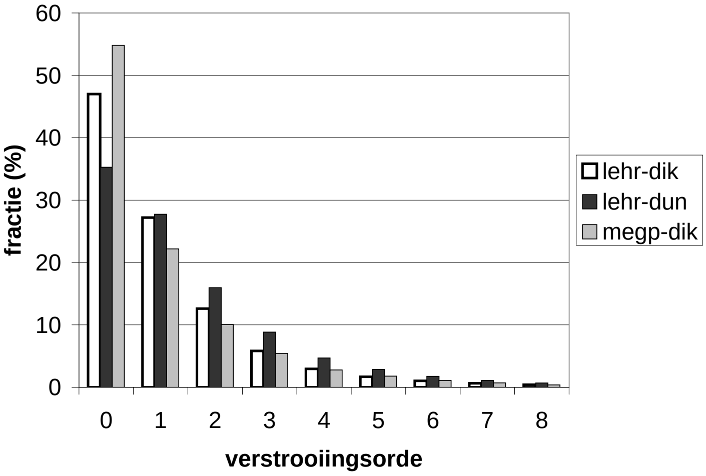

Figuur 12: Verstrooiingsorde voor de drie opstellingen: LEHR-dik kristal, LEHR-dun kristal, MEGP-dik kristal; verstrooiingsorde = 0 duidt op primaries.

de relatieve bijdrage van elke verstrooiingsorde tot het resulterend aantal gedetecteerde fotonen aan. Er werden minder niet-verstrooide fotonen gedetecteerd bij een dun kristal en veelvoudige verstrooiing heeft een grotere invloed vergeleken met de twee andere opstellingen. Dit duidt op terugverstrooiing aan de einddelen van de detector, wat bevestigd wordt in figuur 13. Terugverstrooiing zorgt ervoor dat de fotonen een grote hoeveelheid energie verliezen, waardoor de hoge energie ^{133}Ba-fotonen in het lage-energie-emissiebereik terecht komen. Dit is gedemonstreerd in figuur 14 die het spectrum van een typische opstelling toont. Bovendien is dit het meest uitgeproken bij de opstelling met het dunne kristal aangezien de fotonenflux op de einddelen dan groter is door het kleinere stoppend vermogen. In figuur 15 blijkt duidelijk dat de sensitiviteit voor transmissiebeeldvorming doorheen de MEGP-collimator een stuk lager ligt dan bij de LEHR-opstellingen wat ervoor zorgt dat het contrast van attenuatiemappen bij simultane medium-energie-emissie- en transmissiestudies te laag ligt, vooral bij dikke patiënten. Daarom stellen we voor om medium-energie-emissiestudies uit te voeren op LEHR collimatoren wat intrinsiek gepaard gaat met een ernstige fotonverstrooiing. In sectie 0.7 zullen we echter aantonen dat het incorporeren van Monte-Carloinformatie in de reconstructie een indrukwekkend resolutieherstel oplevert voor de variant van de LEHR-collimator en dat de medium-energiefotonspreiding volledig geïnverteerd wordt. In sectie 0.7 zal blijken dat dit performantieherstel min-

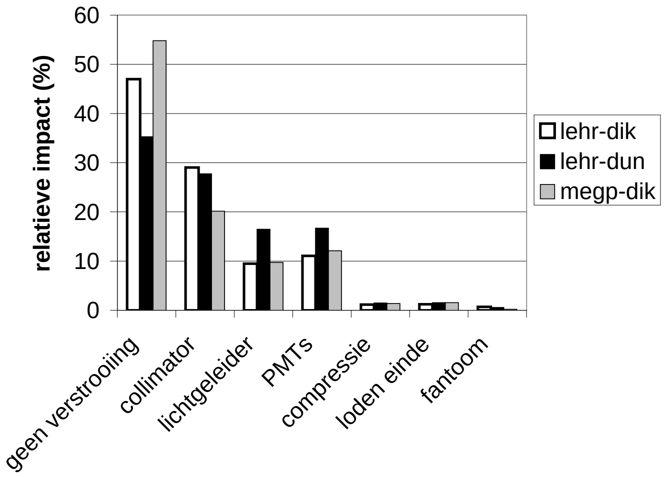

Figuur 13: Relatief belang van elk detectordeel bij de drie opstellingen: LEHR-dik kristal, LEHR-dun kristal, MEGP-dik kristal door telling van de verstrooiingsgebeurtenis in elke afzonderlijk deel, gedeeld door het totaal aantal gedetecteerde gebeurtenissen.

der is bij de MEGP-collimator omdat de individuele positie van de grotere gaten te belangrijk wordt. In alle gevallen levert de reconstructie van medium-energie-isotopen op LEHR dus het beste resultaat, op voorwaarde dat de systeemrespons volledig gesimuleerd en in rekening gebracht wordt.

0.4.3 Verstrooiingsanalyse bij PET

De karakterisatie van verstrooiing is een heel belangrijk onderwerp bij 3D PET. Het hoofddoel van deze sectie is om door middel van simulaties te begrijpen welke objectverstrooiingsorde overheerst in het fotopiekvenster. Een tweede doel is om het verschil tussen verstrooiingsinvloeden van het fantoom en van kristalverstrooiing te kwantificeren.

Methoden

Er werd een Monte Carlo GATE-model van de Philips Allegro PET-scanner geïmplementeerd. Aangezien het belang van kristalverstrooiing sterk afhankelijk is van de fotoelektrische fractie (verhouding van het aantal waarnemingen in het fotopiekbereik van fotoelektrisch effect tot het totaal aantal waarnemingen, met inbegrip van meervoudige Compton- en fotoelektrische gebeurtenis-

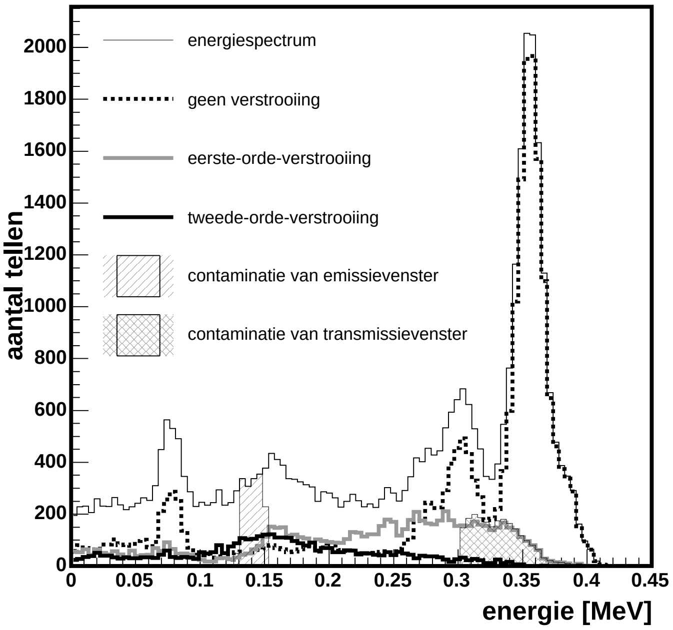

Figuur 14: ^{133}Ba-spectrum van een typische opstelling:neerwaartse verstrooiings-contaminatie van de ^{133}Ba fotonen in het energiebereik van de ^{99m}Tc-emissie en intrinsieke verstrooiing in het ^{133}Ba-transmissievenster zijn gearceerd, eerste- en tweede-orde-verstrooiingsbijdragen voor de 356 keV transmissiefotonen werden afgebeeld.

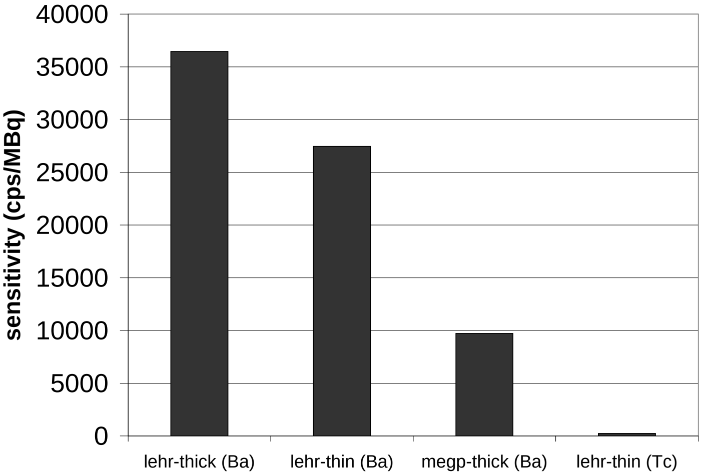

Figuur 15: Sensitiviteit van de drie opstellingen: LEHR-dik kristal, LEHR-dun kristal, MEGP-dik kristal; vergeleken met een typische ^{99m}Tc emissieopname.

sen), werd deze scanner gesimuleerd met verschillende materiaaltypes: GSO, LSO, BGO, en twee nieuwe materialen ($LaBr_3$ en LuI_3). Geometrische aspecten van de Allegro werden constant gehouden. Voor elk kristalmateriaal werd een geschikte energieresolutie en dode tijd toegepast. Er werden twee fantoomstudies uitgevoerd.

NEMA-fantoomstudie en antropomorfe fantoomstudie

Een eerste fantoomstudie, een gesimuleerde 6 min durende acquisitie van het NEMA 2001 verstrooiingsfantoom [83] gevuld met een ^{18}F bron van 1μCi, werd gebruikt om de ruisequivalente telkadans (NEC) van de kristalmaterialen als een waardemeter te bepalen. Aangezien willekeurige coïncidenties verwaarloosbaar zijn bij deze lage activiteit, definiëren we de NEC als volgt: $NEC = \frac{T^2}{T+S}$ met T de ware coïncidenties en S de verstrooide gebeurtenissen. Tabel 1 toont dat de fantoomverstrooiing van eerste orde de fantoomverstrooiing van tweede en hogere orde overheerst in het fotopiekbereik voor alle courante en nieuwe kristallen. Wanneer we de performantie van de gebruikte detectormaterialen vergeleken, vonden we dat de NEC van LSO en BGO superieur was aan de andere (figuur 16(a)). Dit is vooral te wijten aan hun hogere sensitiviteit (figuur 16(b)) aangezien de fotoelektrische fractie in deze systemen hoger is. Een hogere fotoelektrische fractie betekent ook dat de

Tabel 1: Bijdragen tot de verstrooiingsorde van het fantoom.

	BGO	LSO	GSO	$LaBr_3$	LuI_3
1ste orde (%)	90.2	90.0	88.9	91.0	90.5
2de orde (%)	9.1	9.6	10.3	8.4	8.8
≥3de orde (%)	0.7	0.4	0.8	0.6	0.7

spatiale en energieresolutie minder gedegradeerd zijn ten gevolge van Comptonverstrooiing van het kristal. Deze effecten zijn weergegeven in Figuur 17 waar de relatieve invloed van kristalverstrooiing, fantoomverstrooiing en verstrooiing in de detectoronderdelen weergegeven is. Een tweede fantoomstudie bestond uit het simuleren van een antropomorf gevoxelizeerd fantoom. Het Hoffman-hersenfantoom werd gebruikt als een gevoxelizeerde emissiebron en terzelfdertijd als een attenuatiemedium [105]. De laatste studie was bedoeld om te verifiëren of de conclusies van de eerste studie geldig waren voor patiëntachtige objecten. Het belang van hogere verstrooiingsordebijdragen in het fotopiekvenster bedroeg bij deze fantoomstudie 9.6 % terwijl dit 9.9% bedroeg in de NEMA-studie.

Reconstructie

Het werd duidelijk dat alleen verstrooiing van eerste orde de fotopiekacquisities significant degradeert bij alle kristaltypes aangezien de bijdrage van hogere verstrooiingsorde in beide fantoomstudies lager dan 10 % is. Voor het incorporeren van de verstrooiingscorrectie in de reconstructie stellen we voor om gesimuleerde data te gebruiken. Om te corrigeren voor patiëntverstrooiing in de reconstructie kan men de verstrooiingsbijdrage simuleren met een initieel geschatte emissieverdeling om dan die gesimuleerde bijdrage op te tellen bij de voorwaartse projectie. Detectorverstrooiing kan gemodelleerd worden in de voorwaartse projector zelf om te corrigeren voor verkeerde kristallokalisatie wat belangrijk is bij materialen met een lage fotoelektrische fractie. De kristalverstrooiing moet dus gemodelleerd worden in de systeemmatrix of geïncorporeerd worden in een natuurlijke-pixelbenadering wat besproken zal worden in sectie 0.7.

0.4.4 Besluit en originele bijdragen

In deze sectie werden suggesties gedaan voor protocoloptimalisatie in Beacon-PET op een hybride camera. De belangrijke detectoronderdelen voor conta-

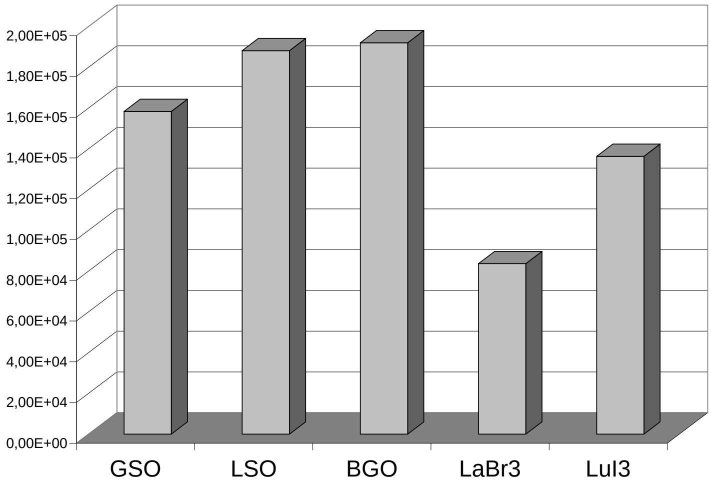

(a)

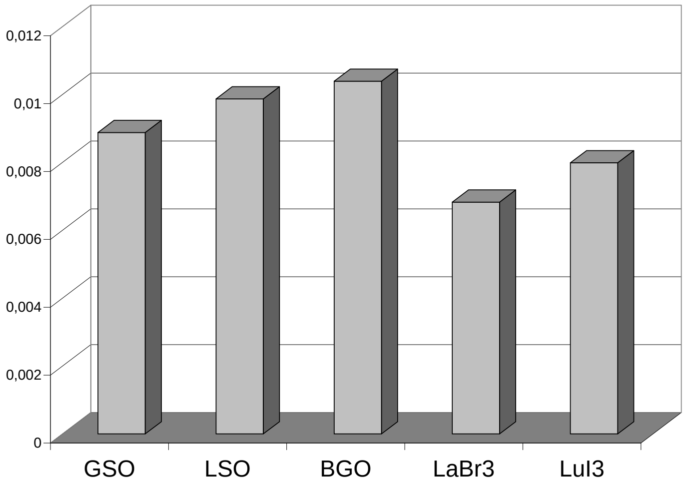

(b)

Figuur 16: (a) NEC: $T^2/(T+S)$; (b) sensitiviteit: gedetecteerde tellen/emissies.

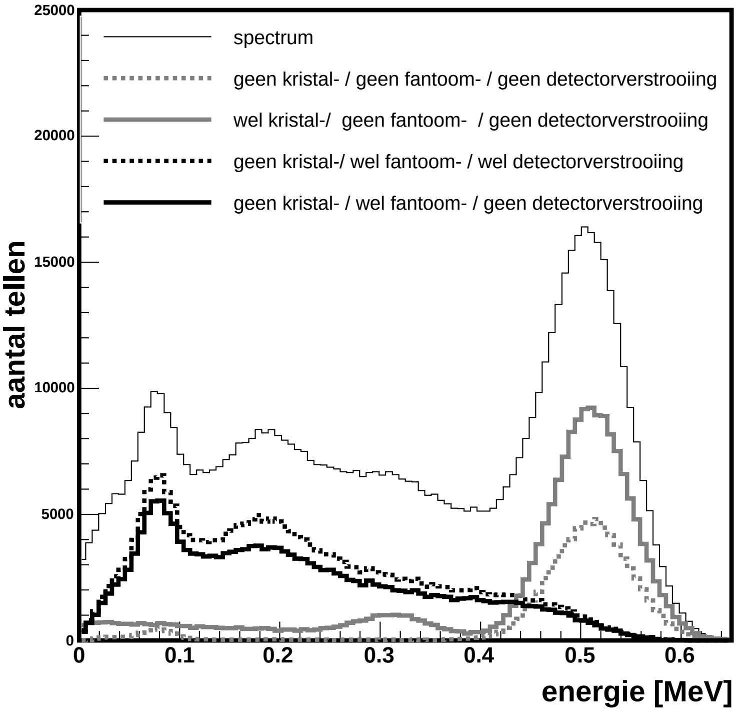

Figuur 17: Illustratie van de relatieve verstrooiingsbijdragen bij GSO.

minatie van het attenuatiebeeld door neerwaartse verstrooiing van het emissie-isotoop werden uitgetekend en ontwerpinspanningen moeten hierop geconcentreerd worden. De hoofdconclusie voor Beacon-SPECT anderzijds is dat een dikke kristaldetector gekoppeld aan een LEHR-collimator de beste oplossing is om attenuatiemappen in lage- en in medium-energietoepassingen te verkrijgen. Voor medium-energie-emissiestudies moet wel de Monte-Carlogebaseerde reconstructie gebruikt worden die in sectie 0.7 gedetailleerd uitgewerkt wordt. Daarnaast werd ook een kwalitatieve interpretatie getoond voor het belang van meervoudige verstrooiing in 3D-PET. Het werd duidelijk dat alleen verstrooiing van eerste orde de fotopiekacquisities significant degradeert voor alle detectormaterialen. Het werk voorgesteld in deze sectie resulteerde in een tijdschriftartikel [106] en in drie publicaties in de proceedings van internationale conferenties [105, 108, 109]. Het is de eerste simulatiestudie die zo uitgebreid gebruik maakt van de virtuele GATE-kloksynchronisatie. Het is ook de eerste simulatiestudie in het domein die het belang van patiëntverstrooiing van veelvoudige orde op antropomorfe fantomen evalueert voor verschillende kristalmaterialen, in het bijzonder wat $LaBr_3$ en LuI_3 betreft.

0.5 Beeldvormingssystemen en collimatorontwerp

0.5.1 Inleiding

Beeldformatiemodellering is een van de belangrijkste bestaansredenen van Monte-Carlosimulaties in de nucleaire geneeskunde. In deze sectie gebruiken we Monte-Carlosimulaties om een nieuw SPECT-ontwerp, bestaande uit een roterende-vlakkencollimator geplaatst op een strookvormige vastestofdetector, te onderzoeken. De studie bestond meer specifiek uit het modelleren van het Solstice prototype (Eng.: Solid State with Compact Electronics) dat een hogere spatiale resolutie bij een vergelijkbare sensitiviteit beoogt.

0.5.2 Solstice-detector: basiskenmerken

Het concept van de Solstice-camera (figuur 18(a)) [43, 52] bestaat uit een roterende-vlakkencollimator geplaatst op een strookvormige detector, vervaardigd uit Cadmium Zink Telluride (CZT). De collimatorschotten zijn gemaakt uit wolfraam en lood. We modelleerden de CZT-strook met de correcte pixelisatie-periode van 1.8 mm (CZT-RV). Elke fysische interactie, behalve de productie van elektron-gat paren en het verval naar subniveau's, werd gemodelleerd (figuur 18(b)). Figuur 19 toont dat de spatiale resolutie van het ontwerp met de roterende schotten beter is dan bij een klassiek

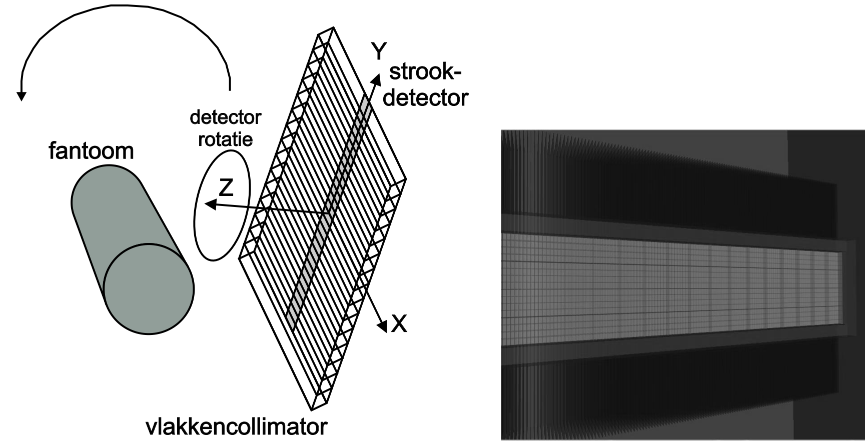

(a) (b)

Figuur 18: Solstice: (a) illustratie van de Solstice-detector; (b) model van deze opstelling: visualisatie van de CZT-strook en de collimatorschotten.

commercieel SPECT-systeem aangezien de typische referentie spatiale resolutie 0.53 cm is op 10 cm van de detector in vergelijking met 0.66 cm voor de AXIS-detector op dezelfde afstand. Om het mogelijk te maken de sensitiviteit en de energieresolutie van dit nieuwe toestel in relatie tot andere prototypes te onderzoeken bij vergelijkbare spatiale resolutie, werden twee additionele Monte-Carlomodellen geïmplementeerd: enerzijds een parallelle-bundelcollimator die gemodelleerd werd zodat elke pixel van de vaste-stofdetector gepaard is met een collimatorgat en anderzijds een traditionele monokristal NaI-Angercamera met dezelfde parallelle-bundelcollimator. Figuur 20 toont duidelijk dat de hoogste sensitiviteit verkregen wordt voor de opstelling met roterende-vlakkencollimator hoewel moet opgemerkt worden dat bij deze laatste opstelling de fotonen opgenomen worden in vlakken en dus minder informatie bevatten. De referentie energieresolutie voor een CZT-detector in de Solstice opstelling is 5 % terwijl dit oploopt tot 10 % bij een klassieke NaI-detector. De bijdrage van kristalverstrooiing in het fotopiekbereik is dus heel wat belangrijker bij de NaI-detector dan bij de CZT-detector. Figuur 21 toont een vergelijking van de fotopiekverstrooiingscontaminatie bij de drie toestellen. De verstrooiingsbijdrage voor beide toestellen met vaste-stofdetector is vrijwel gelijk, en ze overtreffen beide de klassieke scintillatiecamera op dit vlak.

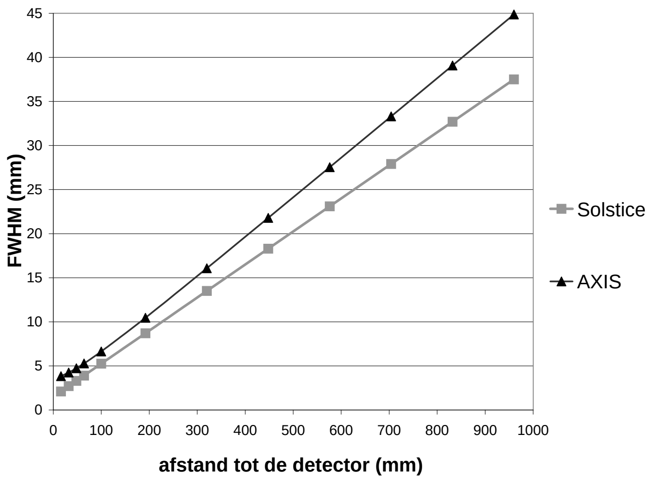

Figuur 19: Vergelijking van de spatiale resolutie van een traditionele AXIS-SPECT-camera (zwart) met Solstice (grijs).

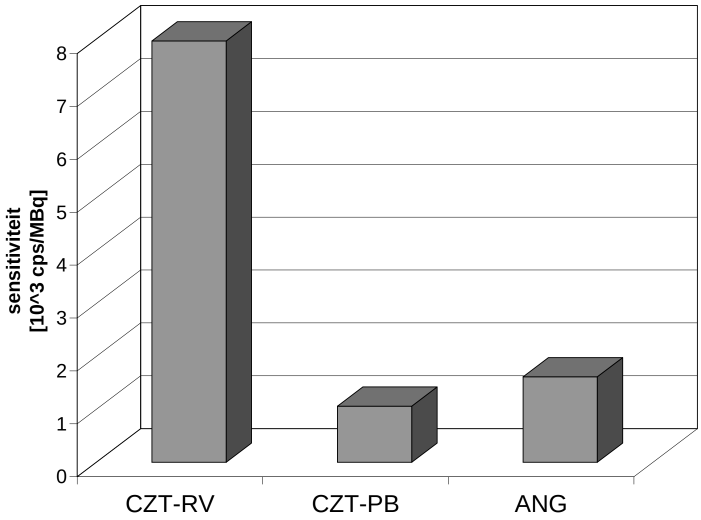

Figuur 20: Vergelijking van sensitiviteit: (a) voor ontwerp met roterende vlakken (kernwoord: CZT-RV); (b) voor de gepixeliseerde vaste-stofdetector met parallelle-bundelcollimator (kernwoord: CZT-PB); (c) voor de klassieke NaI-Angercamera (kernwoord: ANG) met diezelfde parallelle-bundelcollimator.

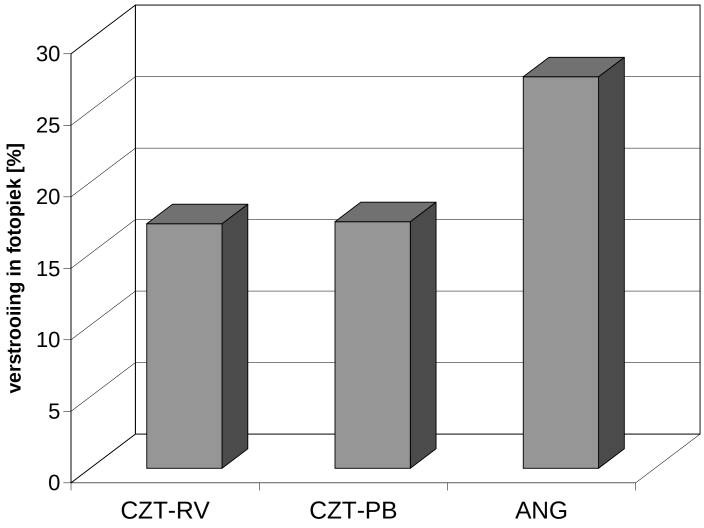

Figuur 21: Verstrooiingscontaminatie in het fotopiekbereik voor de drie toestellen, CZT-RV = kernwoord voor toestel met roterende-vlakkencollimator, CZT-PB = kernwoord voor parallelle-bundelcollimator en ANG = kernwoord voor een klassieke Angercamera.

0.5.3 Algemene geometrische transfertfunctie voor een vlakkencollimator op een strookvormige detector

De geometrische resolutie- en sensitiviteitseigenschappen van een collimator kunnen beschreven worden met de zogenaamde effectieve puntspreidingsfunctie van de collimator. Dit is de detectorrespons voor een puntbron uitgemiddeld over alle mogelijke relatieve openingsposities. In deze sectie willen we de effectieve puntspreidingsfunctie voor een strookvormige detector met een vlakkencollimator afleiden. De geometrische transfertfunctie van de collimator, die de Fouriertransformatie is van de effectieve puntspreidingsfunctie, zal geanalyseerd worden en dit zal toelaten om relevante analytische en kwantitatieve conclusies te trekken in verband met sensitiviteit en spatiale resolutie. Deze bevindingen zullen geverifieerd worden door gebruik te maken van Monte-Carlosimulaties.

Formalisme

Om de detectorrespons van een strookvormige detector uitgerust met een vlakkencollimator te modelleren, veronderstellen we een continue onbegrensde detector en een puntbron op een afstand Z van de voorkant van de vlakkencollimator. De openingsfunctie van de strookvormige oppervlakte, bepaald door de opening tussen twee schotten is $a(\overline{r},\overline{r}_c)$. Straling komend van de puntbron en gedetecteerd door het openingsoppervlak met centrum op positie $\overline{r}_c$ zal passeren door een bijbehorend oppervlak op het voorvlak van de vlakkencollimator bepaald door de openingsfunctie $d(\overline{r}',\overline{r}'_c)$ (figuur 22). De projectie van de openingsfunctie van het voorvlak van de collimator op het detectoroppervlak is $a'(\overline{r},\overline{r}_c)$. De overlappingsgraad tussen $a(\overline{r},\overline{r}_c)$ en $a'(\overline{r},\overline{r}_c)$ zal het gedrag van de detector in dat punt bepalen. De fotonflux $\phi_{L,B,W}(\overline{r},Z,D)$ die een detectiepunt $\overline{r}$ vanuit een puntbron op afstand Z van het voorvlak van de collimator bereikt, wordt bepaald door integratie over het aantal openingsoppervlakken waarvoor het detectiepunt behoort tot de doorsnede van $a(\overline{r},\overline{r}_c)$ en $a'(\overline{r},\overline{r}_c)$. De detectorrespons ver van de schotten ($Z >> L$) van een strookvormige detector met vlakkencollimator wordt uiteindelijk na een extensieve afleiding:

$$\begin{aligned}\Phi_{L,B,W}(\nu_x,y,Z,D) \cong & \frac{kB^2\,(Z+L)^2}{L\left((Z+L)^2+y^2\right)^{\frac{3}{2}}} \\ & \Pi^2\left(\frac{y-D}{W}\right)\text{sinc}\left(\pi B\frac{Z+L}{L}\nu_x\right)^2 .\end{aligned} \tag{1}$$

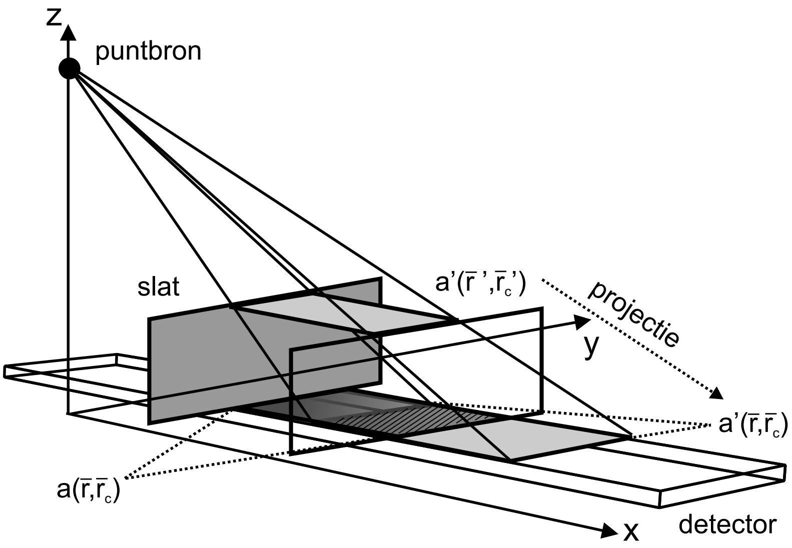

Figuur 22: Detail van twee naburige schotten om de overlap van het actieve detectoroppervlak en de projectie van de openingsfunctie op het collimatoroppervlak in dat gebied te visualiseren. De overlappingsgraad tussen $a(\overline{r}, \overline{r}_c)$ en $a'(\overline{r}, \overline{r}_c)$ zal het gedrag van de detector in dat punt bepalen.

met L de hoogte van de vlakkencollimator, W de breedte van de strookvormige detector, B de afstand tussen twee schotten en

$$\Pi\left(x\right)=\begin{cases}0 & for|\ x\ |>\frac{1}{2}\\ \frac{1}{2} & for|\ x\ |=\frac{1}{2}\\ 1 & for|\ x\ |<\frac{1}{2}.\end{cases}$$

Analyse

Aan de hand van deze geometrische transfertfunctie analyseerden we de spatiale resolutie, de sensitiviteit en de lijnspreidingsfuncties en verifieerden de resultaten door middel van nauwkeurige GATE Monte-Carlosimulaties.

Sensitiviteit: uit uitdrukking 1 bekomt men voor een detectiepunt $\overline{r}=(x,y)$ dat deel uitmaakt van de strookvormige detector een DC-frequentiecomponent die benaderend gewogen is door een factor evenredig met $\frac{\cos^2(\theta)}{\left((Z+L)^2+y^2\right)^{\frac{1}{2}}}$, met θ de incidentiehoek tussen een straal van de puntbron en de normaalvector op de detector en met $\left((Z+L)^2+y^2\right)^{\frac{1}{2}}$ de afstand tussen puntbron en detector. Deze wegingsfactor bepaalt de sensitiviteit voor een locatie in de FOV. Als verificatie werd een rechthoekig grid van puntbronnen gesimuleerd in de FOV op verschillende afstanden van het voorvlak van de vlakkencollimator en van het centrum van de detectorstrip. De resultaten van deze simulatiestudie bevestigden dat het verloop van de sensitiviteit omgekeerd evenredig is met de afstand. We voerden bijkomende simulaties uit om de invloed van de incidentiehoek op de sensitiviteit te evalueren. De vergelijking tussen de simulatieresultaten en de theoretische berekeningen is getoond in figuur 23. De hoogste sensitiviteit werd geregistreerd bij puntbronnen voor de detector, terwijl de sensitiviteit vermindert volgens $\cos^2(\theta)$ voor schuin invallende fotonen, hetgeen theoretisch voorspeld wordt door vergelijking 1.

Spatiale resolutie: afgezien van de wegingsfactor is uitdrukking 1 enkel afhankelijk van Z of dus van de verticale afstand tussen de puntbron en het collimatoroppervlak. Vandaar dat het resolutiegedrag van een strookvormige detector met een vlakkencollimator alleen bepaald zal worden door de loodrechte afstand tussen de bron en het collimatoroppervlak. Om dit gedrag te verifiëren werden vier afzonderlijke puntbronnen in de FOV geplaatst op zekere afstand van het voorvlak van de collimatorschotten en op verschillende afstand van het

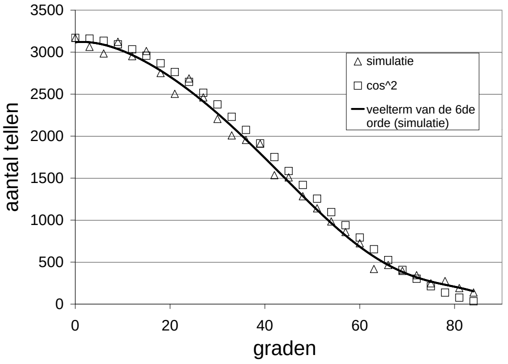

Figuur 23: Vergelijking tussen het gesimuleerde en het berekende sensitiviteitsverloop: resultaten voor de hoekafhankelijkheid.

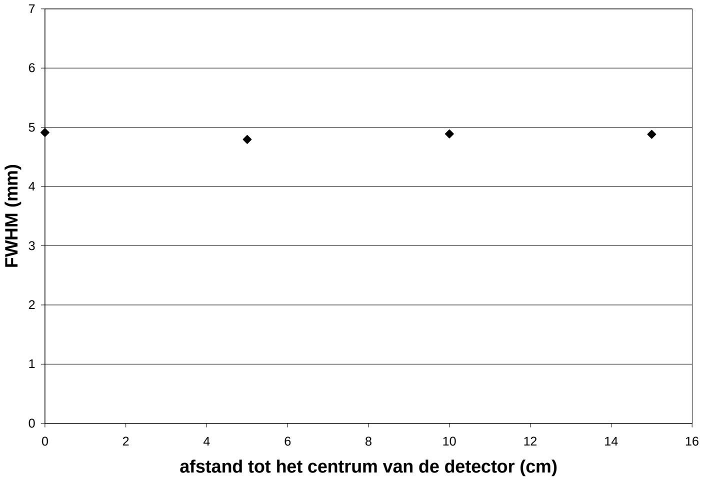

Figuur 24: Resolutiegedrag voor puntbronnen op een afstand $Z = 10$ cm van het voorvlak van de vlakkencollimator.

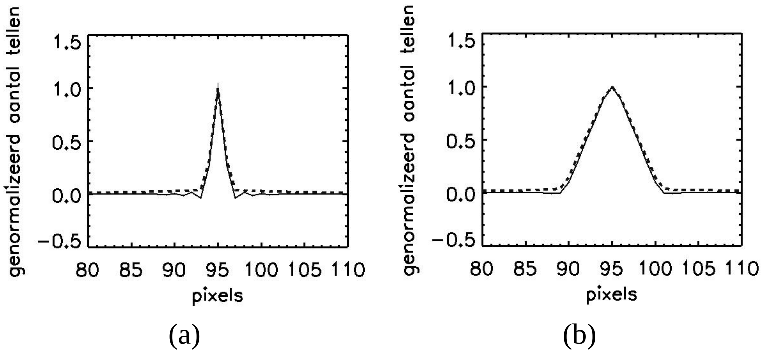

Figuur 25: Vergelijking van de gesimuleerde (streeplijn) en de berekende transaxiale profielen van een lijnbron geplaatst in een vlak evenwijdig aan het collimatoroppervlak; (a) op 2,5 cm van de collimator; (b) op 20 cm van de collimator. De abscis is uitgedrukt in pixels (1.8 mm periode) die in dit geval de 192 openingen van het detectorsysteem (34.56 cm) langs de x-as zijn. De lijnbron is geplaatst op pixel 95.

centrum van de detectorstrook. De resultaten van deze simulaties zijn weergegeven in Figuur 24 waar het resolutiegedrag van deze puntbronnen getoond is op een afstand van 10 cm van het voorvlak van de vlakkencollimator. Hieruit blijkt dat de resolutie constant blijft op vaste afstand.

Profielen: aangezien de inverse ééndimensionale Fouriertransformatie toegepast op uitdrukking 1 de lijnspreidingsfunctie oplevert, zijn we in staat het transaxiaal profiel van een lijnbron in een vlak evenwijdig aan het collimatorvlak, op zekere afstand van de collimator, te verkrijgen. We namen deze opstelling over in simulaties door lijnbronnen op verschillende afstanden van het collimatoroppervlak te plaatsen en we vergeleken zo de resulterende gesimuleerde profielen met de berekende resultaten, zoals getoond in figuur 25. Er werd een goede overeenkomst gevonden en het driehoekig profiel, resulterend uit de convolutie van twee rechthoeksfuncties, wordt bevestigd door de simulaties. Deze geometrische transfertfunctie is een ver-veld model en dicht bij de detector moeten extra factoren in rekening gebracht worden zoals we aantonen in [129]. Uit verder onderzoek bleek dan ook dat het verminderen van de openingsafmeting het belang van de exacte posities van de individuele openingen vermindert en de discrepantie dicht bij de detector (figuur 25(a)) wegwerkt.

0.5.4 Studie van waarnemersperformantie

De informatieinhoud van een foton gedetecteerd op de drie systemen besproken in voorgaande paragrafen, is verschillend. Dit zorgt ervoor dat de sensitiviteit geen objectieve waardemeter is en bijgevolg werd additioneel een ROC-studie (Eng.: Receiver Operating Characteristics) [115] uitgevoerd op gesimuleerde datasets om de hotspot-detecteerbaarheid van de drie systemen te evalueren. Daartoe werden de datasets van hotspots gesimuleerd terwijl de achtergronden gereproduceerd werden, daarbij gebruik makend van de bootstrapmethode [20] op gesimuleerde lijstmodebestanden (LMF, Eng.: List Mode Files).

Studieontwerp

Om de datasets van de hierboven besproken performantiestudie te genereren, werden drie simulatiestudies uitgevoerd: simulatiestudie 1 met een niet-attenuerend medium, simulatiestudie 2 met een attenuerend fantoom en simulatiestudie 3 met een hotspot in datzelfde fantoom.

Reconstructie

Er werd een pas ontwikkelde reconstructietechniek, gebaseerd op natuurlijke pixels, gebruikt om de lijstmodebestanden, die resulteren uit de eerder vermelde simulatiestudies, te reconstrueren. Natuurlijke-pixelreconstructie wordt besproken in sectie 0.7. De eerste simulatiestudie (zonder attenuerend fantoom) werd gebruikt om de systeemmatrices voor de verschillende systemen te genereren. De Algebraïsche Reconstructietechniek (ART) werd gekozen om de reconstructievergelijking iteratief op te lossen.

Performantieanalyse: ROC-studie

Voor de vaste-stofdetector met roterende-vlakkencollimator, voor de vaste-stofdetector met parallelle-bundelcollimator en voor de klassieke Anger-camera werden drie reeksen van beelden opgesteld. We toonden die 3 reeksen van 100 beelden aan 4 menselijke waarnemers: 50 als set om te oefenen en 50 beelden die moesten geëvalueerd worden. In 25 beelden van elke set was een hotspot aanwezig terwijl de andere 25 beelden alleen bestonden uit achtergrondactiviteit. Daartoe werden simulatiestudie 2 en simulatiestudie 3 toegepast voor alle drie de acquisitiesetups. Simulatiestudie 2 werd voor elke reeks eenmaal uitgevoerd om de achtergrondactiviteit te simuleren. Die uitvoer werd dan 50 maal gereproduceerd door middel van bootstrapping. Dit levert dezelfde menselijke waarnemersperformantie op, op voorwaarde dat de

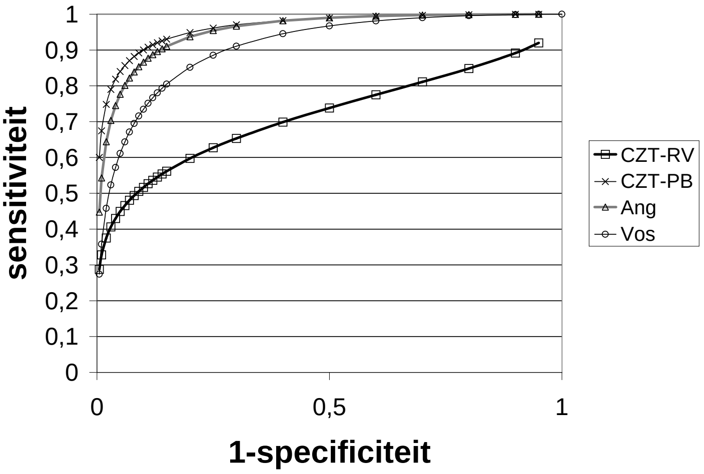

Figuur 26: Vergroten van het stripvullend oppervlak achter de schotten: ROC-curve (kernwoord:Vos).

reconstructie van de originele LMF afgetrokken wordt van elk beeld en wordt vervangen door een mediaan gefilterde versie. Simulatiestudie 3 zorgde voor 25 hotspot-ruisrealisaties voor elke reeks.

Het resultaat van de gemiddelde menselijke waarnemer bij de drie reeksen van elk 50 beelden is getoond in figuur 26. We kunnen besluiten dat de opstelling met de vlakkencollimator een slechtere performantie vertoont vergeleken met de opstellingen met een parallelle-bundelcollimator. Het is echter interessant om te onderzoeken hoe de performantie van het toestel met roterende-vlakkencollimator evolueert voor hotspot-detecteerbaarheid wanneer de CZT-strook het oppervlak achter de schotten volledig vult (kernwoord=Vos). We zien dat de performantie van het roterende-schottenysteem met volle strook uitdrukkelijk beter is, zoals aangetoond in figuur 26, met een actief detectoroppervlak dat nog steeds slechts de helft vormt van de twee andere opstellingen. De roterende-vlakkencollimator presteert echter nog steeds iets minder goed, vergeleken met de opstellingen met parallelle-bundelcollimatoren. Deze performantiestudie moet in toekomstig onderzoek uitgebreid worden op beelden die gereconstrueerd werden met een volledig 3D reconstructiealgoritme dat recent werd ontwikkeld door Zeng *et al* in [147] en door Wang *et al* in [135]. Op die manier kan de roterende-vlakkenopstelling de additionele $1/r$-sensitiviteitsafhankelijkheid beter uitbuiten wat de performantie ten goede zal komen.

0.5.5 Conclusie

We onderzochten een nieuw acquisitiesysteem met een strookvormige vastestofdetector en met een vlakkencollimator. We vergeleken dit systeem met opstellingen bestaande uit een parallelle-bundelcollimator op een gepixeliseerde vaste-stofdetector en bestaande uit diezelfde collimator op een monokristal NaI-detector. Verder werd er een theoretische formulering afgeleid voor de effectieve puntspreidingsfunctie van een vlakkencollimator op een strookvormige detector en werd additioneel een performantiestudie uitgevoerd die de drie bovenvermelde systemen vergeleek wat hotspot-detecteerbaarheid betreft. Suggesties werden gemaakt voor het vergroten van de strook en voor het uitbreiden van de performantiestudies. We breidden het werk van Metz [79] en Tsui [121] over de geometrische transfertfunctie van een vlakkencollimator op een strookvormige detector uit. Bovendien beschrijft dit hoofdstuk de eerste menselijke-waarnemerstudie over de Solstice beeldvormingsperformantie. Dit werk resulteerde in twee tijdschriftartikels [104, 130] en in drie publicaties in de proceedings van internationale conferenties [70, 102, 129].

0.6 Modellering van de detector

0.6.1 Inleiding

In de vorige sectie bespraken we het gebruik van Monte-Carlosimulaties voor het modelleren van prototype-acquisitiesystemen. Een ander belangrijk interesseveld is het simuleren van intrinsieke detectoreigenschappen. De belangrijkste toepassing daarvan is resolutieherstel in PET. De eindige pixelisatie en het beperkte aantal PMT's veroorzaken een intrinsieke puntspreidingsfunctie op alle detectielokaties. In deze sectie zullen we dan ook een theoretisch model voor deze spatiale onzekerheid van een LOR beschrijven, te wijten aan de onvolmaakte lokalisatie van gebeurtenissen op de detectorkoppen. De penetratie van fotonen in het kristal zorgt echter voor een verplaasting en een anisotropie in deze puntspreidingsfunctie zodat het nodig zal blijken om de kristalpenetratie in rekening te brengen voor schuin invallende fotonen. Voor alle gevallen zal een grondige afleiding van het theoretisch model besproken worden en voorbeelden van probabiliteitsdichtheidsfuncties (pdf's) zullen gegeven worden. Bovendien zullen geschikte functies gefit worden aan de transversale profielen van deze pdf's en hun karakteristieken zullen onderzocht worden. Evaluatie van het model dient te gebeuren aan de hand van Monte-Carlosimulaties aangezien de hedendaagse technolgie niet voldoende resolutiebereik heeft om de vereiste diepteafhankelijke informatie op te leveren. Na deze verificatie kan het beschreven model dan gebruikt worden om het intrinsiek resolutie-effect in te bouwen in de reconstructie door middel van een beter gedefinieerd acquisitieproces. In deze sectie zullen we daartoe twee reconstructiemethodes voorstellen waarvan de meestbelovende in sectie 0.7 gedetailleerd besproken zal worden.

0.6.2 Theoretische afleiding

We behandelen eerst het tweedimensionaal geval van loodrecht invallende fotonen op een acquisitieopstelling bestaande uit twee parallelle detectorkoppen waarna we dit uitbreiden tot drie dimensies. Vervolgens zullen we schuin invallende fotonen in twee en drie dimensies bestuderen.

Loodrecht invallende fotonen

We hebben een model nodig voor het voorwaarts probleem van de onzekerheid op de detectielocatie. We veronderstellen een Gaussverdeling (standdaarddeviatie σ_{0y}) voor de actuele interactiepositie op de detectorkop, gecentreerd op de gemeten positie. We zijn geïnteresseerd in de a posteriori waarschijnlijkheid $S(p,q)$ dat een gebeurtenis voortkomt uit een punt (p,q) in de FOV als de detectielocaties gegeven zijn. Daartoe integreren we alle mogelijke LOR's door dat punt, gewogen met de Gaussiaanse detectiewaarschijnlijkheid aan de eindpunten van die respectievelijke LOR's (figuur 27). Deze a posteriori waarschijnlijkheidsfunctie kan dan overgenomen worden in een meer accurate versie van een lijstmodereconstructiealgoritme. We verkrijgen de volgende uitdrukking voor de waarschijnlijkheid:

$$\begin{aligned} S(p,q) &= \int_{-|\theta_{min}|}^{|\theta_{max}|} s(\theta) d\theta \\ S(p,q) &= \frac{1}{2\pi\sigma_{0y}^2} \int_{-|\theta_{min}|}^{|\theta_{max}|} e^{w(\theta)} d\theta \\ w(\theta) &= -\frac{[(D/2-p)\tan\theta + q]^2 + [-(D/2+p)\tan\theta + q]^2}{2{\sigma_{0y}}^2}. \end{aligned} \quad (2)$$

We nemen aan dat de kristaldikte geen invloed heeft op de detectiewaarschijnlijkheid, wat in dit geval zinvol is aangezien de incidentiehoek van beide fotonen heel klein is wanneer σ_{0y} realistisch gekozen wordt. Wanneer we voor de interactiepositie op de detectorkoppen een tweedimensionale Gaussverdeling aannemen, wordt de resulterende formule voor de waarschijnlijkheid in

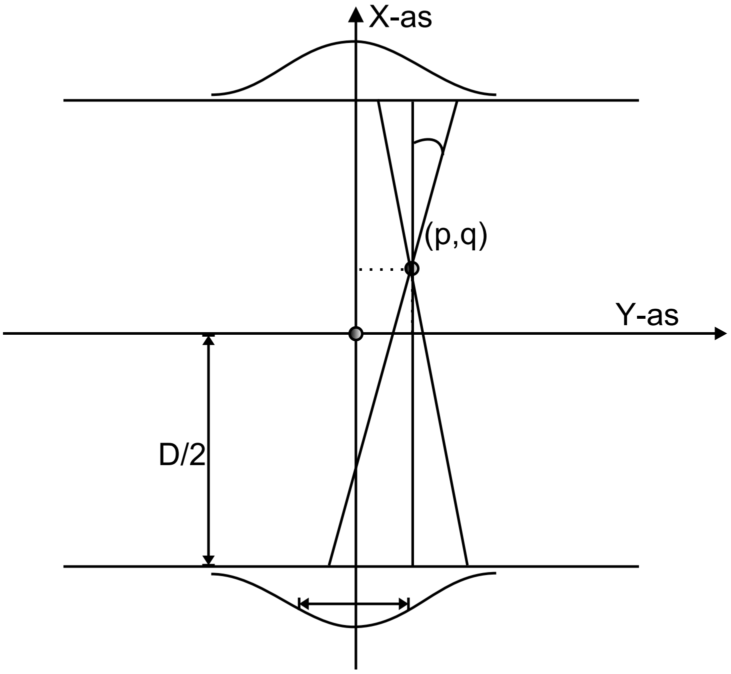

Figuur 27: Loodrecht invallende fotonen met tegenoverliggende positie van de detectorkoppen, D = afstand tussen de detectorkoppen, θ = incidentiehoek.

het driedimensionale geval:

$$\begin{aligned}
S(p,q,r) &= \int_{-|\varphi_{min}|}^{|\varphi_{max}|}\int_{-|\theta_{min}|}^{|\theta_{max}|} s(\theta,\varphi)\sin\theta d\theta d\varphi \\
S(p,q,r) &= \frac{1}{4\pi^2{\sigma_{0y}}^2{\sigma_{0z}}^2}\int_{-|\varphi_{min}|}^{|\varphi_{max}|}\int_{-|\theta_{min}|}^{|\theta_{max}|} e^{w(\theta,\varphi)}\sin\theta d\theta d\varphi \\
w(\theta,\varphi) &= \\
&-\Big\{\frac{[(D/2-p)\tan\theta\cos\varphi+q]^2+[-(D/2+p)\tan\theta\cos\varphi+q]^2}{2{\sigma_{0y}}^2} \\
&+\frac{[(D/2-p)\tan\theta\sin\varphi+r]^2+[-(D/2+p)\tan\theta\sin\varphi+r]^2}{2{\sigma_{0z}}^2}\Big\},
\end{aligned} \tag{3}$$

waarbij de Z-coördinaat voorgesteld wordt door r en φ de azimutale hoek voorstelt.

Schuin invallende fotonen

Eerst wordt het geval van een detector zonder fysische dikte (perfecte detector) besproken. Daarna wordt de invloed van de interactiediepte van de fotonen in rekening gebracht om een theoretisch model voor PET-detectoren met een realistische kristaldikte te verkrijgen.

Perfecte detector: voor schuin invallende fotonen op perfecte detectoren kunnen dezelfde beschouwingen gemaakt worden als in sectie 0.6.2. We kiezen de positie van de X-as nu wel halfweg de twee detectieposities (Y_1 en Y_2). De resulterende formule is:

$$\begin{aligned}
S(p,q) &= \int_{-|\theta_{min}|}^{|\theta_{max}|} s(\theta)d\theta \\
S(p,q) &= \frac{1}{2\pi\sigma_{0y}^2}\int_{-|\theta_{min}|}^{|\theta_{max}|} e^{w(\theta)}d\theta \\
w(\theta) &= -\Big\{\frac{\{[(D/2-p)\tan\theta+q]-Y_1\}^2}{2{\sigma_{0y}}^2} \\
&+\frac{\{[-(D/2+p)\tan\theta+q]+Y_1\}^2}{2{\sigma_{0y}}^2}\Big\}.
\end{aligned} \tag{4}$$

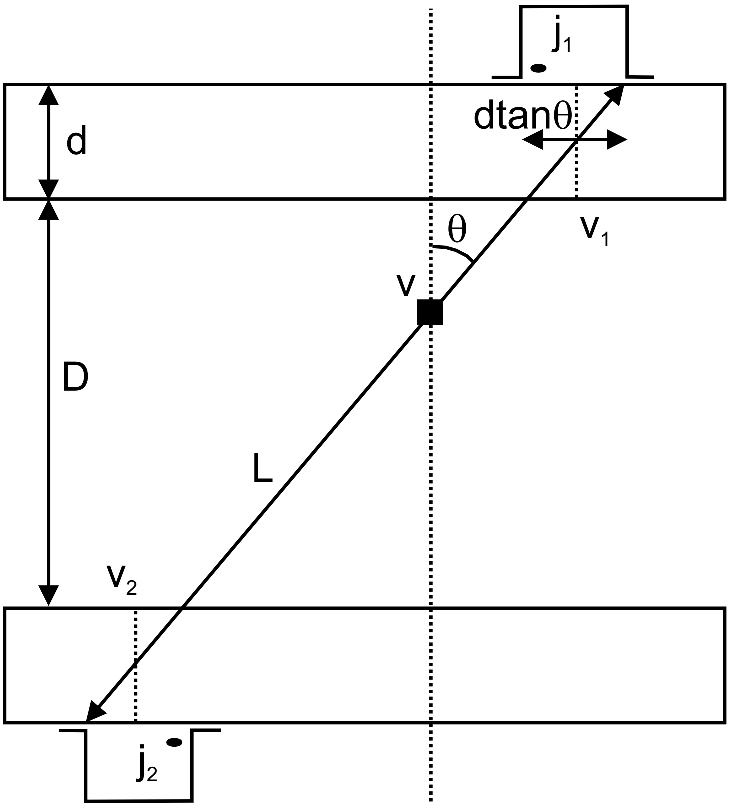

Figuur 28: In rekening brengen van de kristaldikte d.

Beperkte kristaldikte: als de detectoren een eindige dikte hebben dan moet de kristalpenetratie in rekening gebracht worden. In de volgende paragrafen veronderstellen we de interactiewaarschijnlijkheid van een 511 keV-foton langs zijn weg door de detector daartoe als uniform, dus proportioneel met zijn trajectlengte, wat conform de literatuur is [3, 122]. Wanneer we de invloed van de kristaldikte d in het theoretisch model in rekening brengen, wordt het Gaussiaanse model voor de detectorrespons vervangen door een ander functiemodel dat zal afgeleid worden gebruikmakend van figuur 28. De LOR L wordt geparametrizeerd door de incidentiepunten v_1 en v_2 terwijl de detecties geregistreerd worden in j_1 en j_2. De waarschijnlijkheid $p(j_1, j_2|v_1, v_2)$ voor een beperkte kristaldikte is het product van twee convoluties: een convolutie van een genormaliseerde blokfunctie, B, en een Gaussiaan, G, voor j_1; vermenigvuldigd met een convolutie van dezelfde functies voor j_2. De breedte van B in dit tweedimensionaal geval is $d \tan\theta$, t is het interactiepunt langs de Y-

as en H verwijst naar de Heavisidefunctie. Het resultaat voor de voorwaartse waarschijnlijkheid is:

$$p(j_1, j_2|v_1, v_2) \quad = \quad F_U(y_u) \ \cdot \ F_D(y_d), \tag{5}$$

met:

$$F_U(y_u) \quad = \quad \frac{\mathrm{erf}(\frac{y_u+d\tan\theta}{\sqrt{2}\sigma_{0y}}) - \mathrm{erf}(\frac{y_u}{\sqrt{2}\sigma_{0y}})}{2d\tan\theta}, \tag{6}$$

en:

$$F_D(y_d) \quad = \quad \frac{\mathrm{erf}(\frac{y_d}{\sqrt{2}\sigma_{0y}}) - \mathrm{erf}(\frac{y_d-d\tan\theta}{\sqrt{2}\sigma_{0y}})}{2d\tan\theta}. \tag{7}$$

Vergelijking 5 is equivalent met vergelijking 4 in de limiet voor $d \to 0$. Voor incorporatie in de reconstructie hebben we echter de a posteriori waarschijnlijkheid nodig dat een gebeurtenis die detecties veroorzaakt in j_1 en j_2, voortkomt van de voxel v. Die wordt gegeven door:

$$\begin{aligned} S(p,q) &= \int_{-|\theta_{min}|}^{|\theta_{max}|} s(\theta) d\theta, \\ s(\theta) &= p(v_1, v_2|j_1, j_2). \end{aligned} \tag{8}$$

In vergelijking (8) stelt $p(v_1, v_2|j_1, j_2)$ de a posteriori waarschijnlijkheid voor dat een annihilitie in het FOV aanleiding geeft tot de detecties in j_1 en j_2. Gebruik makend van de regel van Bayes en na enkele wiskundige afleidingen voor dit geval, verkrijgen we het volgende:

$$p(v_1, v_2|j_1, j_2) \approx p(j_1, j_2|v_1, v_2). \tag{9}$$

Via vergelijking 9 kunnen we het resultaat van vergelijking 5 in rekening brengen in vergelijking 8 om de a posteriori waarschijnlijkheid van een gebeurtenis in voxel v te vinden. Het eerder vermelde model voor de detectiewaarschijnlijkheid kan ook uitgebreid worden naar drie dimensies, zoals figuur 29(a) en figuur 29(b) aantonen. Dit 3D-geval impliceert verschillende blokfuncties voor beide transversale richtingen. Na convolutie met de respectievelijke Gaussianen, gekarakteriseerd door σ_{0y} en σ_{0z}, resulteren de functies T_{1U}, T_{1D} en T_{2U}, T_{2D} analoog als in F_U, F_D maar nu voor twee transversale richtingen. Voor dit driedimensionaal geval bekomt men de volgende a posteriori waarschijnlijkheid :

$$\begin{aligned} S(p,q,r) \quad &= \quad \int_{-|\varphi_{min}|}^{|\varphi_{max}|} \int_{-|\theta_{min}|}^{|\theta_{max}|} s(\theta,\varphi) \sin\theta d\theta d\varphi, \\ s(\theta,\varphi) \quad &= \quad T_{1U}(y_u) \ \cdot \ T_{1D}(y_d) \ \cdot \ T_{2U}(z_u) \ \cdot \ T_{2D}(z_d). \end{aligned} \tag{10}$$

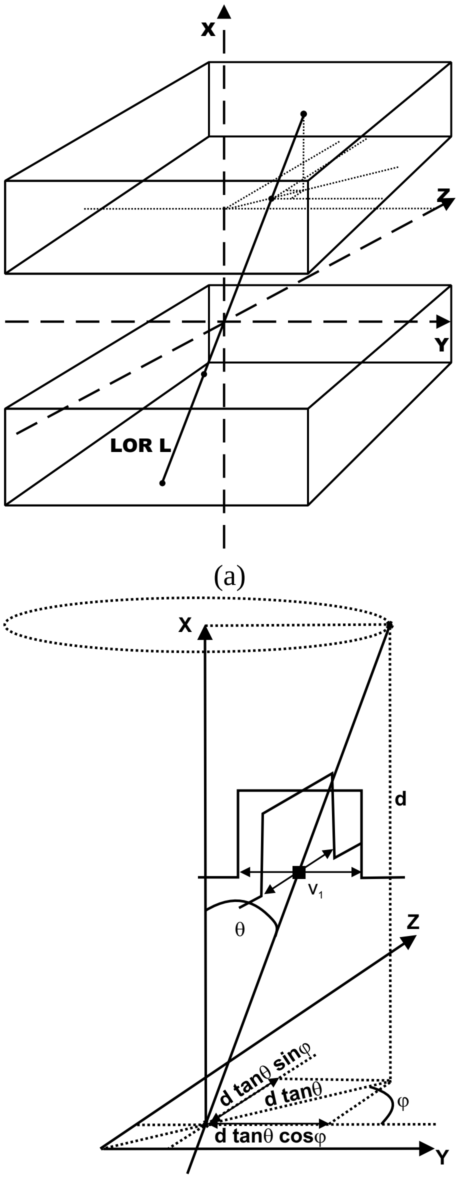

(a)

(b)

Figuur 29: (a) Schuin invallende fotonen met tegenoverliggende positie van de detectorkoppen: 3D-uitbreiding, (b) effect van de kristaldikte in beide transversale richtingen.

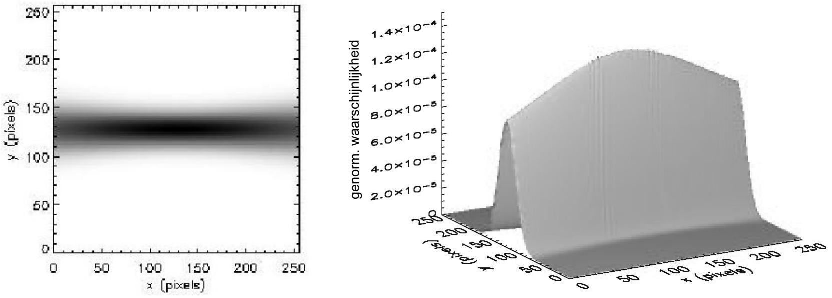

(a) (b)

Figuur 30: Pdf's voor loodrecht invallende fotonen en tegenoverliggende detectoren: (a) grijswaardenbeeld, (b) oppervlakteplot.

0.6.3 Modelanalyse

Er werd een typische opstelling geïmplementeerd: we kozen de FOV 25.6 cm op 25.6 cm en de afstand tussen de detectorkoppen werd eveneens op 25.6 cm vastgelegd. In alle figuren is een voxel 1 x 1 x 1 mm^3. De FWHM van de respectievelijke Gaussiaan werd op 40 mm ingesteld en het kristal werd op 1.9 cm standaarddikte gezet. Voor schuin invallende fotonen werd de LOR gedefinieerd door $(12.8, 5)$ en $(-12.8, -5)$, terwijl het $(12.8, 5, 5)$ en $(-12.8, -5, -5)$ betrof in het driedimensionale geval.

Loodrecht invallende fotonen

De pdf voor de FOV is weergegeven in figuur 30. Na verificatie konden we besluiten dat de transversale profielen van deze pdf kunnen voorgesteld worden door een Gaussiaan, gefit met een foutenmarge van grootteorde 10^{-3}. De FWHM van deze Gaussianen is minimaal in het centrum en maximaal aan het oppervlak van de detector en kent een kwadratisch verloop. De resultaten werden ook uitgebreid naar drie dimensies.

Schuin invallende fotonen

De resultaten voor het tweedimensionaal geval van schuin invallende fotonen zijn weergegeven in figuur 31. Voor dunne kristallen kunnen Gaussianen gefit worden aan de transversale profielen van de pdf met een fout van 10^{-2}. Opnieuw is de FWHM minimaal in het centrum en maximaal aan het oppervlak van de detector. Deze resultaten werden ook uitgebreid naar drie dimensies.

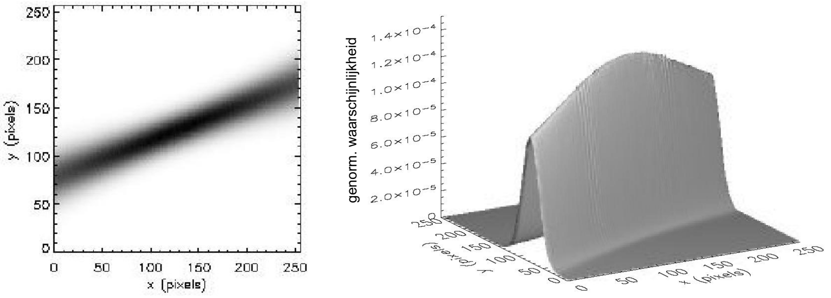

(a) (b)

Figuur 31: Pdf voor schuin invallende fotonen en tegenoverliggende detectoren: (a) grijswaardenbeeld en (b) oppervlakteplot: kristal van 1.9 cm.

0.6.4 Validatie door Monte-Carlosimulaties

Aangezien de twee overliggende detectoren in coïncidentie werken is het theoretisch telprofiel van een bron in het centrum tussen beiden gegeven door een verschoven convolutie van twee Gaussianen en heeft het telprofiel dus een standaarddeviatie die $1/\sqrt{2}$ kleiner is dan de standaarddeviatie ter hoogte van de detectoren. Wanneer we $\tan\theta$ in vergelijking 2 benaderen door zijn argument θ, wat correct is voor deze kleine hoeken, bekomt men een gesloten Gaussiaanse uitdrukking voor het middelpunt van de FOV (integratiegrenzen $\pm 3\sigma_{0y}$):

$$S(0,q) = \frac{\text{erf}(\frac{3D}{2})e^{(\frac{-q^2}{\sigma_{0y}^2})}}{\sqrt{\pi}\sigma_{0y}D}. \tag{11}$$

Vergelijking 11 verwijst naar dit resultaat, waarbij q de afstand langs de detector voorstelt. In het argument van de exponentiële functie zien we inderdaad σ_{0y}^2 die een FWHM veroorzaakt die een factor $\sqrt{2}$ kleiner is dan de Gauss-verdeling, $e^{-q^2/2\sigma_{0y}^2}$, op de detector. De FWHM op de detector en in het centrum van de FOV zijn bijgevolg dus gekend zodat we kunnen besluiten dat de FWHM als volgt kan uitgedrukt worden, gebruik makend van het eerder vermelde kwadratisch verloop:

$$2\sqrt{2\ln 2}\sigma = (2/D)^2 2\sqrt{2\ln 2}\sigma_{0y}(1 - 1/\sqrt{2})p^2 + 2\sqrt{2\ln 2}\sigma_{0y}/\sqrt{2}. \tag{12}$$

In vergelijking (12) stelt p de afstand tot de detector voor. We bevestigen deze resultaten voor onze basisformule van vergelijking (2) door gebruik te maken van een geometrische Monte-Carlosimulator [124]. De responsfunctie van de detector werd in overeenstemming met ons model gekozen en er

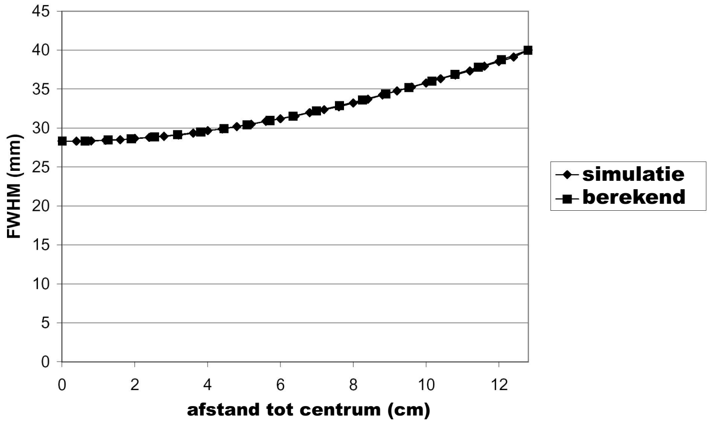

Figuur 32: Monte-Carlovalidatie van het theoretisch model: vergelijking van de FWHM.

werd geen attenuatieverstrooiing in rekening gebracht. Uit de resultaten voor de FWHM van de berekende en de gesimuleerde Gaussianen, getoond in figuur 32, konden we besluiten dat het theoretisch model correct is. Om de validiteit van de interactieuniformiteitsaanname bij schuin invallende fotonen te verifiëren, voerden we Monte-Carlosimulaties van verschillende opstellingen uit door middel van GATE. Voor fotonen van 140 keV die een 19 mm NaI-kristal penetreerden (gammacamera-PET bijvoorbeeld), vonden we dat de interactiediepte (DOI, Eng.: Depth Of Interaction) exponentieel afneemt omdat fotoelektrische interacties overheersen in het fotopiekbereik. Voor 511 keV fotonen invallend op alle gangbare detectormaterialen, vonden we echter dat de Comptonbijdrage het belangrijkst was. Dit zorgt ervoor dat het DOI-verloop eerder uniform in plaats van exponentieel is wat de uniformiteitsaanname geldig maakt. Bovendien kunnen die resulterende gesimuleerde DOI-curven in rekening gebracht worden in het theoretisch model als een additionele, kristal- en energieafhankelijke parameter. Een validatie versus experimentele data is nog vereist. We zijn er echter van overtuigd dat de variatie in de breedte van de Gaussiaan belangrijker zal blijken te zijn dan de discrepantie in de DOI-uniformiteitsbenadering voor het afgeleid theoretisch model. Deze variaties in de FWHM zijn waarschijnlijk te wijten aan de positionering van de PMT's die determinerend zijn in de Angerlogica van het uitleesschema.

0.6.5 Reconstructie: resolutieherstel

Het afgeleide en geverifieerde theoretisch model kan in rekening gebracht worden in een reconstructiealgoritme om de spatiale resolutie van de resulterende gereconstrueerde beelden te verbeteren. Twee mogelijke invalshoeken voor incorporatie in de reconstructie worden voorgesteld. De eerste benaderingswijze is de incorporatie van dit model in een iteratief lijstmode Maximum Likelihood Expectation Maximization algoritme. Niet alleen de voxels doorkruist door de LOR moeten in rekening gebracht worden, maar ook de voxels binnen het bereik van de pdf ten gevolge van detectieonzekerheid. Hierbij moet het object geparametrizeerd worden aan de hand van symmetrische basisfuncties zodanig dat de voxelbijdrage enkel afhankelijk is van de afstand tot de LOR en niet van de oriëntatie. Een tweede, elegantere, benaderingswijze bestaat erin natuurlijke pixels te gebruiken om het object te parametrizeren wat in sectie 0.7 besproken zal worden. Hier zijn discrete projecties aan de continue beelddistributiefunctie gerelateerd door een ruimtelijk variërende fotondistributiefunctie die de geometrische respons van de detector modelleert, in dit geval dus Gaussianen met variërende breedte afhankelijk van de afstand tot de detector.

0.6.6 Conlusie en originele bijdragen

We hebben een theoretisch model afgeleid om de onzekerheid van de detectielocatie in rekening te brengen in continue detector-PET. Loodrecht en schuin invallende fotonen werden bestudeerd in twee en drie dimensies. We concludeerden dat transversale profielen van de pdf's konden benaderd worden door Gaussianen, zowel voor loodrechte (10^{-3} foutenmarge) als voor schuine inval (10^{-2} foutenmarge). De resultaten die we bekwamen werden geverifieerd door middel van theoretische voorspellingen en geometrische Monte-Carlosimulaties en een goede overeenstemming werd bereikt. In het geval van schuin invallende fotonen konden we afleiden dat de interactiediepte van een foton in belangrijke mate bijdraagt tot de detectieonzekerheid. Door middel van realistische Monte-Carlosimulaties konden we ook bevestigen dat de interactiewaarschijnlijkheid van een 511 keV foton quasi uniform is in alle gangbare PET-detectormaterialen. Na evaluatie bleek dat het gebruikte model geschikt is voor incorporatie in een reconstructiealgoritme, met als doel het acquisitieproces accurater te modelleren en de spatiale resolutie van de tomografische beelden te verbeteren. Dit theoretisch model kan ook gebruikt worden om de spatiale resolutie te berekenen van systemen die nog in ontwerp zijn. Naar wij weten is dit het eerste theoretisch LOR-model voor PET-systemen met continue detectoren dat de detectieonzekerheid van de annihilatiefotonen accuraat in rekening brengt in functie van de afstand tot de detectorkoppen. Dit resulteerde in een tijdschriftartikel [103] en in twee publicaties in de proceedings van internationale conferenties [100, 101].

0.7 Monte-Carlogebaseerde reconstructie

In parallelle-bundelcollimator SPECT wordt de reconstructie meestal uitgevoerd als een set van 2D analytische of iteratieve reconstructies. Dit negeert de intrinsieke 3D natuur van het verstrooiingsproces. Om daarmee expliciet rekening te houden kan een 3D projector gesimuleerd worden voor gebruik in een 3D reconstructie-algoritme. Monte-Carlogebaseerde reconstructie voor PET is vooral doeltreffend bij resolutieherstel door incorporatie in de reconstructie van beelddegraderende effecten zoals onder andere interkristalverstrooiing en kristalpenetratie.

0.7.1 Passende Monte-Carlogebaseerde reconstructie voor SPECT-toepassing

Het werd reeds aangegeven in sectie 0.4 dat het Beacon-attenuatiebeeld in de nabijheid van het centrum van zware patiënten vaak gedegradeerd is wanneer de transmissieacquisitie gelijktijdig of opeenvolgend uitgevoerd wordt met een medium-energie-emissiestudie. We toonden aan dat het, in dit bijzonder geval, sterk aangewezen is om de MEGP-collimatoren te vervangen door de LEHR-varianten voor een groot energiebereik van medium-energiebronnen, wanneer men de toegenomen fotonspreiding kan corrigeren. Daartoe implementeerden we een passend reconstructiealgoritme dat de Monte Carlo gegenereerde systeemrespons incorporeert.

Implementatie

De benaderingswijze bestaat uit het simuleren van een driedimensionale systeemmatrix voor elke mogelijke opstelling, waarbij alle beelddegraderende effecten in rekening gebracht worden. Nadien wordt die systeemmatrix omgerekend naar de gemiddelde detectorresponsfunctie, die de systeemrespons is uitgemiddeld over alle detectielocaties en die dus alle degraderende processen in drie dimensies bevat. Om deze detectorrespons in de reconstructie in te bouwen, werd afhankelijk van de afstand tot de detector, een specifieke tweedimensionale functie opgelegd in de voorwaartse projectiestap van het Maximum Likelihood Expectation Maximization (MLEM) algoritme. Deze tweedimensionale functie stelt de gemiddelde respons van het systeem voor en is

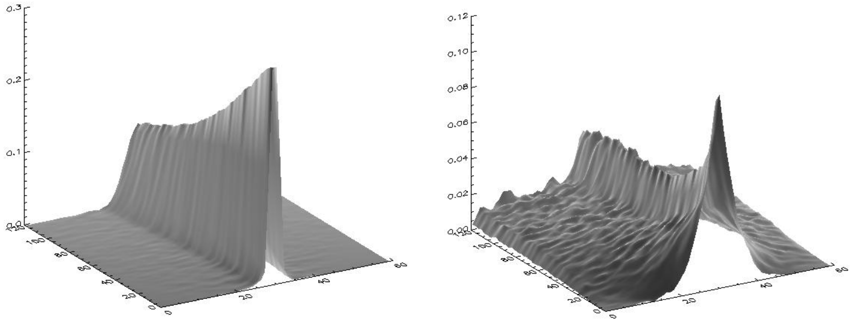

(a) (b)

Figuur 33: Systeemrespons: (a) eendimensionale gemiddelde systeemrespons voor 128 vlakken parallel aan de detector bij een MEGP-opstelling, (b) eendimensionale gemiddelde systeemrespons voor 128 vlakken parallel aan de detector bij een LEHR-collimatoropstelling.

afhankelijk van de afstand tot de detector en van de energie van het isotoop. In figuur 33 is een voorbeeld weergegeven. Figuur 33(a) toont de gemiddelde systeemrespons in één dimensie voor 128 vlakken parallel aan de detector en voor fotonen met een (medium-)energie van 245 keV op een MEGP-collimator, terwijl figuur 33(b) de penetratie van dezelfde fotonen op een LEHR-collimator weergeeft. Om de opslagvereisten van onze systeemmatrix te beperken en om de ruisgerelateerde problemen beschreven in [22] op te lossen, kan de gesimuleerde systeemmatrix gebruikt worden in een reconstructie gebaseerd op natuurlijke pixels, of de beeldmatrix kan geroteerd worden met bilineaire interpolatie. Op die manier bekomt men steeds een beeldmatrix die loodrecht staat op de detector zodat de afgeleide systeemrespons kan toegepast worden voor elke afstand. In het laatste geval blijft het bovendien mogelijk om attenuatie in rekening te brengen in de reconstructie.

Herstel van medium-energie-fotonspreiding op LEHR

Figuur 34 toont de reconstructie van een puntbron van 1 cm doorsnede op 30 cm van de detector, gevuld met een emissiebron van 300 keV, na gesimuleerde acquisitie op een LEHR-collimator. Figuur 34(a) is een beeld dat gereconstrueerd is door middel van traditionele parallelprojectie MLEM, terwijl figuur 34(b) gereconstrueerd is met incorporatie van de driedimensionale Monte-Carlosysteemrespons. Aan de profielen van beide beelden werd een Gaussiaan gefit: voor figuur 34(a) resulteert een Full Width at Half Maximum (FWHM) van 22.6 mm, wat op die afstand niet meer dan 14.3 mm mag

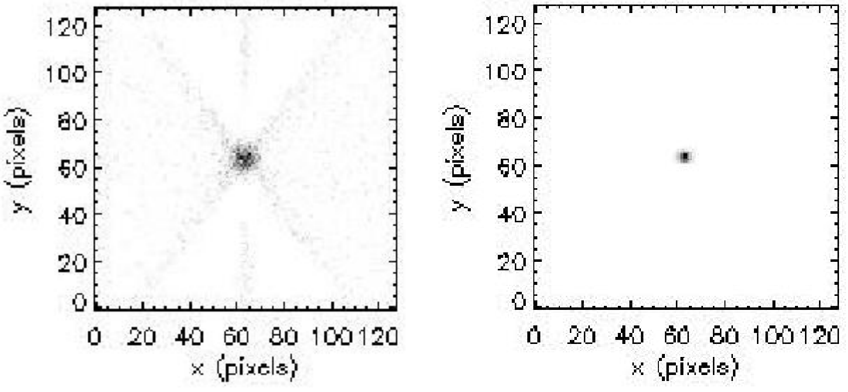

(a) (b)

Figuur 34: Gereconstrueerde beelden (axiaal zicht) van een puntbron met 300 keV medium energie. De detector is voorzien van een LEHR-collimator: (a) parallelprojectie MLEM, (b) Monte-Carlogebaseerde MLEM.

zijn wanneer geen fotonpenetratie toegelaten is. De FWHM van de Gaussiaan gefit aan figuur 34(b) resulteert in een waarde van 9.3 mm, wat de originele afmeting van de puntbron (1 cm) is binnen de foutenmarges van de curvefit. Dit is samengevat in figuur 35, die het succesvol resolutieherstel van de Monte-Carlogebaseerde reconstructie aantoont. De validatie van deze methode werd uitgebreid naar andere energiebereiken, andere fantomen en andere collimatoren. De acquisitie van drie puntbronnen van 1 cm, gescheiden door 2 cm en met een activiteitsratio van 1:2:6 werd gesimuleerd, waarbij alle drie de bronnen geplaatst werden op 30 cm van de collimator. Figuur 36 toont de resultaten voor fotonen van 170 keV. Het beeld van figuur 36(a) toont de traditionele reconstructie door middel van parallelprojectie MLEM bij de geschikte MEGP-collimator, terwijl figuur 36(b) dezelfde reconstructie toont bij een LEHR-acquisitie. Men kan een sterk toegenomen fotonspreiding vaststellen. Figuur 36(c) en figuur 36(d) tonen de reconstructie met Monte-Carloinformatie respectievelijk voor een MEGP-collimator en voor een LEHR-collimatoropstelling. Uit figuur 36(c) blijkt dat de gaten bij een MEGP te groot zijn waardoor het onmogelijk is hun individuele positie uit te middelen in de systeemrespons. Figuur 36(a), figuur 36(b) en figuur 36(c) zijn dus suboptimaal. Monte-Carlogebaseerde reconstructie van een dataset van een isotoop met medium energie, opgenomen op LEHR-collimatoren, resulteert in een beter gereconstrueerd beeld van de fantoomopstelling, zoals is weergegeven in figuur 36(d).

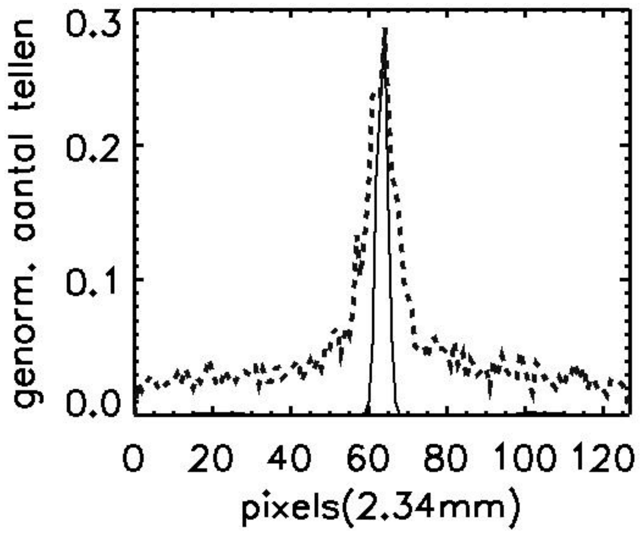

Figuur 35: Gereconstrueerde beelden van een puntbron met 300 keV medium energie. De detector is voozien van een LEHR-collimator: FWHM parallelprojectie MLEM (puntlijn), FWHM Monte-Carlogebaseerde MLEM (volle lijn).

0.7.2 Reconstructie gebaseerd op natuurlijke pixels bij PET

Er zijn een aantal algoritmen voorgesteld om data van 3D PET te reconstrueren, onder andere het analytisch 3D-herprojectiealgoritme (3DRP) [69] en rebinning (FORE) [35]. Een nadeel van beide methodes is dat deze algoritmen afgeleid zijn door gebruik te maken van de aanname dat gemeten data overeenkomt met lijnintegralen doorheen de ongekende activiteitsdistributie. Zoals reeds herhaaldijk aangehaald zijn er echter een aantal fysische effecten die deze aanname ongeldig maken. Reconstructie gebaseerd op natuurlijke pixels daarentegen laat toe om alle beelddegraderende effecten door Monte-Carlosimulatie in rekening te brengen en beperkt de opslaggrootte van de systeemmatrix door de in PET aanwezige symmetrieën uit te buiten.

Deze reconstructietechniek vormt het onderwerp van een project dat recent door onze groep werd ingediend en zal de hoofdlijn van ons onderzoek voor de komende jaren uitmaken. De techniek en het verwachte resolutieherstel zullen hierna besproken worden aan de hand van preliminaire resultaten. Sectie 0.7.2 schetst op die manier ook de grote lijnen van het toekomstig onderzoek dat resulteerde uit onderliggend manuscript.

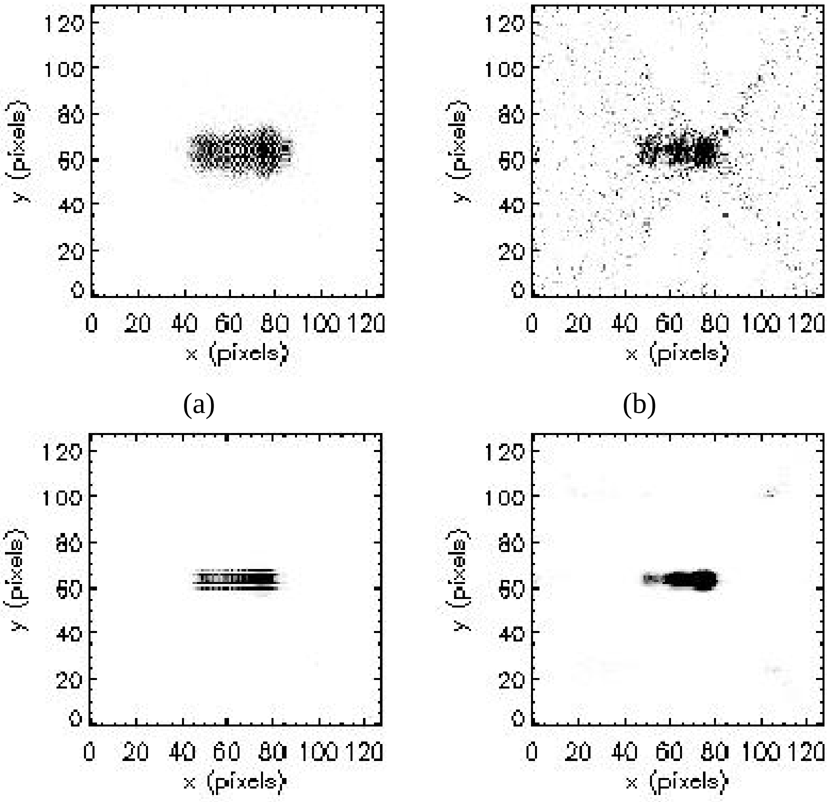

(a) (b)

(c) (d)

Figuur 36: Gereconstrueerde beelden (axiaal zicht) van een puntbronnenfantoom met 170 keV medium energie: evaluatie van reconstructieperformanties voor LEHR- en MEGP-collimator: (a) MEGP-collimator en parallelprojectie MLEM, (b) LEHR-collimator en parallelprojectie MLEM, (c) MEGP-collimator en Monte-Carlogebaseerde MLEM, (d) LEHR-collimator en Monte-Carlogebaseerde MLEM.

Theoretische achtergrond en geometrische resultaten

Natuurlijke pixels: de relatie tussen de meting g_i van een detectorpaar in een PET-scanner en het continue object dat moet afgebeeld worden, $f(x, y, z)$, kan beschreven worden door gebruik te maken van een spatiaal variërende detectorresponsfunctie $h_i(x, y, z)$. Hierin stelt $h_i(x, y, z)$ de waarschijnlijkheid voor dat een positron uitgezonden op locatie (x, y, z) gedetecteerd wordt in detectorpaar i. Het reconstructieprobleem bij PET is dus het schatten van het continue object $f(x, y, z)$ wanneer een gemeten set van data g_i gegeven is. Een mogelijke beschrijving voor het tomografisch probleem bekomt men door gebruik te maken van een reconstructiemodel met natuurlijke pixels als basisfuncties [7, 19, 54, 59]. In deze benaderingswijze is de geschatte reconstructie een lineaire combinatie van de basisfuncties $h_j(x, y, z); j = 1 \ldots J$, die de probabiliteitsdichtheidsfuncties van de detectorparen zijn. We verkrijgen uiteindelijk:

$$\begin{aligned} g_i &= \sum_{j=1}^{J} q_j \int_{FOV} h_j(x,y,z) h_i(x,y,z) dxdydz, \\ g_i &= \sum_{j=1}^{J} M_{ij} q_j, \end{aligned} \tag{13}$$

waarbij

$$M_{ij} = \int_{FOV} h_j(x,y,z) h_i(x,y,z) dxdydz. \tag{14}$$

M_{ij} wordt de natuurlijke pixelmatrix genoemd. In deze natuurlijke-pixelbenadering gebeurt de discretizatie van het object in een voorgedefinieerde voxelgrid pas op het einde bij de terugprojectie van $\tilde{q}$ $(= A^T q)$. Voor een perfect beeldvormingssysteem zou M_{ij} de intersectie van twee LOR's zijn maar we hebben in sectie 0.6 aangetoond dat dit eerder Gaussiaanse gewogen tubes zijn waarvan de breedte afhankelijk is van de afstand tot de detector. In figuur 37(a) is een illustratie weergegeven die de respons (in 2D) van twee detectorparen in een 2D PET ringscanner toont. Deze hypothetische scanner heeft slechts 20 detectorparen en alleen geometrische effecten worden beschouwd. De resulterende matrix M voor dit ontwerp is getoond in figuur 37(b). Het is belangrijk om op te merken dat de matrix M blok-circulant is (alle blokkolommen zijn verschoven versies van de eerste blokkolom), wat impliceert dat de systeemresponsmatrix voor ringvormige PET-scanners kan opgeslagen worden met aanzienlijk minder geheugenvereisten dan met de conventionele voxelbasisfuncties het geval is.

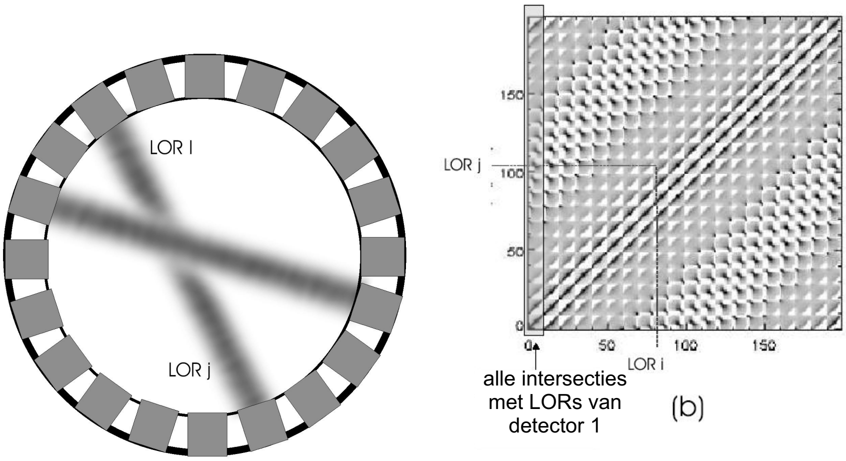

(a) (b)

Figuur 37: (a) berekening van de natuurlijke pixelwaarde gevormd door LOR i en LOR j. De grijswaarde van de niet-uniforme strips is de waarschijnlijkheid dat een detectie in een LOR afkomstig was van een bepaald punt in de FOV, (b) matrix M bevat de natuurlijke pixelwaarden voor een PETring van 20 detectoren. Elke detector kan combineren met 10 overliggende detectoren. Dit resulteert in 200 mogelijke LORs.

Gegeneraliseerde natuurlijke pixels: de uiteindelijke terugprojectieoperatie bij de natuurlijke pixelreconstructie leidt tot een grote computerbelasting, en daarom stellen we voor om een gegeneraliseerde natuurlijke pixelbasis te gebruiken, die gevormd wordt door de combinatie van een verschillende projectie- en terugprojectieoperator. Een snelle en efficiënte terugprojector die we voorstellen is een strookvormige terugprojector met parallelle geometrie in 2D of een vierkante tube in 3D. Om de gegeneralizeerde natuurlijke-pixelmatrix te verkrijgen wordt een Monte-Carlomethode gebruikt. Daarbij wordt een willekeurig gelokaliseerde annihilatie gedetecteerd in een zeker detectorpaar i. Een tweede LOR wordt dan geprojecteerd vanuit dezelfde emissielocatie naar de detectoren die georiënteerd zijn in een parallelle geometrie. Door gebruik te maken van Monte-Carlosimulaties om de gegeneraliseerde natuurlijke-pixelmatrix te verkrijgen, kunnen alle beelddegraderende effecten in rekening gebracht worden en moeten de sensitiviteitsfuncties van de detector niet analytisch berekend worden.

Verbeteringen door gebruik te maken van GATE

Recent werk door onze groep [125, 126, 131] toonde aan dat er een resolutieverbetering van 1 mm verkregen wordt bij de gegeneraliseerde natuurlijke-pixelreconstructie, in vergelijking met een standaard lijstmode MLEM-algoritme. Daarnaast was ook het ruisgedrag en de hotspot-detecteerbaarheid superieur bij de gegeneralizeerde natuurlijke-pixelreconstructie. De resultaten werden verkregen door gebruik te maken van een zeer eenvoudige Monte-Carlosimulator die alleen geometrische effecten in rekening bracht om de gegeneralizeerde natuurlijke-pixelmatrix te simuleren. Krachtiger resolutieherstel kan verkregen worden door gebruik te maken van GATE aangezien we in sectie 0.4 en sectie 0.6 hebben aangetoond dat interkristalverstrooiing en kristalpenetratie belangrijke beelddegraderende effecten zijn. Dit is geïllustreerd in figuur 38. We geloven dat Monte-Carlogebaseerde (gegeneraliseerde) natuurlijke-pixelreconstructie een van de elegantste en krachtigste manieren is om beelddegraderende effecten in rekening te brengen in de reconstructie, rekening houdend met een beperkte opslaggrootte dankzij de intrinsieke symmetrieën.

0.7.3 Conclusie en originele bijdragen

We beschreven een benaderingswijze die de gemiddelde systeemrespons simuleert voor een medium-energiestudie op LEHR collimatoren met de bedoeling de MEGP-collimatoren te vervangen door de LEHR-variant. Uit sectie 0.4 volgde immers dat de Beacon transmissiebeeldvorming gekoppeld aan

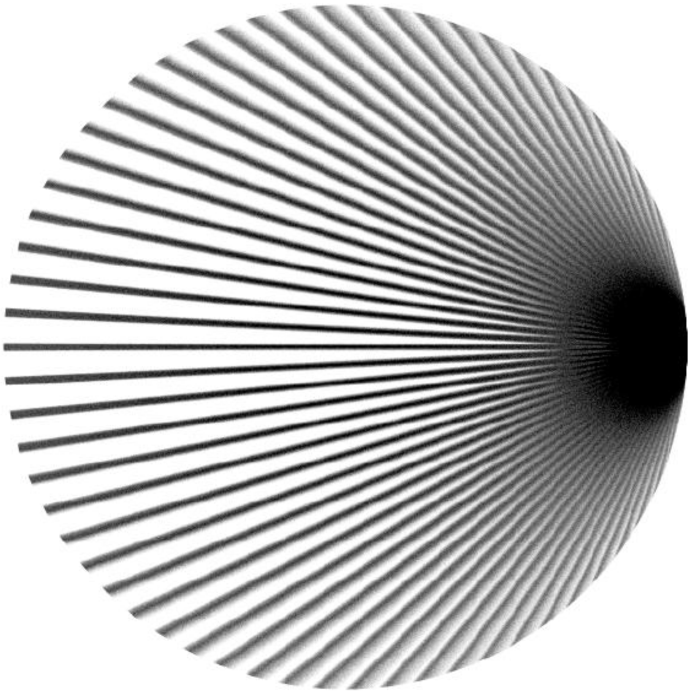

(a)

Figuur 38: Gesimuleerde responsen voor BGO 2D PET-scanner (7 mm breed): geen positieblurring, alleen kristalverstrooiing en kristalpenetratie.

een medium-energie-emissiestudie attenuatiemappen met een laag contrast oplevert. We toonden aan dat het aangewezen is ook een medium-energie-emissiestudie uit te voeren op een LEHR op voorwaarde dat de gesimuleerde systeemrespons in rekening gebracht wordt in de reconstructie. We hebben bijgevolg een belangrijke richtlijn afgeleid voor transmissiebeeldvorming in medium-energie-emissiestudies. Dit werk resulteerde in een tijdschriftartikel [106]. Er werd ook een meerjarenproject vastgelegd waarin de potentiële voordelen van natuurlijke-pixelreconstructie beschreven zijn en waarin we toekomstig onderzoekswerk belichten. Onderzoek naar gegeneraliseerde natuurlijke-pixelreconstructie gebaseerd op Monte-Carlosimulaties zal een van onze belangrijkste onderzoekthema's zijn voor de volgende vijf jaar. De implementatie besproken in sectie 0.7.2 beschrijft hoe onze groep in staat was om 1 mm reconstructieresolutie te winnen door gebruik te maken van een gegeneraliseerde natuurlijke-pixelreconstructie waarin de systeemmatrix gesimuleerd werd met een eenvoudige geometrische Monte-Carlosimulator. We zijn ervan overtuigd dat het simuleren van de natuurlijke-pixelmatrix gebruikmakend van GATE een additionele resolutiewinst zal opleveren aangezien we in sectie 0.4 en sectie 0.6 hebben aangetoond dat interkristalverstrooiing en kristalpenetratie belangrijke beelddegraderende effecten zijn. Het bovenvermelde onderzoeksproject moet resulteren in een van de meest performante methodes om resolutie te herstellen bij PET.

0.8 Algemeen besluit

In sectie 0.2 werd een kort overzicht gegeven van de nucleaire geneeskunde, met inbegrip van reconstructie, met als doel onderliggend proefschrift te kaderen. Verder werd het GATE-simulatiepakket geïntroduceerd als bovenlaag van Geant4. Overeenkomstig werd een grondige literatuurstudie voorgesteld die de vier hoofdtoepassingsgebieden belichtte waarin Gate van significant belang kan zijn. Specifiek onderzoek op deze vier subdomeinen wordt toegelicht in dit manuscript.

Sectie 0.3 beschrijft de SPECT-validatiestudie die uitgevoerd werd om de accuraatheid van GATE-simulaties versus metingen op een commercieel SPECT-acquisitiesysteem te verifiëren. Dit leidt tot het gebruik van GATE voor het simuleren van bestaande cameraopstellingen in verschillende acquisitiemodes, met diverse parameters, verschillende isotopen en verscheidene collimatoren. Multiprocessordistributie en gridificatie zijn naast de validatie voor dosimetrische toepassingen de belangrijkste interessevelden voor toekomstig onderzoek.

Sectie 0.4 handelde over attenuatie- en verstrooiingscorrectie bij

Beacon(gammacamera)-PET en Beacon-SPECT. Het is de eerste simulatiestudie die in zo een belangrijke mate gebruik maakt van de virtuele GATE-kloksynchronisatie om protocoloptimalizaties voor te stellen. We onderzochten simultane emissie- en transmissiestudies. Voor gammacamera-PET bleek dat vooral de ingangsfilters en de einddelen van de detector een intrinsieke inter-venstercontaminatie veroorzaakten. Bij Beacon-SPECT concludeerden we dat de laagste inter-venstercontaminatie en het beste transmissiecontrast bereikt wordt als een LEHR collimator gekoppeld aan een dik kristal gebruikt wordt, zelfs voor medium-energie-emissiestudies. In dit laatste geval moet wel de fotonspreiding van de medium-energiefotonen op de suboptimale LEHR collimator geïncorporeerd worden in een Monte-Carlogebaseerde reconstructie zoals besproken werd in sectie 0.7. Ook werd in sectie 0.4 een kwalitatieve interpretatie gegeven voor het belang van meervoudige verstrooiing bij 3D PET. Het werd duidelijk dat alleen objectverstrooiing van eerste orde de fotopiekacquisities significant degradeert. De incorporatie van kristalverstrooiing in de reconstructie bleek vereist en daartoe werden twee oplossingen voorgesteld waarvan één werd toegelicht in sectie 0.7.

In sectie 0.5 onderzochten we een nieuw ontwerp voor een SPECT-acquisitiesysteem dat een hogere resolutie bij een vergelijkbare sensitiviteit nastreeft. Het Solstice-prototype bestond uit een strookvormige vaste-stofdetector met een roterende vlakkencollimator. We vergeleken de prestaties van dit prototype met een parallelle-bundelcollimator op een overeenkomstig gepixeliseerde vaste-stofdetector en met een typische monokristal NaI-detector gekoppeld aan diezelfde collimator. We vonden een betere resolutie en een hogere sensitiviteit, gekoppeld aan een superieure energieresolutie. We breidden ook het werk van Metz (parallelle-bundelcollimator) en Tsui (waaierbundel- en kegelbundelcollimator) uit voor de geometrische transfertfunctie van een vlakkencollimator op een strookvormige detector. Daar een foton opgenomen op een roterende vlakkencollimator niet evenveel informatie bezit als op een parallelle-bundelcollimator voerden we additioneel ook nog een hotspot-detecteerbaarheidsstudie met menselijke waarnemers uit voor alle drie de systemen. We vonden een lagere performantie-waardemeter voor de roterende-vlakkencollimator op de strookvormige vaste-stofdetector. Deze projectiestudie moet echter uitgebreid worden op 3D beeldensets, gereconstrueerd met de recent ontwikkelde algoritmes van Zeng [147] en Wang [135].

In sectie 0.6 hebben we een theoretisch model voor incorporatie van de onzekerheid omtrent detectielocatie in continue detector PET afgeleid. De resulterende detectorsensitiviteitsfunctie kan niet analytisch uitgedrukt worden en werd dus telkens berekend door middel van numerieke integratie. We vonden dat de transversale profielen van de probabiliteitsdensiteitsfuncties door een

Gaussiaan konden benaderd worden. We incorporeerden ook het effect van de kristaldikte in het theoretisch model en concludeerden dat de traditionele Gaussiaan voor de spatiale onzekerheid in dit geval moet vervangen worden door een meer accurate functie die rekening houdt met de kristalpenetratie. Na evaluatie bleek het model geschikt voor incorporatie in de reconstructie maar dit theoretisch model kan ook gebruikt worden om de spatiale resolutie te berekenen van systemen die nog in ontwerp zijn. Dit is het eerste theoretische LOR-model voor een PET-systeem met continue detector, dat de detectieonzekerheid van de annihilatiefotonen nauwkeurig in rekening brengt in functie van de afstand tot de detectorkoppen.

In sectie 0.7 beschreven we een reconstructie-implementatie die de gemiddelde systeemrespons afleidt uit een volledig 3D gesimuleerde systeemmatrix en dit voor medium-energiestudies op LEHR-collimatoren. Het in rekening brengen van de systeemrespons in een gepaste Monte-Carlogebaseerde reconstructie herstelt op een accurate wijze de medium-energiefotonspreiding op een LEHR en recupereert op die manier het resolutieverlies. In alle gevallen gaf de reconstructie van medium-energie-isotopen op LEHR het beste resultaat (mits incorporatie van de systeemrespons), omdat de gaten van de aangewezen MEGP collimator te groot zijn om uitgemiddeld te kunnen worden in de systeemrespons. Daarnaast werd een meerjarenproject vastgelegd waarin de potentiële voordelen van natuurlijke-pixelreconstructie beschreven worden. Sectie 0.4 en sectie 0.6 toonden immers aan dat kristalverstrooiing en kristalpenetratie belangrijk zijn in PET-resolutieherstel. Toekomstig werk zal onderzoeken welk additioneel resolutieherstel kan verkregen worden door middel van een gegeneralizeerde natuurlijke-pixelreconstructie waarbij de systeemmatrix gesimuleerd wordt met GATE. Op die manier kan kristalverstrooiing en kristalpenetratie voor verschillende detectormaterialen in rekening gebracht worden, resulterend in nauwkeurige detectorsensitiviteitsfuncties. Gezien GATE een van de meest accurate simulatietools is voor SPECT en PET, en gezien de veelbelovende inleidende resultaten van de gegeneraliseerde natuurlijke-pixelreconstructie, zijn we ervan overtuigd dat deze methode zich kan ontwikkelen tot een van de belangrijkste technieken van resolutieherstel die beschikbaar zijn in de nucleaire geneeskunde.

Chapter 1

Introduction

Non-invasive diagnostic imaging can be performed with different technologies: X-ray radiography, computed radiography, direct radiography, mammography, Computed Tomography (CT), UltraSound (US), and Magnetic Resonance Imaging (MRI), which all give anatomical information, and also with functional MRI (fMRI), optical imaging, thermography, planar isotope imaging, Single Photon Emission Tomography (SPECT), Positron Emission Tomography (PET), and gamma camera PET which return functional information. Recent devices combine two modalities on the same gantry in order to achieve hardware fusion of anatomical and functional images. Given the demographic aging in Western Europe, there exists a large interest in what is popularly referred to as a GPS-tool for cancer, i.e. a diagnostic tool for oncology that detects small malignant lesions in a very early stadium and that can be used for disease staging. Therefore research in nuclear medicine has a social support and bearing. In nuclear medicine examinations, a radiopharmaceutical is injected in the patient, marked with a radionuclide emitting one single photon with an energy of 100-200 keV in SPECT and a positron emitting radionuclide in PET. The emission of a positron finally results in two annihilation photons of 511 keV. Those photons are detected, mostly using a scintillation crystal that generates optical photons which travel through a light guide before reaching the PhotoMultiplierTubes (PMTs). Those PMTs convert the optical photons to electrons, which are in their turn used to generate a position and energy encoding signal. In PET there is an electronic collimation to acquire directional information while this information is obtained by applying a lead collimator in SPECT. The acquired data is afterwards reconstructed to result in a threedimensional radioactive tracer distribution within the patient. Optimization, evaluation and (re)design of all elements in this detection chain is mostly done using simulations. Given the possibility of modeling different physical processes, the Monte Carlo method has also been applied in nuclear medicine to a wide range of problems that could not be addressed by experimental or analytical approaches.

Monte Carlo methods are numerical calculation methods based on random variable sampling. This approach has been used to solve mathematical problems since 1770 and has been named 'Monte Carlo' by Von Neumann [78] because of the similarity of statistical simulations to games of chance, represented by the most well known center for gambling: the Monte Carlo district in the Monaco principality. The Monte Carlo method is very appropriate for medical physics due to the stochastic nature of radiation emission, particle transport and detection processes. Moreover nuclear medicine was advantaged by the possibility of using general purpose codes developed for high-energy physics experiments. Dr. Anger (who gave his name to the Anger gamma camera) was in the early 1960's the first researcher to predict the physical response of his new scintillation camera using simulations. The breakthrough for Monte Carlo methods in the medical physics field came with the review paper of Raeside [86] in 1976 and since then simulations are applied for detector modeling, system design, scatter correction technique evaluation, protocol optimization, reconstruction, dosimetry, external beam radiotherapy, radionuclide therapy, brachytherapy and pharmokinetic modeling. Due to computer limitations the method has not yet fully lived up to its potential. With the market of affordable mini-clusters rapidly gaining importance in nuclear medicine there has been a renewed interest in the topic for the past 3-5 years. Around 1976 only 175 scientific papers on Monte Carlo in medical physics were published a year, while this is now more than 1600 a year [142]. The major aim of the work discussed in this dissertation was to contribute to these new trends in nuclear medicine research.

Chapter 2 of this manuscript gives the reader a short overview of the nuclear medicine field, introduces the GATE software package and details again the relevance of accurate Monte Carlo modeling in emission tomography. This extensive introduction will highlight and select the most important application fields in which simulations can be of significant benefit for breakthrough performance: attenuation and scatter correction technique evaluation, design of acquisition systems and collimators, detector response modeling, up to Monte Carlo based reconstruction. All these different subtopics will be discussed in the remaining chapters. Chapter 3 describes a validation and a verification of the GATE simulation package versus measurements on a commercial scanner setup. Simulations can also enhance understanding of existing systems as is shown in chapter 4 where a transmission imaging device is modeled in order to optimize the specific clinical attenuation correction protocol. A scatter correction study has been performed for 3D PET which will also be discussed in this chapter. Chapter 5 describes the use of simulations for assisting in the design of a new small animal device using a novel collimator setup, aiming for a higher spatial resolution. In chapter 6 a theoretical model is deduced for the detector response in order to recover the intrinsic spatial resolution of a continuous detector PET system after iterative reconstruction. Simulations were used to verify this non-measurable analytical model. The results of Chapter 4 and Chapter 6 obviate the need for a Monte Carlo based approach to reconstruct the acquired data. Accurate simulations of the system matrix are necessary for incorporation in a dedicated reconstruction algorithm that solved storage and computer time issues. This will be discussed in chapter 7 and significant improvement in the reconstructed image quality will be shown since simulations allow to take into account all image degrading effects.

Research performed within the context of this PhD thesis resulted in 4 articles as a first author in peer reviewed high-impact international journals and in 9 publications as first author in international conference proceedings. Another 5 coauthored peer reviewed journal articles and 12 coauthored international proceedings resulted. References to these publications are given in a separate bibliographic section at the end of this dissertation.

Chapter 2

Monte Carlo simulations in emission tomography

2.1 Nuclear Medicine

Nuclear medicine imaging involves the use of radioactively labelled pharmaceuticals to diagnose and assess disease in the human body. The radiopharmaceutical is intravenously injected, inhaled or ingested: the choice of pharmaceutical and route of administration depends on the disease under investigation. Position sensitive detectors are used to detect the radiation emitted from the pharmaceutical and so, in principle, both the temporal and spatial distribution of the pharmaceutical within the body can be determined. Nuclear medicine stands in contrast to other medical imaging modalities. Ultrasound, MRI and X-ray CT predominantly give anatomical information, whereas nuclear medicine imaging gives functional information. Modern nuclear medicine imaging primarily consists of two main branches: single photon imaging and positron annihilation photon imaging, in which two annihilation photons are detected simultaneously [26, 88, 99].

2.1.1 SPECT

Single photon imaging requires at minimum just one detector fixed in one position to obtain a twodimensional projection of a threedimensional radiopharmaceutical distribution. A typical imaging system suitable for this task is the gamma camera (figure 2.1). A typical gamma camera consists of a collimator which limits the angle of incidence of the detected photons to almost perpendicular to the detector. The deposited energy is converted by a scintillator to visible light which travels through the crystal and the light guide towards a set

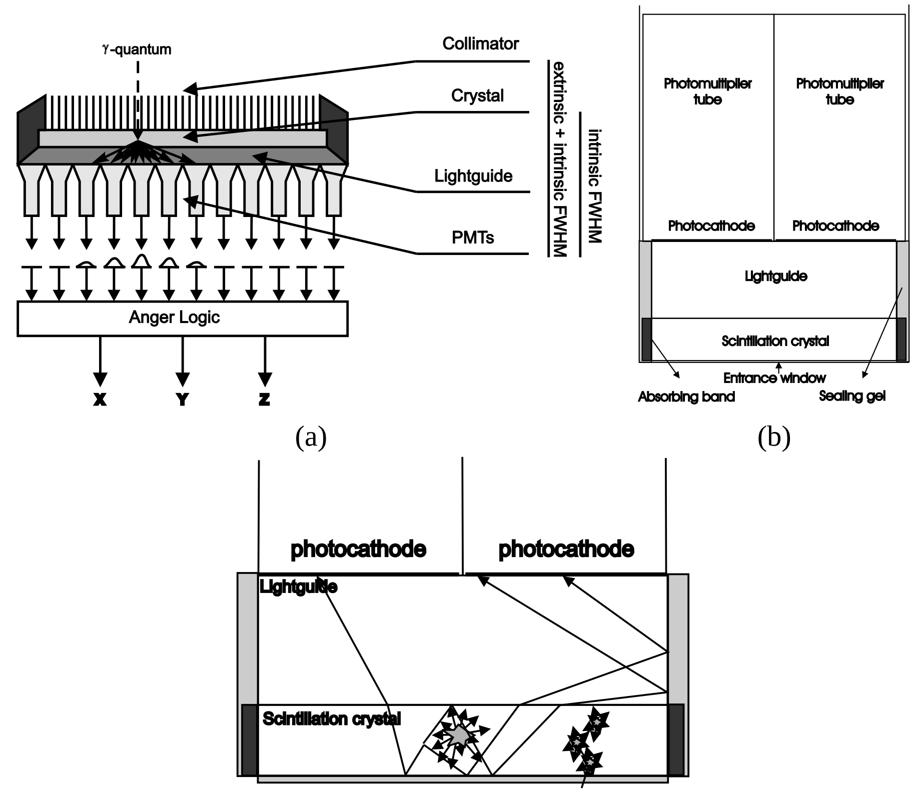

(a) (b)

(c)

Figure 2.1: Gamma Camera : (a) technical scheme, (b) detailed view, (c) optical photon transport.


(a) (b)

Figure 2.2: (a) SPECT: Philips Irix, (b) PET camera: Philips Allegro.

of PMTs containing a photocathode which converts the optical photons (figure 2.1(c)) into electrons that are transported over dynodes towards an Anger logic readout for position and energy signal calculation. More details on the collimation system will be given in chapter 3. Single projection imaging can be improved upon by simply rotating the gamma camera around the patient, thus obtaining a series of 2D projections. These can be used to retrieve depth information, which is known as SPECT. The quality of the information (i.e the time dependent reconstructed radiopharmaceutical images) obtained from SPECT depends considerably on the imaging time, camera sensitivity and position resolution. Consequently the temporal and spatial resolution of SPECT can be improved through the simultaneous use of more than one detector, and most systems consist of two or three heads mounted on a single gantry (figure 2.2(a)). The radionuclide mostly used in SPECT is ^{99m}Tc which has a half life of 6.03h and which emits photons of 140.5 keV. SPECT application fields in order of importance are cardiac imaging, bone scanning, neurology, renal and liver function imaging.

2.1.2 PET

Pharmaceuticals can also be labelled with neutron-deficient isotopes which are positron emitters. A number of elements which are fundamentally used by the human body can be positron emitters, allowing more scope for radiopharmaceutical design than is possible with single photon emitters. However, production costs are higher since a cyclotron is needed to generate these instable radionuclides. ^{18}F is mostly used to label the fluorodeoxyglucose (FDG) com-

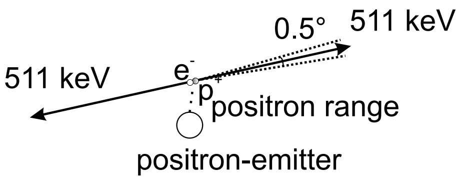

Figure 2.3: Positron range and gamma-gamma non-collinearity.

pound, which is a glucose analogue and thus suitable for functional (metabolic) visualization. The emitted positron annihilates with an electron giving rise to two virtually anti-parallel 511 keV photons, corresponding to the conversion of the rest mass of the two particles into energy (figure 2.3). The primary advantage of detecting both annihilation photons in time coincidence is the electronic collimation. Detection of two photons is sufficient to determine the line on which the annihilation took place and so no physical collimation is required, allowing higher sensitivity. PET (figure 2.2(b)) typically consists of a series of ring detectors, having a large number of separate crystals coupled to PMTs. Depending on the required sensitivity, the individual detectors can be in coincidence only with other opposing detectors in the same ring (using lead septa) or also with detectors in other rings (3D mode). This increases the sensitivity but also increases the scatter image degradation. PET application fields in order of importance are oncology, neurology, and cardiology.

2.1.3 Gamma Camera PET

An alternative geometry to that of the ring scanner is the rotating planar detector geometry. Rather than to surround the patient with detectors, this acquisition system relies on rotating opposing detectors which is potentially cheaper, at the cost of sensitivity. Some manufacturers have equiped their SPECT gamma cameras with coincidence timing modules and thicker crystals in order to be used as a gamma camera PET device, next to clinical SPECT applications. The Philips Irix, shown in figure 2.2(a), has a NaI(Tl) crystal of 19 mm and is suitable for gamma camera PET. This will be discussed further in chapter 4.

2.1.4 Hybrid devices

Recently a new trend and an important extension of the nuclear medicine field has been the upcoming of hybrid devices. The advantages of fused anatomical and functional images have long been appreciated, where the fusion was

(a) (b)

Figure 2.4: (a) SPECT/CT: Siemens TruePoint, (b) PET/CT: Philips Gemini

achieved by software methods [77]. While generally succesful for the brain, software approaches often encounter significant difficulties with the rest of the body. Routine fusion software requires access to images of different modalities, and the alignment procedures are generally time-consuming and uncertain of success. Most alignment algorithms specifically use a mutual information content measure of the two image sets and will generally fail to converge when the content of the two sets is highly dissimilar. This will typically be the case when either the functional image contains little or no correlative anatomical information or when the anatomical information in the functional image represents a different anatomy owing to, for example, patient movement or discrepancies in patient positioning between the two scans. While some of the discrepancies may be overcome by alignment using non-linear image warping techniques and 3D elastic transformations, an alternative approach to this post hoc image fusion is to combine the imaging technologies into one scanner, a scanner that can acquire accurately aligned anatomical and functional images in the same scanning session (figure 2.4). An additional advantage, when CT is combined with SPECT or PET, is that the CT images can be scaled in energy and used to perform an attenuation correction, thus eliminating the need for a separate time consuming transmission scan [120]. Chapter 4 proposes a solution to eliminate this transmission scan for the gamma camera PET case as well. To illustrate the potential of those new technologies, two case studies for SPECT/CT and PET/CT are described hereafter. The SPECT/CT case study [61] consists of a 74 year-old female that was complaining of pelvic pain during the follow-up of breast cancer (figure 2.5). A ^{99m}Tc-HDP whole body bone scan revealed focal increased tracer uptakes on the lumbar spine and the sternum. The question was raised to differentiate the lesions between osteoarthritis which is a degenerative joint disease, or metastases from an un-

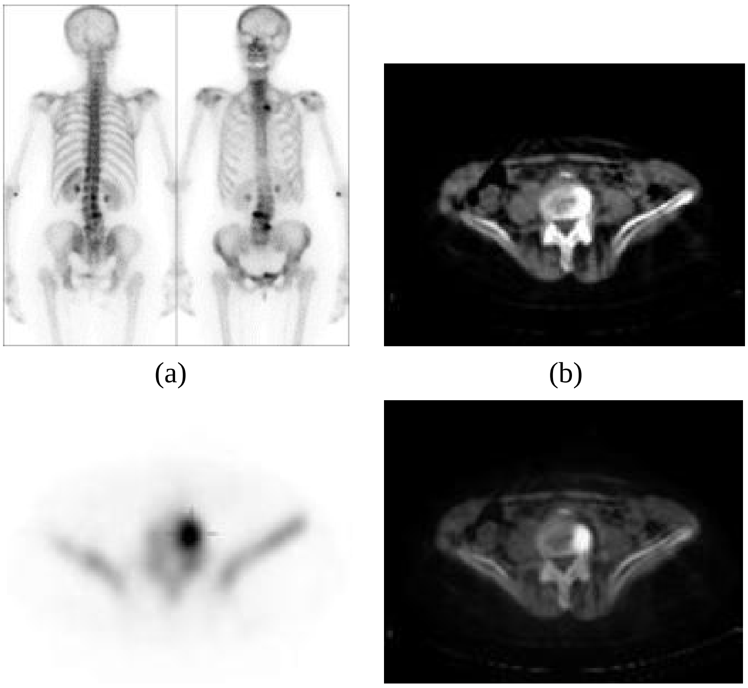

(a) (b)

(c) (d)

Figure 2.5: (a) whole body SPECT scan, (b) CT, (c) SPECT, (d) SPECT/CT hardware image fusion : lesion at the edge of the vertebral body.

known primary cancer. An abdominal and pelvic SPECT/CT scan was then performed. Bone SPECT confirmed the spinal lesions in the lumbar area, with an intense tracer uptake. CT images revealed high density lesions at the edge of the vertebral bodies. Fused images demonstrated perfect correlation between CT and SPECT lesions. Final diagnosis was osteoarthritis. The PET/CT case study consists of a 73-year old male with a history of colorectal cancer who had undergone a sigmoidectomy, which is the surgical removal of the sigmoid colon, and chemotherapy [120] (figure 2.6). A CT scan suggested a possible liver lesion and an abnormal para-aortic node. The PET/CT scan clearly showed intense uptake of FDG in a right anterior para-aortic lymph node and in a liver lesion both consistent with a malignancy.

2.1.5 Small animal imaging

The previous section discussed the recent advances in human SPECT/PET devices. However, the past four to five years were also a major breakthrough for small animal imaging, which has received considerable attention in the field of medical imaging. Dedicated high-resolution small animal imaging systems have recently emerged as important new tools for cancer research. These new imaging systems permit researchers to noninvasively screen animals for mutations or pathologies and to monitor disease progression and response to therapy. Several research groups have extended the use of imagers from human to small animal applications. Multiple modalities are already validated and available for research purposes.

- small animal MRI: research areas of growth pertaining to MR microscopy studies are focused on phenotyping of genetically engineered mice models of human neurological diseases and of rodent brain atlases [14].
- microCT: microCT systems provide high-resolution images (typically 50 microns or less), rapid data acquisition (typically 5 to 30 minutes), excellent sensitivity to skeletal tissue and good sensitivity to soft tissue, particularly when contrast-enhancing media are employed [85].
- microPET: application fields are neurosciences, neuroradiology, oncology, and gene expression imaging. Most small animal PET scanners [24] make use of recently developed high-end electronics, of new scintillator materials and are able to return a Depth of Interaction (DOI) estimate if using dual layer crystals (figure 2.7 [62]).
- microSPECT: microSPECT has been used to study cerebral binding sites, to image the expression of reporter genes, and for applications

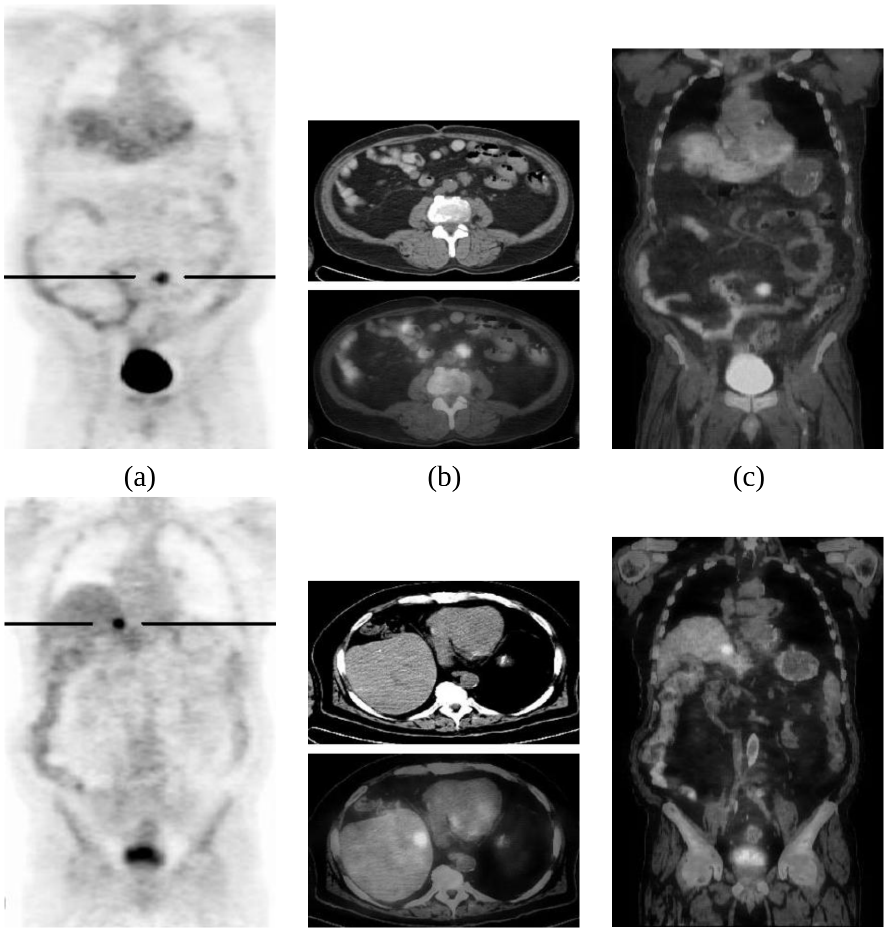

(a) (b) (c)

(d) (e) (f)

Figure 2.6: (a) a coronal PET image showing focal FDG uptake in a right anterior para-aortic lymph node, (b) transaxial CT image (upper) and fused PET/CT image (lower) taken at the level indicate by the line in (a), (c) the fused PET/CT image, corresponding to the PET image in (a), (d) coronal PET image, (e) CT image (upper) and fused PET/CT image (lower) taken at the level indicate by the line in (d), (f) the fused PET/CT image, corresponding to the PET image in (d).

(a) (b)

Figure 2.7: (a) Philips Mosaic small animal scanner, (b) clinical image of a rat.

in cardiology and oncology. High resolution SPECT can be approached in various ways:

  - pinhole collimator: the image spatial resolution depends both on the pinhole size and on the image magnification factor due to the imaging geometry. The sensitivity is low (figure 2.8(a)) [37].
  - multiple pinhole collimator: the sensitivity issue is partly solved by using a multiple pinhole design (figure 2.8(b)). Moreover higher resolution can be obtained by focusing the multiple pinholes at the region of interest (ROI) [12].
  - slit collimator: a slit collimator can accept much more photons than a pinhole collimator. During data acquisition (weighted planar integrals) the detector spins around its axis while rotating around the object (figure 2.8(c)). It is used in combination with a strip detector and returns a higher spatial resolution in a cost-effective way [145].
  - slat collimator: a slat collimator consists of a number of slats, parallel [43, 147] or convergent [146]. During data acquisitions (weighted planar integrals) the detector spins around its axis while rotating around the object (figure 2.8(d)). This collimation scheme is able to deliver a better sensitivity-resolution trade-off as will be extensively discussed in chapter 5.

- optical imaging for small animals

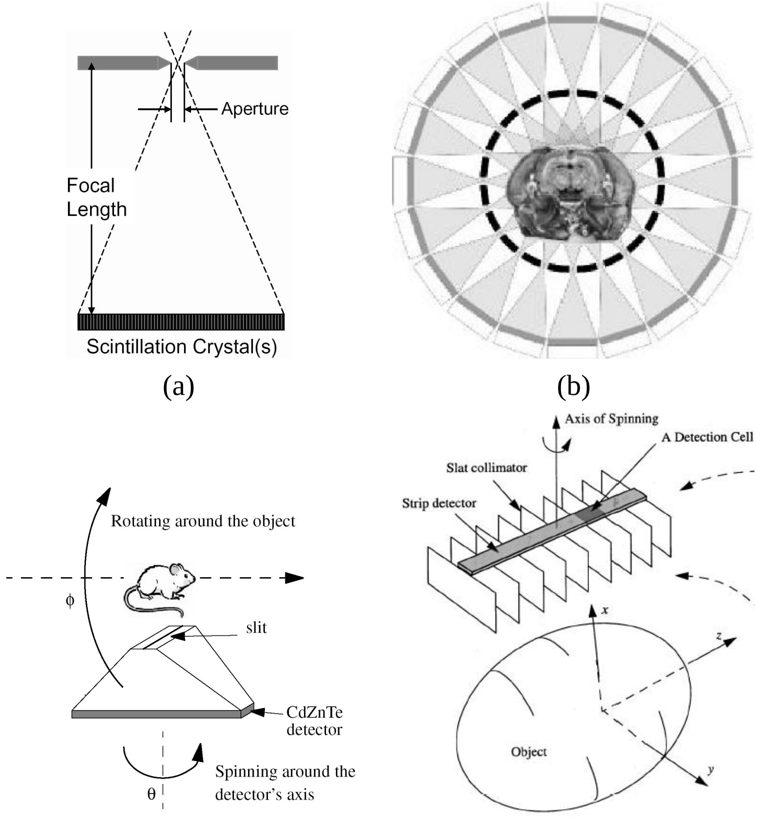

(a) (b)

(c) (d)

Figure 2.8: (a) pinhole imaging , (b) multiple pinhole imaging [12], (c) slit collimator [145], (d) slat collimator [43].

  - bioluminescence: this technique provides information on both spatial localization as well as the number of metabolically active cells and may also report function. Photoactive reporters linked to specific gene promoters provide information on gene expression in vivo [29].
  - fluorescence: this imaging modality is emerging as an important alternative because of its operational simplicity, safety, and cost-effectiveness. Fluorescence imaging has recently become particularly interesting because of advances in fluorescent probe technology, including targeted fluorochromes as well as fluorescent switches sensitive to specific biochemical events [51].

2.1.6 Reconstruction

Image reconstruction from projection data acquired under different angles can be performed in several ways [26, 95]:

- analytical reconstruction
  - Filtered BackProjection: analytical inversion of the X-Ray Transform based on the Central Slice Theorem
- deterministic iterative reconstruction
  - ART: Algebraic Reconstruction Technique
  - SIRT: Simultaneous Iterative Reconstruction Technique
- statistical iterative reconstruction
  - MLEM: Maximum Likelihood Expectation Maximization
  - MAP: Maximum a Posteriori

A deterministic model is obtained when the system characteristics are incorporated. Accordingly, the reconstruction problem can be solved analytically. If we assume the acquisition process to be statistical, then a statistical reconstruction technique is mandatory. Often used statistics are the Poisson model for the radioactive decay process and the Gaussian model for acquisition intrinsic features (detector response). The main advantage of a statistical model is that a smaller variance results in the reconstructed image if the appropriate models are used. Iterative reconstruction techniques are capable of incorporating image degrading effects in the reconstruction algorithm in order to improve the reconstructed image quality. MLEM [95, 132], which is an algorithm that incorporates the Poisson statistics of the radioactive decay in the reconstruction will be discussed as a basic statistical iterative reconstruction technique hereafter.

Let us consider a parametrized family of probability density functions: $F \rightarrow f(F|P)$ with F the reconstructed image and P the measurement. When $f(F|P)$ is viewed as a function of F with P fixed, it is a **probability density function**, and when viewed as a function of P with F fixed, it is a **likelihood function**. When we write down the Bayes' rule, we find:

$$Pr(F|P) = \frac{Pr(P|F)Pr(F)}{Pr(P)}, \tag{2.1}$$

wherein $Pr(P|F)$ is the likelihood (true forward probability) that the true tracer distribution F gives rise to a particular measurement P. This is the well-studied forward problem of the acquisition setup, commonly referred to as the detector response function. $Pr(F|P)$ however is the probability of an image, given the measurements. This is the a posteriori probability which is not known. For a posteriori knowledge of the true tracer distribution: $Pr(F|P)$, the likelihood $Pr(P|F)$ is needed. Assuming that the acquisition model (system matrix A) is known, the following expression for the expected value r in the projectionbin i is:

$$r_i = \sum_{j=1}^{N} a_{ij} f_j, \tag{2.2}$$

With N the number of pixels in the image. In reality p_i is measured rather than r_i. p_i is Poisson distributed with the expectation value r_i as mean:

$$Pr(p_i|r_i) = \exp(-r_i)\frac{{r_i}^{p_i}}{p_i!}. \tag{2.3}$$

All measured photons are independent and the total likelihood is the multiplication of the individual likelihoods:

$$Pr(P|F) = \prod_i \exp(-r_i)\frac{{r_i}^{p_i}}{p_i!}. \tag{2.4}$$

Maximizing this term is equivalent to maximizing the logarithm which is less complicated. This function is referred to as the log-likelihood function:

$$L(P|F) = \sum_i (-r_i + p_i \ln r_i - \ln p_i!). \tag{2.5}$$

The projection data can not be altered, so the last term is omitted. Maximization of this expression can be done in various ways but the Expectation-Maximization algorithm guarantees convergence. The derivation will not be discussed in detail [95, 96, 132]. The iterative EM algorithm is given by the following expression:

$$f_j^{(k+1)} = \frac{f_j^{(k)}}{\sum_{i=1} a_{ij}} \sum_{i=1}^{M} a_{ij} \frac{p_i}{\sum_{j'=1}^{N} a_{ij'} f_{j'}^{(k)}}, \tag{2.6}$$

where M is the number of detection bins and $\sum_{j'=1}^{N} a_{ij'} f_{j'}^{k}$ is the forward projection of the previous estimation f^k in the projection bin i. The ratio of the measured value p_i and this estimation is backprojected for each projection bin. These values are normalized and then multiplied with the current image estimate to obtain an updated estimate of the true tracer distribution. In a MAP reconstruction, a priori anatomical or analytical information is included in the reconstruction algorithm which accordingly includes a penalisation factor ($Pr(F)$) next to the data-fit term ($Pr(P|F)$) [48, 49, 74]. This is illustrated using the formula for the one-step-late algoritm:

$$f_j^{(k+1)} = \frac{f_j^{(k)}}{\sum_{i=1} a_{ij} + \beta \frac{\partial U}{\partial f_j^{(k)}}} \sum_{i=1}^{M} a_{ij} \frac{p_i}{\sum_{j'=1}^{N} a_{ij'} f_{j'}^{(k)}}, \tag{2.7}$$

where the function U is called the total energy function. U can for instance be expressed as a weighted sum of potential functions given by quadratic differences between pixel intensities. The influence of this regularization is tuned by an additional parameter β which expresses the relative importance of the data-fit term and of the smoothing regularization. If β is small, then the reconstructions are forced to fit the data, resulting in noisier images.

In the previous discussion we assumed the system matrix to be known exactly. The success of an iterative algorithm is indeed mainly dependent on the accuracy of modeling the system matrix: a_{ij} denotes the possibility that a decay in voxel i will be detected in bin j. The reconstruction problem is addressed in the most realistic way when reconstructions are performed using a Monte Carlo simulated projector in an iterative algorithm. Moreover, scatter and gamma camera spatial response are processes that can not be accounted for when reconstructing twodimensional slices from onedimensional projections as the photon distibution spreads over several slices. Therefore optimal reconstruction quality is obtained with a fully 3D projector. Limitations by computing power have to be accounted for [22], although feasible techniques have been proposed [13]. Monte Carlo based reconstruction will be discussed in chapter 7 showing results for a dedicated SPECT implementation.

2.2 The Monte Carlo method

Monte Carlo methods are statistical simulation methods wherein a statistical simulation is any simulation that uses a sequence of random numbers. In order to do Monte Carlo calculations some a priori information about the occuring physics processes in the simulations is needed; this information is expressed in the form of probability density functions (pdfs). When simulating photon interactions, the partial and total cross section data (based on the material constitution) represent such information used to calculate path length and type of interaction. Afterwards these pdfs are sampled by predefined sampling rules using randomly generated numbers. The energy of such a photon can be dissipated along its path or the photon can penetrate all scattering and attenuating media to reach the detector where a new pdf-sampling decides whether it should be accounted for in the scoring region or whether it should be discarded [141].

2.2.1 Random numbers

Random numbers are key important when modeling a physical system by a statistical model. Therefore, every random number generator has to deliver uncorrelated, uniform and reproducable sequences with a very long period in a short amount of time. A computer algorithm can be used to generate that random number from seed numbers. An example of such an algorithm is the linear congruental algorithm where a series of random numbers I_n is calculated from a first seed value I_0, according to the relationship

$$I_{n+1} = (aI_n + b)\text{mod}(2^k), \tag{2.8}$$

where a en b are constants and k is the integer word size of the computer. The seed value must be randomly changed, for instance by triggering a value from a call to the system clock.

2.2.2 Sampling methods

To obtain a stochastic variable that follows a particular pdf three different sampling methods can be used.

The distribution function method: a cumulated distribution function $cpdf(x)$ is constructed from the integral of $pdf(x)$ over the interval $[a, x]$ according to:

$$cpdf(x) = \int_a^x pdf(x')dx'. \tag{2.9}$$

The variable x is then sampled by replacing $cpdf(x)$ in (2.9) with a uniformly distributed random number in the range of $[0, 1]$ and solving for x. This sampling method is used if the inverse of the $cpdf(x)$ is easily obtainable.

The rejection method: possibly there can arise some mathematical difficulties in calculating the inverse of the $cpdf$. In the latter case the rejection method can be used. Let the $pdf(x)$ be defined in the range $[a, b]$ and calculate the normalized $pdf^*(x)$ as in

$$pdf^*(x) = \frac{pdf(x)}{max[pdf(x)]}, \tag{2.10}$$

so the maximum of $pdf^*(x)$ is 1. Then sample a uniform distributed value of x within the range $[a, b]$ from the relation

$$x = a + R_1(b - a), \tag{2.11}$$

where R_1 is a random number. Let a second random number decide whether the sampled x should be accepted. This is done by checking

$$R_2 < pdf^*(x). \tag{2.12}$$

If this relation is fulfilled, then x is accepted as a properly distributed stochastic value, otherwise x needs to be resampled.

Mixed methods: when the previous two methods are impractical, a mixture of the two methods above is used. Accordingly, the $pdf^*(x)$ is the product of two probability distribution functions $pdf_A^*(x).pdf_B^*(x)$, both normalized to unity. Now one determines an x value using the distribution method on $pdf_A^*(x)$ and applies then (with that x) the rejection method to $pdf_B^*(x)$ [76].

Non analog sampling: a direct Monte Carlo simulation using true pdfs may require an unacceptable long time to produce statistically relevant results. It may thus be desirable to bias the sampling by introducing stratification (limit source distribution), importance sampling (splitting or Russian Roulette using production tables) or by implementing forced detection (by imposing a registration in a scoring region).

2.2.3 Photon transport

Compton incoherent scattering and photoelectric effect are the two most important interaction mechanisms in nuclear medicine simulations. The total photoelectric cross section for a given energy, E, is calculated using discretized libraries by means of interpolation. The incident photon is absorbed and an electron is emitted in the same direction of the incident photon. The kinetic energy of the electron is defined as the difference between the energy of the original photon and the binding energy of the electron. The subshell of emission is again randomly sampled, thereby using cross sectional data for all subshells. When simulating the Compton scattering of a photon from an atomic electron on the other hand, an empirical cross section formula is used and sampling of the final state is done by a variant of the mixed Monte Carlo method as noted in 2.2.2. The quantum mechanical Klein-Nishina differential cross section per atom is:

$$\frac{d\sigma}{d\epsilon} = \pi r_e^2 \frac{m_e c^2}{E_0} Z[\frac{1}{\epsilon} + \epsilon][\frac{1 - \epsilon \sin^2 \theta}{1 + \epsilon^2}], \tag{2.13}$$

where

r_e = classical electron radius
$m_e c^2$ = electron mass
E_0 = energy of the incident photon
E_1 = energy of the scattered photon
$\epsilon = \frac{E_1}{E_0}$.

Assuming an elastic collision, the scattering angle θ is defined by the Compton formula:

$$E_1 = E_0 \frac{m_e c^2}{m_e c^2 + E_0(1 - \cos\theta)}. \tag{2.14}$$

The value of ϵ corresponding to the minimum photon energy (backscatter) is given by:

$$\epsilon_0 = \frac{m_e c^2}{m_e c^2 + 2E_0}, \tag{2.15}$$

hence $\epsilon \in [\epsilon_0, 1]$. One may state that:

$$\begin{aligned} \Phi\epsilon &\approx [\frac{1}{\epsilon} + \epsilon][\frac{1 - \epsilon \sin^2 \theta}{1 + \epsilon^2}] \\ &= f(\epsilon).g(\epsilon) \\ &= [\alpha_1 f_1(\epsilon) + \alpha_2 f_2(\epsilon)].g(\epsilon), \end{aligned} \tag{2.16}$$

where

$$\begin{aligned} \alpha_1 &= ln(\frac{1}{\epsilon_0}) \\ f_1(\epsilon) &= \frac{1}{\alpha_1 \epsilon} \\ \alpha_2 &= \frac{(1-\epsilon_0^2)}{2} \\ f_2(\epsilon) &= \frac{\epsilon}{\alpha_2}. \end{aligned} \tag{2.17}$$

f_1 and f_2 are probability density functions defined on the interval $[\epsilon_0, 1]$, and $g(\epsilon)$ is set to:

$$g(\epsilon) = [\frac{1-\epsilon\sin^2\theta}{1+\epsilon^2}], \tag{2.18}$$

being the rejection function $\forall\, \epsilon \in [\epsilon_0, 1] \Rightarrow 0 < g(\epsilon) \leq 1$. Given a set of 3 random numbers r,r',r'' uniformly distributed on the interval $[0, 1]$, the sampling procedure for ϵ is the following:

1. decide whether to sample from $f_1(\epsilon)$ or $f_2(\epsilon)$: if $r < \frac{\alpha_1}{(\alpha_1+\alpha_2)}$ select $f_1(\epsilon)$ otherwise select $f_2(\epsilon)$,

2. sample ϵ from the distributions to f_1 or f_2:
   for f_1 : ϵ=$\epsilon_0^{r'}$ ($\equiv \exp(-r'\alpha_1)$)
   for f_2 : ϵ^2=ϵ_0^2+$(1-\epsilon_0^2)$r’,

3. calculate $\sin^2\theta$=$t(t-1)$ where $t \equiv (1-\cos\theta)$=$\frac{m_e c^2(1-\epsilon)}{E_0\epsilon}$,

4. test the rejection function: if $g(\epsilon) \geq r''$ accept ϵ, otherwise go to (i).

The polar angle θ is deduced from the sampled ϵ value and in the azimuthal direction the angular distributions of both the scattered photon as the recoil electron are considered to be isotropic [1].

2.2.4 Scoring

A selection of relevant physical quantities such as energy, detection location and scatter events must be accumulated into tallies or scores. Also, an estimate of the statistical error as a function of the number of trials (and other quantities) must be determined.

2.3 GATE, a simulation platform for SPECT and PET

Dedicated codes exists to address problems specific to Single Photon Emission Computed Tomography (SPECT) such as SimSET [55], SIMIND [75], SimSPECT [140], and to Positron Emission Tomography (PET) such as PET-SIM [119] and Eidolon [143]. Dedicated packages are very powerful for their specific design-goal but are both not detailed and flexible enough to allow realistic simulations of emission tomography detector geometries. Moreover, they do not account for time explicitly, which limits their use for modeling time dependent processes such as decay, tracer kinetics, patient and bed motion, dead time or detector orbits. One may therefore prefer to use general purpose nuclear physics codes such as EGS4 [16], Geant4 [1, 46] or MCNP [17]. The main advantages of these general purpose codes are: they are widely used and extensively tested, they can be regarded as long-term existent as well as supported, and they are continuously evolving and therefore use the best of current hardware and software capabilities. There are fewer limitations on their possible applications, and fewer simplifying assumptions are made: for example, the processes taking place in the collimator can be thoroughly simulated whereas dedicated codes often use a parametric model. Next to that, time-dependent processes can be simulated and their non-specific design also offers the opportunity to implement future developments in SPECT and PET cameras [21], whereas dedicated codes are limited by the time of their design.

Therefore a new code-concept was designed as an upper layer for the Geant4 nuclear physics code and was tuned for use in nuclear medicine, more specifically to fulfill its role as a simulation platform for PET and SPECT incorporating all Geant4 features including well-validated physics models, basic event timing information, geometry modeling tools, visualization, and a scripting language for commanding the simulation. Object-oriented software design was envisaged to ensure high modularity and re-usability and the implementation effort was shared by a large research community in order to provide long-term support and maintenance.

Final specifications were circulated in December 2001 [110]. The development strategy was defined by the research groups involved in the GATE software development at Lausanne University (UNIL), Ghent University (ELIS) and Clermont-Ferrand University (LPC) who decided to start the OpenGATE collaboration [45]. The initial coding and validation of GATE was done by those research groups which resulted in 4 publications on the basics of GATE [73, 92, 107, 111].

Afterwards the collaboration grew very rapidly and focused mainly on the validation of GATE by evaluating simulation results versus measurements on both commercial and experimental imaging systems. This was done for PET, for SPECT and for small animal imaging systems. This will be further discussed in chapter 3 which is dedicated to validation.

A large effort was also invested in order to provide GATE with enough flexibility to model novel detection systems [104] still under design. Chapter 5 will provide a detailed discussion on a case study demonstrating this flexibility. After initial validation more effort was spent to verify whether the GATE simulation platform would be useful in clinical practice [106]. Results on this subtopic will be discussed in chapter 4. Finally, current work focuses most on further improvement of the digitization process in order to mimick the acquisition process (electronics) more accurately [91, 97, 103]. Chapter 6 will describe a deduced theoretical model that can be included in the digitizer to implement the accurate spatial resolution in continuous detector PET.

At the 2003 IEEE Medical Imaging Conference, the OpenGATE collaboration announced the first public release of GATE which took place on May 7th 2004. The ultimate aim of the OpenGATE collaboration is to further develop and validate GATE so that it becomes the gold standard in nuclear medicine Monte Carlo simulations [4, 68].

The research project discussed in the underlying manuscript contributed substantially, from the early beginning of GATE, to the development and validation of the SPECT platform. Also, an interface for voxelized clinical data was implemented within this context. A complex theoretical model was derived to be implemented as a continuous detector PET spatial resolution module. The last stage of this research project succeeded in developing the necessary GATE interface modules for Monte Carlo based reconstruction.

2.3.1 GATE: basic features

Software architecture

GATE is a C++ design, enabling a modular structure built on three fundamental layers: the core layer which defines the basic mechanisms available in GATE for geometry definition, time management, source definition, digitization, and data output, the application layer that is composed of classes derived from the base classes to model specific objects or processes and finally the user layer. The latter enables the user to simulate a setup through the use of scripting. Each functionality has its own messenger that translates the command to a straightforward instruction. Accordingly, a complete nuclear medicine experiment can be defined using this particular script language, including the camera geometry, the phantom geometry, detector electronics, the passing of time and the kinematic parameters, the output format, the physics processes, and the radioactive sources. The most important modeling instructions will be demonstrated hereafter using script-examples while discussing the implemented functionality.

Geometry

The following script example demonstrates the construction of the world volume, which defines the reference frame of the simulation. It can contain one or several sub-volumes referred to as daughter volumes.

```
#Definition of the world
/gate/world/geometry/setXLength 100 cm
/gate/world/geometry/setYLength 100 cm
/gate/world/geometry/setZLength 100 cm

#Creation of one detector head
/gate/world/daughters/name SPECThead
/gate/world/daughters/insert box
/gate/SPECThead/geometry/setXLength  5. cm
/gate/SPECThead/geometry/setYLength 20. cm
/gate/SPECThead/geometry/setZLength 30. cm
/gate/SPECThead/placement/setTranslation  20. 0. 0. cm
```

A logical volume is defined by all its properties except its position in the world. These properties include its name, shape, size, and material composition. When logical volumes are placed at specific positions they form physical volumes. Repeaters replicate and then place logical volumes at multiple positions and orientations to form physical volumes. Repeaters are basically elementary geometrical transformations such as rotations and translations applied in succession. The next script example demonstrates the use of a ring repeater to generate a triple headed scanner:

```
#Multiply head to create triple headed system
/gate/SPECThead/repeaters/insert ring
/gate/SPECThead/ring/setRepeatNumber 3
/gate/SPECThead/ring/setAngularPitch 120. deg
```

Complex structures are created by combining ring, linear, quadrant and cubicarray repeaters as is shown in figure 2.9 which demonstrates how the construction of a folded lead collimator for SPECT simulations was performed by repeating a hexagon on a rectangular array. This array was then filled with a translated duplicate, creating the correct distribution of air holes.

Accessing a material database file is the primary method for assigning material properties to volumes. This file contains all material parameters

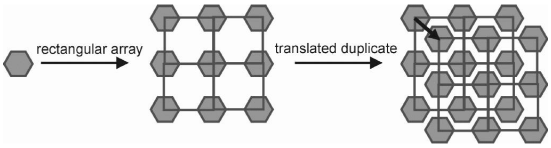

Figure 2.9: Detail of a collimator modeling process.

required by Geant4 to calculate the interaction cross-sections. The following example shows how breast material is obtained by defining the fraction of constituting elements.

```
#[Elements]
Hydrogen:   S= H   ; Z=  1  ; A=   1.01  g/mole
Carbon:     S= C   ; Z=  6  ; A=  12.01  g/mole
Nitrogen:   S= N   ; Z=  7. ; A=  14.01  g/mole
Oxygen:     S= O   ; Z=  8. ; A=  16.00  g/mole
Sodium:     S= Na  ; Z= 11. ; A=  22.99  g/mole
Phosphor:   S= P   ; Z= 15. ; A=  30.97  g/mole
Sulfur:     S= S   ; Z= 16. ; A=  32.066 g/mole
Chlorine:   S= Cl  ; Z= 17. ; A=  35.45  g/mole

#[Mixture]
Breast: d=1.020 g/cm3 ; n = 8
+el: name=Oxygen;     f=0.5270
+el: name=Carbon;     f=0.3320
+el: name=Hydrogen ;  f=0.1060
+el: name=Nitrogen;   f=0.0300
+el: name=Sulfur ;    f=0.0020
+el: name=Sodium ;    f=0.0010
+el: name=Phosphor;   f=0.0010
+el: name=Chlorine ;  f=0.0010
```

Specific guidelines with respect to the geometrical hierarchy must be followed. Most PET scanners are built following comparable concepts: one or more rings, each ring consisting of several scintillator blocks, each block being subdivided in crystal pixels, etc. For SPECT: a gamma camera with a continuous or pixelated crystal and a collimator. Most of these geometrical concepts are common to many different imaging systems. To facilitate this process and to provide a dedicated hierarchical output, predefined global *systems* are used. From the user's point of view, the main property of a *system* is that its geometric hierarchy is automatically accepted by the corresponding data output formats. ASCII and ROOT [18] output files are available for all *systems* and can easily be transformed to a list mode file for reconstruction pur-

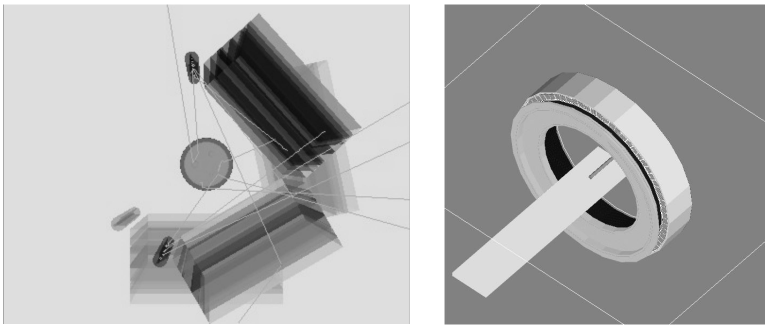

(a) (b)

Figure 2.10: Example scanner types modeled in GATE: (a) SPECT system (IRIX-Beacon), (b) PET system (ECAT HR+).

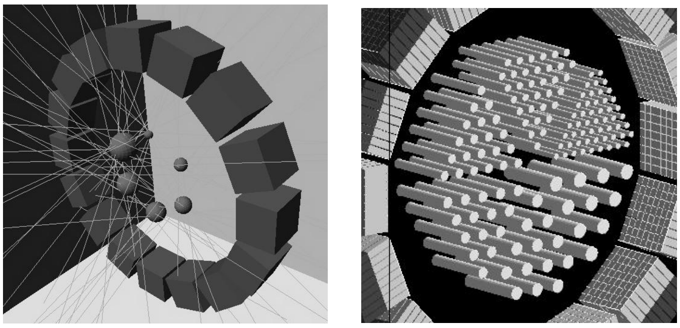

(a) (b)

Figure 2.11: Example of analytical sources: (a) simple phantom, (b) Derenzo phantom.

poses. Examples of a modeled SPECT and PET scanner using these predefined systems are shown in Figure 2.10.

Sources

The spatial distribution of a General Particle Source (GPS) can be specified using five two-dimensional shapes, *i.e.* circle, annulus, ellipse, square, and rectangle, and four three-dimensional shapes, *i.e.* sphere, ellipsoid, cylinder, and parallelepiped. A GPS can also be confined to an element of the geometry. This is shown in Figure 2.11 which shows the simulation of simple analytical sources. Moreover, the angular distribution of the decay particles can be tuned by using azimuthal and polar angles, making it possible to emit particles in different angular spans. Positron range and photon non-collinearity can be included for PET applications. However, the user can also force the annihilation photons to be emitted back-to-back to significantly decrease the simulation time. The following script example shows how these aforementioned parameters can be tuned by using script commands: a cylindrical ^{99m}Tc source of 3 MBq, emitting in a limited angular span is simulated:

```
/gate/source/addSource Source
/gate/source/Source/gps/type Volume
/gate/source/Source/gps/shape Cylinder
/gate/source/Source/gps/radius 5. cm
/gate/source/Source/gps/halfz 10. cm
/gate/source/Source/gps/centre 0. 0. 0. cm
/gate/source/Source/gps/particle gamma
/gate/source/Source/gps/energy 140. keV
/gate/source/Source/gps/setActivity 3000000. Bq
/gate/source/Source/gps/angtype iso
/gate/source/Source/gps/mintheta 0. deg
/gate/source/Source/gps/maxtheta 180. deg
/gate/source/Source/gps/minphi 0. deg
/gate/source/Source/gps/maxphi 360. deg
```

Voxelized phantom or patient data can be used as inhomogeneous, anthropomorphic sources to reproduce realistic acquisitions [105]. A voxelized source can be read either as an ASCII file or as an Interfile image [63]. The image gray scale is then converted into activities using either a linear translator or a range translator. The gray scales are therefore discretized in numerous intervals. Afterwards those activity levels are used to determine the number of primary particles for each voxel. In the case of a range translator, only numbers greater than zero are converted into voxels. Figure 2.12(a) shows the result of the digital Hoffman brain phantom that is converted into an activity distribution in GATE. In addition, GATE can read in voxelized attenuation geometries. An example of a patient attenuation map and its counterpart for GATE simulation purposes is shown in figure 2.12(b).

The following script example reads in an Interfile based Hoffman hardware phantom and assigns the appropriate material mixtures of plastic and water to the individual voxels based on their image gray value:

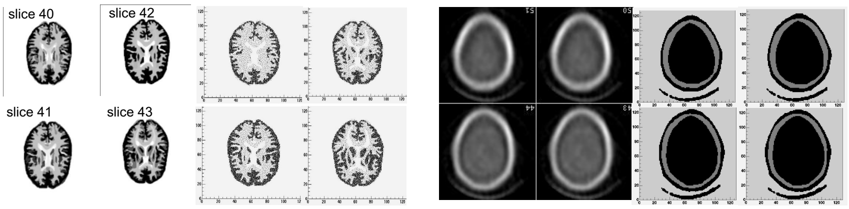

(a) (b)

Figure 2.12: Clinical extension for an inhomogeneous image: example of how an emission and attenuation map are represented by the simulator: (a) emission map (left: digital Hoffman phantom data - right: read in by the simulator), (b) attenuation map (left:actual patient data - right:read in by the simulator).

```
# Insert a replica-based voxel-matrix geometry
/gate/world/daughters/insert replicaMatrix
/gate/replicaMatrix/geometry/insertReader interfile
/gate/replicaMatrix/interfileReader/insertTranslator range
/gate/replicaMatrix/interfileReader/rangeTranslator/readTable range.dat
/gate/replicaMatrix/interfileReader/rangeTranslator/describe 1
/gate/replicaMatrix/interfileReader/readFile hoffman.h33
/gate/replicaMatrix/interfileReader/describe 1
/gate/replicaMatrix/attachPhantomSD
```

In this case, the gray scale is converted into material definitions using a range translator as is shown by the script example hereafter:

```
# Example of the range translator: range.dat
   6
   0   12  Plastic
  13   25  Pla3Wa1
  26   50  Pla2Wa2
  51   75  Pla1Wa3
  76  100  Water
 101  250  Air
```

Simulated projection data of this Hoffman hardware phantom (voxelized source) with and without a voxelized attenuation geometry is shown in figure 2.13. To demonstrate the effect of the attenuation, both projection data are compared by plotting two midway horizontal profiles of the sagittal projections as is shown in figure 2.14. The voxelized nature of the results is obvious, as well as the appropriate attenuation effect.

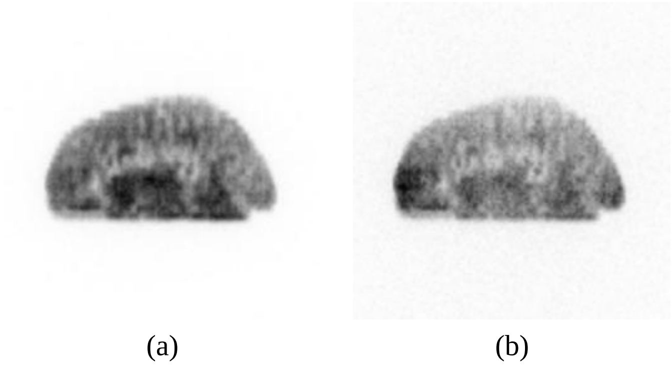
(a) (b)

Figure 2.13: Interfile reader : simulated projection data of the Hoffman brain phantom: (a) without attenuation; (b) with a voxelized attenuation geometry based on the same phantom.

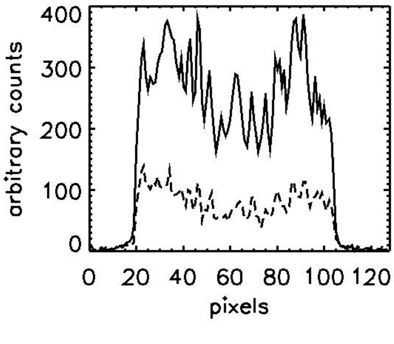

Figure 2.14: Midway horizontal profile of the simulated voxelized source sagittal projection data of the Hoffman brain phantom with (dashed line) and without (full line) the voxelized attenuation geometry.

Physics

The electromagnetic interactions used in GATE are derived from Geant4 . The electromagnetic physics package manages electrons, positrons, γ-rays, X-rays, optical photons, muons, hadrons, and ions. When using the low energy package, the treatment of photons and electrons is extended and verified down to 250 eV and includes Rayleigh scattering. This is the most accurate package for biomedical applications but comes at the price of increased computing time.

The non-collinearity of two annihilation photons for PET applciations is not taken into account by Geant4. An additional module has been incorporated in GATE that models the angular distribution model of these photons based upon a Gaussian angular distribution in water (0.58^o FWHM) [64].

The following script command lines show how the physics of the simulation can be adapted:

```
/gate/physics/gamma/selectRayleigh lowenergy
/gate/physics/gamma/selectPhotoelectric lowenergy
/gate/physics/gamma/selectCompton lowenergy
/gate/physics/gamma/selectGammaConversion inactive
/gate/physics/gamma/listProcesses
/gate/physics/setXRayCut 200. keV
/gate/physics/setElectronCut 1. km
/gate/physics/setDeltaRayCut 1. GeV
```

2.3.2 GATE: Time Management

One of the most important features of GATE is the management of time-dependent phenomena, such as detector movement or source decay kinetics, which are kept synchronized to allow a coherent description of the acquisition process [92, 106]. This will appear to be mandatory for the simultaneous emission and transmission imaging study, to be discussed in chapter 4. The following script example shows the movement of the gantry at a speed of 1 deg per second as well as a translation of the patient support. Moreover, the rotation of the gantry and the translation of the table are kept synchronized which allows to simulate whole body acquisitions.

```
#Movement of the gantry
/gate/SPECThead/moves/insert orbiting
/gate/SPECThead/orbiting/setSpeed 1 deg/s
/gate/SPECThead/orbiting/setPoint1 0 0 0 cm
/gate/SPECThead/orbiting/setPoint2 0 0 1 cm
#Movement of the patient support
/gate/Table/moves/insert translation
/gate/Table/translation/setSpeed 0 0 1. cm/s

/gate/application/setTimeSlice     1.  s
/gate/application/setTimeStart     0.   s
/gate/application/setTimeStop    360.  s
/gate/application/startDAQ
```

Next to synchonizing the geometry movements, the synchronization of the source kinetics with those movements allows for the simulation of realistic acquisition conditions including patient movement, respiratory and cardiac motions, scanner rotation, or changes in activity distribution over time. Therefore, the start (0 sec in the previous example) and stop time (6 min here) of the acqusition must be provided by the user, as well as the sampling interval (1 sec in this case). In such a time slice, the geometry is kept at rest while the update is performed at the time slice transition. The sources are allowed to decay within the time slice and the particle transport proceeds. Count rates, random coincidences, event pile-up, and detector dead time [97] can be simulated using this intrinsic event sequence timing.

2.3.3 GATE: Digitization

Parts of the scanner geometry are designated as sensitive detectors, and interactions are recorded within these regions. Sensitive detectors are used to store information about particle interactions. Two types of sensitive detectors are defined in GATE: the crystal sensitive detector (crystalSD) and the phantom sensitive detector (phantomSD) as is shown in the following script example:

```
/gate/crystal/attachCrystalSD

/gate/lightguide/attachPhantomSD
/gate/isolation/attachPhantomSD
/gate/phantom/attachPhantomSD
/gate/shielding/attachPhantomSD
```

The crystalSD is used to generate *hits* from interactions that occur inside the detector parts of the scanner (in this example the crystal). The data contained in these *hits* include the energy deposition, interaction positions, origin of the particle, type of interaction, volume name, and time information. The

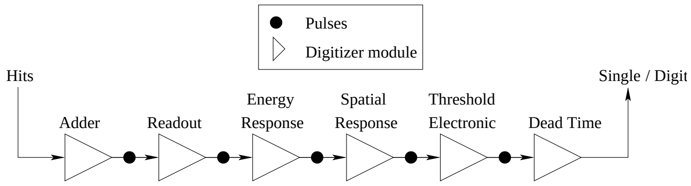

Figure 2.15: The digitizer is organized as a chain of several modules that processes the *hits* to yield a single, which represents a physical observable.

phantomSD on the other hand is used to detect and count the Compton and Rayleigh interactions occurring within the scanner's field-of-view (FOV). For this example the number of scattering interactions that occured in the light-guide, the isolation, the shielding and the phantom are recorded.

The digitizer consists of a chain of processing modules (figure 2.15) that takes a list of *hits* from the sensitive detectors and transforms them into *pulses* referred to as singles. The key elements of this chain will be briefly described hereafter. The inserted detection modules can also be controled by the typical messenger instructions as is shown in the example hereafter:

```
/gate/digitizer/Singles/insert adder
/gate/digitizer/Singles/insert readout
/gate/digitizer/Singles/readout/setDepth 1
/gate/digitizer/Singles/insert blurring
/gate/digitizer/Singles/blurring/setResolution 0.225
/gate/digitizer/Singles/blurring/setEnergyOfReference 511. keV
/gate/digitizer/Singles/insert spblurring
/gate/digitizer/Singles/spblurring/setSpresolution 2.0 mm
/gate/digitizer/Singles/insert deadtime
/gate/digitizer/Singles/deadtime/setDeadTime 100. ns
/gate/digitizer/Singles/deadtime/setMode paralysable
/gate/digitizer/Singles/deadtime/chooseDTVolume crystal
/gate/digitizer/modules/insert thresholder
/gate/digitizer/thresholder/setThreshold 350. keV
/gate/digitizer/modules/insert upholder
/gate/digitizer/upholder/setUphold 650. keV
```

This script example performs several operations on the singles level. Firstly the deposited energy of all interactions in a sensitive detector (*hits*) are summed to yield a *pulse* by the adder. The position of the *pulse* is calculated from the energy-weighted centroid of the *hit* positions, and the time of the *pulse* is set to that of the first *hit* within the volume. If a particle interacts in several sensitive detectors, for instance after crystal scatter or after crystal penetration, the hit adder will generate a list of *pulses*, one for each sensitive detector. The second instruction (readout) implements the readout segmentation of the scanner. The position of this *pulse* is set to that of the *pulse* from the adder that has the most energy (winner-takes-all paradigm).

After this adding and readout instruction the remaining commands of the script example transform these counts into the physical observables of the scanner (*i.e.* singles). The blurring instruction applies a Gaussian blur to the energy of the *pulse*, E, with a full width half maximum (FWHM), $R \times E$. A simple model assumes that the FWHM energy resolution, R, is inversely proportional to $\sqrt{E}$ parametrized by R_0, the user defined FWHM energy resolution (22,5 $\%$ in the example) at a given energy, E_0 (511 keV here). A more elaborate model is available that propagates the relative variances of the physical processes involved with light collection and detection in a spectrometric chain. The spblurring instruction applies a Gaussian blur of the position for SPECT (2 mm in the example). For PET, spatial resolution is calculated by the pulse reader which simulates the intrinsic spatial resolution of the detector. More elaborate models are derived for continuous crystal detector PET systems [103] and will be discussed in chapter 6. Both paralyzable (the detector is dead for a period t after every event, even if the event arrives during the dead period of the previous event) and non-paralyzable dead times (the detector is dead for a period t after every event) can be modeled on an event-by-event basis. In this script example a paralysable model is chosen to implement a 100 ns deadtime on the singles at the crystal level. Finally an energy discrimination is performed to set an acceptance window of 350-650 keV (thresholder-upholder).

Other user defined modules can be added individually to model more specific properties: time resolution, light yield, transfer and quantum efficiency and so on. Moreover, at the end of a digitizer chain a coincidence sorter can be added to find pairs of singles that are in coincidence (whenever the time interval between the singles is less than a user-defined coincidence window). Using the event number and the Compton flag, randoms and scatter events can be differentiated from trues. Multiple coincidences and auto-coincidences are also taken into account.

The optimization of the digitizer chain parameters is very time-consuming. This is best done by comparing the results from different sets of digitizer parameters using the same series of *hits*. To perform this specific task, GATE offers an operating mode named DigiGATE. In this mode, *hits* are read from a data file generated by GATE and fed directly into the digitizer chain. All conditions are kept identical in the simulations including time dependencies.

2.3.4 Calculation time

An important issue of GATE Monte Carlo simulations is the computation time. Benchmark simulations were performed to estimate the simulation time for realistic nuclear medicine setups.

For PET, a whole-body scanner was implemented, consisting of eight detector heads arranged within a 88 cm diameter by 40 cm axial length octagonal cylinder. Each head is made of 400 detector blocks and each block is a 5×5 array of dual-layer LSO-BGO crystals. The heads are equipped with partial septa that rotate in a step-and-shoot mode. The phantom in this benchmark is a 70 cm long water cylinder with one ^{18}F (half-life = 109.8 min) and one ^{15}O (half-life = 2.07 min) line source each with an activity of 100 kBq. The simulated acquisition is 4 min in duration, which represents approximately two ^{15}O half-lives. The computing time for the PET benchmark averaged around twelve hours on a 1.0 GHz processor. This results in 852 generated and tracked events per second and 16 simulated coincidence detections per second.

For SPECT, the following typical setup was implemented: a gamma camera is comprised of 4 heads at 90 degrees each. All heads are identical, consisting of a parallel hole lead collimator (hole diameter: 0.3 cm, collimator thickness: 3 cm, and septa thickness: 0.6 mm), a 1 cm thick NaI crystal, a 2.5 cm thick back-compartment in Perspex, and a 2 cm thick lead shielding. Also, a cylindrical phantom (5 cm in diameter and 20 cm long) filled with water with an inner cylinder (2 cm in diameter, 5 cm long) filled with 30 kBq of ^{99m}Tc. The phantom lies on a table (0.6 cm thick, 8 cm wide, and 34 cm long). During the simulated acquisition, the table and phantom translate together at 0.04 cm/s. The simulated acquisition consists of 64 projections (16 projections per head), acquired along a circular orbit with a 7 cm radius of rotation and a speed of 0.15 deg/s. Sixteen runs of 37.5 s each are performed to simulate the 16 positions of the 4 gamma camera heads. Calculation time comprised eleven hours on a 1 GHz processor, this results in 417 generated and tracked events per second and 0.83 detections per second or 1.2 second per detection.

The reasons for the high computation time in the SPECT simulations with a collimator are fourfold. The total number of registered counts in SPECT is less than 0.02 $\%$ of the generated events because the collimator in front of the crystal stops most of the incoming photons and registers all processes present. This effect is most pronounced in high resolution collimator variants. Secondly, GATE tracks every photon through every object of the experiment, and a typical Low Energy High Resolution (LEHR) collimator for instance consists of 161120 individual air holes. The use of parametrized replicas for the collimator hole arrays can speed up the simulations for certain applications. Thirdly no variance reduction methods were used so far. We are performing research on the latter two [34]. Bootstrapping and jackknifing will also be investigated in that context. Bootstrapping is a method for estimating the sampling distribution of an estimator by resampling with replacement from the original sample, for instance on list mode files. Jackknifing is a another resampling technique where each event is eliminated from the list after selection [36]. Finally the emission angle was not limited into a certain range so as not to influence the scatter processes in the phantoms or the backscattering from the other detector heads.

2.4 Relevance of accurate Monte Carlo modeling in Nuclear Medicine

In the most recent review article on the relevance of accurate Monte Carlo modeling in nuclear medical imaging [141] four important application fields were highlighted. Moreover, Monte Carlo is the only possible approach for all applications where measurements are not feasible or where analytic models are not available due to the complex nature of the problem [2, 76]. Those four main application fields will now be discussed in detail.

2.4.1 Attenuation and scatter correction techniques

The presence of the scatter and attenuation effect in nuclear medicine images limits the accuracy of activity quantitation. Scatter does not produce major artifacts comparable to attenuation but reduces contrast by including a low-frequency blur in the image. The impact of scatter generally depends on the photon energy, camera energy resolution and energy window settings, as well as the object shape, detector geometry and the source distribution. Many of these parameters are non-stationary which implies a potential difficulty when developing proper scatter and attenuation correction techniques. Scatter correction is not only important for quantitation but also for lesion detection and image segmentation. Monte Carlo calculations have been found to be powerful tools to quantify and correct for photon attenuation and scattering in nuclear medicine imaging since the user has the ability to separate the detected photons according to their interaction history: primary events, scatter events, contribution of downscatter events, scatter in patient or detector, etc. [144]. Monte Carlo modeling thus allows a detailed investigation of the spatial and energy distribution of Compton scatter: energy spectra, point-spread functions and scatter fractions can be simulated [107]. This would be impossible to perform using present experimental techniques, even with very good energy resolution detectors.

Much research and development has been concentrated on scatter compensation for quantitative **SPECT** [6, 8, 9, 11]: factor analysis, dual window methods (DW), triple energy window (TEW) corrections, scatter line spread function correction (SLSF), convolution methods (CV), etc. [23]. Attenuation and scatter correction techniques are particularly important for simultaneous emission and transmission imaging where several methods have been proposed to differentiate between the emission and attenuation source [10,42,117] since downscatter of the attenuation source in the emission window is an image degrading factor when performing low- and medium-energy SPECT studies. The same remark is valid for downscatter of the emission source in the attenuation window for gamma camera PET (section 2.1.3) applications. The main objective of Monte Carlo simulations is to characterize this interwindow scatter and to investigate by what parameters it is particularly influenced in order to perform a protocol optimization [106]. This will be discussed in chapter 4.

In **PET** some basic approaches are followed for scatter correction [58]: multi-energy window approaches, integral transformations, curve fitting, model-based approaches, and direct Monte Carlo techniques. Especially in PET, Monte Carlo simulations are important to verify which scatter order is contributing the most in image degradation. Moreover, the relation between object scatter and crystal scatter is relevant to optimally correct for scatter in an iterative algorithm [28, 108]. This will also be discussed to a larger extent in chapter 4.

2.4.2 Imaging systems and collimator design

Image formation modeling is one of the most important reasons for the existence of Monte Carlo simulations in nuclear medicine. By using Monte Carlo methods, the image formation process can be assessed both qualitatively and quantitatively and Monte Carlo methods can assist in the development of new collimator designs, new detector construction, evaluation of new electronics and in optimization of camera motions [137]. Monte Carlo simulations were extensively used to analyze the performance of new long bore parallel collimators as well as fan beam [30], cone beam and pinhole collimators [98]. For the latter, simulations were performed with various aperture span angles, different hole sizes and various materials to evaluate the penetration [123]. The well known imaging performance parameters of parallel hole collimators could be compared with those for fan beam and cone beam which have enjoyed considerable success for brain SPECT in recent years [84]. Monte Carlo methods also play an important role in new system design, for instance in the research field of solid state detectors with improved energy resolution and low-noise electronics [43, 52, 104]. Chapter 5 will give a detailed discussion on the latter two aspects by describing the simulation of a prototype CZT design coupled to a new collimation approach aiming for a higher spatial resolution at a comparable sensitivity. Similarly, in the PET field, Monte Carlo techniques were used to determine the effects of several crystal materials and of interplane septa with varying constitution [53], thickness and geometry, to compare single to true coincidence events ratios in single-slice, multi-slice and open collimator 3D configurations [118], and to assess the effect of collimation on scatter fraction. Moreover, Monte Carlo simulations have been used in the past years to study potential designs of dedicated small animal positron tomographs [56,97].

2.4.3 Detector Modeling

Monte Carlo simulations of detector responses and efficiencies are extremely important since the scintillation crystal is the critical component in emission tomography. Increased light per gamma ray interaction, faster rise and decay times, greater stopping power and improved energy resolution are the desired characteristics. Improvements in these characteristics enable detectors to be divided in smaller elements, thus increasing resolution and minimizing dead time losses. An important field of interest is resolution recovery in PET. The penetration of annihilation photons into the detector material before interaction is a statistical process which leads to significant displacement and anisotropy of the point spread function [60, 103]. Compensation for crystal penetration is thus the most important issue in order to recover the spatial resolution in PET. Theoretical models for that anisotrope spatial resolution can only be verified by Monte Carlo simulations since those depth of interaction (DOI) dependent experiments are very hard to perform with current devices. In chapter 6 a complex mathematical model will be derived for this intrinsic spatial resolution in the case of continuous detector PET systems. This model will be validated in the same chapter by geometrical Monte Carlo simulations [103]. Moreover, Monte Carlo methods can assist in the design of new detectors with DOI information by simulating multilayer crystals and by estimating the gain in reconstructed resolution through incorporation of DOI information [72, 81]. Monte Carlo simulations also prove their usefulness in Time-of-Flight PET (TOF) design. They can be used to test several detector crystals and to simulate the influence of timing resolution on variance reduction [15, 80, 112].

2.4.4 Image reconstruction algorithms

Monte Carlo simulations have shown to be very useful for validation and comparative evaluation of image reconstruction techniques since it is possible to obtain a reference image to which the reconstructed images should be compared. Another research area is Monte Carlo based reconstruction. In parallel hole collimator **SPECT**, image reconstruction is usually performed as a set of 2D analytical or iterative reconstructions. This ignores the 3D intrinsic nature of the scatter process. Approximate analytical models to account for scatter have been proposed [6, 8, 9, 11]. To explicitly deal with the 3D nature of the image formation process, a simulated 3D projector modeling the 3D photon spread and thus including all image degrading effects (attenuation, scatter and camera point spread function) can be used [39,40] in a fully 3D reconstruction algorithm. This will be of particular interest for reconstructing SPECT projection data with a severe photon spread due to a suboptimal collimator choice, a problem that will be discussed in chapter 4. Chapter 7 will discuss the Monte Carlo based reconstruction solution for this in more detail [106]. Emphasis will especially be on the way the storage and reconstruction time issues were solved. Monte Carlo based reconstruction for **PET** is particularly interesting to perform an intrinsic resolution recovery and to incorporate intercrystal scatter. In chapter 7 it will be explained how the detector response function, dicussed in chapter 6, can be incorporated in a Monte Carlo based reconstruction, again avoiding storage and computation time issues [125].

2.4.5 Application in other domains

Monte Carlo simulations are used in dosimetry and radiotherapy research to a large extent. One application is the individual treatment planning in radionuclide or radioimmunotherapy [116] where prospective dose estimates are made in the latter by using a tracer activity of a radiolabeled antibody to obtain biodistribution information prior to administration of a larger therapeutic activity. The Monte Carlo simulations return a dosimetric evaluation of the quantitative tracer distribution image. The clinical implementability of treatment planning algorithms will depend on the time required to generate those absorbed dose estimates for each individual.

Monte Carlo simulations are also used for the evaluation of external beam radiotherapy setups [41]. A complete simulation model of the accelerator head, including scatter foil or X-ray target and flattening filter, multileaf collimator, support plates and so on, is necessary for this purpose. Hybrid devices such as SPECT/CT and PET/CT (section 2.1.4) will allow to better delineate the Planned Target Volume (PTV) on CT using the functional information of the registered nuclear medicine images, thus fundamentally increasing the accuracy. Precise Monte Carlo simulations should be used accordingly in the virtual treatment planning system to maintain the most precise dose estimates [25] and to further improve the treatment plan before sending the patients to the linac simulator for hardware alignment. The latter is done by comparing the beam's eye view of the treatment simulator with the digitally reconstructed radiograph. Meanwhile the practical feasibility of the resulting beams is verified. The actual treatment will only start after verification of the alignments by portal imaging. The SPECT/CT or PET/CT delineations together with the precision of the dosimetric Monte Carlo simulations will thus directly influence the accuracy of the treatment and will assist in further reducing the colateral damage to functional organs at risk.

Another field of interest is to perform a Monte Carlo based dosimetry for brachytherapy applications [89] to provide detailed descriptions of local doses. Hadrontherapy is a Monte Carlo assisted research area [44] where simulations reproduce the beam-induced β^+ emissions of the irradiated target nuclei along the beam path in order to assist to the design of in-beam PET systems with high sensitivity and high spatial resolution.

2.5 Conclusion and original contributions

In this chapter a short overview of nuclear medicine (SPECT, PET, gamma camera PET, hybrid devices, small animal imagers and reconstruction) was given in order to set the scope of the underlying dissertation. The GATE simulation package was introduced as an upper layer of the general-purpose high energy physics code, Geant4. The presented implementation framework of GATE, to which this dissertation contributed, resulted in two peer review collaboration papers [4, 68]. The clinical usefulness of GATE depends on its ability to use voxelized datasets. Therefore a clinical extension was written so that digital patient data can be read in by the simulator as a source distribution or as an attenuating geometry. This resulted in the following journal publication [105].

A thorough literature study was presented in this chapter which highlighted four main application fields of Monte Carlo methods in nuclear medicine imaging: attenuation and scatter correction techniques, imaging systems and collimator design, intrinsic detector modeling and Monte Carlo based reconstruction. Specific research on these four topics will be presented respectively in chapter 4, 5, 6 and 7. Chapter 3 however will start with reporting the SPECT validation study that was performed to verify the accuracy of GATE simulations versus measurements on a commercial SPECT acquisition system.

Chapter 3

Validation

3.1 Introduction

After the GATE simulation platform was developed, extensive validation was needed to verify whether all designed modules were functioning appropriately and whether the simulation package was accurately mimicking realistic acquisitions. In this chapter we present validation results of GATE based on the comparison of simulations against experimental data, acquired with a standard SPECT camera. Photoelectric effect, Compton and Rayleigh scatter are included in simulations of the gamma transport process. The most important components of the scintillation camera were modeled: the cover, the crystal in its aluminum casing, the light guide, the PMTs, the compression plate, the air gap, the lead ending and a collimator. More specifically, a Low Energy High Resolution (LEHR) and a Medium Energy General pupose (MEGP) collimator were modeled as closely as possible with respect to their shape and dimensions. GATE is the only simulation package that allows to model a collimator without using simplifying parametric models. Consequently, investigation of all physics processes involved in the collimator such as scatter, penetration and lead fluorescence becomes possible. In this validation study, we compared the simulated and measured energy spectra of different isotopes: ^{99m}Tc, ^{22}Na, ^{57}Co and ^{67}Ga. The sensitivity was evaluated by using sources at varying distances from the detector surface. Scatter component analysis was performed in different energy windows at different distances from the detector and for different attenuation geometries. Spatial resolution was evaluated using a^{99m}Tc source at various distances.

Figure 3.1: Dual-headed Philips AXIS camera.

3.2 Basic geometry modeling

The camera used for validation is the dual-headed AXIS camera, manufactured by Philips Medical Systems (figure 3.1). Each detector head contains a 54 cm transaxial x 38 cm axial NaI crystal of 0.95 cm thickness. The readout is done by an array of PMTs, diagonally distributed over the crystal. In optimal conditions the energy resolution at 140.5 keV is 9.5 % and the intrinsic spatial resolution is 0.33 cm.

3.2.1 Collimator

In order to achieve accurate models of LEHR and MEGP collimators (figure 3.2(a)), the air holes should be modeled according to the technical specifications concerning the hole diameter and the septal thickness. For this purpose, the typical hexagonal shape was added to the GATE geometry package. The construction of the lead collimators was performed by repeating a hexagon on a rectangular array. This array was then filled with a translated duplicate, creating the correct distribution of air holes (cfr. section 2.3.1).

A collimator may be fabricated in two different ways: by casting in a mould or by folding plates. In the first case, the septa will have the same thickness in all directions (figure 3.3(a),(b)) while in the case of folding the fabrication process causes the septal thickness along one direction to be twice the thickness along the other directions (figure 3.3(d),(e)). The septal penetration will thus be lower along that direction causing the appearance of only four streaks (figure 3.3(f)) instead of the expected six in point source images (figure 3.3(c)). Apart from these artefacts, the construction type also has implications on the energy spectrum (folding implies weaker X-ray peaks at 70-80 keV), on the sensitivity, and on the spatial resolution.

When imaging ^{99m}Tc point sources on the AXIS acquisition system with the LEHR and MEGP collimators, we found four-streak patterns, an effect that was even more obvious when using ^{111}In. With this folded collimator geometry incorporated in the simulator, the appropriate collimator penetration and lead-interactions were registered on the crystal, as could be concluded from the energy spectra around 70-80 keV (X-ray peak of lead). If we replaced the folded collimator model by the inadequate cast model, then an overshoot around this peak would occur due to the overestimation of the septal penetration along one direction. The folded construction of the collimators was confirmed by acquiring X-ray images of their surfaces. These images were used to complete the specifications of the manufacturer concerning hole radius, septal thickness and collimator length for both collimators.

3.2.2 Detector head design

Figure 3.4(a) shows the detailed model of the detector head geometry starting from the collimator and incorporating the crystal in its casing before the light guide, the PMTs and the compression plate, further on to the air gap, the lead ending, and the shielding. Different materials (aluminum, crown glass, NaI, lead, plastic), linked to their cross sections for photon interaction, were specified in order to provide a realistic model for the AXIS detector head. Additionally, the polymethylmethacrylate (PMMA) plastic material was defined to model perspex phantoms, needed for evaluation purposes.

The detector head model was thus composed of an aluminum cover around the NaI crystal of 54 cm x 38 cm x 0.9525 cm. A light guide made of thick crown glass was positioned behind the embedded crystal, followed by the PMTs, modeled as realistically as feasible: glass entrance window, backpart and casings. The back compartment of the detector was ended by an aluminum compression plate, an air gap, and a lead shielding covering all three sides of the detector.

Figure 3.4(b) demonstrates the relative importance of every layer in the model at 140.5 keV by counting the scattered events in each particular part, divided by the total number of scattered events. The phantom used in this simulation is a water filled cylinder of 20 cm in diameter, with a ^{99m}Tc source positioned in its center. The end parts such as light guide, PMTs, compression plate and lead ending become more important as the photopeak energy of the isotope increases or if the crystal thickness decreases. In those cases the photon

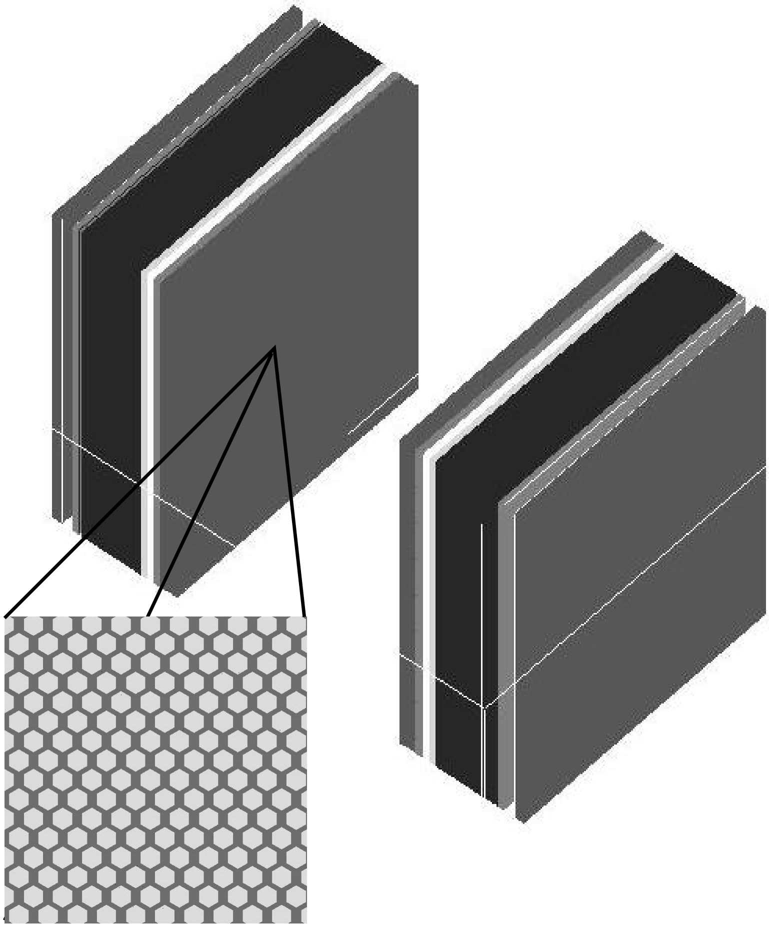

Figure 3.2: Detector model: view of the modeled AXIS detector heads with a zoom on the collimator.

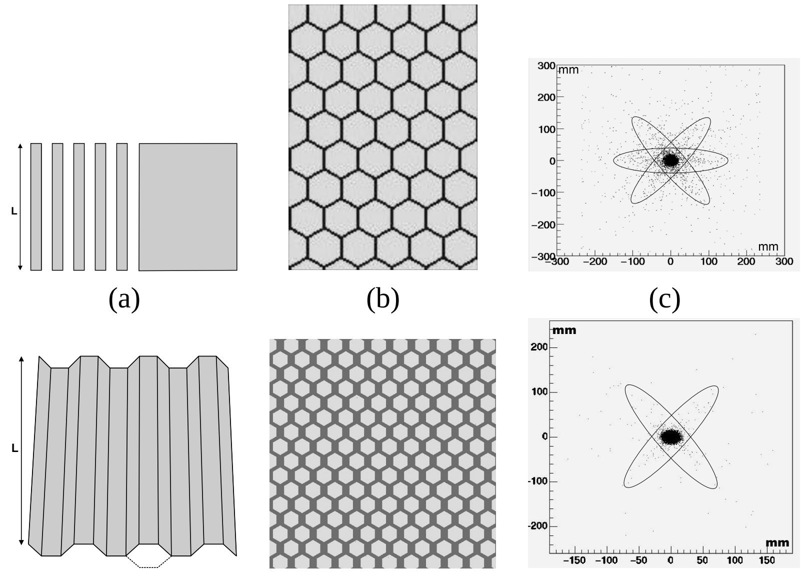

(a) (b) (c)

(d) (e) (f)

Figure 3.3: Simulation of the septal penetration from a point source for two types of collimators: (a) detail cast collimator (length L); (b) transversal image of a cast collimator; (c) cast collimator penetration; (d) detail collimator plate; (e) transversal image of a folded collimator; (f) folded collimator penetration.

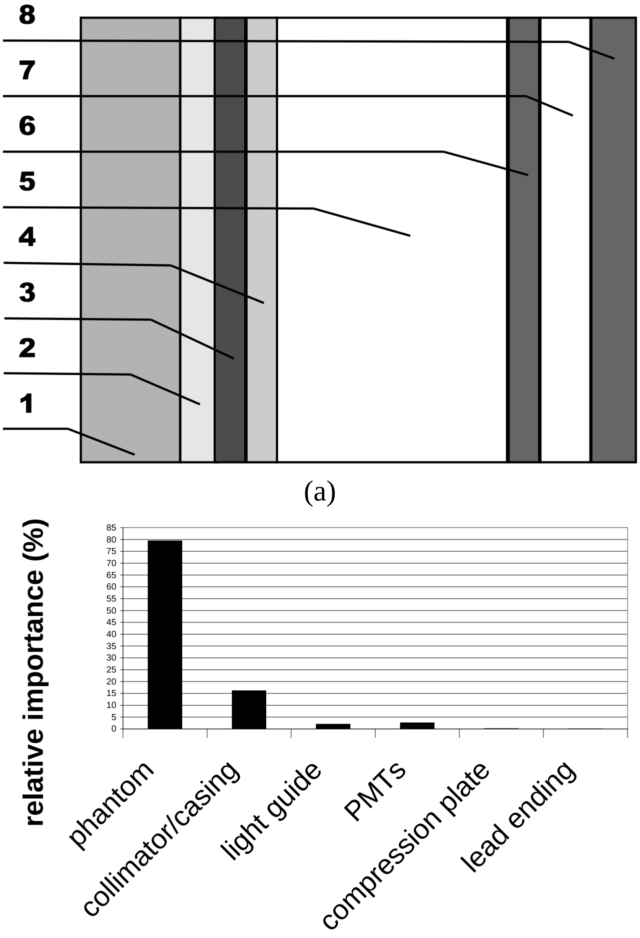

(a)

(b)

Figure 3.4: (a) Axial view of the detector head model with 1: collimator, 2: cover 3: crystal in its aluminum casing, 4: light guide, 5: PMTs, 6: compression plate, 7: air gap and 8: lead ending (top and bottom shielding of the crystal are omitted for visualization purposes); (b) relative importance of every layer for 140.5 keV.

flux on the end parts is larger, augmenting their relative importance. As the AXIS camera is a dual headed camera, both detector heads are modeled in the simulations so that backscattering from one head onto the other can be incorporated, which is important for the sensitivity, spectra, scatter profiles, and for resolution analysis.

3.3 Energy spectra evaluation

3.3.1 Energy resolution module

The scintillation process and the optical photon transport were not modeled for SPECT. An ’energy blurrer’ was used instead, introducing a Gaussian energy distribution with user-defined mean and standard deviation σ. We implemented the energy module to obtain an energy-dependent spectral resolution following $\sim 1/\sqrt{E}$ [99] with an overall resolution of 9.5 $\%$ at 140.5 keV, as stated by the manufacturer for the real detector (cfr. section 2.3.3) [90]. The behavior of the energy blurrer for the energy resolution satisfies most needs of SPECT studies, since there is only one crystal block in SPECT, so that the scintillation photons are averaged over a high number of PMTs. Moreover, with a LEHR or MEGP collimator, all incidences are nearly perpendicular.

The energy resolution at 140.5 keV was confirmed by the following study: real data were taken with a ^{99m}Tc (peak energy at 140.5 keV) point source of 29 MBq, 15 cm away from the detector surface (with collimator), and the results were compared to the energy spectrum simulated with GATE in an identical configuration. In a second phase the same source was inserted in a cylindrical water filled phantom, placed at 10 cm from the detector. The dimensions of the Perspex cylinder were: 10.75 cm inner and 11.25 cm outer radius and 20 cm height. In both experiments 500×10^6 events were simulated. The spectrum from the Pulse Height Analyzer (PHA) of the camera was plotted together with the simulation results, normalized to the peak height and analyzed with ROOT [18].

In figure 3.5(a) the simulated spectrum and the acquired spectrum of a ^{99m}Tc source in air at 15 cm from the detector are compared. Good agreement was found regarding the position and height of the photopeak and of the lead peak. Slight differences may be observed at some points but these discrepancies remain fairly limited. It can be concluded from the general shape alignment that the camera is well modeled and that scatter processes in the detector are accurately simulated. Additionally the good alignment of the 70-80 keV peak indicates that the appropriate amount of lead X-rays are simulated. Figure 3.5(b) visualizes the spectrum of a radioactive ^{99m}Tc source in an attenuating and scattering medium at 10 cm from the detector. The simulation and the experiment fully agree on the increased contribution at lower energies, caused by photons that were scattered in the water-filled phantom. Agreement for the energy resolution is reached, indicating the accurate simulation of phantom scatter.

3.3.2 Shape of the energy spectra of various isotopes

We also did an evaluation for various other isotopes. The energy resolution module described in the previous section was adapted to allow for setting the right energy resolution at the appropriate main photopeak energy for each isotope (cfr. section 2.3.3). These energy resolutions were derived from spectra measurements on the camera.

The validation experiments were performed without a collimator, the source of each isotope being placed 20 cm away from the detector head. Simulations were performed with the same configuration. The spectra visualized with the PHA tool from the acquisition software of the camera were compared to the results of 2×10^6 simulated events. The relative normalization was done by setting the statistical mean of their peaks equal. Evaluation was done for ^{22}Na, ^{57}Co and ^{67}Ga. A wide range of energies was thus covered as ^{67}Ga has its photopeak around 93 keV, ^{57}Co around 122 keV, and ^{22}Na around 511 keV. The spectral distributions for various other isotopes are summarized in figure 3.6. For all of these isotopes, showing various energy distributions and photopeak energies, the experimental spectral distributions are perfectly reproduced by the simulations proving that the energy blurrer accurately covers a wide energy range.

Due to the fact that the system was operated in a non-clinical mode (no collimators were attached to the detectors), the lower and upper threshold may vary and may be different from the simulations. This is however of no importance for these spectra validations. These thresholds are accurately set in the following section since sensitivity will be validated.

3.4 Sensitivity validation

We also evaluated the absolute sensitivity (in cps/MBq) of the GATE model of our detector using a ^{57}Co source of 9.3 MBq $\pm$ 3 %. This particular ^{57}Co source is used to calibrate our well counters and therefore its activity was accurately recorded. We performed a planar acquisition of this source during 600 s and registered the total number of counts in an open but finite energy window.

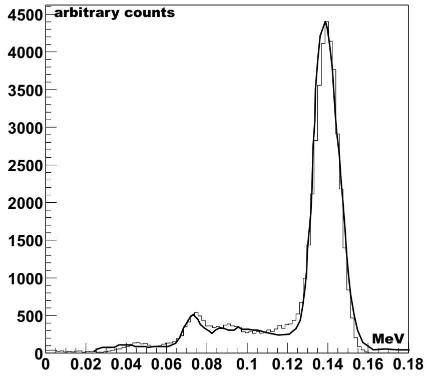

(a)

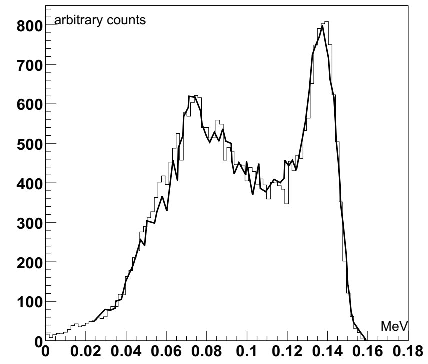

(b)

Figure 3.5: Comparison of simulated and measured ^{99m}Tc spectrum : (a) source in air; (b) with H_2O scattering medium. Black line : measurement, gray line: binned simulation.

Spectrum of ^{22}Na

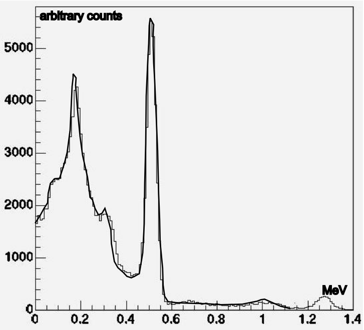

(a)

Spectrum of ^{57}Co

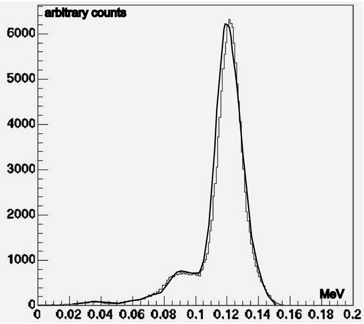

(b)

Spectrum of ^{67}Ga

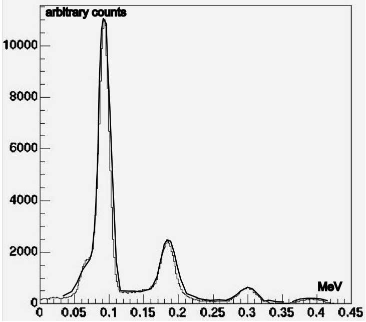

(c)

Figure 3.6: Comparison of simulated and measured spectra in air: (a) spectrum of ^{22}Na; (b) spectrum of ^{57}Co; (c) spectrum of ^{67}Ga. Black line : measurement, gray line: binned simulation.

Dead time correction was not necessary because of the resulting low count rate at the detector. We simulated the same experiment with GATE.

For error bar determination we can assume both the source distribution as the data to be Gaussian based on the central limit theorem. The convolution of two Gaussians is a Gaussian distribution and the variance equals the sum of the variances. The absolute sensitivity measured with the ^{57}Co source was accordingly 231 $\pm$ 17 cps/MBq and the simulated absolute sensitivity was 246 $\pm$ 16 cps/MBq, showing a difference on the mean of only 6.1 $\%$ which is within the error bars. This small discrepancy was probably due to the lack of knowledge on the behavior of the camera below 40 keV in the measurement.

However, in this experiment no energy windows were set and the possibility existed that processes were overestimated in one energy range and underestimated in another. So, additionally we evaluated the sensitivity in two separate windows to make sure that there were no errors compensating each other in the simulations. In the first experiment we performed a static scan (with the LEHR collimator) of a point source (1 ml sphere, 2.6 MBq ^{99m}Tc) at different distances from the detector: 5, 15, 25, 30 cm. We acquired data in the photopeak window (129-151 keV) and in the Compton window (92-126 keV). We set up corresponding simulations for each experiment and we compared the simulated and experimental sensitivities. For each simulation $150{\times}10^6$ events were tracked. In figure 3.7(a) the results are shown for the photopeak and the Compton window. We can conclude a good agreement between the experiments and the simulations.

We repeated a similar experiment with the MEGP collimator where the same source was used and acquisitions were made at 0, 15, 30, and 45 cm from the detector. Again the experiments were reproduced using GATE. The results of the MEGP experiments are shown in figure 3.7(b) where again the sensitivity in both energy windows is plotted, demonstrating a good agreement between simulations and reality.

We could conclude that the simulated values for both windows and for both collimator types were equal within the error bars that arise from the uncertainty in the activity determination of the ^{99m}Tc source (for the experiment) and from Poisson statistics (for the simulations). This rules out the possibility of interwindow compensating errors and confirms a positive sensitivity validation. This also supports the analysis (camera behavior $<$ 40 keV) made for the small 6.1$\%$ absolute sensitivity discrepancy. Furthermore the sensitivity stayed constant with distance, as is analytically proven for parallel hole collimators. Applying one of GATE's dead time models in the simulations was redundant in all these low count studies.

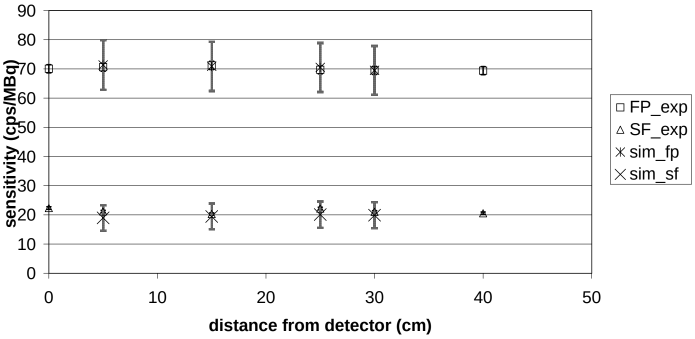

(a)

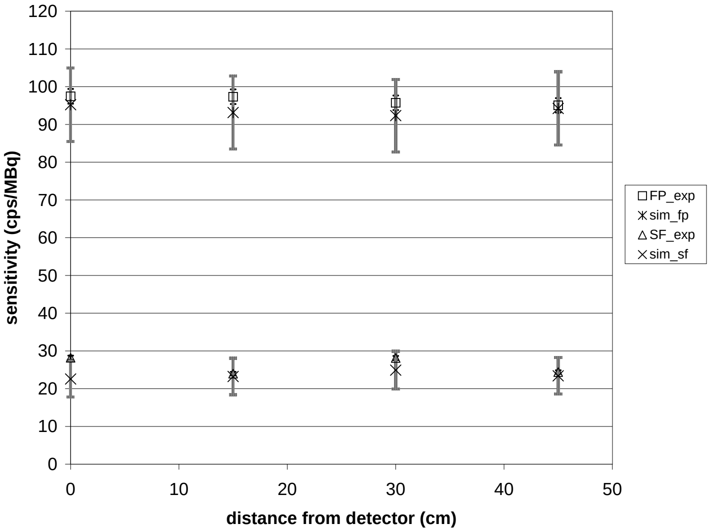

(b)

Figure 3.7: Sensitivity: (a) LEHR collimator; (b) MEGP collimator. FP = photopeak window (129-151 keV), SF=scatter in the 92-126 keV range (Compton window).

3.5 Scatter profiles

We extended the validation by acquiring scatter profiles at different distances from the detector, with and without attenuation, in the Compton (92-126 keV) and photopeak window (129-151 keV).

In the first experiment we performed a static scan of a point source (1 ml sphere, 2.6 MBq ^{99m}Tc) in air at 5, 15, 25, 30 cm from the detector with the LEHR collimator. This was done for the photopeak window and for the Compton window. Simulated point spread functions of a point source in air for the photopeak window are plotted in figure 3.8 as an indication for the effect of distance on the FWHM. Figure 3.9 shows the simulated and measured scatter profiles of point sources in air for the Compton window (92-126 keV) at different distances, thus evaluating the simulation of scatter within the detector head. The good sensitivity agreement in the Compton window for the LEHR and MEGP collimators (section 3.4) was a first indication of the correct simulation of scattered events in the collimator and in the other parts of the detector head as there was also no phantom present in that particular sensitivity experiment. The scatter profiles for the Compton window confirm this expectation as can be concluded from the good agreement between experiment and simulation. In a second experiment the point source was replaced by a line source (0.1 cm diameter, 10 cm long, 2MBq ^{99m}Tc) placed in a water-filled cylindrical phantom of 22.3 cm diameter at 10 cm from the detector heads with the LEHR collimators attached. Acquisitions were made in the photopeak window at both detector heads for the line source in the center of the phantom, at 1 cm, 5 cm, 10 cm, 15 cm and 20 cm depth. For each simulation 500×10^6 events were tracked and the simulated scatter profiles were compared with experimental acquisitions through a best fit plot. This is shown in figure 3.10.

We may thus conclude that the scatter processes in the phantom are appropriately modeled for all cases and that the FWHM increases with depth, as expected.

3.6 Spatial resolution comparison

A 'spatial blurrer' module (cfr. section 2.3.3) was created to model the intrinsic spatial resolution, caused by crystal scatter and signal readout, while the extrinsic resolution (caused by all other parts of the detector) was simulated. The spatial blurrer replaces the recorded position of every count in the crystal by a Gaussian blurred position, in the same way as explained in section 3.3.1 for the energy resolution. This is a reasonable assumption, based on the fact that at 140.5 keV (^{99m}Tc was used in the following experiments) the scatter

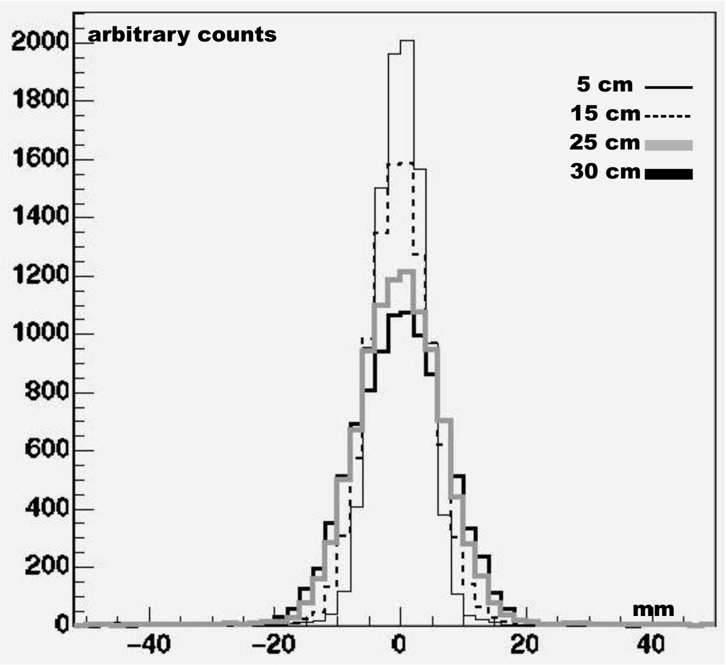

Figure 3.8: Simulated scatter profiles of a point source in air for the photopeak window at different distances from the LEHR collimator.

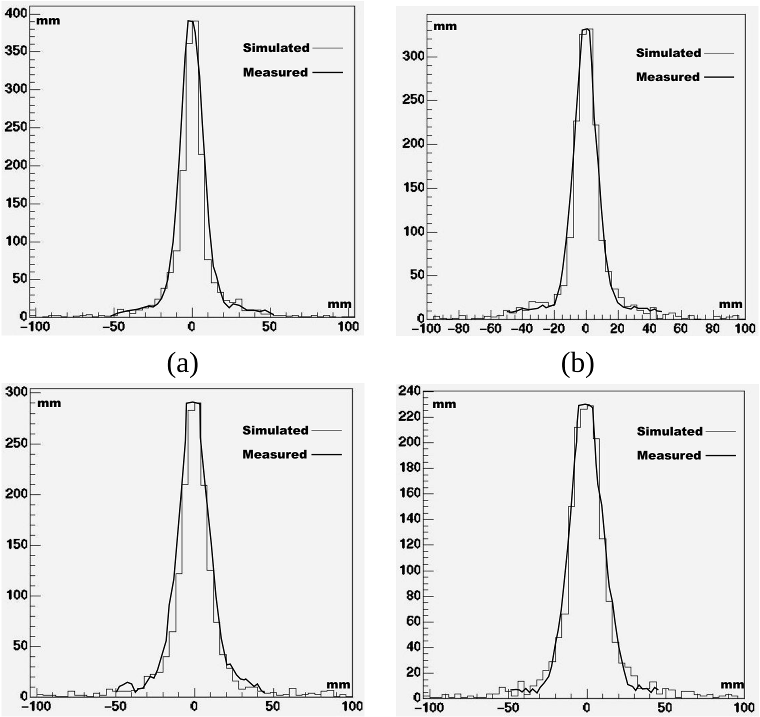

(a) (b)

(c) (d)

Figure 3.9: Simulated and measured scatter profiles of a point source in the Compton window in air: (a) 5 cm; (b) 15 cm; (c) 25 cm; (d) 30 cm. LEHR collimator attached.

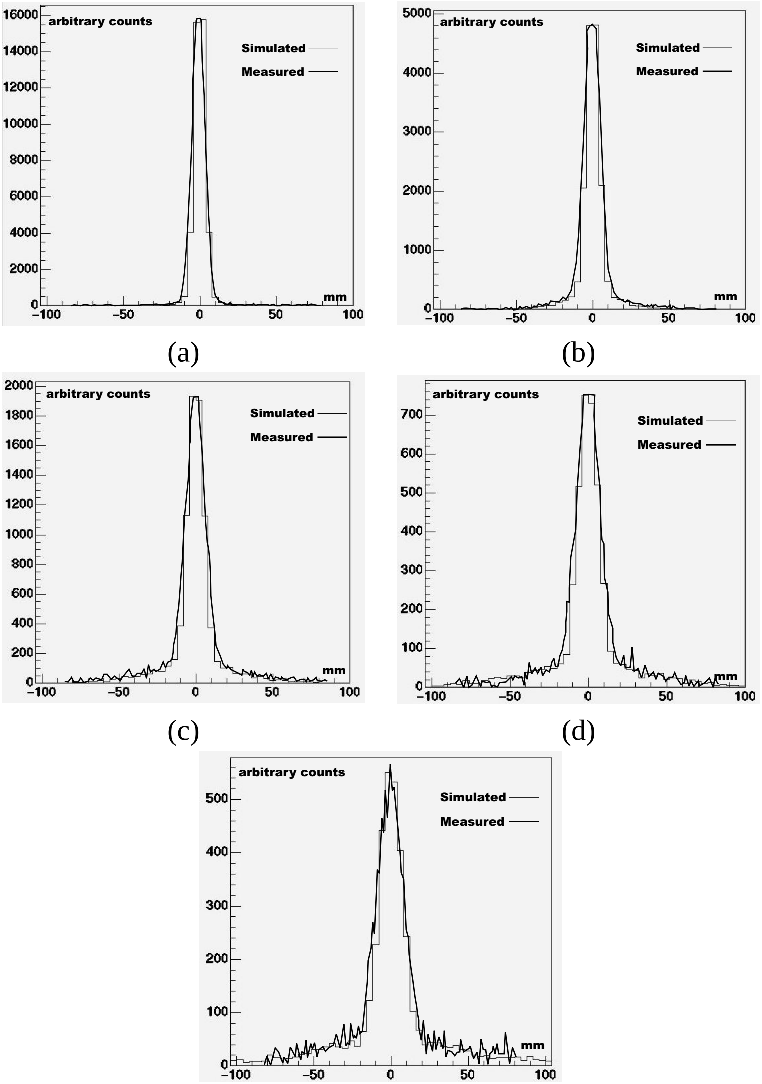

(a) (b)

(c) (d)

(e)

Figure 3.10: Simulated and measured scatter profiles of a line source in the photopeak window with H_2O scattering medium: (a) 1 cm depth; (b) 5 cm depth; (c) 10 cm depth; (d) 15 cm depth; (e) 20 cm depth. LEHR collimator attached.

level in the crystal is very low: only 17 % of the interactions in the crystal are due to scatter, which influences mostly the Full Width at Tenth Maximum (FWTM) rather than the spatial resolution, i.e the Full Width at Half Maximum (FWHM). The FWTM is only used as a parameter to provide a second measure because the curve slightly deviates from a true Gaussian. The actual value of the intrinsic resolution was thus set in the simulations according to the estimate given by the manufacturer (0.33 cm). The contribution of the collimator to the spatial resolution was fully simulated. In order to check the validity of both the spatial blurrer for the intrinsic resolution and the collimator model, experiments were conducted. We performed scans of a line source phantom of 0.1 cm diameter and 5 cm height, filled with 19 MBq ^{99m}Tc, at different distances from the detector with the LEHR collimators attached: 5, 10, 20 and 40 cm. The FWHM of each acquisition was determined. The same procedure was used for the simulations where 20×10^6 events were simulated each time, followed by a ROOT analysis for determination of the FWHM. This was repeated for a line source of 0.2 cm diameter filled with 66 MBq^{99m}Tc at 5, 15, 27, 35, and 45 cm from the detector with the MEGP collimators attached to it.

Figure 3.11 shows the result of the spatial resolution experiments where the simulated FWHMs are compared with the measured FWHMs of line sources in air. A good agreement is reached within the error bars, both for the LEHR and for the MEGP collimator.

Finally we extended the LEHR experimental setup by inserting the line source in the center of a water filled phantom with the same specifications as in section 3.3.1. This phantom was placed at 10 cm from the detector head so that the line source was at 21 cm from the detector. We found an FWHM of 1.3 cm $\pm$ 0.1 cm on the real data, while this was 1.36 cm $\pm$ 0.02 cm in the simulation which confirms that the spatial resolution is accurately simulated, also in the presence of an attenuating medium. For all three experiments, FWHM measurements were repeated for error bar determination while the error bars on the simulation results were derived from the ROOT fitting procedure.

3.7 Conclusion and original contributions

In this chapter we have discussed the software extensions that were implemented to make GATE an accurate simulation tool for SPECT imaging. We have therefore modeled all aspects of a scintillation camera, including different collimators. The most important aspects for SPECT imaging were validated: energy spectra of different isotopes, sensitivity, scatter profiles, and spatial resolution. The results of this validation process were accurate and promising for future applications.

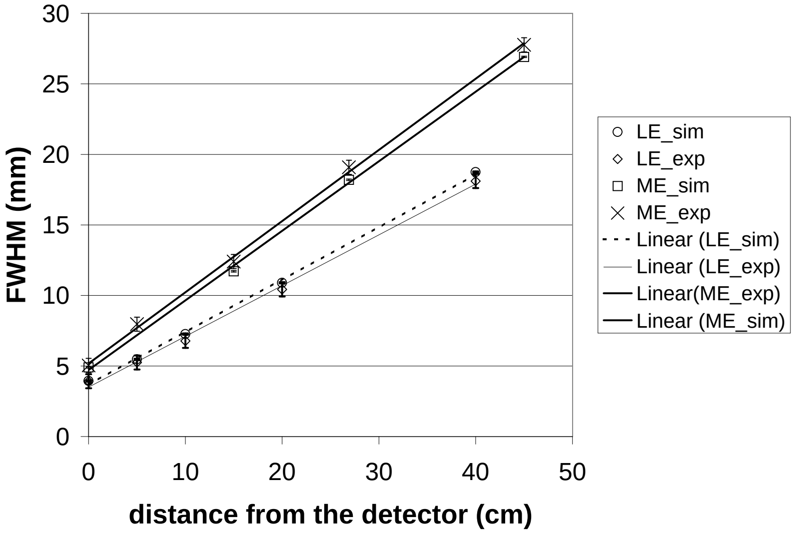

Figure 3.11: Comparison of spatial resolution for a LEHR and for a MEGP collimator (LE = Low Energy, ME = Medium Energy, sim = simulated values, exp = experimental values): LE_sim shows the simulated spatial resolution, LE_exp shows the acquired spatial resolution for the LEHR collimator while ME_sim and ME_exp illustrate simulated and acquired spatial resolution for the MEGP collimator; a linear curve is fitted to each data plot.

Table 3.1: The validation result summaries of commercial systems already or currently considered for GATE validation in SPECT. The column labeled *Agreement* indicates the percent differences of the Figure Of Merit (FOM) between real and simulated data.

SPECT system	Studied FOM	Agreement	References
IRIX, Philips	None reported	n/a	Staelens *et al* [106]
AXIS, Philips	Spatial resolution	<5%	Staelens *et al* [107]
	Energy resolution	<1%	
	Energy spectra	visual assessment	
	Sensitivity	<4.6%	
	Scatter profiles	visual assessment	
Solstice, Philips	Sensitivity	good with theoretical data	Staelens *et al* [107]
			Staelens *et al* [104]
			Staelens *et al* [102]
DST Xli, GEMS	Energy spectra	excellent	Assié *et al* [5]
	Spatial resolution	<2% in air, <12% in water	
	Sensitivity	<4%	

We believe to have demonstrated that GATE needs very little simplifications when describing real camera designs. More specifically, the fact that no essential parts of the camera needed to be represented by an approximative model led to the possibility of using GATE for simulating existing camera setups in different acquisition modes with different parameters, different isotopes and different collimators.

The work described in this Chapter resulted in the first peer reviewed journal publication worldwide on GATE validation [107]. Since then, many collaboration members have extended the validation to other camera types and to other modalities such as PET and small animal imagers with reference to this original work [5, 27, 65–67, 71, 73, 87, 91, 93]. A comprehensive summary of the global validation effort is given in Table 3.1, 3.2 and 3.3. Ongoing work is being performed on the validation of GATE for dosimetric applications.

Table 3.2: The validation result summaries of commercial systems already or currently considered for GATE validation in PET. The column labeled *Agreement* indicates the percent differences of the Figure of Merit (FOM) between real and simulated data.

PET system	Studied FOM	Agreement	References
ECAT EXACT HR$^+$, CPS	Spatial resolution	$\sim 3\%$	Jan *et al* [66]
	Sensitivity	<7%	
	Count rates	good at activity concentrations <20 kBq/ml	
	Scatter fraction	about 3%	
Allegro, Philips	Count rate	<8%	Lamare *et al* [71]
	Scatter fraction	8%	
GE Advance, GE MS	Energy spectra	qualitative	Schmidtlein *et al* [93]
	Scatter fraction	<1%	
MicroPET 4, Concorde	Spatial resolution	about 7%	Jan *et al* [65]
	Sensitivity	<4%	
	Miniature Derenzo phantom	visual assessment	
MicroPET Focus, Concorde	Spatial resolution	about 5%	Jan *et al* [67]
	Sensitivity	about 3%	

Table 3.3: Prototypes dedicated to small animal imaging modeled using GATE and features that have been studied using simulated data. The column labeled *Agreement* indicates the percent differences of the Figure of Merit (FOM) between real and simulated data.

Prototype	Studied FOM	Agreement	Reference
LSO/LuYAP phoswich PET	Sensitivity	n/a	Rey *et al* [91]
	NEC curves	n/a	
High resolution dual head PET	Spatial resolution	$<$6%	Chung *et al* [27]
	Sensitivity	$<$8%	
	Line phantom	visual assessment	
CsI(Tl) SPECT camera	Energy spectra	good	Lazaro *et al* [73]
	Energy resolution	$<$1%	
	Spatial resolution	$<$1%	
	Scatter fraction	$<$2%	
	Sensitivity	$<$2%	
	Line phantom	visual assessment	
OPET	Spatial resolution	n/a	Rannou *et al* [87]
	Sensitivity	n/a	

Chapter 4

Attenuation and scatter correction techniques

4.1 Introduction

Monte Carlo calculations enable the user to separate detected photons into their components or into their event location: primary events, scatter events, contribution of downscatter events, scatter in patient or detector, etc. Monte Carlo modeling thus allows a detailed investigation of the spatial and energy distribution of Compton scatter: energy spectra, pointspread functions and scatter fractions can be simulated as was discussed in chapter 2. In **SPECT**, attenuation and scatter correction techniques are particularly important for simultaneous emission and transmission imaging where several methods have been proposed to differentiate between emission and attenuation source. With SPECT/CT and PET/CT (section 2.1.4) this is intrinsically feasible, while this chapter will present guidelines for protocol optimization in simultaneous emission and transmission for gamma camera PET and for SPECT as well. In **PET**, Monte Carlo simulations are important to verify which scatter order is contributing the most in image degradation. Also the relation between object scatter and crystal scatter is relevant to optimally correct for scatter in a reconstruction algorithm.

In this chapter we will discuss the latter two aspects of attenuation and scatter correction techniques by addressing the simultaneous emission and transmission scans with the Beacon transmission imaging setup and by investigating the relative importance of multiple patient scatter order in PET images.

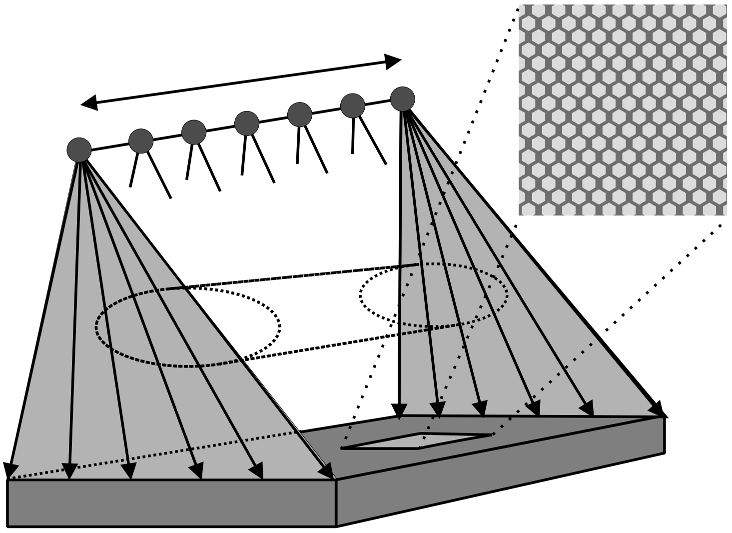

Figure 4.1: Beacon^{TM} acquisition setup: photons emitted by a moving ^{133}Ba point source irradiating the opposite detector (zoom on the collimator): asymmetric (Beacon attached to side of the detector) fan beam (emisison confined to plane) imaging.

4.2 Beacon attenuation correction for gamma camera PET and SPECT

Transmission scans are an important tool to acquire non-uniform patient attenuation maps in order to improve SPECT and PET images. In some cases this is done using an axially moving point source of a high energy isotope that emits a fan of photons (figure 4.1) resulting in an asymmetric fan beam imaging geometry [148]. This system relies on the substantial septal penetration of these photons to form an image. Transmission scans are often performed simultaneously with an emission acquisition to reduce patient scanning time and to increase the patient throughput. Several methods have been proposed to differentiate between photons originating form the emission and from the transmission source [10, 42, 117]. These systems are mostly based on an electronic windowing of the signals to differentiate between emission signals of the subject and transmission signals from the transmission source. In gamma camera PET (section 2.1.3) applications, cross-contamination from the emission source to the transmission energy window remains. The same remark is valid for downscatter of the transmission source in the emission window when performing low- and medium-energy SPECT studies. The aforementioned differentation methods reduce the scatter contamination to a large extent but in all cases an image degradation persists. Some manufacturers advise an additional scatter (mock) scan to estimate the remaining contamination. The Beacon^{TM} (Philips) device (figure 4.2) was studied in particular to evaluate our simulations. It consists of two moving ^{133}Ba sources of 10 mCi. When using the Beacon device in PET mode there are no degrees of freedom for crystal (19 mm) and collimator. The openframe collimator. The openframe collimators allow to measure coincidences in 3D mode. The casing is plastic and entrance sheets made of lead, tin, copper and aluminum filter out low energies. The interwindow contamination was thus examined in order to derive possible protocol optimizations for that dedicated setup. For the case of Beacon-SPECT, we performed multiple types of simulations including different crystal thicknesses and different collimators to evaluate the interwindow contamination in order to propose protocol guidelines.

4.2.1 Methods

Measurements have been performed on Philips' IRIX triple headed scintillation camera. The Beacon device can also be coupled to the AXIS camera which is a dual headed camera. Both cameras were simulated using GATE including all processes in the collimator. An example of a realistic (AXIS) Beacon setup and its simulated counterpart is shown in figure 4.2. Figure 4.3 shows a detail of the modeled folded collimator (hypothetical hole dimensions) of the detector heads described above. As described in chapter 3 GATE was validated for the AXIS SPECT acquisition system. The code was also validated for a typical Beacon experiment [109].

As discussed in section 2.3.2, a central virtual clock object models the passing of time during an acquisition so that it becomes possible to simulate time-dependent processes and keep them synchronized. It is also possible to simulate moving sources, like the ^{133}Ba point sources of a Beacon transmission imaging device, in this case by giving a translation speed to source geometry elements. This particular aspect is demonstrated in figure 4.4 where the detectors of a dual headed AXIS-camera are shown, rotating simultaneously with the linear movement of the ^{133}Ba point sources that are decaying according to their simulated activity and according to the half-life of ^{133}Ba. The latter physical effect is neglible since ^{133}Ba has a half life of 10.54 year which is useful since it avoids the replacement of the transmission source. The virtual clock keeps these three time-dependent processes (detector rotation, linear movement, and decay of the ^{133}Ba point sources) synchronized. Additionally the virtual clock can also synchronize decay of emission sources with respect

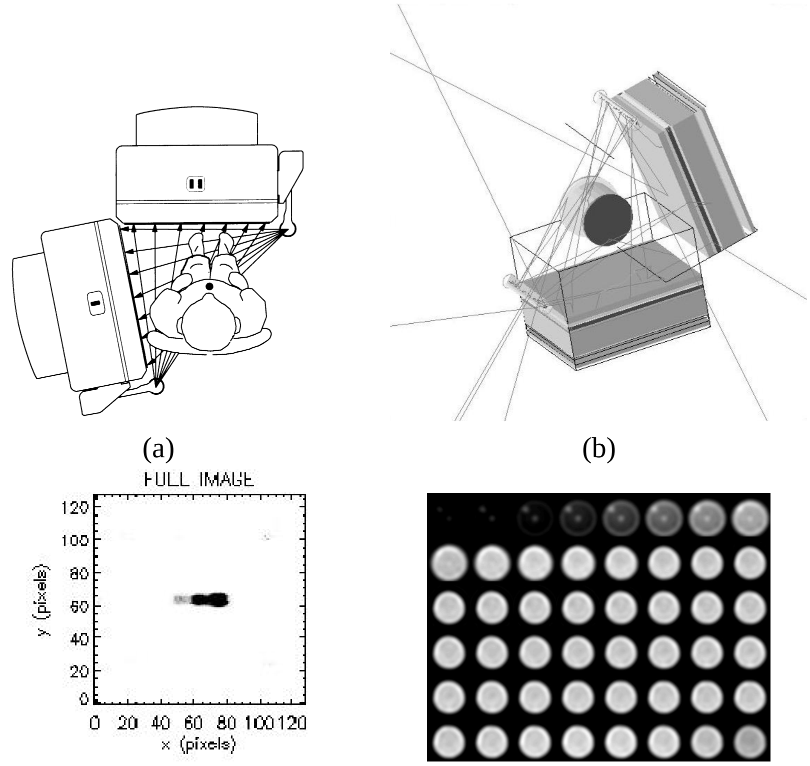

(a) (b)

(c) (d)

Figure 4.2: (a) realistic Beacon setup; (b) simulated counterpart with a cylindrical phantom shown; (c) axial projection of cylindrical phantom acquisition; (d) transaxial profile of cylindrical phantom acquisition.

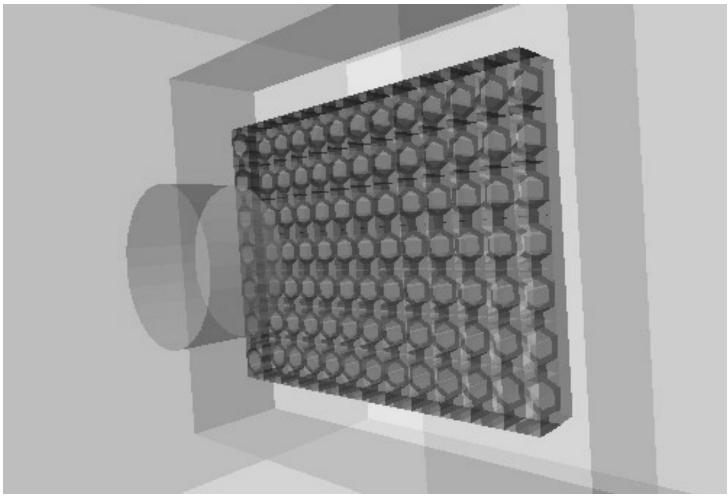

Figure 4.3: Illustration of the collimator, modeled in the detector heads discussed above: detail of the collimator hole pattern that was omitted in previous figures; hole dimensions are purely illustrative.

to the other three processes. This setup can thus be extended to simultaneous emission and transmission imaging. In figure 4.5, a simulation of three hot spheres (filled with ^{99m}Tc) in an attenuating medium is shown. This simulation was done for an IRIX triple headed camera where all three heads are used for the emission acquisition while only two of them are used for acquiring the Beacon attenuation image. The powerful ROOT [18] data-analysis modules of GATE make it possible to separate the detected events coming from the emission sources and the registered photons generated by the Beacon transmission sources so that an emission image and a transmission image can be reconstructed when the simulation is finalized.

4.2.2 Gamma Camera PET

In a first stage, gamma camera PET simulations were performed to evaluate which parameters are important to quantify the downscatter from the ^{18}F emission isotope (511 keV) on the ^{133}Ba attenuation energy window. The simulation consisted of the acquistion of a ^{18}F point source inserted in a cold, water-filled, cylindrical phantom using the model of the IRIX camera with a 1.905 cm thick crystal and with the openframe collimators attached but with the Beacon transmission sources stored.

Figure 4.6 shows an intrinsic scatter contamination of the ^{18}F emission

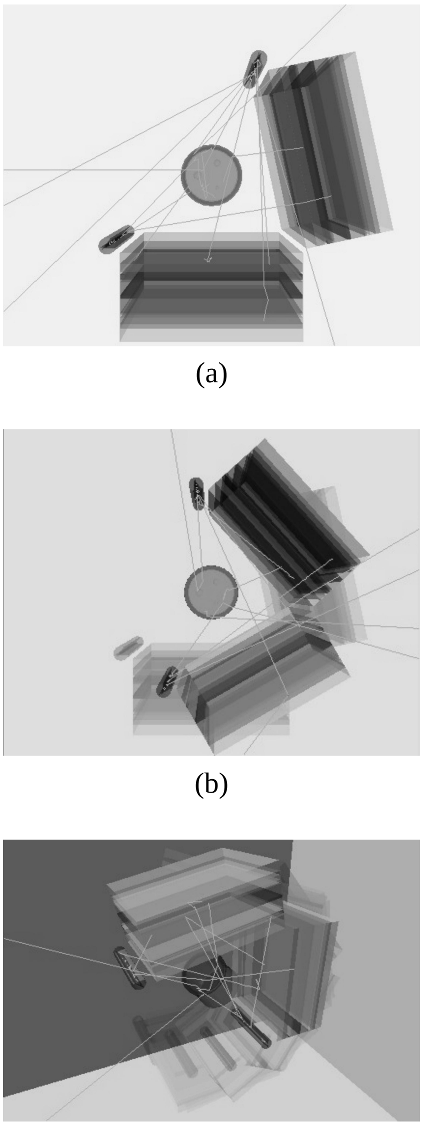

(a)

(b)

(c)

Figure 4.4: Simulated model of a dual headed AXIS-camera: collimator, cover, crystal in its aluminum casing, light guide, PMTs, compression plate, air gap and lead ending are shown for each detector head (top and bottom shielding of the crystal are omitted for visualization purposes as well as the detail of the collimator holes). A water filled cylindrical phantom is modeled in the center of the field of view: (a) detail of the photon emissions of the moving ^{133}Ba point sources, (b) rotation of the detector, (c) idem.

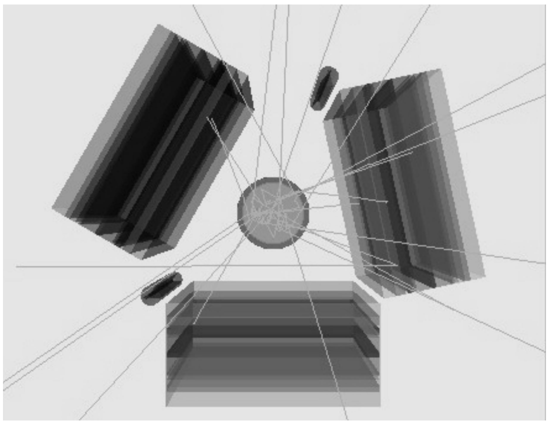

(a)

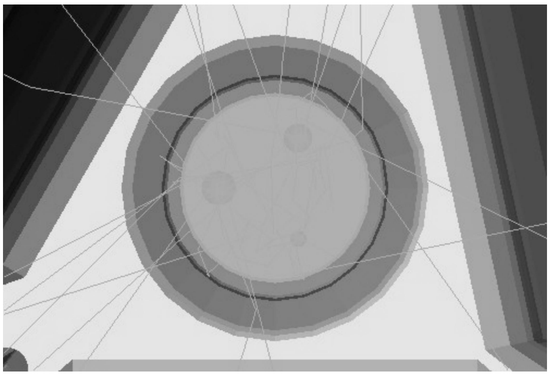

(b)

Figure 4.5: Simulated model of a triple headed IRIX-camera: two of the three heads have a Beacon transmission imaging device attached, the third head is only used for the emission acquisition: (a) water filled cylindrical phantom in the center of the field of view with three hot spheres (filled with ^{99m}Tc) for emission imaging purposes; (b) detailed view of the phantom.

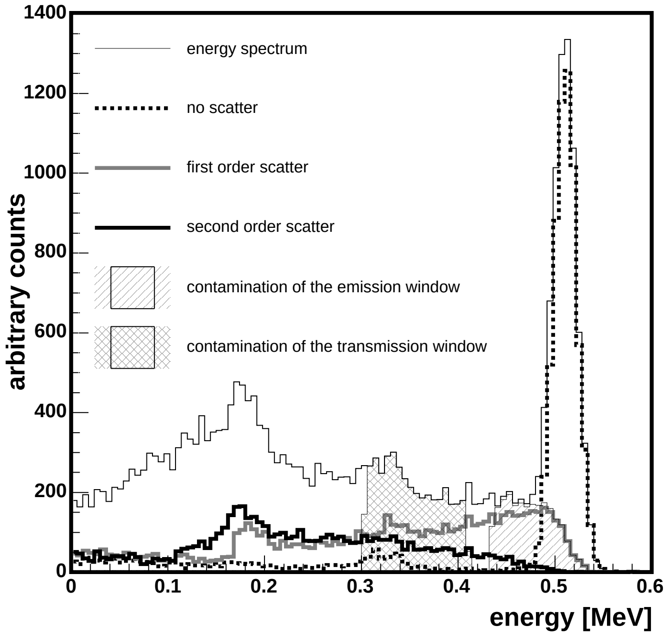

Figure 4.6: ^{18}F spectrum of a coincidence gamma camera PET setup: intrinsic scatter contamination of the ^{18}F emission source in the emission window and downscatter of the ^{18}F emission source in the ^{133}Ba transmission energy window are shown as well as first and second order scatter contributions of the 511 keV photons. Higher order scatter is not shown here since it mostly influences the spectrum around lower energies (0.2 MeV).

source in the emission window (434-587 keV) for this gamma camera PET application and also a downscatter contamination of the emission isotope in the attenuation window (276-436 keV). Figure 4.7 demonstrates the scatter order (number of scatter events along photon path before being detected) contributions and the relative importance of each part of the setup. As stated before, the emission source is inserted in a water filled phantom causing the high value of the phantom scatter. If we discard the primaries (no scatter) and the intrinsic scatter events from the phantom, then it is shown that the largest degradation is caused by the openframe filtering sheets and by the end parts of the detector. The latter is due to the fact that the stopping power of NaI for 511 keV is rather low, causing the flux on the end parts to be large. Protocol optimization should thus be performed in further studies focusing on these aspects for gamma camera PET imaging in order to design new detector entrance sheets and end parts that will limit the number of degrading detections.

4.2.3 Beacon-SPECT

For Beacon-SPECT on the other hand, three types of simulations were performed using the GATE platform and using the appropriate models since there are two additional degrees of freedom in this application: collimator and crystal thickness. The acquistion of a cold (no activity), water-filled, cylindrical phantom's attenuation map was simulated using the model of the IRIX (1.905 cm crystal) camera with the LEHR collimators (0.061 cm inner radius and 0.0203 cm septal thickness) attached and the Beacon device deployed. The object was placed at 25 cm from the detectors and had a diameter of 20 cm. This was repeated for the same camera with a thin crystal of 0.9525 cm and with the identical LEHR collimators. Finally, simulations were performed with the MEGP collimators (0.170 cm inner radius and 0.0864 cm septal thickness) attached to the original 1.905 cm thick crystal detectors. This setup is clinically applied for all medium energy studies (e.g. ^{67}Ga study of the liver).

In the following paragraphs, the three setups are compared in order to qualify the downscatter from the transmission source on the emission window for low- and medium-energy applications. Figure 4.8 demonstrates the relative contribution of each scatter order to the resulting number of detected photons. There are less primary photons detected for a thin crystal and multiple scattering has a higher importance compared to the two other setups. This suggests backscattering from the end parts of the detector on the crystal, which is confirmed by figure 4.9. The contribution of the light guide and the PMTs is larger for the thin crystal setup. The fact that less photons are stopped in the crystal causes the photonflux on the end parts of the detector to be larger and increases the possibility of backscattering. Backscattering causes the photons to lose a vast amount of energy, redirecting the high energy ^{133}Ba photons towards the low energy emission window. This is demonstrated by figure 4.10 which shows the spectrum of a typical setup. First and second order scatter are shown as well as the total scatter contributions of the photons emitted by the ^{133}Ba source in the ^{133}Ba transmission energy window (276-436 keV) and downscatter of the photons emitted by the ^{133}Ba source in the ^{99m}Tc emission window (129-151 keV).

In figure 4.11 the sensitivity for all three setups is shown and the comparison is made with a typical ^{99m}Tc emission scan on a thin crystal detector with the LEHR collimators attached. The sensitivity of the thick crystal, LEHR setup is highest as the photon path length in the crystal is longer compared to

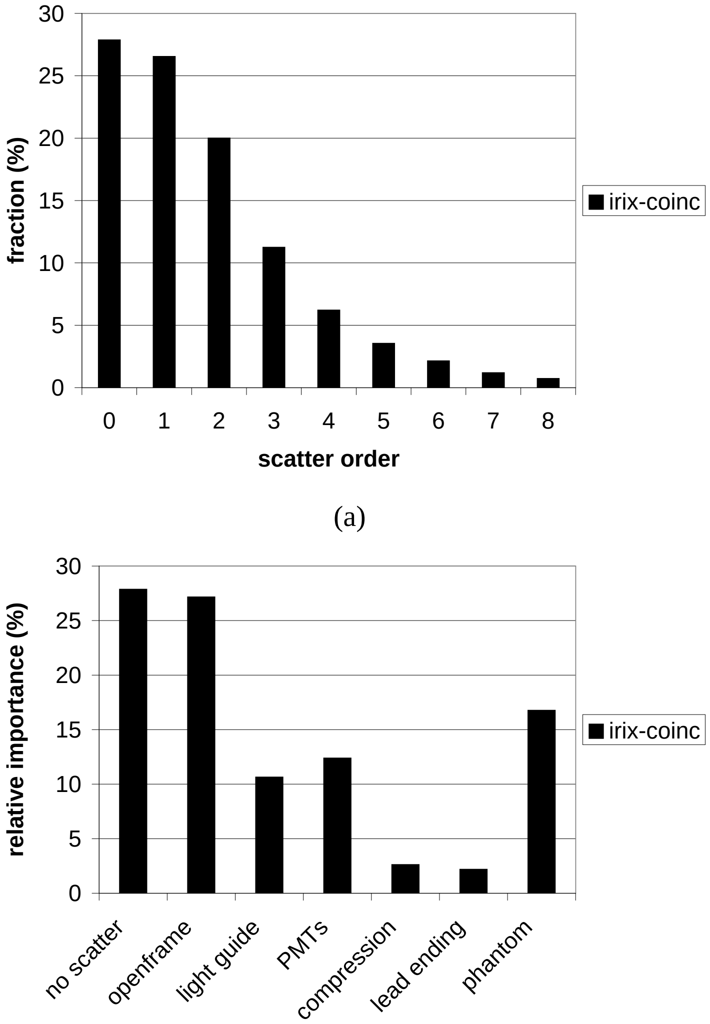

(a)

(b)

Figure 4.7: Gamma Camera PET setup: thick crystal, openframe collimators : (a) scatter order and (b) relative importance of each detector part by counting the scattered events in each particular part, divided by the total number of detected events.

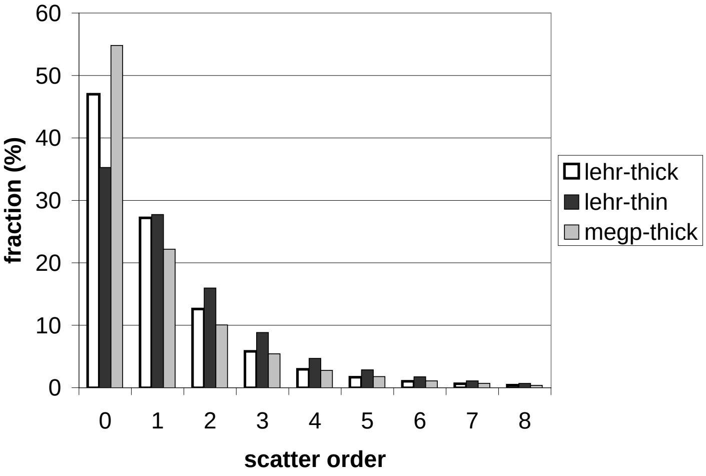

Figure 4.8: Scatter order for all three setups: LEHR-thick crystal, LEHR-thin crystal, MEGP-thick crystal; scatter order = 0 denotes primaries.

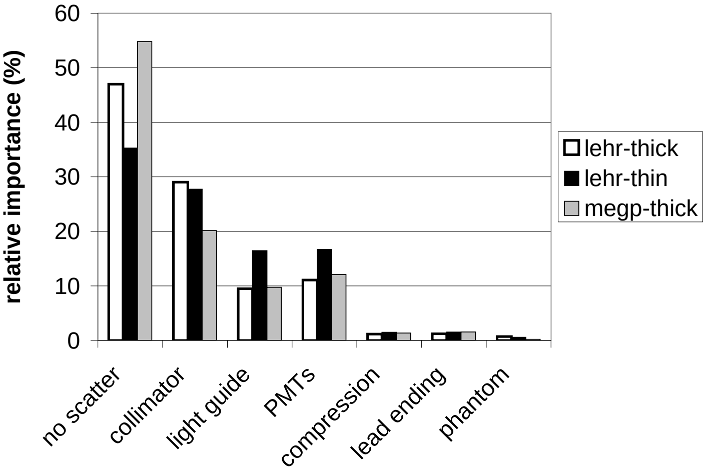

Figure 4.9: Relative importance of each detector part for all three setups: LEHR-thick crystal, LEHR-thin crystal, MEGP-thick crystal by counting the scattered events in each particular part, divided by the total number of detected events.

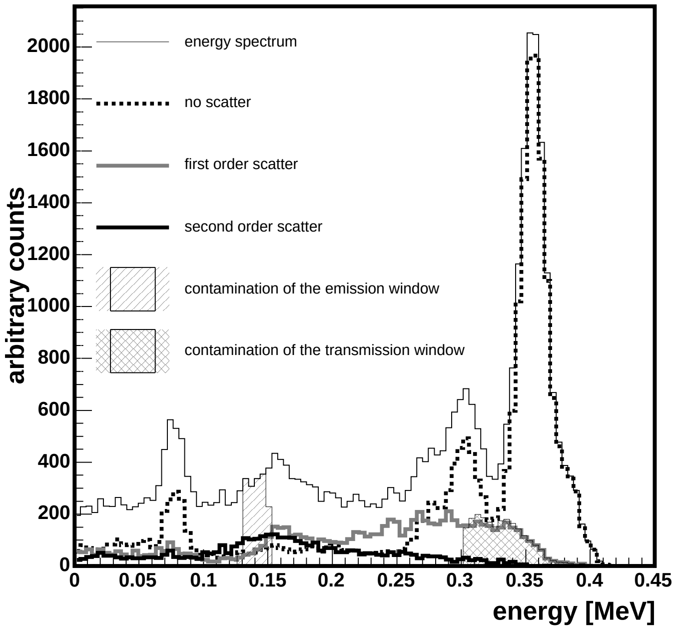

Figure 4.10: ^{133}Ba spectrum of a typical setup: scatter contamination of the photons emitted by the ^{133}Ba source in the ^{133}Ba transmission energy window and downscatter of the photons emitted by the ^{133}Ba source in the ^{99m}Tc emission window are shown as well as first and second order scatter contributions.

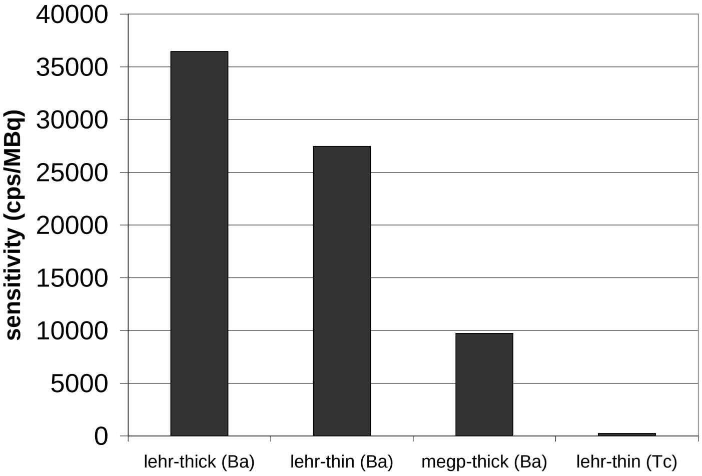

Figure 4.11: Sensitivity for all three setups: LEHR-thick crystal, LEHR-thin crystal, MEGP-thick crystal; compared to a typical ^{99m}Tc emission study.

the thin crystal setup. Moreover, more collimator penetration is possible compared to the MEGP setup as the septa are smaller. The sensitivity is clearly higher than in an analogous experiment with ^{99m}Tc. The photons emitted by the ^{133}Ba source have an energy of 356 keV that enables them to penetrate the collimator while this is impossible for ^{99m}Tc photons which have an energy of only 140 keV. This collimator penetration for transmission imaging is largely hindered in the MEGP setup by the thicker septa, causing the attenuation image quality to be inferior, in particular near the center of a large patient where most attenuation occurs and most photon energy losses are registered. A correction method has been proposed to tackle this problem consisting of a rescaling of the attenuation map based on air flood calibration data [38]. Unfortunately, this approach needs an additional calibration scan, again increasing the patient scanning time and reducing the patient throughput.

We propose another approach where a medium energy experiment on LEHR collimators is simulated in order to obtain the system matrix for reconstruction from these Monte Carlo simulations. In this way the high sensitivity of a LEHR collimator can be exploited and the arising image degrading effects due to the photon penetration on this LEHR collimator can be incorporated in the simulated system matrix. Limitations by computing power have to be accounted for [22], although feasible techniques have been proposed [13]. To limit the storage size of our system matrix and to solve the problems described in [22] the simulated system matrix can be used in a natural pixel based reconstruction [59, 125] or the image matrix can be bilinearly rotated in order to apply an averaged system response blur. In the latter way it remains possible to include attenuation in the reconstruction which is not the case at first sight for natural pixel based SPECT reconstruction. We succeeded in solving these issues and in implementing a dedicated Monte Carlo based reconstruction. Incorporating Monte Carlo information in the reconstruction results in an impressive resolution recovery if the LEHR collimator is used and cancels out the medium energy photon spread. This recovery performance is inferior for the MEGP collimator where the individual hole positions become important given their size, since this is not accounted for in an averaged system response. In all cases the reconstruction of medium energy isotopes on LEHR gives the best result, provided that the system response is fully simulated and incorporated. This will be discussed in further detail in Chapter 7. We will show that it is recommendable to replace the MEGP collimators by the LEHR variants for a large range of medium energy sources (170 keV - 300 keV).

4.3 PET scatter analysis

The characterization of scatter is a very important issue in 3D PET. The main objective of this section is to understand by means of simulations which patient scatter order is significantly predominating in the photopeak window. A second goal is to qualify the difference between phantom and crystal scatter influences. Since this is dependent of the photo-electric fraction (ratio of the number of detections in the photopeak window after photo-electric effect to the total of the detections including multiple Compton and photo-electric events), several crystal materials were investigated: GSO, LSO, BGO. We also included two new materials: $LaBr_3$ and LuI_3. Figure 4.13 shows the detected events after photo-electric interaction and after multiple Compton interactions for the photopeak window and for various detector materials. If the photo-electric fraction of a crystal material is large then the total (Compton and photo-electric interactions) number of detections in function of the depth of interaction will be exponentially decreasing while this is a more uniform distribution if the photo-electric fraction is lower. A low photo-electric fraction implies a large contribution of multiple Compton events in the photopeak. The Compton interaction process needs a build-up region causing the uniform distribution in thin crystals.

Figure 4.12: Simulation setup: GATE model of the Philips Allegro.

4.3.1 Methods

A Monte Carlo GATE model of the Philips Allegro PET scanner (GSO) was implemented (figure 4.12) since GATE was already extensively validated against this commercial PET system [71]. As the importance of crystal scatter is dependent of the photo-electric fraction the above scanner was simulated with several material types (figure 4.13). Geometrical aspects of the Allegro were kept constant. According to crystal material and its scintillation decay time, the appropriate proportional simplified paralysable dead time for each event was applied as well as the energy resolution for each crystal material as summarized in Table 4.1. Two phantom studies were performed, which will be discussed in the following sections.

4.3.2 NEMA phantom study

Firstly, a simulated 6 min. acquistion of the NEMA 2001 scatter phantom [83], filled with a ^{18}F source of 1μCi was performed. This study was used to determine the Noise Equivalent Countrate (NEC) [57] for the crystal materials as a figure of merit. Since random coincidences are negligible with this low activity we defined the NEC as follows : $NEC = \frac{T^2}{T+S}$ with T being the trues (no scatter along path) and S being the scattered events.

Figure 4.14 illustrates the results for the NEMA-2001 scatter phantom

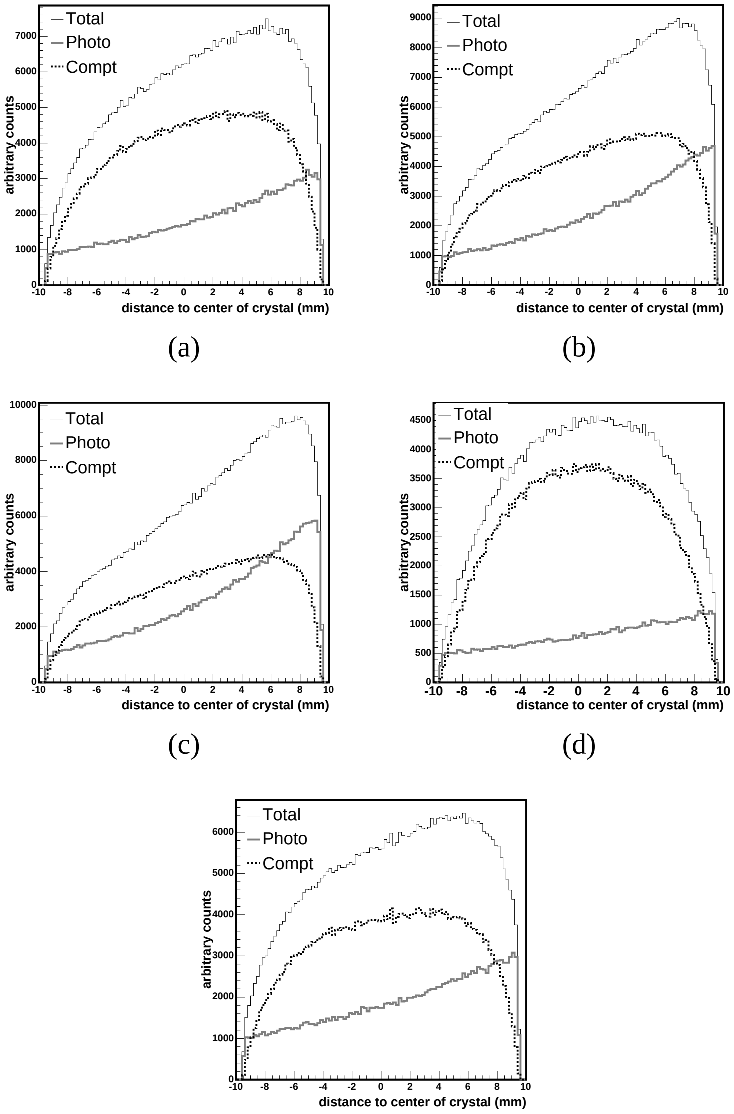

(a) (b) (c) (d) (e)

Figure 4.13: Compton and photoelectric interactions for each implemented crystal material: (a) GSO, (b) LSO, (c) BGO, (d) $LaBr_3$, (e) LuI_3. Distance to the center of the crystal= 10 is the crystal front entrance.

Table 4.1: Detection chain parameters.

	BGO	LSO	GSO	$LaBr_3$	LuI_3
En. resol(%)	27	22.5	18	6.75	15.75
Dead time(ns)	700	100	120	60	70

Table 4.2: Phantom scatter order contributions.

	BGO	LSO	GSO	$LaBr_3$	LuI_3
1st order (%)	90.2	90.0	88.9	91.0	90.5
2nd order (%)	9.1	9.6	10.3	8.4	8.8
$\geq$3rd order (%)	0.7	0.4	0.8	0.6	0.7

setup. It can be concluded by comparing figure 4.14(b) with figure 4.14(c) and (d) and it is shown by table 4.2 that the first order phantom scatter is dominating over second and higher order phantom scatter in the photopeak window (30 % around 511 keV) for all current and innovative crystals. When comparing the performance of the detector materials used, we found the NEC of LSO and BGO to be superior to the other ones (figure 4.15(a)). This is mainly due to their increased sensitivity (figure 4.15(b)) as the photo-electric fraction in these systems is higher (figure 4.13). Figure 4.16 shows the relative influence of crystal scatter, phantom scatter and detector parts scatter on the energy resolution. It can be seen that Compton scatter in the crystal degrades the energy resolution to a large extent. A higher photo-electric fraction thus means that spatial and energy resolution are less degraded by this crystal Compton scatter. Besides these degradations, crystal Compton scatter is also causing inter-crystal mispositioning. One has to realize however that this is a low count simulation study (1μCi) and that BGO has a large decay time causing it to be less appropriate for high count rate acquisitions.

4.3.3 Anthropomorphic phantom study

The second phantom study consisted of simulating an anthropomorphic voxelised phantom. The Hoffman brain phantom was used as a voxelised emission source (translation gray scale to activity) and at the same time as an attenuating medium (tabular translation gray scale to material definitions) [105]. The phantom contained a total of 90μCi ^{18}F which was acquired during one sec-

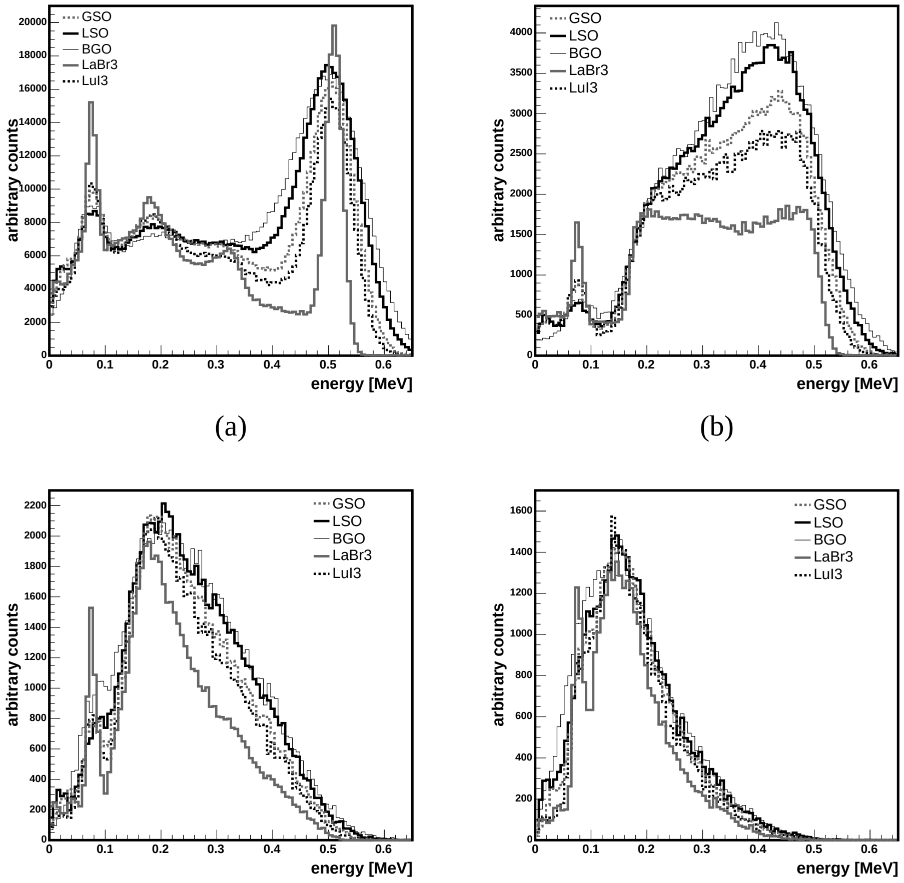

(a) (b)

(c) (d)

Figure 4.14: NEMA-2001 setup: Evaluation of phantom scatter orders for 5 crystals: BGO, LSO, GSO, $LaBr_3$ and LuI_3: (a) energy spectrum, (b) first order scatter, (c) second order scatter, (d) third order scatter.

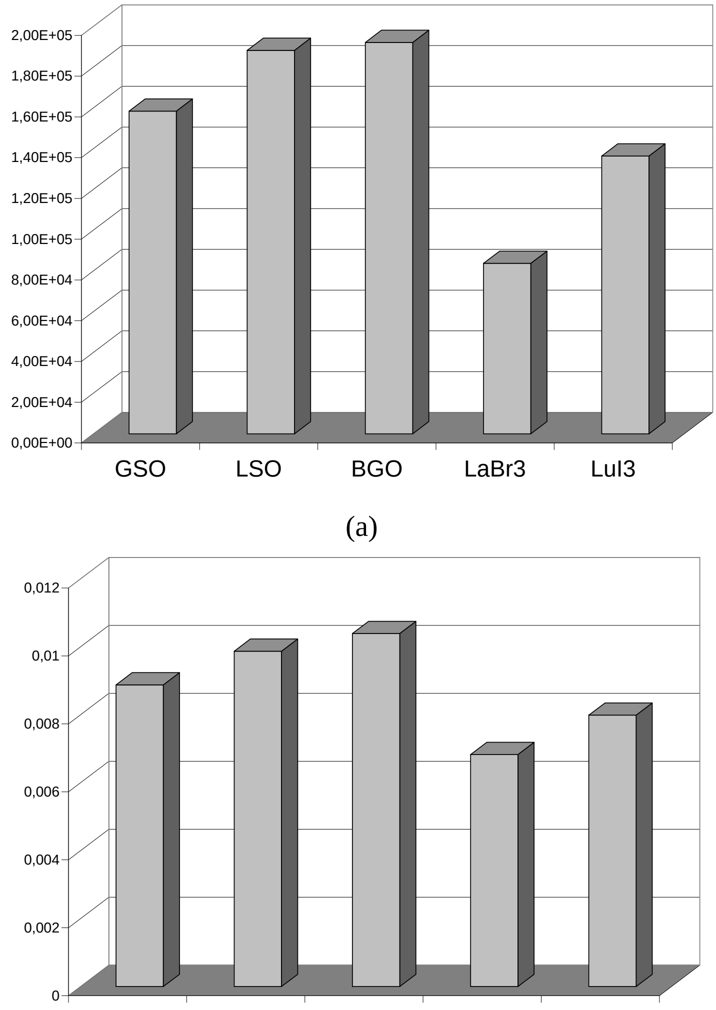

(a)

(b)

Figure 4.15: (a) NEC:$T^2/T + S$ (1μCi source), (b) Sensitivity: detected counts/emissions.

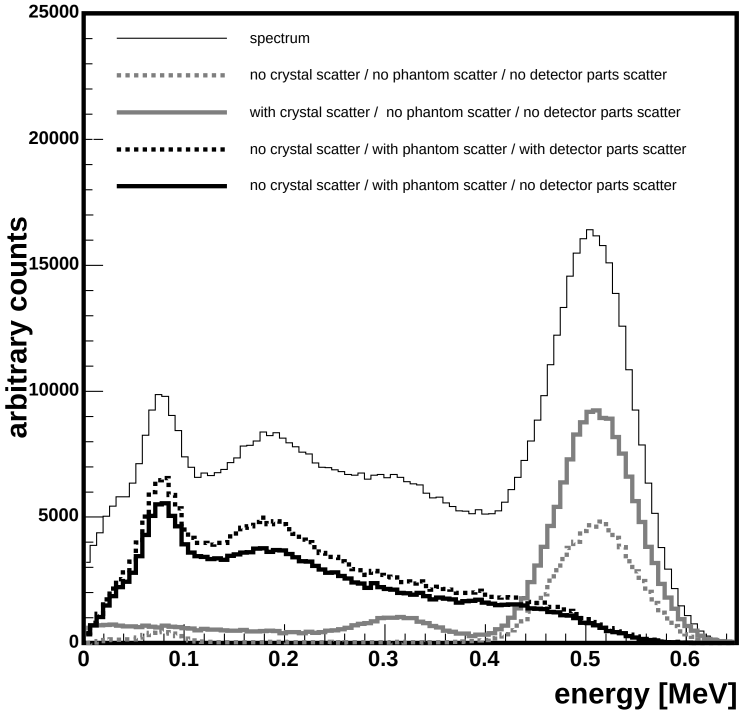

Figure 4.16: Illustration of importance ratio for scatter contributions on GSO.

ond. The latter study was intended to verify whether the conclusions of the first study were valid for patient-like objects.

Figure 4.17 repeats the results of section 4.3.2 in an analog manner for the Hoffman brain phantom. The importance of higher order scatter in the anthropomorphic phantom setup was 9.6% while it was 9.9% in the NEMA setup.

4.3.4 Reconstruction

It became clear that only first order scatter is significantly degrading the photopeak acquisitions for all crystal types. The importance of multiple order scatter is less than 10% both for the NEMA-2001 scatter phantom and for an anthropomorphic phantom.

For the incorporation of scatter correction in the reconstruction we propose to use simulated data. To correct for patient scatter in the reconstruction, one can estimate it from a short simulation of an initially estimated emission distribution (e.g. FBP reconstruction) and add that estimate to the forward projection since only first order uncorrelated scatter is contributing. In section 2.1.6 we discussed MLEM as an iterative statistical reconstruction algorithm. In order to add this simulated patient scatter contribution the term $\sum_{j'=1}^{N} a_{ij'} f_{j'}^{(k)}$ of eq. 2.6 should accordingly be replaced as $\sum_{j'=1}^{N} a_{ij'} f_{j'}^{(k)} + n_i$ with n_i the object scatter contribution. Detector scatter can be modeled in the projector itself so that it can be recovered as inter-crystal mispositioning appears to be important for those crystals that have a low photo-electric fraction (figure 4.13) [94]. The crystal scatter should thus be modeled in the sytem matrix: a_{ij} of eq. 2.6, or in a natural pixel approach as will be discussed in Chapter 7.

4.4 Conclusion and original contributions

In section 4.2 suggestions for protocol optimization studies in Beacon PET on a hybrid gamma camera were made. The important detector parts for contamination of the attenuation image by the 511 keV emission isotope were delineated: entrance sheets and end parts. Design work should focus on those aspects to further reduce cross-contamination if one wants to keep using gamma camera PET before switching to PET or PET/CT.

The interwindow contamination of the emission energy window in the case of simultaneous emission/transmission imaging for Beacon-SPECT is smallest in the LEHR, thick crystal setup. The contamination is larger for the thin crystal setup as the relative importance of the backscattering is superior. Moreover we found that the Beacon attenuation image is often degraded near the center

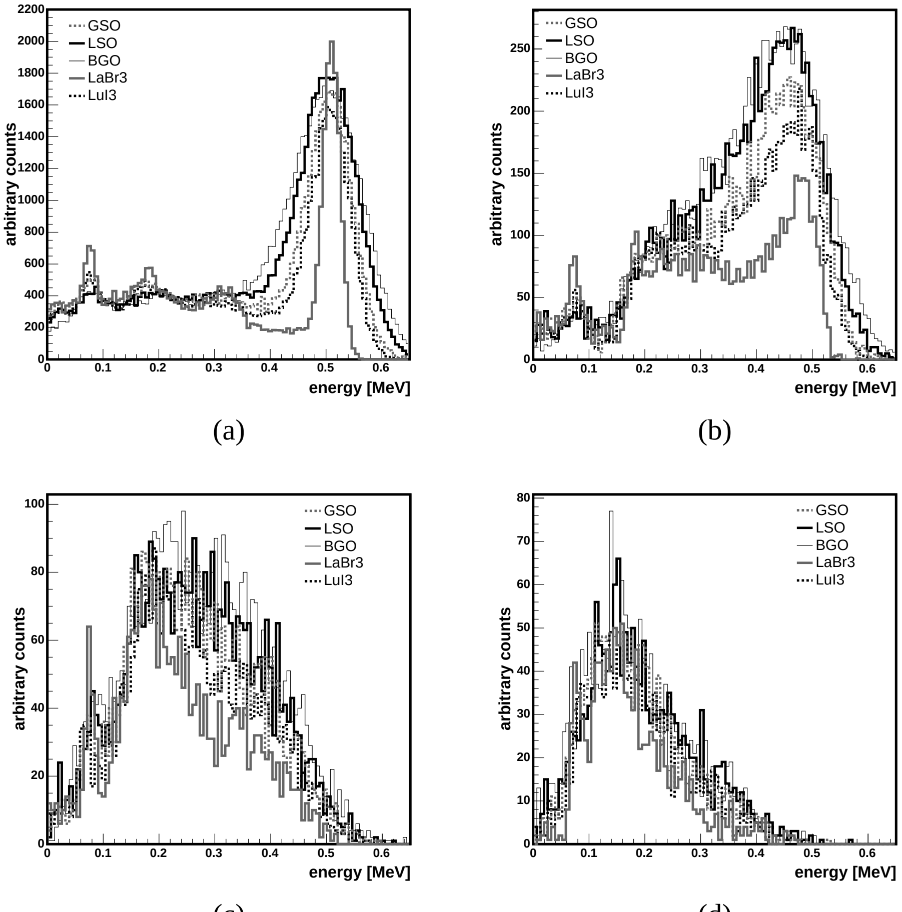

(a) (b)

(c) (d)

Figure 4.17: Anthropomorphic phantom setup: Evaluation of phantom scatter orders for 5 crystals: BGO, LSO, GSO, $LaBr_3$ and LuI_3: (a) energy spectrum, (b) first order scatter, (c) second order scatter, (d) third order scatter.

of large patients when a medium energy emission study is performed simultaneously or sequentially with the transmission acquisition. This is due to the fact that the ^{133}Ba sources have to form an image through the collimator of the opposite detector head, which has thick septa in a medium energy emission setup. It was shown that, in this particular case, it would be recommendable to replace the MEGP collimators by the LEHR variants for a large range of medium energy sources (170 keV - 300 keV). Incorporating Monte Carlo information in the reconstruction will be necessary to perform a resolution recovery for the LEHR collimator variant and to cancel out the medium energy photon spread. The main conclusion for Beacon-SPECT is that a thick crystal detector coupled to a LEHR collimator is the best solution for acquiring attenuation maps in low **and** medium energy applications if one uses the Monte Carlo based reconstruction that will be detailed in Chapter 7.

In section 4.3 a qualitative interpretation was shown for the importance of multiple order scatter in 3D PET. Various crystal types, including innovative materials such as $LaBr_3$ and LuI_3, were examined. It became clear that only first order scatter is significantly degrading the photopeak acquisitions for all crystal types. The importance of multiple order scatter is less than 10% both for the NEMA-2001 scatter phantom and for an anthropomorphic phantom. It was also shown that BGO and LSO give rise to higher NECs on the NEMA-scatter study. This will not be the case for BGO in higher count rate studies since dead time effects will become predominant due to the slow scintillation time of the crystal material. Simulation studies showed that only first order scatter is significantly degrading PET image quality. The effect of higher order scatter in the photopeak window is negligible.

The work presented in this chapter resulted in a peer reviewed journal article [106] and in three publications in the proceedings of international conferences [105, 108, 109]. It is the first simulation study using the GATE virtual clock synchronisation to such a large extent: detector rotation, linear movement, decay of the ^{133}Ba point sources and decay of emission sources are synchronized. Also it is the first simulation study in the field evaluating the importance of multiple order patient scatter on anthropomorphic phantoms for various crystal materials, especially for $LaBr_3$ and LuI_3.

Chapter 5

Imaging systems and collimator design

5.1 Introduction

Image formation modeling is one of the most important reasons for the existence of Monte Carlo simulations in nuclear medicine. Monte Carlo methods can be used to assess the image formation process both qualitatively and quantitatively and can assist in the development of new collimator designs, new detector construction, new electronics and in optimized camera motions. In this chapter we use GATE to investigate a new design of SPECT acquisition with a rotating slat collimator mounted on a strip detector. Although gamma cameras with parallel hole collimators have been optimized during the past years, their major limitation remains the limited sensitivity for an acceptable spatial resolution. The sensitivity-resolution tradeoff can be improved by using focusing collimators like fan beam and cone beam collimators, but those are limited by their FOV. The main purpose of the aforementioned new design is to improve the resolution versus sensitivity tradeoff by the rotating collimator, coupled to an improved energy resolution by using the semiconductor detector. The study consisted of modeling the prototype of the Solid State with Compact Electronics (Solstice) camera which aims for a higher spatial resolution at a comparable sensitivity of classical SPECT devices.

5.2 Solstice detector: basic characteristics

The concept of the Solstice detector (figure 5.1(a)) [43] consists of a rotating slat collimator mounted on a strip detector (35 cm×5.6 cm×0.5 cm), made of

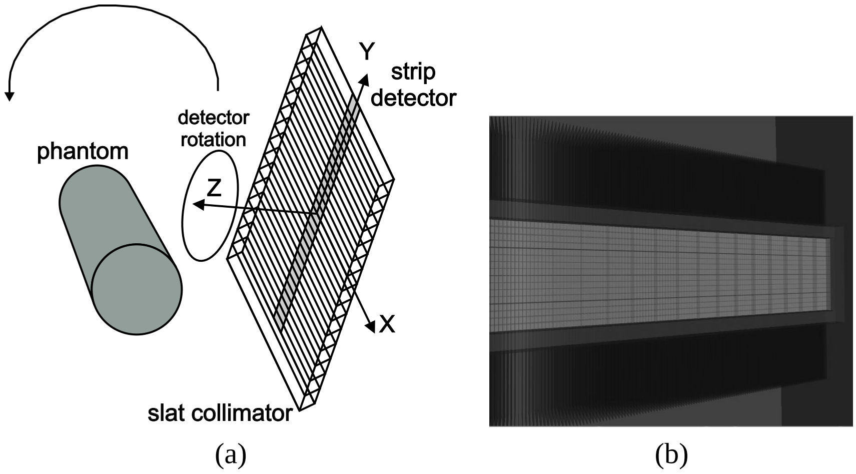

Figure 5.1: Solstice: (a) illustration of the Solstice detector; (b) model of this setup: Solstice detector : CZT strip and collimator slats visualized.

Cadmium Zinc Telluride (CZT), and subdivided into an array of 88 crystals. The bias voltage was applied to the single electrode cathode side of the crystal. The anode side of the individual crystals was further subdivided into 32 anodes connected to an ASIC charge sensitive preamplifier-shaper circuit for each pixel that provided a virtual ground for the anodes so that pixel position and energy deposition could be transferred. The collimator slats are made of wolfram and lead and have a pitch of 0.18 cm and a thickness of 0.03 cm. The detector assembly is spinning to get 2D images and revolves around the object for 3D reconstruction. Details on the electronic design and the readout schemes are reported in literature [52].

We modeled a rotating slat collimator in GATE on a CZT strip with the correct pixelization (CZT-RS). Every physical interaction, except for the production of electron-hole pairs and the electron hole trapping, was modeled (figure 5.1(b)).

Figure 5.2 shows that the spatial resolution of the rotating slat design is better than for a classical commercial SPECT system as the typical reference spatial resolution is 0.53 cm at 10 cm from the detector compared to 0.66 cm at 10 cm from an AXIS detector.

To be able to investigate the sensitivity and energy resolution of this new device at comparable spatial resolution in relation to other prototypes, two additional Monte Carlo models were used. The second camera (CZT-PH) type (figure 5.3) is a CZT detector of ($35\ cm \times 35\ cm \times 0.5\ cm$) subdived in 576

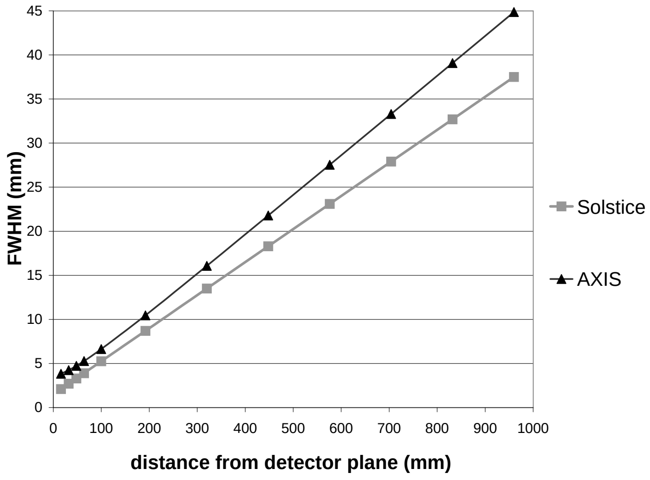

Figure 5.2: Spatial resolution comparison between traditional AXIS SPECT camera and Solstice.

modules of 8×8 pixels each. A parallel hole collimator, made of Tungsten and with a square hole pattern, is mounted on this detector so that it is perfectly matched to the pixelisation. The third setup (ANG) is a typical Anger camera simulation model with a detector that is made of NaI, not pixelated and 9.5 mm thick, to comply with standard commercial designs. The same parallel hole collimator is mounted on that detector in order to achieve a comparable spatial resolution. Fully realistic simulations are performed for this system except for the generation of light photons after scintillation in the sodium-iodide (NaI) detector.

Figure 5.4 clearly shows the highest sensitivity for the rotating slat setup. However it should be noted that the photons are collected in planes and will accordingly contain less information. The imaging performance will be investigated with a human observer study in section 5.4.

In figure 5.5(a) results are shown for the performance of the 3 cameras in terms of energy resolution. Typical experimental values are 5% energy resolution at 140 keV for CZT compared to 10% energy resolution at 140 keV for NaI. The same is repeated in figure 5.5(b) for a simulation study with an attenuation phantom where we see the attenuation effect (rescaled $Y-$axis) and the broadening of the photopeak as well as a Compton tail due to scatter events in the phantom. This is shown in figure 5.5(c) for both parallel hole collimator setups. Here the better energy resolution of the solid state device can be seen

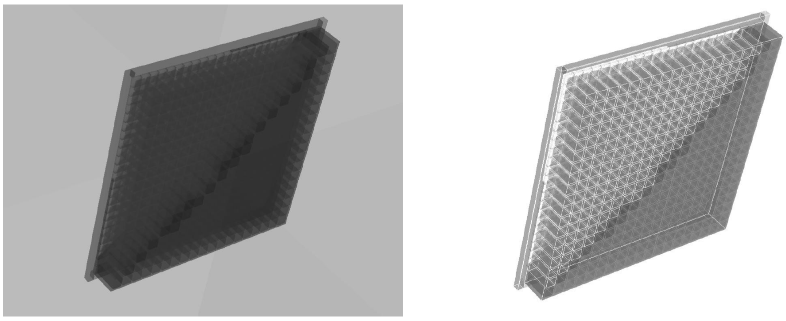

(a) (b)

Figure 5.3: (a) Solid state detector with parallel hole collimator, detail of the matched collimator square hole pattern and the pixelisation is shown; (b) Wireframe view of (a).

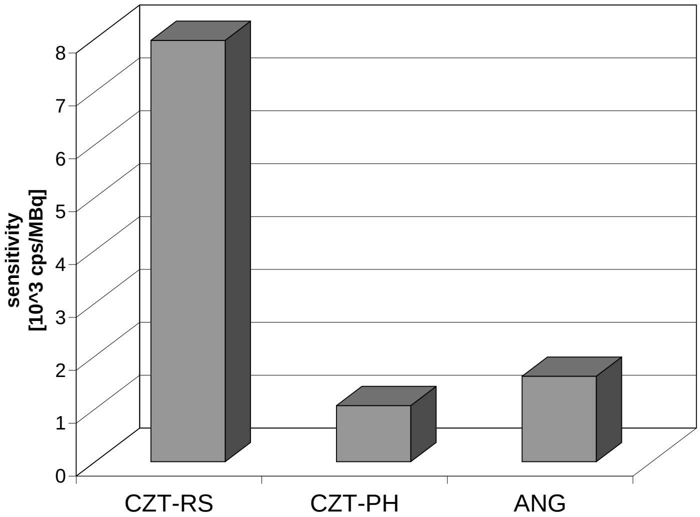

Figure 5.4: Comparison of sensitivity: for rotating slat setup (keyword:CZT-RS); for parallel beam collimator on solid state detector (keyword: CZT-PH); for classical NaI Anger camera (keyword: ANG).

more clearly. The two K-shell escape peaks of Cd en Te can also be seen for CZT at low energies whereas the K-peak of Zn is not visible due to its very low concentration (Cd_9ZnTe_{10}). In figure 5.6(a) we show the first order scatter contribution from the phantom. We can conclude a non-negligible contribution to the photopeak window around 140 keV. Figure 5.6(b) shows the less important contribution of second order scatter. In both plots scatter contamination is most pronounced for the classical Anger camera setup. In figure 5.6(c) the crystal scatter contribution is shown. The contribution of crystal scatter in the photopeak window is far more important for the NaI detector than for the CZT detector. Figure 5.6(d) sums up all these effects and shows the scatter contamination of the photopeak window which is much worse for a classical scintillation crystal. The results shown in figure 5.6 are confirmed by figure 5.7 where the comparison is made for all three devices. The photopeak window is chosen to be 10% around 140 keV for CZT detectors and 20% for the NaI detector so that the sensitivity of the photopeak window is comparable. The scatter contribution for both solid state devices is almost similar, apart from small differences resulting from collimator scatter, and they both outperform the classical scintillation camera in this respect.

5.3 General Geometric Transfer Function for a slat collimator mounted on a strip detector

The geometric resolution and sensitivity properties of a collimator can be described by the so-called effective point spread function of the collimator. This is the detector response for a point source averaged over all possible relative gap positions. This approach does not need the knowledge of the exact location of the different gaps relative to the position of the point source. This effective point spread function has already been described for parallel beam, fan beam and cone beam collimators [79,121]. In this section we want to apply the same strategy to deduce the effective point spread function for a strip detector with a slat collimator. The geometric transfer function of this collimator, which is the Fourier transform of the effective point source image, will be analyzed in Fourier space and will allow to make some valuable analytical and quantitative conclusions on sensitivity and spatial resolution. These findings will be verified using Monte Carlo simulations. The derived geometric transfer function can be interpreted as a description of the average spatial resolution provided by the geometrically collimated photons when the relative lateral positions of a source and a stationary collimator are unspecified or as a description of the directly measurable spatial resolution provided by these photons when the col-

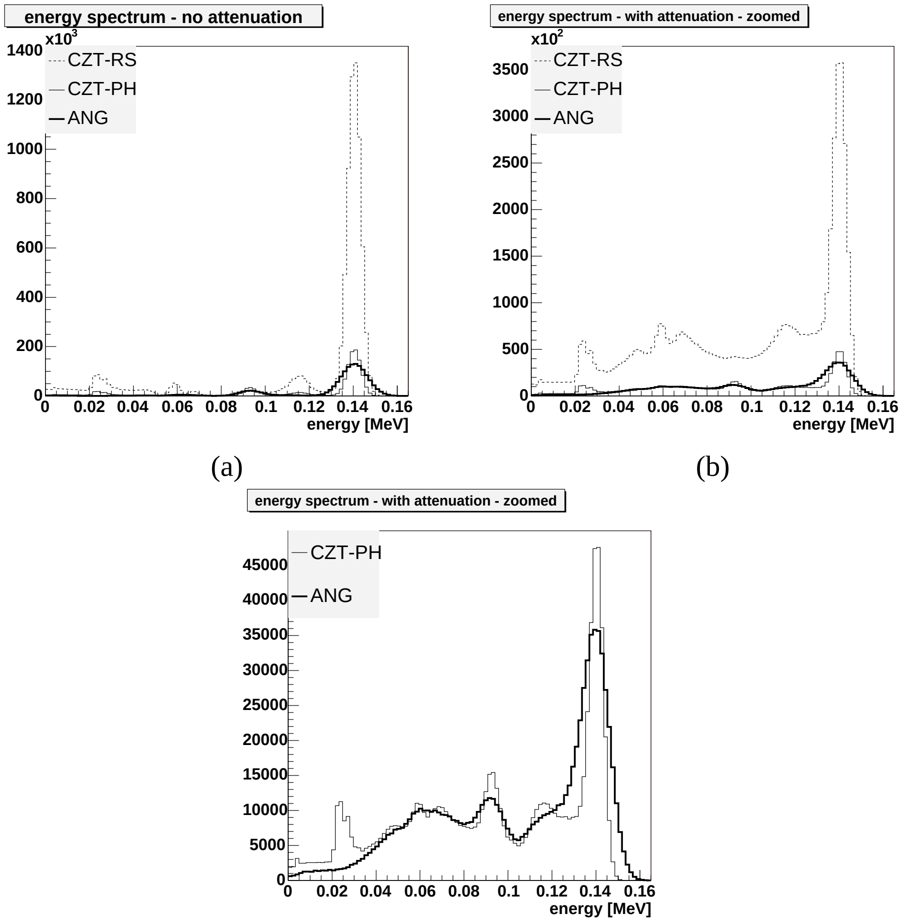

(a) (b)

(c)

Figure 5.5: Results of simulation studies : energy spectra for all three devices; CZT-RS=keyword for rotating slat device, CZT-PH=keyword for parallel hole on solid state and ANG=keyword for a classical Anger camera: (a) simulation study without attenuating medium; (b) simulation study with water cylinder on an appropriate scale; (c) comparison for the same collimator mounted on two different detectors (NaI and CZT).

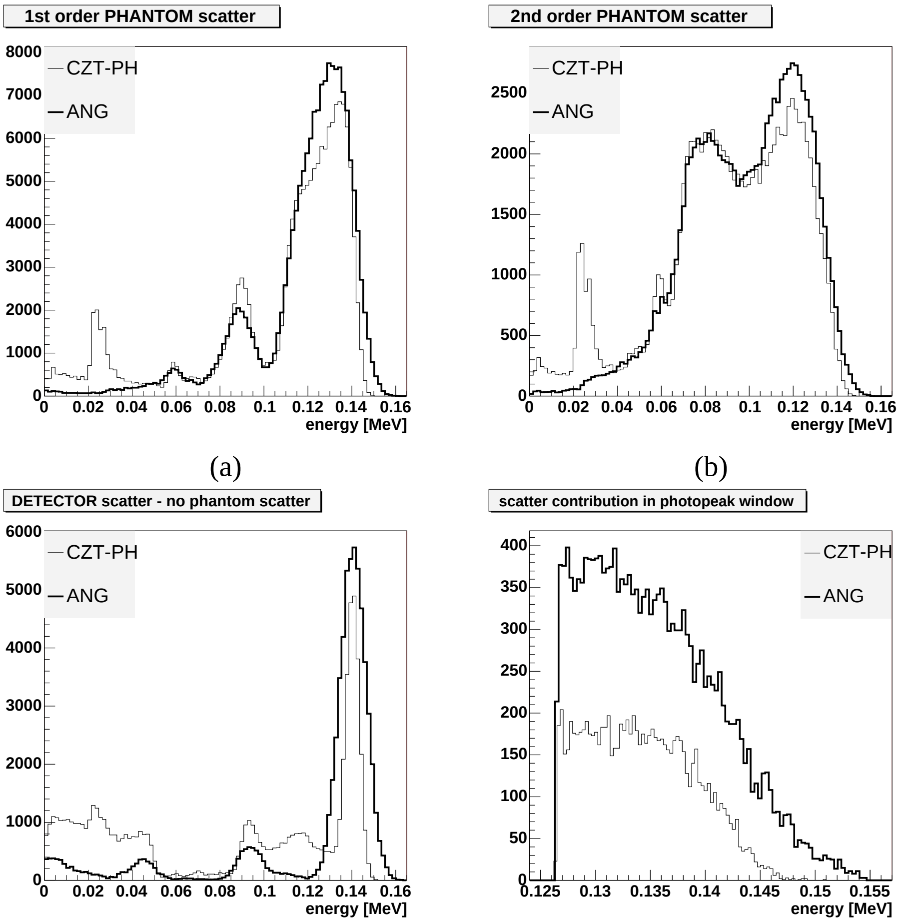

(a) (b)

(c) (d)

Figure 5.6: Results of simulation study, CZT-PH=keyword for parallel hole on solid state and ANG=keyword for a classical Anger camera : (a) first order scatter in the phantom; (b) second order scatter in the phantom; (3) crystal scatter contribution; (d) summary of scatter contamination.

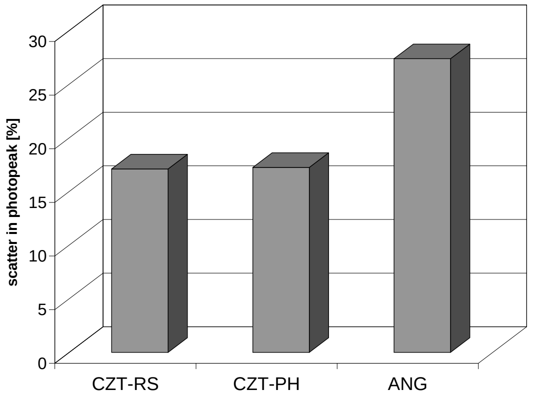

Figure 5.7: Scatter contamination in the photopeak window for all three devices, CZT-RS=keyword for rotating slat device, CZT-PH=keyword for parallel hole on solid state and ANG=keyword for a classical Anger camera.

limator is moved in an essentially random way during acquisition [79].

5.3.1 Formalism

In order to model the detector response of a strip detector equiped with a slat collimator, we assume a continuous infinite detector. Suppose we have a point source at distance Z from the slat collimator face (Figure 5.8). We choose the z-axis perpendicular to the collimator plane through the point source. The x-axis is chosen along the strip detector and the y-axis perpendicular to the strip detector, both in the detector plane. The aperture function of the strip area defined by the gap between two slats can be written as $a(\overline{r},\overline{r}_c) = a_x(x - x_c)a_y(y - D)$, giving a value of 1 for points $\overline{r}$ belonging to the gap area with the center at position $\overline{r}_c = (x_c, D)$ and 0 for other points. Both the aperture functions a_x and a_y are rectangle functions, respectively given by $\Pi\left(\frac{x-x_c}{B}\right)$ and $\Pi\left(\frac{y-y_c}{W}\right)$ with W the width of the detector strip, B the distance between two slats and with

$$\Pi\left(x\right) = \begin{cases} 0 & for | \, x \, | > \frac{1}{2} \\ \\ \frac{1}{2} & for | \, x \, | = \frac{1}{2} \\ \\ 1 & for | \, x \, | < \frac{1}{2}. \end{cases}$$

Radiation coming from the point source and detected by the gap area with center at position $\overline{r}_c$ will pass through a corresponding area at the slat collima-

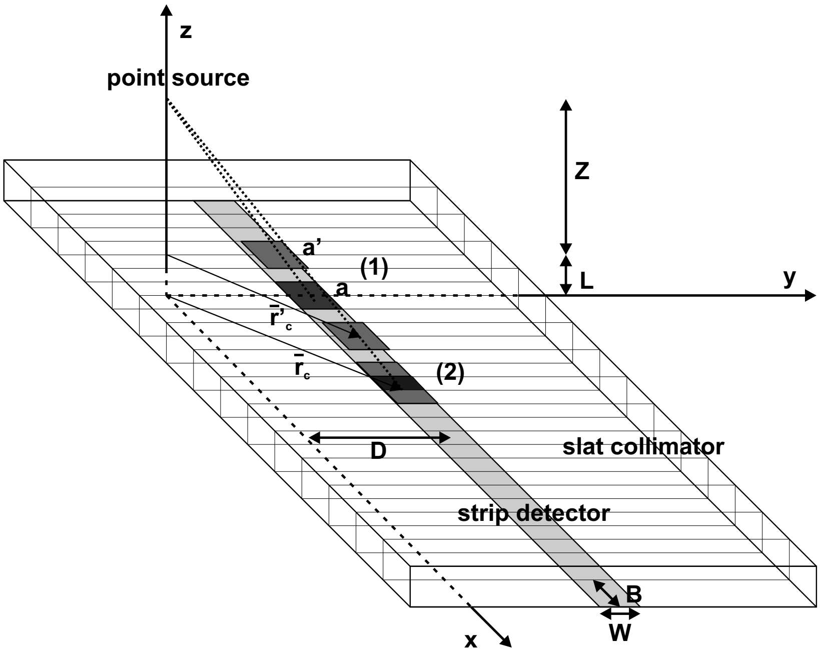

Figure 5.8: Schematic overview of the strip detector with slat collimator. $a(\overline{r}, \overline{r}_c)$ is the aperture function at the detector while $a'(\overline{r}', \overline{r}'_c)$ is the aperture function at the collimator face with $\overline{r}', \overline{r}'_c$ being coplanar. The overlap of $a(\overline{r}, \overline{r}_c)$ and the projection of $a'(\overline{r}', \overline{r}'_c)$ at the detector ($a'(\overline{r}, \overline{r}_c)$) is a measure for the detectability. At site (1) perfect overlap and maximum detectability is shown while at site (2) partial overlap is demonstrated.

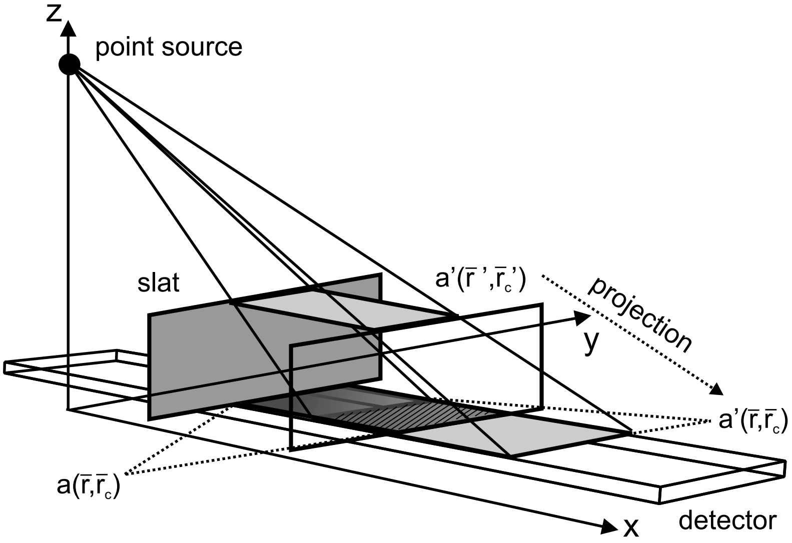

Figure 5.9: Zoom on two neighbouring slats to visualize the overlap of the active detector area (in fading black on the detector) and the projection of the aperture function at the collimator face on that area (in grey on the detector). The overlap is outlined by the hatched region. The degree of overlap between $a(\overline{r}, \overline{r}_c)$ and $a'(\overline{r}, \overline{r}_c)$ will determine the behavior of the detector at that point.

tor face defined by the aperture function $a'(\overline{r}', \overline{r}'_c) = a(\frac{Z+L}{Z}\overline{r}', \frac{Z+L}{Z}\overline{r}'_c)$, with $\overline{r}'_c = (x_c, \frac{Z}{Z+L}D)$ the corresponding aperture center at the collimator face and $\overline{r}' = \frac{Z}{Z+L}\overline{r}$ the intersection of the line connecting the point source and the detection point $\overline{r}$ with the front plane of the collimator (figure 5.9). Substitution yields the following expression for the collimator face aperture function projected to the detector area: $a'(\overline{r}, \overline{r}_c) = a_x(x - \frac{Z+L}{Z}x_c)a_y(y - D)$. The degree of overlap between $a(\overline{r}, \overline{r}_c)$ and $a'(\overline{r}, \overline{r}_c)$ will determine the behavior of the detector at that point. Maximum overlap will occur for the closest gap to the point source with center at position $\overline{r}_c = (0, D)$.

The photon flux $\phi_{L,B,W}(\overline{r}, Z, D)$ reaching a detection point $\overline{r}$ from a point source at distance Z ($z = Z + L$) from the collimator face is determined by the integration of the number of gap areas for which the detection point $\overline{r}$ belongs to the intersection of $a(\overline{r}, \overline{r}_c)$ and $a'(\overline{r}, \overline{r}_c)$, integrated over all possible center positions $\overline{r}_c$

$$\phi_{L,B,W}(\overline{r}, Z, D) \cong \frac{k\,(Z+L)}{\left((Z+L)^2 + |\overline{r}|^2\right)^{\frac{3}{2}}} \int_{-\infty}^{+\infty} a(\overline{r}, \overline{r}_c) a'(\overline{r}, \overline{r}_c) d\overline{r}_c. \quad (5.1)$$

The multiplicative prefactor $\frac{k(Z+L)}{\left((Z+L)^2+|\overline{r}|^2\right)^{\frac{3}{2}}}$ consists of k which models the detection efficiency of the detector and of $\frac{\cos\theta}{r^2}$. In this expression, $\cos\theta = \frac{Z+L}{\left((Z+L)^2+|\overline{r}|^2\right)^{\frac{1}{2}}}$ and $r = \left((Z+L)^2 + |\overline{r}|^2\right)^{\frac{1}{2}}$. Due to the inverse square law the photon fluence at a distance r from the point source is decreased inverse quadratically. Additionally, for oblique incidences this factor has to be multiplied with $\cos(\theta)$ to account for the non-perpendicular position of the irradiated surface. Specifying the expressions for a and d one now obtains:

$$\begin{aligned}\phi_{L,B,W}(x, y, Z, D) \cong & \frac{k\,(Z+L)}{\left((Z+L)^2 + x^2 + y^2\right)^{\frac{3}{2}}} a_y^2(y-D) \\ & \int_{-\infty}^{+\infty} a_x(x-x_c) a_x(x - \frac{Z+L}{Z} x_c) dx_c.\end{aligned} \quad (5.2)$$

We introduce a variable $\rho = x_c - x$ so that expression 5.2 can be written as:

$$\begin{aligned}\phi_{L,B,W}(x, y, Z, D) \cong & \frac{k\,(Z+L)}{\left((Z+L)^2 + x^2 + y^2\right)^{\frac{3}{2}}} a_y^2(y-D) \\ & \int_{-\infty}^{+\infty} a_x(-\rho) a_x \left(\frac{Z+L}{Z}\left(-\rho - \frac{L}{L+Z} x\right)\right) d\rho.\end{aligned} \quad (5.3)$$

If we make the following approximation $(Z+L)^2 + x^2 + y^2 \cong (Z+L)^2 + y^2$ (strong collimation by slats) the one-dimensional Fourier transform of expression 5.3 is given by:

$$\begin{aligned}\Phi_{L,B,W}(\nu_x, y, Z, D) \cong & \frac{k\,(Z+L)}{\left((Z+L)^2 + y^2\right)^{\frac{3}{2}}} a_y^2(y-D) \\ & \int_{-\infty}^{+\infty} \left(\int_{-\infty}^{+\infty} a_x(-\rho) a_x \left(-\frac{Z+L}{Z}\rho - \frac{L}{Z} x\right) d\rho\right) \\ & \exp(-i2\pi x \nu_x) dx.\end{aligned} \quad (5.4)$$

If we write $\exp(-i2\pi x\nu_x)$ in terms of the aperture function arguments of expression 5.4:

$$\begin{aligned}\exp(-i2\pi x\nu_x) =& \exp\left(-i2\pi\left(-\frac{Z+L}{L}\nu_x\rho\right)\right)\\ &\times\exp\left(-i2\pi\left(-\frac{Z}{L}\nu_x\left(-\frac{Z+L}{Z}\rho-\frac{L}{Z}x\right)\right)\right),\end{aligned} \tag{5.5}$$

then the following expression for $\Phi_{L,B,W}(\nu_x, y, Z, D)$ results:

$$\begin{aligned}\Phi_{L,B,W}(\nu_x, y, Z, D) \cong& \frac{k\left(Z+L\right)}{\left((Z+L)^2+y^2\right)^{\frac{3}{2}}}a_y^2(y-D)\\ &\int_{-\infty}^{+\infty} a_x(-\rho)\exp\left(-i2\pi\left(-\frac{Z+L}{L}\nu_x\rho\right)\right)d\rho\\ &\int_{-\infty}^{+\infty} a_x\left(-\frac{Z+L}{Z}\rho-\frac{L}{Z}x\right)\\ &\exp\left(-i2\pi\left(-\frac{Z}{L}\nu_x\left(-\frac{Z+L}{Z}\rho-\frac{L}{Z}x\right)\right)\right)dx.\end{aligned} \tag{5.6}$$

If A_x is the Fourier transform of the aperture function a_x, expression 5.6 can be written as:

$$\begin{aligned}\Phi_{L,B,W}(\nu_x, y, Z, D) \cong& \frac{kZ\left(Z+L\right)}{L\left((Z+L)^2+y^2\right)^{\frac{3}{2}}}\\ &a_y^2(y-D)A_x\left(-\frac{Z}{L}\nu_x\right)A_x\left(\frac{Z+L}{L}\nu_x\right).\end{aligned} \tag{5.7}$$

The Fourier transform of a rectangle function $\Pi\left(x\right)$ is given by $\operatorname{sinc}\left(\pi\nu_x\right)$. Substitution of these expressions yields the following result for the detector response of a strip detector with slat collimator:

$$\begin{aligned}\Phi_{L,B,W}(\nu_x, y, Z, D) \cong& \frac{kB^2Z\left(Z+L\right)}{L\left((Z+L)^2+y^2\right)^{\frac{3}{2}}}\\ &\Pi^2\left(\frac{y-D}{W}\right)\operatorname{sinc}\left(\pi B\frac{Z}{L}\nu_x\right)\operatorname{sinc}\left(\pi B\frac{Z+L}{L}\nu_x\right).\end{aligned} \tag{5.8}$$

For $Z >> L$ expression 5.8 reduces to:

$$\begin{aligned}\Phi_{L,B,W}(\nu_x, y, Z, D) \cong & \frac{kB^2\,(Z+L)^2}{L\left((Z+L)^2+y^2\right)^{\frac{3}{2}}} \\ & \Pi^2\left(\frac{y-D}{W}\right)\text{sinc}\left(\pi B\frac{Z+L}{L}\nu_x\right)^2 .\end{aligned} \tag{5.9}$$

5.3.2 Analysis

Multiple points can be discussed about this expression. We analyzed spatial resolution, sensitivity and line spread functions and verified the results derived from the above discussed theoretical model by means of accurate Monte Carlo simulations. For this purpose GATE was used to model the Solstice detector geometry (cfr. section 5.2 for the technical specifications).

Sensitivity

Given expression 5.8, one obtains for a detection point$\overline{r} = (x, y)$ being part of the strip detector a DC frequency component that is approximately weighted by a factor proportional to $\frac{\cos^2(\theta)}{\left((Z+L)^2+y^2\right)^{\frac{1}{2}}}$ with θ the angle of incidence between a ray from the point source and the normal vector to the detector and with $\left((Z+L)^2+y^2\right)^{\frac{1}{2}}$ the distance between point source and detector. This weighting factor determines the sensitivity for a location in the field of view (FOV) and depends on the position of the point source relative to the strip detector, in the plane perpendicular to the detector strip direction. As a verification a rectangular grid of point sources was simulated in the FOV at different distances from the face of the slat collimator and from the center of the detector strip. The results of these simulations are listed in figure 5.10. The sensitivity throughout the FOV as a function of the distance from the face of the collimator and as function of the distance from the strip detector is plotted. Notice the $\frac{1}{\left((Z+L)^2+D^2\right)^{\frac{1}{2}}}$ dependence ($= \frac{1}{distance}$) at the center of the strip detector as calculated from equation 5.8. We performed additional simulations to evaluate the influence of the angle of incidence on the sensitivity. We placed 30 point sources on an arc with an aperture of 90 degrees so that the distance to the detector stayed constant for each point source. The comparison of simulation results and theoretical calculations is shown in figure 5.11. This setup, incorporating 30 point sources with a 3 degree angular separation provided the

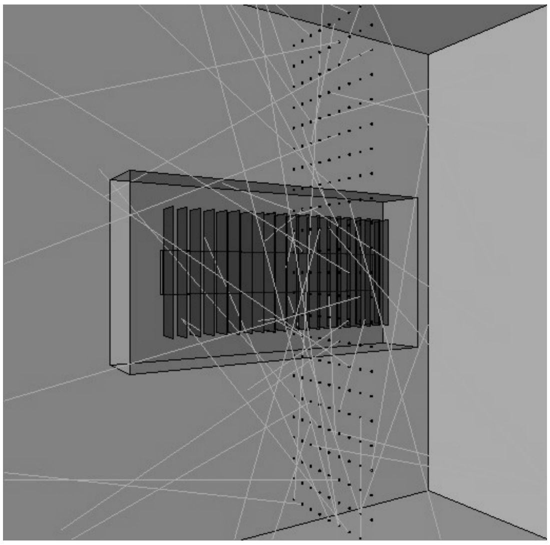

(a)

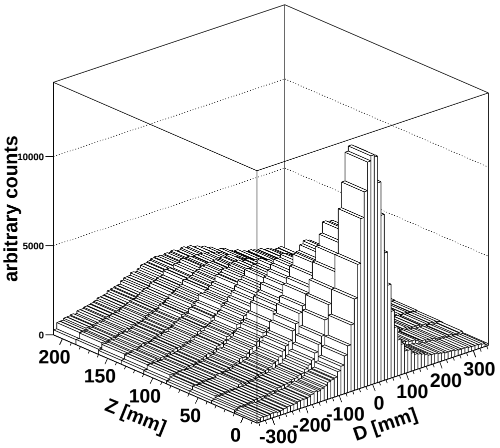

(b)

Figure 5.10: Sensitivity as a function of the distance from the face of the collimator (Z from 0 mm to 200 mm) and as function of the distance from the center of the detector (D from -300 to 300 mm): (a) simulation setup: the grid of point sources is shown together with the camera, consisting of the CZT detector with the mounted slats, 50 photon tracks are also plotted as an illustration; (b) results: sensitivity.

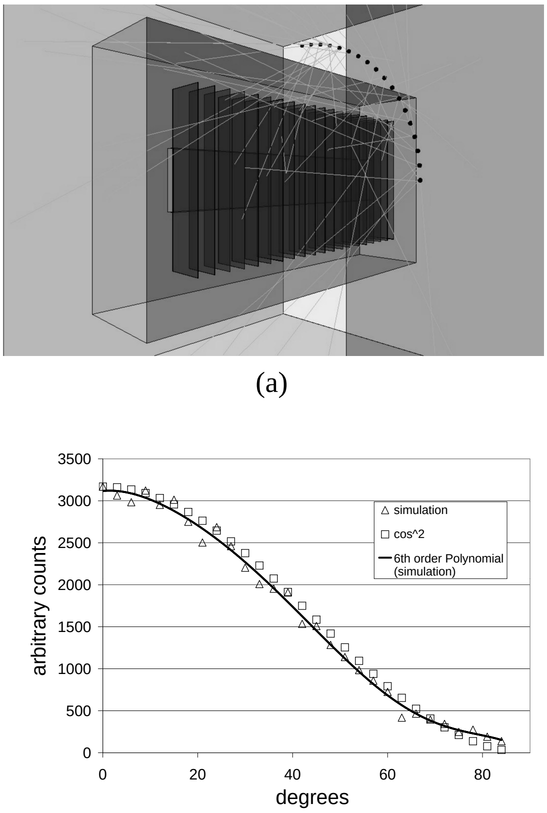

(a)

(b)

Figure 5.11: Comparison simulated versus calculated angular dependency: (a) setup of the simulation: the spherical grid of point sources is shown together with the camera, consisting of the CZT detector with the mounted slats, 50 photon tracks are also plotted as an illustration; (b) results: angular dependency of the sensitivity.

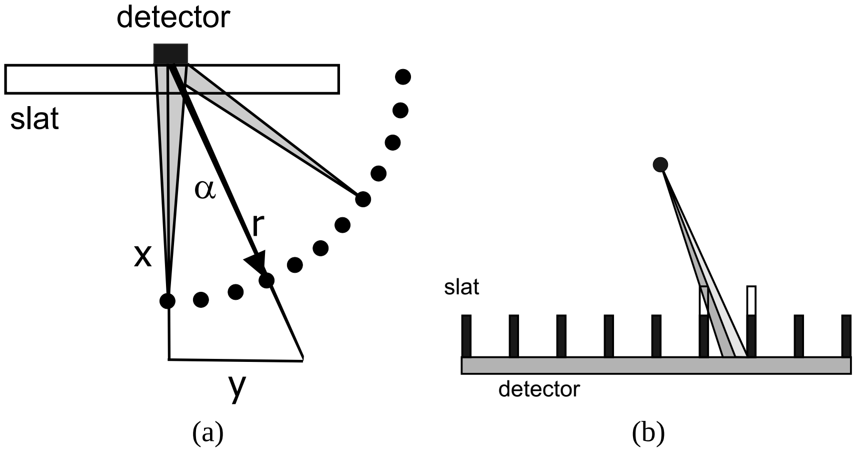

Figure 5.12: Evaluation of the simulated Solstice sensitivity at a constant distance from the detector: (a) oblique irradiation effect; (b) slats longer for oblique incidences.

number of detected counts for each source separately, in order to form the sensitivity variation. The highest sensitivity was registered for point sources in front of the detector, while the sensitivity decreases with $\cos^2(\theta)$ for oblique incidences as was theoretically predicted by equation 5.8. A good agreement with the predicted sensitivity behavior is shown in both discussed figures.

The $\frac{\cos^2(\theta)}{r}$ dependence of the sensitivity can also be understood on a more straightforward geometrical basis as is shown by figure 5.12. The non-perpendicular radiation on the detector (figure 5.12(a)) causes the sensitivity to decrease ($\cos(\theta)$) for sources at $\theta \neq 0$ as was stated above. Moreover, for these sources the collimator slat length is longer ($L/\cos(\theta)$) due to the oblique path which causes an additional decrease ($\cos(\theta)$) (Figure 5.12(b)). Integration over all gap positions reduces $1/r^2$ of the inverse square law to $1/r$.

Spatial resolution

Apart from the weighting factor, expression 5.8 only depends on Z or the perpendicular distance between the point source and the collimator surface. Therefore the resolution behavior of a strip detector with a slat collimator will only be determined by the perpendicular distance between source and collimator surface. To verify this behavior, 4 separate point sources were placed in the FOV at a certain distance from the face of the collimator slats and at varying distances from the center of the detector strip. The results of these simulations are shown in figure 5.13 where the resolution behavior for those point sources

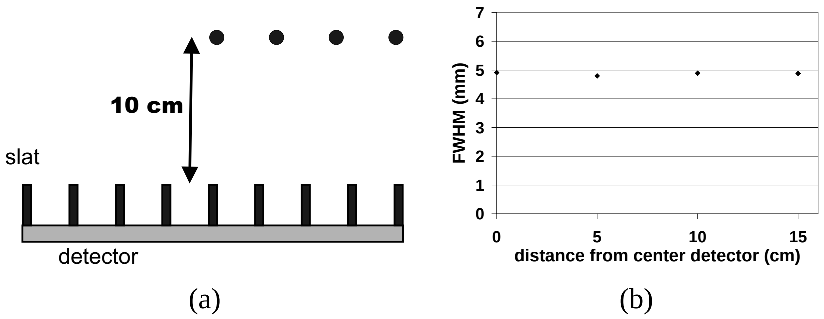

Figure 5.13: Resolution behavior for point sources at a distance of Z=10 cm from the face of the slat collimator: (a)illustration of the setup, (b) simulation results.

is illustrated. It is clear from this figure that the resolution stays constant, as was predicted by the theoretical model.

Profiles

Since the inverse one-dimensional Fourier transform applied to expression 5.8 delivers the line spread function, we are able to obtain the transaxial profile of a line source in a plane parallel to the collimator surface at a certain distance from the collimator. We copied that setup in a simulation by placing line sources at different distances from the collimator surface and we compared the resulting simulated profiles with the calculated results as is shown in figure 5.14. A good agreement is seen and the triangular profile, resulting from the convolution of two rectangular functions, is confirmed by the simulations. However, this theoretical formulation is mostly a far field model and other effects have to be taken into account close to the detector as we describe in [129]. Figure 5.14(a) at 2.5 cm and figure 5.14(b) at 5 cm from the collimator surface show a discrepancy between calculation and simulation in the close field of a large gap detector system, which disappears further away along the z-axis. We investigated this discrepancy by reducing the gap size with a factor of 10 and by increasing the number of slats by an equal factor 10. Figure 5.15 shows the result at 5 cm from the collimator face. There is a perfect agreement now between simulation and calculation with that particular detector setup. This demonstrates that decreasing the gap size reduces the importance of the x^2 factor in expression 5.3 and also reduces the importance of the exact gap positions, making the approximations of this theoretical formulation valid.

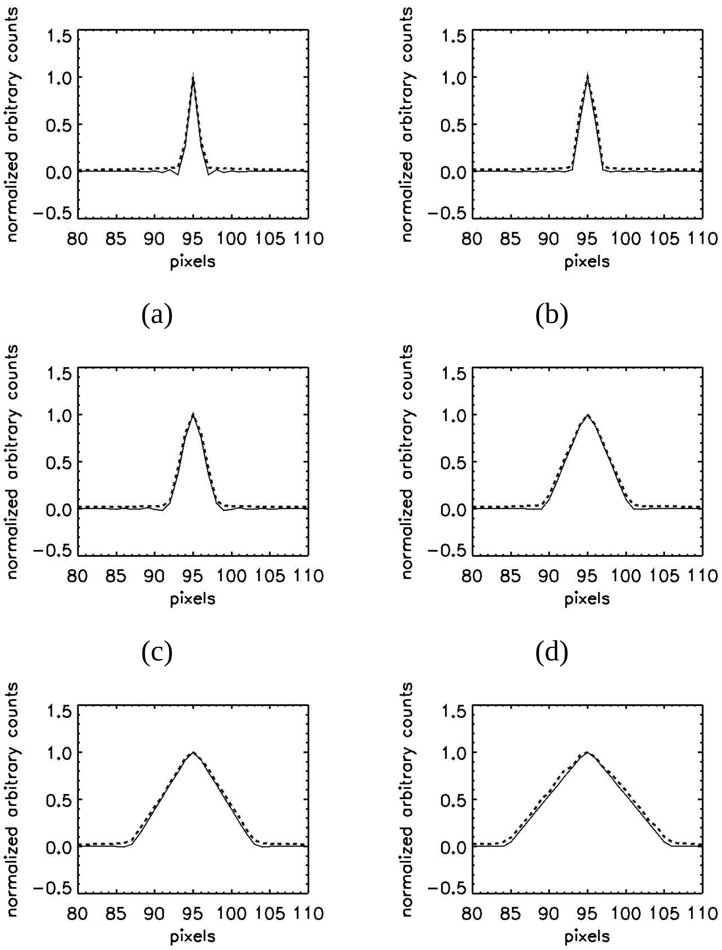

(a) (b)

(c) (d)

(e) (f)

Figure 5.14: Comparison of simulated (dashed line) and calculated transaxial profiles of a line source placed in a plane parallel to the collimator surface (a) at 2.5 cm from the collimator ; (b) at 5 cm from the collimator; (c) at 10 cm from the colimator ; (d) at 20 cm from the collimator; (e) at 30 cm from the colimator ; (f) at 40 cm from the collimator. The abscis is expressed in pixels (1.8 mm pitch) which are in this case the 192 gaps of the detector system (34.56 cm) along the x-axis. The line source is positioned at pixel 95.

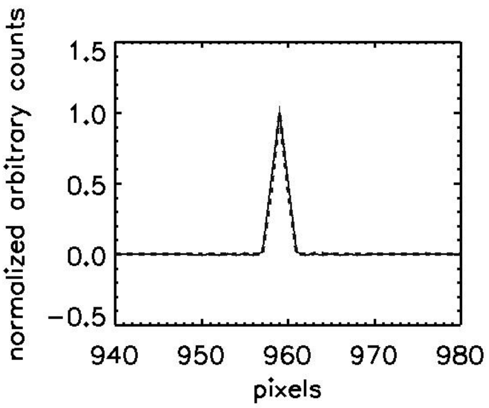

Figure 5.15: Comparison of simulated (dashed line) and calculated transaxial profiles at 5 cm from the collimator for ultrafine setup. The abscis is expressed in pixels (.18 mm pitch) which are in this case the 1920 gaps of the detector system (34.56 cm) along the x-axis. The line source is positioned at pixel 959.

5.4 Observer performance study

A Receiver Operating Characteristic (ROC) study on simulated data sets is additionally performed to evaluate the hot spot detectability of the three systems discussed in section 5.2. The sensitivity and specificity of a diagnostic test depends on more than just the quality of the test, they also depend on the definition of what constitutes an abnormal test. The position of this cutpoint will determine the number of true positive, true negatives, false positives and false negatives. An ROC curve is a plot of the true positive rate against the false positive rate for the different possible cutpoints of a diagnostic test. For this purpose, datasets of hot spots are simulated and backgounds are reproduced using the bootstrap method on simulated List Mode Files (LMF) [20]. Based on our findings a task dependent application of these different devices should become possible.

5.4.1 Study setup

In order to generate the data sets for the above discussed observer performance study, three simulation studies were performed:

- **Simulation study 1: No attenuating medium**

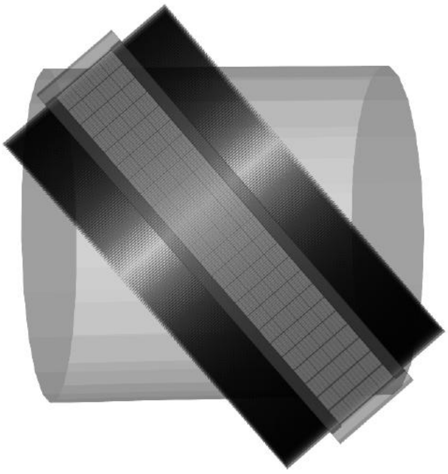

Figure 5.16: Rotating slat detector with the attenuation phantom, placed within the FOV.

In this simulation setup a uniform source of 225 MBq of ^{99m}Tc was inserted in the Field Of View (FOV). The activity was contained in a cylindrical non-attenuating phantom of 35 cm diameter and 35 cm height in order to fill the FOV.

- **Simulation study 2: Attenuating phantom**

This setup is analogous to the previous one but the activity is now contained in a water-filled cylinder of the same dimensions (figure 5.16). The water filled cylinder is placed as closely as possible to the collimator.

- **Simulation study 3: Hot spot**

The third setup is an extension of the previous one where a hot spot source is now inserted in the center of the water cylinder. The hot spot is a 1 cm sphere and the activity for the sphere is depending on the desired count level for the ROC study. The simulation results are returned in list mode format wherein several fields are stored: source position, energy, detection location (crystalID, pixelID, position), rotation angle and/or spin angle.

5.4.2 Reconstruction

A reconstruction method was needed to reconstruct the planar integrals acquired by the rotating slat system. A newly developed reconstruction technique, based on natural pixels, is used to reconstruct the list mode files that result from the aforementioned simulation studies [125]. This natural pixel approach will be discussed in Chapter 7. The first simulation study (without attenuating phantom) is used to generate system matrices for the different setups. For each detected event, the source position is stored in these list mode files making it possible to obtain a system matrix in that way. The Algebraic Reconstruction Technique (ART) (section 2.1.6) is chosen to solve the reconstruction equation iteratively as the convergence is faster than for other algorithms and as it is not constrained to positive values only so that subdivisions of image space can be eliminated in the backprojection.

5.4.3 Performance Analysis: ROC study

In order to evaluate the hot spot detectability for different collimator setups we compared the two solid state devices with respectively a parallel beam and rotating slat collimator together with the NaI setup using a dedicated ROC-analysis [115]. We presented four human observers 3 series of 100 images: 50 as a training set and 50 images to be scored. In 25 images of each set a hot spot was present while the other 25 images consisted of only background activity. For this purpose Simulation study 2 and Simulation study 3 (section 5.4.1) were applied for all acquisition setups. The count level in the hot spot was chosen so that the ROC area under the curve would be around 0.8 to 0.9 for the rotating slat acquistion module. This resulted in a background file of 1.7 million counts registered over a 35 cm by 5.76 cm area for the 360 spin angles. The detected number of counts for the hot spot was 7.5 kcounts for a sphere of 1 cm diameter, again for the 360 spin angles. We then simulated the same activity for the parallel hole setups and generated in that way two other series of 50 images of which half contained a hot spot signal. In order to obtain these three datasets, 3×25 signal (hot spot) realisations were simulated while only one background file was simulated for each series. That background list mode file was then bootstrapped [20] in order to achieve 50 separate background files. In recent literature this was proven to be a correct technique for ROC analysis with numerical observers [31, 47]. We showed very recently [32,33] that this technique is also extensible to human observers, preserved that the background of all reconstructed files is replaced by a median smoothed version of the original background file. The main difference between bootstrapped images and noisy realisations is this mean background. For the bootstrapped images this is the reconstruction of the original file which results in a doubled variance. In numerical observer studies the background is subtracted which solves this issue. Human observers however can not do this and therefore the reconstructed image of the original background list mode file

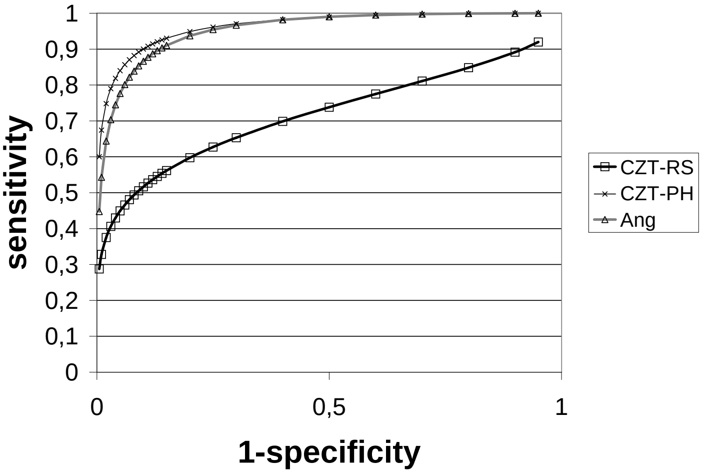

Figure 5.17: ROC performance results.

must be subtracted and replaced by a median smoothed version. In that way the averaged human observer performance on bootstrapped data sets is equivalent to the observer performance on noisy realisations.

The result of the averaged human observer on the three series of each 50 images is shown in figure 5.17. It can be concluded that the slat collimator setup shows an inferior performance compared to the parallel beam setups. Probably this is due to the fact that the higher sensitivity of the rotating slat device can not be fully exploited as the direction of detection of the photons is only confined to a plane while this is a narrow cone in small pitch parallel beam collimators. It is especially interesting to investigate how the performance of the rotating slat device for hot spot detectability evolves when the CZT strip completely fills the area behind the slats as shown in figure 5.18. Accordingly, we simulated a fourth setup (FUS). A new dataset was simulated and scored in a analogue manner by the four human observers. We see now that the performance of the full strip rotating slat system is improved to a large extent as demonstrated in figure 5.19 with an active detector area which is still only half of the two other setups. However, the performance of the rotating slat collimator remains slightly inferior compared to the parallel beam setups. This observer study should be extended on a data set generated using a dedicated 3D reconstruction algorithm as was very recently derived by Zeng *et al* in [147] and by Wang *et al* in [135]. In those implementations the incorporated $1/r$ sensitivity information for the rotating slat design could result in an im-

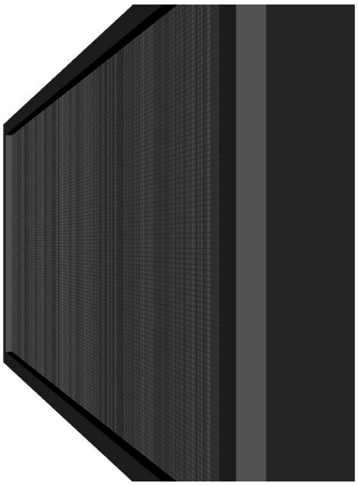

(a)

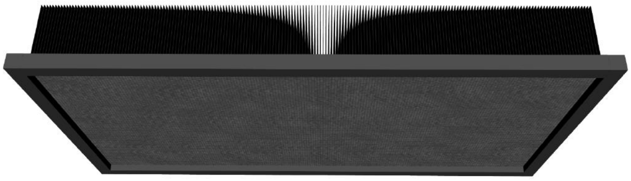

(b)

Figure 5.18: Increasing the strip filling area behind slats (keyword:FUS): (a) side view, (b) downside view

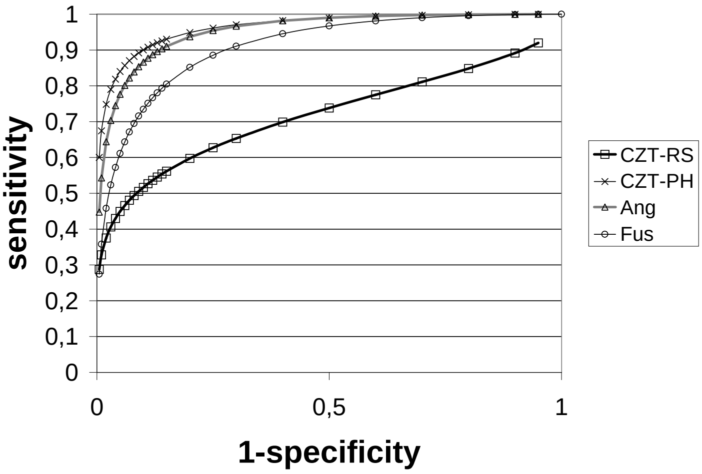

Figure 5.19: Increasing the strip filling area behind slats (keyword:FUS): ROC curve.

proved performance on reconstructions and could cancel out the performance deficit in this projection based study.

5.5 Conclusion

We investigated a new acquisition system design with a strip solid state detector and with a slat collimator by comparison with parallel beam setups on a pixelated solid state detector and on a single crystal NaI detector. We found that solid state devices have a better energy resolution making them more appropriate for dual isotope imaging. The rotating slat collimator results in a better resolution and in a higher sensitivity.

A theoretical formulation for the effective point spread function of a slat collimator on a strip detector was derived. We found that the sensitivity depends on the angle of incidence and on the distance to the detector, while the spatial resolution of this particular imaging system is constant in a plane at a fixed distance from the collimator. For both properties as well as for transaxial profiles of line spread functions we could calculate closed analytical behavior formulations, derived from the analytical expression for the geometric transfer function in the Fourier domain. The presented formulation of the geometric transfer function will be useful in iterative reconstruction algorithms in order to incorporate distance dependent effects. It will be applied in combination with additional simulation study results which account for collimator scatter and septal penetration of the slats, a contribution that only gains importance with higher energy isotopes.

A rotating slat collimator has a higher sensitivity but each photon is collected in a plane and thus contains less information. So, additionally, a comparison between three types of imaging devices has been performed. As far as the contrast and hot spot detectability is concerned, the classical collimator setup on a CZT and on a NaI detector outperforms the rotating slat equivalent. However when we increased the strip width behind the slats, the performance of the rotating slat collimator closed in on the parallel beam setup performances. This is promising since the active detector area in the rotating slat design is, in this case, still only half of the two other acquisition models. The solid state setups have the disadvantage of economic cost however as the CZT material is far more expensive than a NaI crystal.

This work resulted in two peer reviewed journal articles [104, 130] and in three publications in the proceedings of international conferences [70, 102, 129]. We extended the work of Metz [79], and Tsui [121] for the geometric transfer function of a slat collimator on a strip detector. Additionally, this chapter describes the first human observer study on Solstice imaging performance in order to allow a task dependent application of those modalities in future clinical practice.

Chapter 6

Detector modeling

6.1 Introduction

In the previous chapter we demonstrated the use of Monte Carlo simulations for new acquisition system design. Another important application field of Monte Carlo simulations is intrinsic detector modeling: detector responses, efficiencies, light per gamma ray interaction, rise and decay times, stopping power, spatial and energy resolution. One of the main fields of interest is resolution recovery in PET. Due to the finite pixelization and due to the limited number of PMTs there is an intrinsic detection location uncertainty causing an inherent pointspread function on all registrations. However, the penetration of annihilation photons into the detector material before interaction is a statistical process which leads to significant displacement and anisotropy of this pointspread function.

Iterative reconstruction algorithms for PET imaging require an accurate modeling of the acquisition process. In the past, our group has developed a list mode reconstruction algorithm for continuous detector PET, making use of a simple line of response (LOR) model [127, 128], in which intersection lengths describe the probability that an emission occured in a voxel of the Field Of View (FOV). This simple model does not account for the intrinsic resolution discussed above. In this chapter we will describe a theoretical model of the spatial uncertainty for a line of response, due to the imperfect localization of events on the detector heads in order to recover this intrinsic spatial resolution.

For oblique incidences the incorporation of the effect of the crystal thickness will appear to be necessary to account for the aforementioned crystal penetration. A thorough study of the theoretical model and examples of probability density functions (pdfs) will be described for all cases. Moreover, appropriate functions will be fit to the transversal profiles of these pdfs and their characteristics will be investigated. The features of the derived model can only be verified by Monte Carlo simulations since those Depth of Interaction (DOI)-dependent experiments are very hard to perform with current state of the art technology (limited resolution). After an affirmative accuracy verification, the described model can be used to incorporate the intrinsic resolution effect in the reconstruction process by means of a better defined acquisition process. This should improve the spatial resolution of the resulting tomographic images. Two different approaches for incorporation in reconstruction algorithms will be proposed. The most promising of those reconstruction methods will then be discussed in Chapter 7.

6.2 Theoretical derivation

We will deal with the twodimensional case of perpendicular incidences on an acquisition setup consisting of two parallel continuous detector heads first, and extend it into three dimensions afterwards. We will then study oblique incidences in two and three dimensions.

6.2.1 Perpendicular incidences

We will start with the twodimensional case of perpendicular incidences. For this purpose we need a model for the forward problem of the uncertainty in detection location. This detector response function is well studied in literature [50, 113, 114]. We assume a Gaussian distribution (standard deviation σ_{0y}) for the actual position of interaction on the detector head, centered at the measured position for the likelihood that an event at a given point in the field of view gives rise to that particular detection location. For the evaluation of the a posteriori probability $S(p,q)$ that an event originates from a point (p,q) in the FOV, given the detection locations, we integrate all possible LORs through that point, weighted with the Gaussian detection likelihood at the LOR's end points (figure 6.1). This a posteriori probability density function can then be incorporated in an upgraded version of the aforementioned list mode reconstruction algorithm. We obtain the following expression for the probability:

$$\begin{aligned}
S(p,q) &= \int_{-|\theta_{min}|}^{|\theta_{max}|} s(\theta) d\theta \\
S(p,q) &= \frac{1}{2\pi\sigma_{0y}^2} \int_{-|\theta_{min}|}^{|\theta_{max}|} e^{w(\theta)} d\theta \\
w(\theta) &= -\frac{[(D/2-p)\tan\theta + q]^2 + [-(D/2+p)\tan\theta + q]^2}{2{\sigma_{0y}}^2}. \qquad (6.1)
\end{aligned}$$

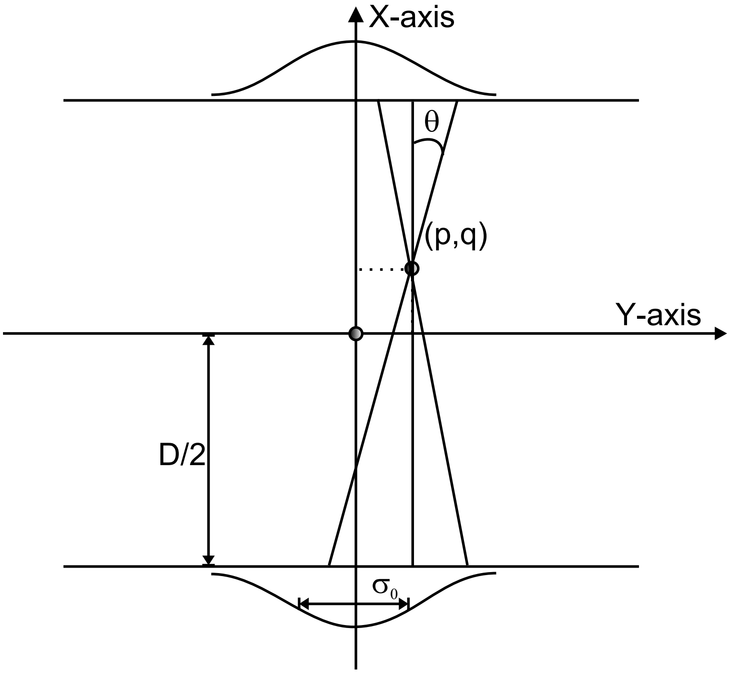

Figure 6.1: Perpendicular incidences with opposite position of the detector heads, D = distance between the detector heads, θ = angle of incidence.

In equation (6.1) $[(D/2 - p)\tan\theta + q]$ is the position of interaction on the upper detector while $[-(D/2+p)\tan\theta+q]$ is the position of interaction on the lower detector head, both expressed in the coordinate system of figure 6.1. We assume that the crystal thickness has no influence on the detection probability, which is appropiate in this case as the angle of incidence of both photons is very small when σ_{0y} is realistically chosen.

This theoretical model can be extended to three dimensions by assuming a twodimensional Gaussian distribution for the position of interaction on the detector heads. The Z-axis is perpendicular to the X- and Y-axis (cfr. figure 6.1). The resulting formula is:

$$\begin{aligned}
S(p,q,r) &= \int_{-|\varphi_{min}|}^{|\varphi_{max}|}\int_{-|\theta_{min}|}^{|\theta_{max}|} s(\theta,\varphi)\sin\theta d\theta d\varphi \\
S(p,q,r) &= \frac{1}{4\pi^2{\sigma_{0y}}^2{\sigma_{0z}}^2}\int_{-|\varphi_{min}|}^{|\varphi_{max}|}\int_{-|\theta_{min}|}^{|\theta_{max}|} e^{w(\theta,\varphi)}\sin\theta d\theta d\varphi \\
w(\theta,\varphi) &= \\
&-\Bigg\{\frac{[(D/2-p)\tan\theta\cos\varphi+q]^2+[-(D/2+p)\tan\theta\cos\varphi+q]^2}{2{\sigma_{0y}}^2} \\
&+\frac{[(D/2-p)\tan\theta\sin\varphi+r]^2+[-(D/2+p)\tan\theta\sin\varphi+r]^2}{2{\sigma_{0z}}^2}\Bigg\}.
\end{aligned} \tag{6.2}$$

In equation (6.2) the Z-coordinate is denoted by r and φ denotes the azimuthal angle.

6.2.2 Oblique incidences

We will discuss the case of oblique incidences in the next paragraphs. A detector with no physical thickness (perfect detector) is discussed first. Afterwards the influence of the photons' depth of interaction is incorporated in order to obtain a theoretical model for PET dedicated detectors with a realistic finite crystal thickness.

Perfect detector

The same considerations as in paragraph 6.2.1 can be made for the case where the incidences are oblique (figure 6.2). We chose the position of the X-axis to

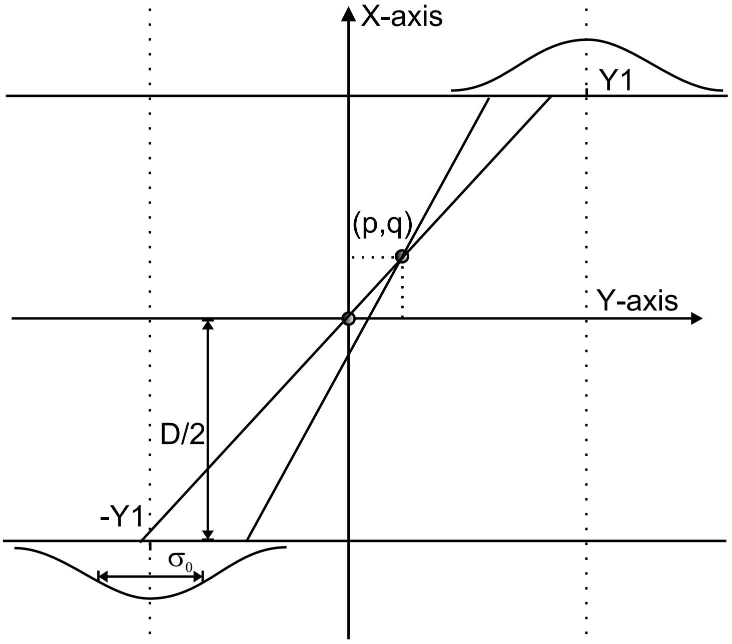

Figure 6.2: Oblique incidences with opposite position of the detector heads, D = distance between the detector heads.

be half way the two detection positions. The resulting formula is:

$$
\begin{aligned}
S(p,q) &= \int_{-|\theta_{min}|}^{|\theta_{max}|} s(\theta) d\theta \\
S(p,q) &= \frac{1}{2\pi\sigma_{0y}^2} \int_{-|\theta_{min}|}^{|\theta_{max}|} e^{w(\theta)} d\theta \\
w(\theta) = -\Big\{ & \frac{\{[(D/2-p)\tan\theta + q] - Y_1\}^2}{2{\sigma_{0y}}^2} \\
&+ \frac{\{[-(D/2+p)\tan\theta + q] + Y_1\}^2}{2{\sigma_{0y}}^2} \Big\}. \qquad (6.3)
\end{aligned}
$$

In equation (6.3) the positions of interactions on the upper and the lower detector are now $[(D/2-p)\tan\theta + q] - Y_1$, relative to the upper detector measurement in Y_1, and $[-(D/2+p)\tan\theta + q] + Y_1$, relative to the lower detector measurement in $-Y_1$ respectively. Equation (6.3) is only correct for a detector with no physical thickness.

Finite crystal thickness

In the next paragraphs we state the interaction probability of a 511 keV photon along its path through the detector to be uniform. Literature [3, 122] confirms that this hypothesis is a valid approximation for (gamma camera) PET applications on NaI(Tl) detectors. The total interaction probability of 511 keV photons is thus assumed to be proportional to its path length through the detector. When we incorporate the influence of the crystal thickness d in the theoretical model, the Gaussian model for the detector response is replaced by another function as will be derived using figure 6.3. The LOR L is parametrized by the points of incidence v_1 and v_2 (defined in the middle of the crystal) while the detections are registered in j_1 and j_2. The likelihood $p(j_1, j_2|v_1, v_2)$ for a finite crystal thickness is the product of two convolutions: a convolution of a normalized boxcar function, B, and a Gaussian, G, for j_1; multiplied with a convolution of the same functions for j_2. The width of B in this twodimensional case is $d\tan\theta$, t is the interaction point along the Y-axis: $t \in [v_1 - \frac{d\tan\theta}{2}; v_1 + \frac{d\tan\theta}{2}]$ for the upper detector and H refers in the following equations to the Heaviside

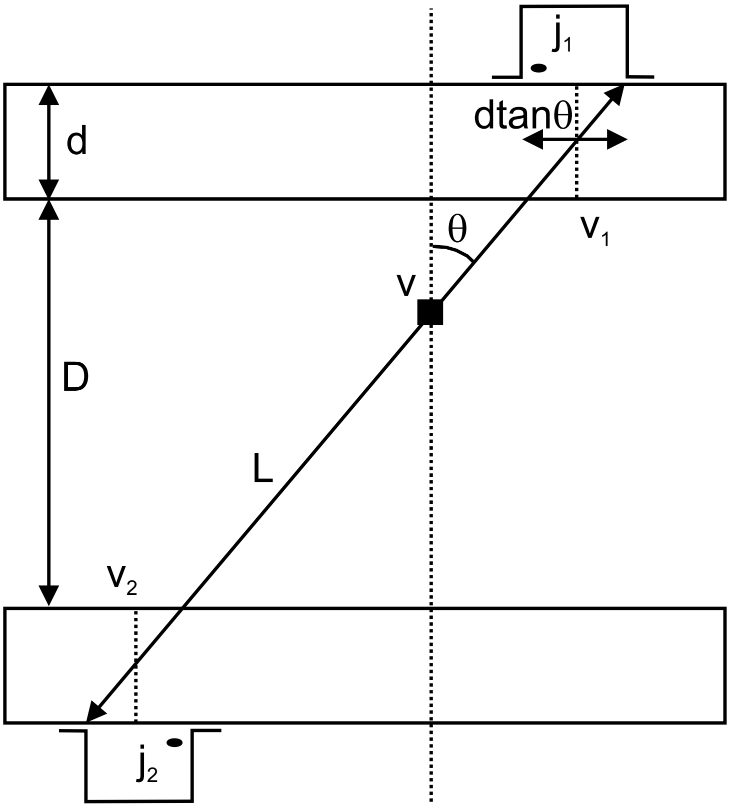

Figure 6.3: Incorporation of the crystal thickness d.

function:

$$\begin{aligned} B(t) &= \frac{H(t - v_1 + \frac{d\tan\theta}{2}) - H(t - v_1 - \frac{d\tan\theta}{2})}{d\tan\theta} \\ G(j_1, t) &= \frac{1}{\sqrt{2\pi}\sigma_{0y}} e^{\frac{-(t-j_1)^2}{2\sigma_{0y}{}^2}} \\ p(j_1|v_1) &= B(t) * G(t) = \int_{-\infty}^{+\infty} B(t) \cdot G(t) dt \\ &= \frac{1}{\sqrt{2\pi}\sigma_{0y} d\tan\theta} \int_{v_1 - \frac{d\tan\theta}{2}}^{v_1 + \frac{d\tan\theta}{2}} e^{-\frac{1}{2}(\frac{t-j_1}{\sigma_{0y}})^2} dt. \qquad (6.4) \end{aligned}$$

Substituting $\frac{(t-j_1)}{\sqrt{2}\sigma_{0y}}$ by u we get the following:

$$\begin{aligned} p(j_1|v_1) &= \frac{2}{\sqrt{\pi} 2d\tan\theta} \int_{\frac{\sqrt{2}(2v_1 + d\tan\theta - 2j_1)}{4\sigma_{0y}}}^{\frac{\sqrt{2}(2v_1 - d\tan\theta - 2j_1)}{4\sigma_{0y}}} e^{-u^2} du \\ &= \frac{\mathrm{erf}(\frac{\sqrt{2}(2v_1 + d\tan\theta - 2j_1)}{4\sigma_{0y}}) + \mathrm{erf}(\frac{\sqrt{2}(-2v_1 - d\tan\theta + 2j_1)}{4\sigma_{0y}})}{2d\tan\theta}. \qquad (6.5) \end{aligned}$$

When we subsitute j_1 by Y_1 and v_1 by $(D/2 + d/2 - p)\tan\theta + q$ in equation (6.5), then we get:

$$p(j_1|v_1) = \frac{\mathrm{erf}(\frac{\sqrt{2}(2((\frac{D}{2} - p)\tan\theta + q + d\tan\theta - j_1))}{4\sigma_{0y}}) + \mathrm{erf}(\frac{\sqrt{2}(-2((\frac{D}{2} - p)\tan\theta + q - Y_1))}{4\sigma_{0y}})}{2d\tan\theta}. \qquad (6.6)$$

Written as function of the upper detection location $y_u = (D/2 - p)\tan\theta + q - Y_1$ this gives the following:

$$F_U(y_u) = \frac{\mathrm{erf}(\frac{y_u + d\tan\theta}{\sqrt{2}\sigma_{0y}}) - \mathrm{erf}(\frac{y_u}{\sqrt{2}\sigma_{0y}})}{2d\tan\theta}. \qquad (6.7)$$

For the lower detection location $y_d = -(D/2 + p)\tan\theta + q + Y_1$ we find in the same manner with $j_2 = -Y_1$ and $v_2 = -(D/2 + d/2 + p)\tan\theta + q$:

$$F_D(y_d) = \frac{\mathrm{erf}(\frac{y_d}{\sqrt{2}\sigma_{0y}}) - \mathrm{erf}(\frac{y_d - d\tan\theta}{\sqrt{2}\sigma_{0y}})}{2d\tan\theta}. \qquad (6.8)$$

This results in the following expresssion for the forward likelihood:

$$p(j_1, j_2|v_1, v_2) = F_U(y_u) \cdot F_D(y_d). \qquad (6.9)$$

Equation (6.9) is equivalent with equation (6.3) for the limit of $d \rightarrow 0$. For incorporation in reconstruction we need however the a posteriori probability that an event originates from the voxel v given detections in j_1 and j_2 which is:

$$\begin{aligned} S(p,q) &= \int_{-|\theta_{min}|}^{|\theta_{max}|} s(\theta) d\theta \\ s(\theta) &= p(v_1, v_2 | j_1, j_2). \end{aligned} \tag{6.10}$$

In equation (6.10) $p(v_1, v_2|j_1, j_2)$ denotes the a posteriori probability that an annihilation in the FOV (represented by the LOR L which is defined by v_1 and v_2) gives rise to the particular detections in j_1 and j_2. The integration in equation (6.10) returns the a posteriori event probability over all LORs. In order to calculate this integral, an expression for $p(v_1, v_2|j_1, j_2)$ has to be found using Bayes' rule :

$$p(v_1, v_2|j_1, j_2) = \frac{p(j_1, j_2|v_1, v_2)p(v_1, v_2)}{p(j_1, j_2)}. \tag{6.11}$$

This expression can be simplified as the efficiency of detection of a LOR is assumed to be proportional to the product of the path length of both photons in the crystal. Both path lengths need to be calculated by comparing equivalent triangles as is shown in equation (6.12):

$$\begin{aligned} p(v_1, v_2) \sim d^2 + (dtan\theta)^2 &= d^2(1 + tan^2\theta) = d^2(1 + (\frac{v_1 - v_2}{D + d})^2) \\ p(j_1, j_2) &\sim d^2(1 + (\frac{j_1 - j_2}{D + d})^2) \\ \Rightarrow \frac{p(v_1, v_2)}{p(j_1, j_2)} &\approx 1. \end{aligned} \tag{6.12}$$

Using the result of equation (6.12) in equation (6.11) we obtain the following :

$$p(v_1, v_2|j_1, j_2) \approx p(j_1, j_2|v_1, v_2). \tag{6.13}$$

Through equation (6.13) we can incorporate the result of equation (6.9) in equation (6.10) in order to find the a posteriori probability of an event in voxel v. $s(\theta)$ is thus no longer the multiplication of two Gaussians evaluated in the upper and lower detection localization as it was in all previous cases. $s(\theta)$ is now replaced by the multiplication of the function $F_{U/D}$ evaluated in the same detection locations. The aforementioned forward model for the detection likelihood can also be extended into three dimensions as figure 6.4(a) and figure 6.4(b) demonstrate. This implies different boxcar functions for both

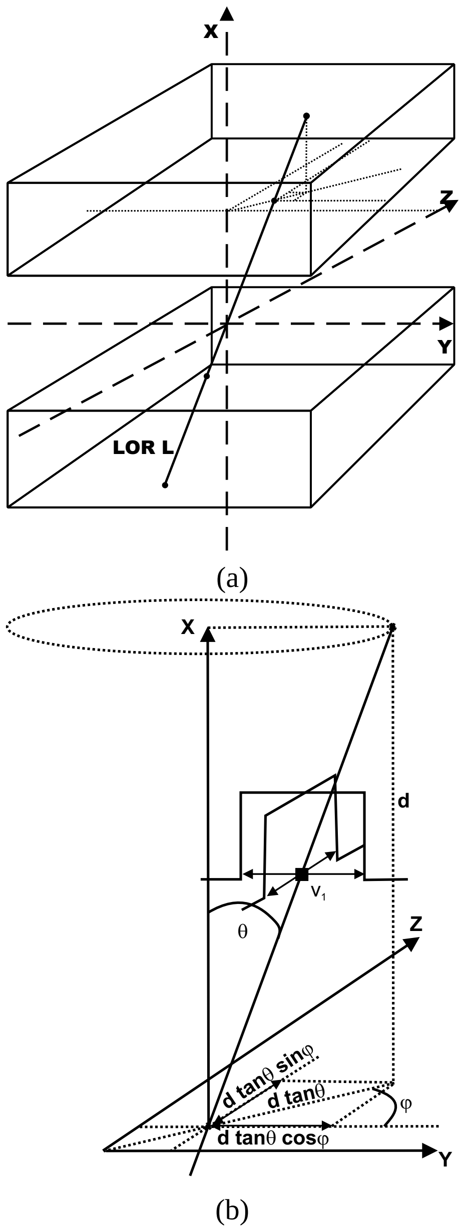

Figure 6.4: (a) Oblique incidences with opposite position of the detector heads: 3D extension, (b) effect of the crystal thickness in both transversal directions.

transversal directions. In the Y-direction the width of the boxcar function is $d \tan\theta \cos\varphi$ and in the Z-direction it is $d \tan\theta \sin\varphi$. After convolution with the respective Gaussians, characterized by σ_{0y} and σ_{0z}, the functions T_{1U}, T_{1D} and T_{2U}, T_{2D} result analogous to F_U, F_D but now for two transversal directions.

$$\begin{aligned}
T_{1U}(y_u) &= \frac{\mathrm{erf}(\frac{y_u + d\tan\theta\cos\varphi}{\sqrt{2}\sigma_{0y}}) - \mathrm{erf}(\frac{y_u}{\sqrt{2}\sigma_{0y}})}{2d\tan\theta\cos\varphi} \\
T_{1D}(y_d) &= \frac{\mathrm{erf}(\frac{y_d}{\sqrt{2}\sigma_{0y}}) - \mathrm{erf}(\frac{y_d - d\tan\theta\cos\varphi}{\sqrt{2}\sigma_{0y}})}{2d\tan\theta\cos\varphi} \\
T_{2U}(z_u) &= \frac{\mathrm{erf}(\frac{z_u + d\tan\theta\sin\varphi}{\sqrt{2}\sigma_{0z}}) - \mathrm{erf}(\frac{z_u}{\sqrt{2}\sigma_{0z}})}{2d\tan\theta\sin\varphi} \\
T_{2D}(z_d) &= \frac{\mathrm{erf}(\frac{z_d}{\sqrt{2}\sigma_{0z}}) - \mathrm{erf}(\frac{z_d - d\tan\theta\sin\varphi}{\sqrt{2}\sigma_{0z}})}{2d\tan\theta\sin\varphi}. \qquad (6.14)
\end{aligned}$$

wherein:

$$\begin{aligned}
y_u &= [(D/2 - p)\tan\theta\cos\varphi + q] - Y_1 \\
y_d &= [-(D/2 + p)\tan\theta\cos\varphi + q] + Y_1 \\
z_u &= [(D/2 - p)\tan\theta\sin\varphi + r] - Z_1 \\
z_d &= [-(D/2 + p)\tan\theta\sin\varphi + r] + Z_1. \qquad (6.15)
\end{aligned}$$

For this threedimensional case the following a posteriori probability results:

$$\begin{aligned}
S(p,q,r) &= \int_{-|\varphi_{min}|}^{|\varphi_{max}|} \int_{-|\theta_{min}|}^{|\theta_{max}|} s(\theta,\varphi) \sin\theta d\theta d\varphi \\
s(\theta,\varphi) &= T_{1U}(y_u) \cdot T_{1D}(y_d) \cdot T_{2U}(z_u) \cdot T_{2D}(z_d). \qquad (6.16)
\end{aligned}$$

6.3 Model analysis

A typical setup was implemented: we chose the FOV to be $25.6 \times 25.6\ cm$ and the distance between the two detector heads was set to 25.6 cm. In all figures the voxel size is accordingly $1 \times 1 \times 1\ mm^3$. The FWHM of the respective Gaussians is set to be 40 mm (factor 10 higher compared to reality) for demonstration purposes as the same conclusions are proven to be valid for realistically chosen values. The crystal is set to 1.9 cm thickness by default. For oblique incidences the LOR was defined by the points of incidence(12.8,5) and (-12.8,-5) while it was (12.8,5,5) and (-12.8,-5,-5) for the threedimensional case.

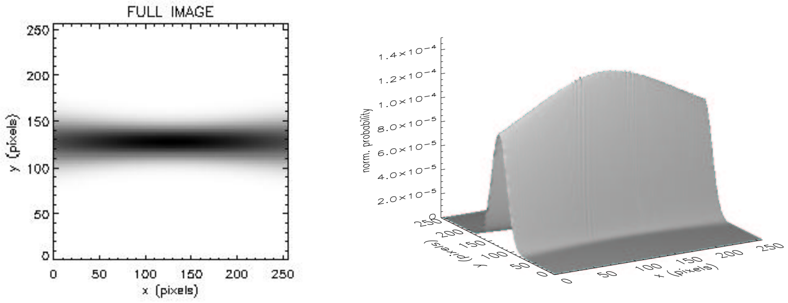

(a) (b)

Figure 6.5: Pdfs for perpendicular incidences and facing detectors (a) FOV,(b) surface plot.

6.3.1 Perpendicular incidences

We implemented the formula described in equation (6.1) and the resulting pdf for the FOV is shown in figure 6.5. We found that the pdf could not be analytically expressed in a closed form, and it was thus calculated by means of numerical integration. We conclude, after verification, that the transversal profiles of this pdf can be represented by a fitted Gaussian. The FWHM of these Gaussians versus the distance from the center of the FOV is shown in figure 6.6 where a quadratic function is concluded. The relative difference between the transversal profile and the fitted Gaussian is of the order of 10^{-3}. These results can also be extended to three dimensions where we implement the formula described in equation (6.2). Figure 6.8(a) and figure 6.8(b) show a twodimensional Gaussian distribution at different distances to the detector as a result of the numerical integration.

6.3.2 Oblique incidences

Analogously with paragraph 6.3.1 we implemented the formulas for oblique incidences of paragraph 6.2.2. The results for the twodimensional case are shown in figure 6.7. Figure 6.7(a) and figure 6.7(b) show the pdf for a crystal with normal thickness of 1.9 cm, while figure 6.7(c) and figure 6.7(d) show the same function for a hypothetical crystal of 30 cm to demonstrate the role of the crystal thickness. These last two figures are only illustrative as it can be expected that the interaction probability uniformity along the photon path is no longer valid at such crystal thicknesses. For thin crystals Gaussians can be fit to the transversal profiles of the pdf. The relative difference in this case is

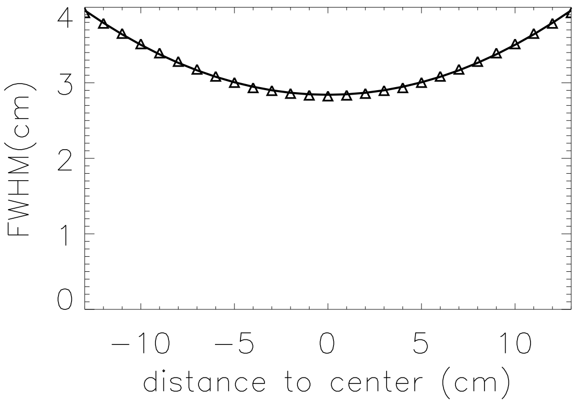

Figure 6.6: FWHM of the fitted Gaussians versus the distance from the center of the FOV (△); quadratic curvefit.

of the order of 10^{-2}. Again the FWHM is minimal in the center and maximal at the detector surface.

This model was also extended into three dimensions, as is shown by figure 6.8(c) and figure 6.8(d) where we evaluate the result at different distances to the detector. Figure 6.8 is illustrated as surface plots in figure 6.9.

6.4 Validation by Monte Carlo simulations

In figure 6.6 we see the FWHM of the Gaussians, fit to the transversal profiles of the pdf for perpendicular incidences. The FWHM is a quadratic function of the distance from the center of the FOV (towards the detector). Since two opposing detectors are in coincidence, the theoretical counting profile for a point source between them is given by the shifted convolution of the two detector response functions [82]. The shifted convolution is performed as follows (figure 6.10):

$$\begin{aligned} f(m) &= \int_{-\infty}^{+\infty} e^{-}\frac{x^2}{2\sigma^2} e^{-}\frac{(x-2m)^2}{2\sigma^2} dx \\ &= \int_{-\infty}^{+\infty} e^{-}4\frac{(x/2)^2}{2\sigma^2} e^{-}4\frac{(x/2-m)^2}{2\sigma^2} dx, \end{aligned} \qquad (6.17)$$

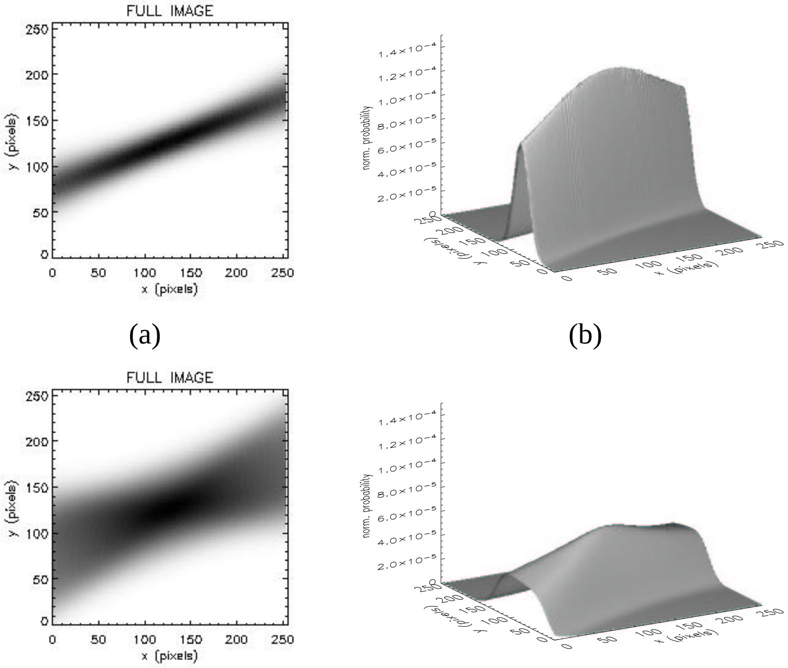

(a) (b)

(c) (d)

Figure 6.7: Pdf for oblique incidences and facing detectors (a) FOV and (b) surface plot: crystal of 1.9 cm thickness; (c) FOV and (d) surface plot: crystal of 30 cm thickness.

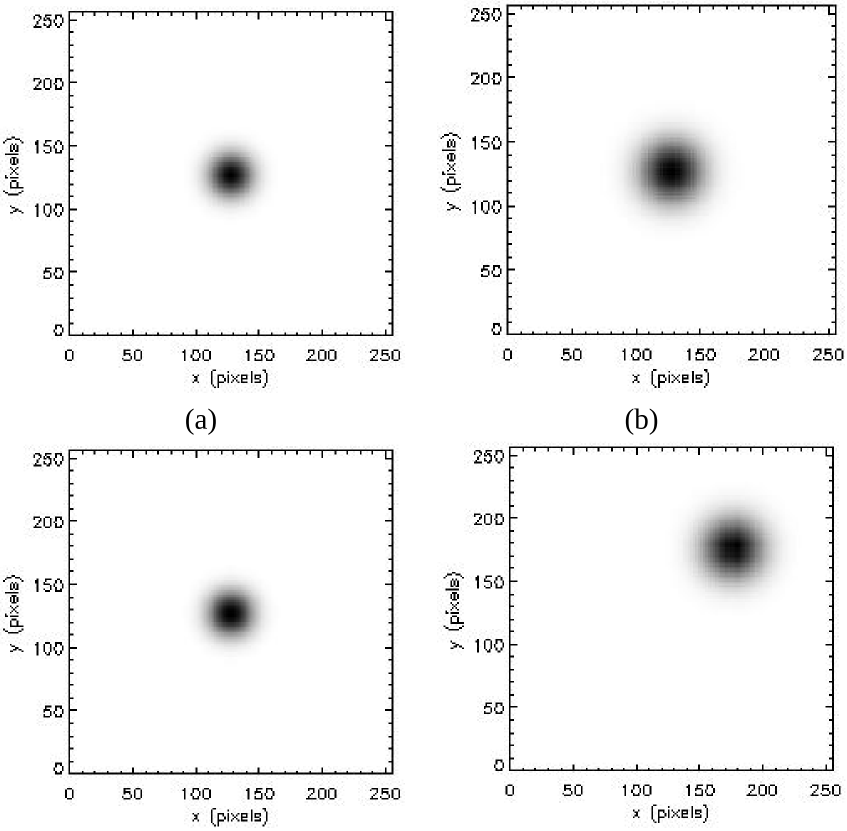

(a) (b)

(c) (d)

Figure 6.8: 3D pdf for perpendicular incidences and facing detectors, (a) pdf in the center of the set up, (b) pdf close to the detector; 3D pdf for oblique incidences and facing detectors, incidence at (12.8,5,5) (c) pdf in the center of the set up, (d) pdf close to the detector.

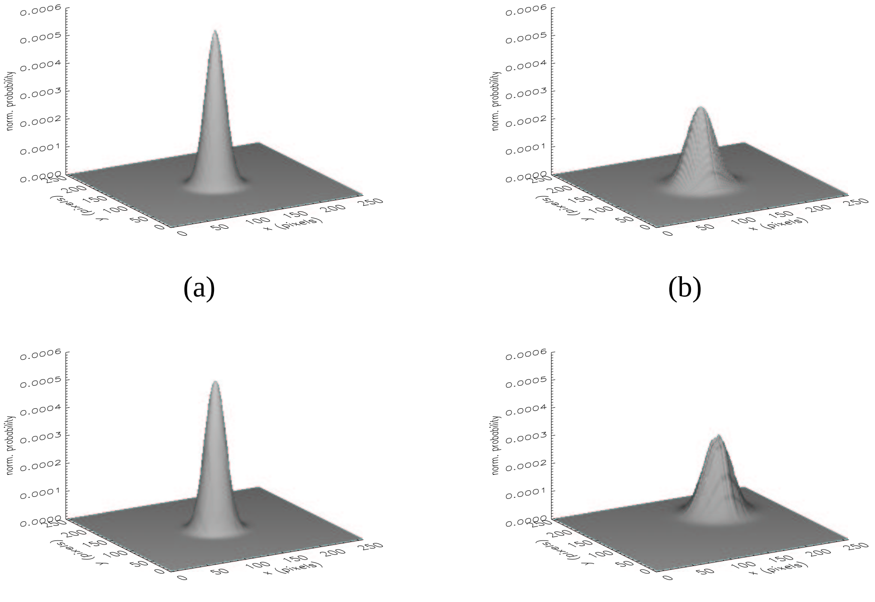

(a) (b)

(c) (d)

Figure 6.9: Surface plot of the 3D pdf for perpendicular incidences and facing detectors, (a) pdf in the center of the set up, (b) pdf close to the detector; 3D pdf for oblique incidences and facing detectors, incidence at (12.8,5,5) (c) pdf in the center of the set up, (d) pdf close to the detector.

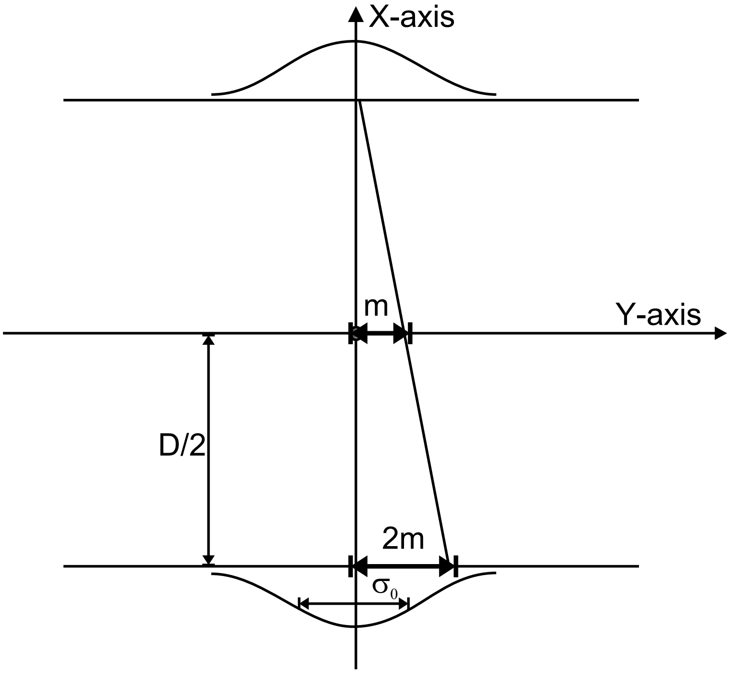

Figure 6.10: Detailed figure in support of the shifted convolution calculation.

if we substitute x by $y = x/2$ then we find:

$$\begin{aligned} f(m) &= 2\int_{-\infty}^{+\infty} e^{-}4\frac{y^2}{2\sigma^2} e^{-}4\frac{(y-m)^2}{2\sigma^2} dy \\ &= 2\int_{-\infty}^{+\infty} e^{-}\frac{y^2}{2(\frac{\sigma}{2})^2} e^{-}\frac{(y-m)^2}{2(\frac{\sigma}{2})^2} dy. \end{aligned} \tag{6.18}$$

Equation (6.18) is the basic formulation of a convolution of two Gaussians of $\sigma/2$. Consequently, the resulting standard deviation is $\sqrt{2}\sigma/2 = \sigma/\sqrt{2}$. For a Gaussian response function with a FWHM of $2\sqrt{2\ln 2}\sigma_{0y}$ this theoretically leads to a Gaussian at the midpoint between the two detectors with a FWHM of $2\sqrt{2\ln 2}\sigma_{0y}/\sqrt{2}$.

This result is confirmed by our analysis. When we approximate $\tan\theta$ in equation (6.1) by its argument θ, which is correct for those small angles, a closed Gaussian expression results for the midpoint of the FOV with a FWHM that was indeed a factor $1/\sqrt{2}$ smaller than on the detectors (integration limits: $\pm 3\sigma_{0y}$):

$$S(0,q) = \frac{\text{erf}(\frac{3D}{2})e^{(\frac{-q^2}{\sigma_{0y}^2})}}{\sqrt{\pi}\sigma_{0y}D}. \tag{6.19}$$

Equation (6.19) refers to this result, q being the distance along the detector. In the argument of the exponential function we see indeed σ_{0y}^2 which causes a FWHM that is a factor $\sqrt{2}$ smaller than the Gaussian distribution, $e^{-q^2/2\sigma_{0y}^2}$ on the detector. The FWHM at the detector and in the center of the FOV are thus known so that we can conclude that the FWHM can be expressed as follows, thereby using the quadratic relation shown in figure 6.6:

$$2\sqrt{2\ln 2}\sigma = (2/D)^2 2\sqrt{2\ln 2}\sigma_{0y}(1 - 1/\sqrt{2})p^2 + 2\sqrt{2\ln 2}\sigma_{0y}/\sqrt{2}. \tag{6.20}$$

In equation (6.20) p denotes the distance towards the detector.

We confirm these results for our basis formula of equation (6.1) (which forms the fundaments for all further developed theories) by the use of geometric Monte Carlo simulator [124]. We used this simple and fast Monte Carlo simulator implemented in C to evaluate the mathematical model. It was designed for gamma camera PET simulations making it appropriate for this continuous detector study. The detector response function was chosen according to our model and no attenuation or scatter were included. Figure 6.11 shows the results of this geometric Monte Carlo evaluation where the simulated and calculated FWHM of the Gaussians, fit to the transversal profiles of the probability density function, are plotted against the distance from the center of the setup. It can be concluded that the theoretical model performs well.

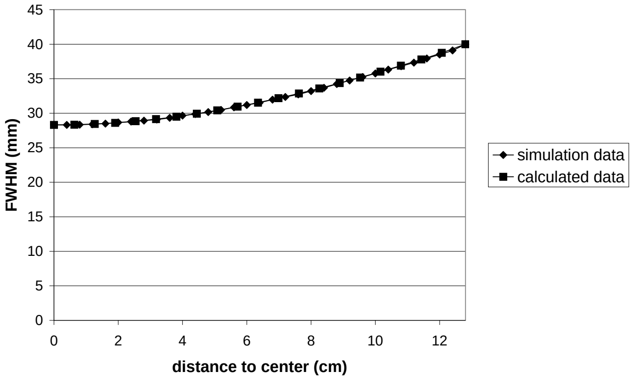

Figure 6.11: Monte Carlo validation of the theoretical model: comparison of FWHM.

To verify the validity of the interaction uniformity assumption for oblique incidences, we performed Monte Carlo simulations of different setups to evaluate the photon's probability of interaction when passing through different crystals at different energies. We studied analogous features for PET detector materials in another context already in section 4.3.1 and the required results will be reapeated in this section. The simulations were done using GATE and the most important components of the scintillation camera were modeled; moreover photoelectric effect, Compton and Rayleigh scatter are included in the gamma transport process. For photons of 140 keV entering a 19 mm NaI crystal we found the DOI to be exponentially decreasing as is shown in figure 6.12(a). Only the photons that were eventually detected in the photopeak energy window were registered. The photons can deposit their total energy in the crystal after one photoelectric interaction or they can undergo multiple Compton scattering processes with the same result. Figure 6.12(a) shows that for this photon energy of 140 keV the main contribution comes from the photoelectric effect. This is confirmed by figure 6.12(c). For PET applications however the photon energy is 511 keV. Figure 6.12(b) shows that for an incident photon energy of 511 keV on a 19 mm NaI crystal, the main contribution comes from multiple Compton scattering. We can conclude that the Compton build up effect is the determining factor here, causing the DOI profile to be completely different and more uniform. Figure 6.12(c) confirms this as the cross section for Compton effect is clearly higher at 511 keV than the cross

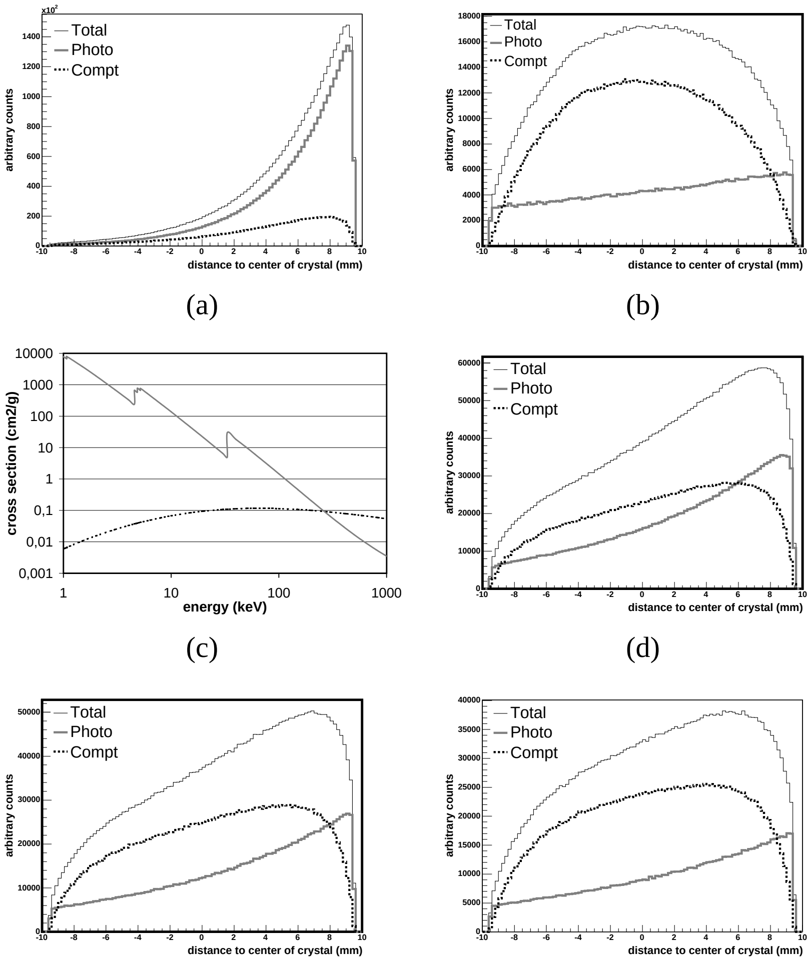

(a) (b)

(c) (d)

(e) (f)

Figure 6.12: Depth of interaction, front of the crystal at +9.525mm: (a) 140 keV photons on a 19 mm NaI crystal, all events registered in 15 % photopeak window around 140 keV; (b) 511 keV photons on a 19 mm NaI crystal, all events registered in 30 % photopeak window around 511 keV; (c) cross sections for NaI; (d) 511 keV photons on a 19 mm BGO crystal, all events registered in 30 % photopeak window around 511 keV; (e) 511 keV photons on a 19 mm LSO crystal, all events registered in 30 % photopeak window around 511 keV; (f) 511 keV photons on a 19 mm GSO crystal, all events registered in 30 % photopeak window around 511 keV.

section for photoelectric interaction. Due to the low cross section for photoelectric effect at this energy the sensitivity of the crystal is lower than for 140 keV photons (optimal sensitivity for 19 mm NaI) causing less detections to be registered. The expected exponential decay of beam particles after photoelectric absorption can be approximated in first order by a linear curve. Results are shown in figure 6.12(d) for BGO, in figure 6.12(e) for LSO and in figure 6.12(f) for GSO. The same conclusion can be made regarding the Compton build up. These simulated DOI curves could also be incorporated into the theoretical model as an extra, crystal and energy dependent, parameter without having to perform the aforementioned simplification. A validation of this against experimental data is still needed. We believe however that the variation on the width of the Gaussians will appear to be more important than the discrepancy on the DOI uniformity approximation for the derived theoretical model. These variations on the FWHM are probably due to the positioning of the PMTs which are determining in the Anger logic of the readout.

6.5 Reconstruction: resolution recovery

The theoretical model described above can be incorporated in a reconstruction algorithm in order to enhance the spatial resolution of the resulting reconstructed images. Two possible approaches for incorporation into reconstruction will be discussed. The first approach is incorporation of this model into an iterative listmode Maximum Likelihood Expectation Maximization (MLEM: section 2.1.6) algorithm. In this case, not only the voxels intersected by the LOR are accounted for but also the voxels within the reach of the pdf due to the detection uncertainty. This raises some difficulties: either the numerical integral has to be calculated on the fly or a lookup table for the pdf values has to be present. Calculation of the integral during the reconstruction is not feasible due to computer limitations. For the lookup table one has to use symmetrical basis functions to parametrize the image as otherwise the contribution of a certain voxel becomes dependent on the LOR orientation which would lead to a very large lookup table. Figure 6.13 demonstrates LOR-orientation dependency if the image is parametrized by pixels: the gray part is additional for a LOR with another orientation at the same distance from the center of the pixel. When using radially symmetric basis functions as, for instance, blobs, the contribution of each voxel is only dependent on the distance between the LOR and the center of that particular voxel, whatever the orientation of the LOR is. The second, more elegant approach, consists of using natural pixels [59]. Here, discrete projections are related to the continuous image distribution function by a spatially varying photon distribution function that models the geometric

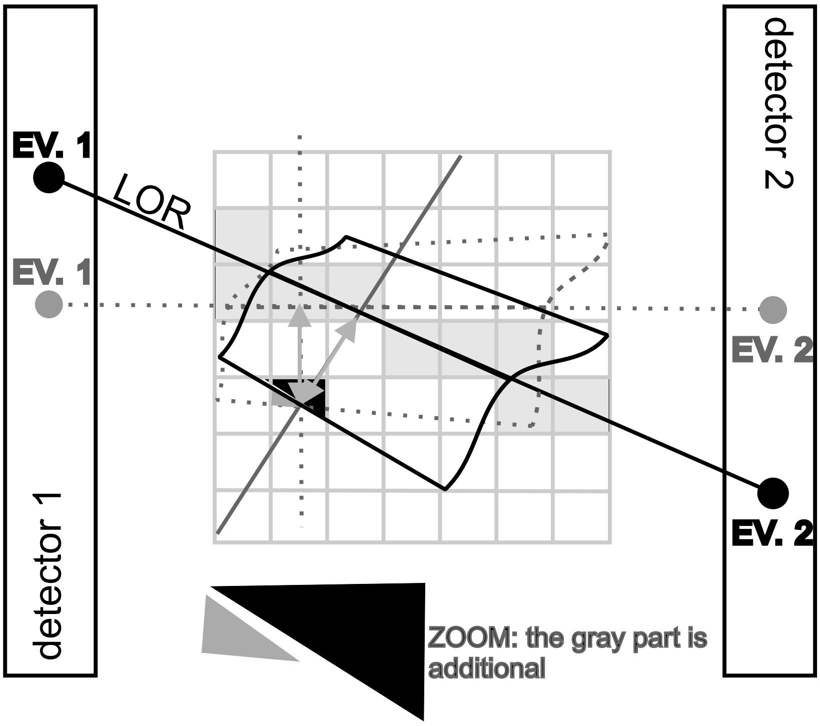

Figure 6.13: Voxel contribution within pdf range dependent on LOR orientation.

response of the detector which should be Gaussian based in this case. This will be discussed in detail in Chapter 7.

6.6 Conclusion + original contributions

We have deduced a theoretical model for incorporation of the detection location uncertainty in continuous detector PET. Perpendicular and oblique incidences were studied in two and three dimensions. In each case we centered a one- or twodimensional Gaussian on the actual detection location to model this uncertainty in the forward problem of acquisition. To calculate the a posteriori probability of an event in a certain voxel v we then integrated all possible LORs through that point, weighted with the appropriate end point detection likelihood. The resulting a posteriori probability density function could not be analytically expressed in a closed form and was thus calculated each time by means of numerical integration. We found that the transversal profiles could be approximated by Gaussians, for perpendicular incidences with an error of 0.1$\%$, while an error of 1$\%$ resulted for oblique incidences on a thin crystal detector. We then verified these results by means of theoretical predictions and geometric Monte Carlo simulations and a very good agreement was reached. Moreover, we deduced a formula that expresses the FWHM of the Gaussian fits as a function of distance to the center of the setup. When dealing with oblique incidences on thicker crystals we found that the depth of interaction of a photon was also contributing to the detection uncertainty. Based on literature we assumed the detection probability of a 511 keV photon through the crystal to be uniform and thus proportional to its path length. We incorporated this into our theoretical model and reached an analytical expression for the function that should replace the traditional Gaussian for the detection uncertainty. The resulting pdfs were then calculated by means of numerical integration using these new weighting functions. All assumptions made, were validated through Monte Carlo simulations. After verification it became clear that this model is valid for incorporation in a reconstruction algorithm in order to more accurately model the acquisition process and to improve the spatial resolution of the tomographic images. This model can also be used to calculate the spatial resolution of systems that are still in design which proves its multiple usefulness.

To our knowledge this is the first theoretical LOR model for a continuous detector PET system accurately incorporating the detection uncertainty of the annihilation photons as a function of distance to the detector heads. This work resulted in a peer reviewed journal article [103] and in 2 publications in the proceedings of international conferences [100, 101].

Chapter 7

Monte Carlo based reconstruction

In parallel hole collimator **SPECT**, image reconstruction is usually performed as a set of 2D analytical or iterative reconstructions. This ignores the intrinsic 3D nature of the scatter process. Approximate analytical models to account for scatter have been proposed [6, 8, 9, 11]. To explicitly deal with the 3D nature of the image formation process, a simulated 3D projector modeling the 3D photon spread and thus including all image degrading effects (attenuation, scatter and camera point spread function) can be used [39, 40] in a fully 3D reconstruction algorithm. Monte Carlo based reconstruction for **PET** is particularly interesting to perform an intrinsic resolution recovery and to incorporate (inter)crystal scatter.

7.1 Dedicated Monte Carlo based reconstruction for SPECT application

It was pointed out in chapter 4 that the Beacon attenuation image is often degraded near the center of large patients when the transmission acquisition is performed simultaneously or sequentially with a medium energy emission study. This is due to the fact that the ^{133}Ba sources have to form an image through the collimator of the opposite detector head, which has thick septa in a medium energy emission setup. In chapter 4 we showed that, in this particular case, it would be highly recommendable to replace the MEGP collimators by the LEHR variants for a large range of medium energy sources if one could recover the increased photon spread on this LEHR collimator. We therefore implemented a dedicated solution that accounts for this issue, as will be dis-

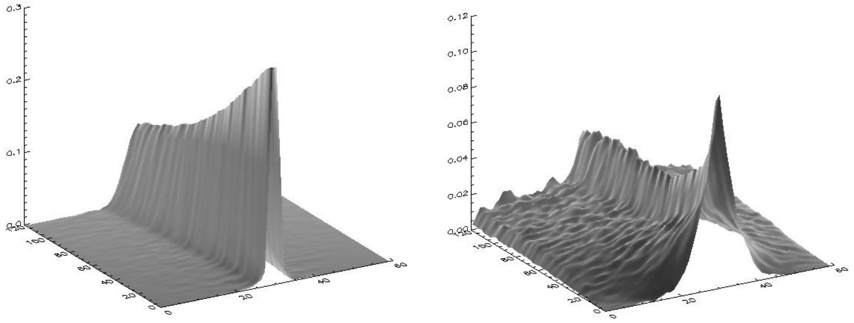

(a) (b)

Figure 7.1: Detector response : (a) one-dimensional averaged system response for 128 planes parallel to the detector and for a MEGP setup, (b) one-dimensional averaged system response for 128 planes parallel to the detector and for a LEHR collimator setup.

cussed hereafter.

7.1.1 Implementation

Our approach consists of simulating a three-dimensional system matrix for each possible setup incorporating all image degrading effects: fluorescence, scatter and penetration in the collimator, intrinsic crystal resolution, etc. Each element of the system matrix denotes the probability that an emission from a certain voxel is detected in a particular projection bin. This system matrix is recalculated afterwards in the detector response function which is the system response averaged over all possible FOV locations in a plane at a certain distance to the detector and which includes all image degrading effects in three dimensions. The aforementioned system response is based on the relative difference in detection and emission location. To incorporate this detector response in the reconstruction, a two-dimensional function for each distance to the detector was applied in the forward projection step of the Maximum Likelihood Expectation Maximization (MLEM) algorithm. This two-dimensional function represents the averaged response of the system as discussed above, and depends on the energy of the isotope. An example is shown in figure 7.1. Figure 7.1(a) shows the detector response in one dimension for 128 planes parallel to the detector and for medium energy photons (245 keV) on a MEGP collimator while figure 7.1(b) shows the severe penetration for the same photons on a LEHR collimator. To limit the storage size of our system matrix and to solve the projector noise problems described in [22], the simulated system matrix can be used in a natural pixel based reconstruction or the image matrix can be bilinearly rotated. If applying a rotator [134], then a matrix perpendicular to the detector is obtained for each projection angle so that the above discussed detector response blur can be applied. In the latter way it remains possible to include attenuation in the reconstruction which is not the case at first sight for natural pixel based reconstruction as will become clear in section 7.2.

Downside of this approach is the computation time necessary to generate the system matrix. An elegant implementation was obtained however on a minicluster of 17 dual processor Intel Xeon 2.4GHz nodes that allows to calculate the Monte Carlo information for each possible setup overnight.

7.1.2 Recovery of ME on LEHR photon spread

Figure 7.2 shows the reconstruction of a 1 cm point source at 30 cm distance, filled with a 300 keV emission source, after Monte Carlo simulated acquisition using a LEHR collimator. Figure 7.2(a) is a traditional parallel projection MLEM reconstructed image while figure 7.2(b) is reconstructed incorporating the three-dimensional Monte Carlo detector response as discussed in 4.2.1. A Gaussian was fit to the profiles of both images and for figure 7.2(a) a Full Width at Half Maximum (FWHM) of 22.6 mm results. The trend lines of figure 3.11 showed in Chapter 3 that the resolution should not be more than 14.3 mm when no photon penetration is allowed by the LEHR collimator and when no resolution recovery is applied in the reconstruction. As was expected the LEHR collimator performs suboptimally for these medium energy photons. If the Monte Carlo detector response is incorporated it should hypothetically be feasible to recover the extrinsic resolution at that distance and also the intrinsic spatial resolution of the camera (3.3 mm). The FWHM of the Gaussian fit of figure 7.2(b) returns a value of 9.3 mm which is the original size of the point source (1 cm) within the error bars of the curve fit. This is summarized by figure 7.3 which demonstrates the succesful resolution recovery of the Monte Carlo based reconstruction.

The validation of this method was extended towards other energy ranges and towards other phantoms and collimators as will be discussed below. The acquisition of three 1 cm point sources, separated by 2 cm and with an activity ratio of 1:2:6 was simulated, all three sources were placed at 30 cm from the collimator. Figure 7.4 shows the results for photons of 170 keV while figure 7.5 shows the analogous images for photons of 245 keV, both on a high intensity scale.

The image of figure 7.4(a) shows the traditional parallel projection recon-

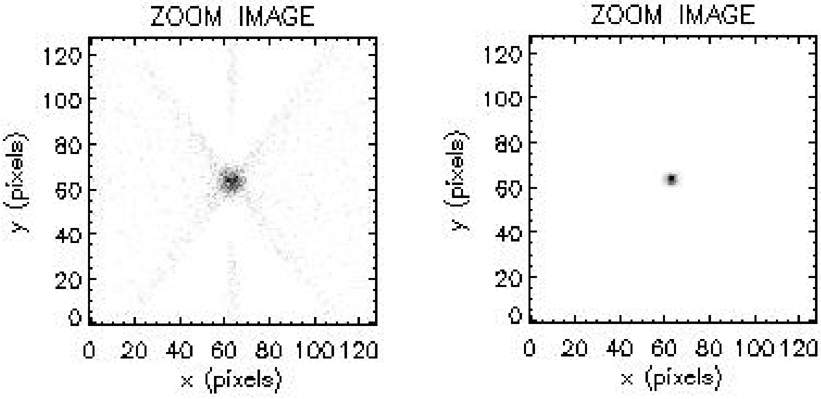

(a) (b)

Figure 7.2: Reconstructed images (axial view) of a 300 keV medium energy point source. The detector is mounted with a LEHR collimator: (a) parallel projection MLEM, (b) Monte Carlo based MLEM.

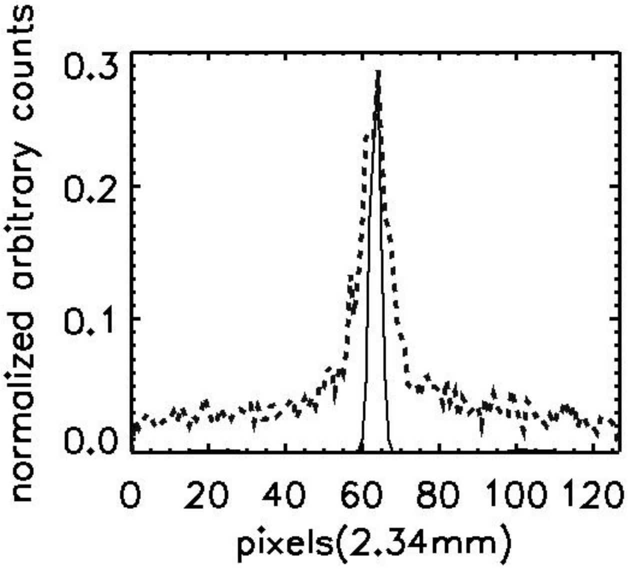

Figure 7.3: Reconstructed images of a 300 keV medium energy point source. The detector is mounted with a LEHR collimator: FWHM parallel projection MLEM (dotted line), FWHM Monte Carlo based MLEM (full line).

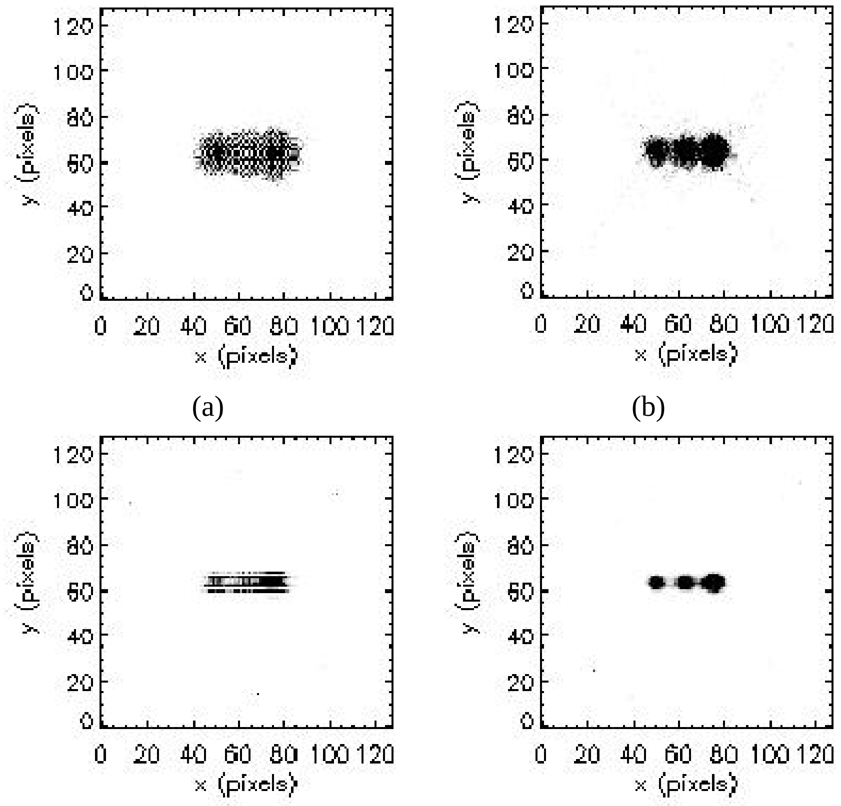

(a) (b)

(c) (d)

Figure 7.4: Reconstructed images (axial view-high intensity scale) of a 170 keV medium energy point source phantom: evaluation of reconstruction performances for LEHR and MEGP collimator: (a) MEGP collimator and parallel projection MLEM, (b) LEHR collimator and parallel projection MLEM, (c) MEGP collimator and Monte Carlo based MLEM, (d) LEHR collimator and Monte Carlo based MLEM.

struction on the appropriate MEGP collimator while figure 7.4(b) shows the same reconstruction on a LEHR acquisition. Figure 7.4(c) and (d) show the reconstructions with Monte Carlo information for a MEGP collimator, and a LEHR collimator setup. The image of figure 7.4(a) is suboptimal due to the limited spatial resolution caused by the large hole openings of the MEGP collimator (0.170 cm inner radius) and due to the 0.0864 cm septal thickness. This inferior spatial resolution is also shown in figure 3.11, compared to a LEHR collimator. Figure 7.4(b) is suboptimal due the substantial photon penetration, caused by the 0.0203 cm low septal thickness of the LEHR collimator. Figure 7.4(c) shows the Monte Carlo based reconstruction for a medium energy isotope on an appropriate MEGP collimator. This image is also suboptimal due to the fact that the averaged Monte Carlo generated system response can not account for the individual positions of the large MEGP collimator holes, which causes artefacts in the resulting image. Finally, Monte Carlo based reconstruction of a medium energy isotope data set acquired on LEHR collimators, results in an optimal reconstructed image of the phantom setup as is shown in figure 7.4(d). The method performs a valid resolution recovery resulting in higher quality images. Figure 7.5 analogously demonstrates that the above discussed conclusions are still valid for higher energy isotopes which was already predicted by figure 7.2. Figure 7.5(b) clearly shows the four streak artefacts caused by photon penetration on the LEHR while figure 7.5(d) shows a magnified version of the resulting reconstructions after incorporation of Monte Carlo information and also shows the appropriate resolution recovery.

The aforementioned reconstruction implementation is computationally demanding since the detector response, which also comes at a computational cost, has to be applied for each detection angle in each iteration step. However, the PC's graphics board provides a cost-effective means for an efficient implementation. GPUs have been used for computed tomography recently since manufacturers now provide high point precision and a larger instruction set [136, 138, 139]. Ongoing research is being performed and future research is scheduled within our group to implement this repetitive detector response blurring on a GPU.

7.2 Natural Pixel based reconstruction for PET

A number of algorithms have been proposed for reconstructing 3D PET data. An early approach that has been implemented on a number of clinical scanners is the analytic 3D reprojection (3DRP) algorithm [69]. Another commonly used approach is rebinning (FORE) which involves converting the 3D data to a 2D set [35], and then reconstructing using a 2D algorithm. One disadvantage

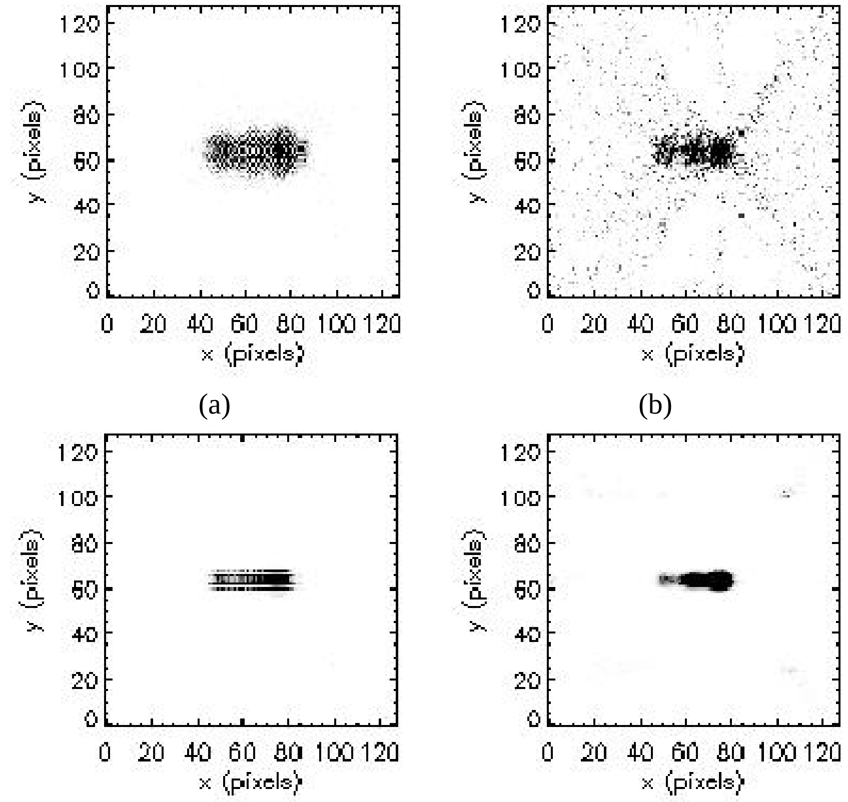

(a) (b)

(c) (d)

Figure 7.5: Reconstructed images (axial view-high intensity scale) of a 245 keV medium energy point source phantom: evaluation of reconstruction performances for LEHR and MEGP collimator : (a) MEGP collimator and parallel projection MLEM, (b) LEHR collimator and parallel projection MLEM, (c) MEGP collimator and Monte Carlo based MLEM, (d) LEHR collimator and Monte Carlo based MLEM.

of both the 3DRP and FORE methods is that these algorithms are derived using the assumptions that measured data correspond to line integrals through the unknown activity distribution. There are a number of physical effects however that invalidate this assumption, including: positron range, gamma-gamma non-collinearity, spatially variant geometric efficiency, crystal scatter and (inter-)crystal penetration. All of these degradations contribute to the spatially variant detector response that reduces spatial resolution if not accounted for. In chapter 4 we discussed the influence of crystal scatter in several detector materials and the main conclusion was that correction in the reconstruction for crystal scatter is imperative for resolution recovery. In chapter 6 we derived an analytical model for the detector response. This clearly demonstrated the inaccuracy of line integrals and proposed Gaussian tubes with varying width, depending on the distance to the detector. A necessary correction in the reconstruction for intrinsic detection resolution and crystal penetration was concluded. These effects can accordingly be included in an iterative reconstruction by fully simulating the system matrix. Unfortunately, due to the large number of scintillation crystals present in current PET scanners, this system matrix can be very large, typically 3×10^{14} elements. Natural pixel based reconstruction allows to account for all image degrading effects through Monte Carlo simulation and limits the storage size of the system matrix by exploiting the symmetries present in PET. This will be discussed hereafter.

We recently filed a multiyear project on this reconstruction technique decsribing the fundamentals and the expected resolution recovery. Next to discussing the work in progress using preliminary results, section 7.2 will also line out the future reserach topics that resulted from this manuscript.

7.2.1 Theoretical background and geometrical results

Natural pixels

The relationship between the measurement g_i of a detector pair in a PET scanner and the continuous object to be imaged $f(x,y,z)$ can be described using a spatially variant detector response function $h_i(x,y,z)$

$$g_i = \int_{FOV} f(x,y,z)h_i(x,y,z)dxdydz, \tag{7.1}$$

where $h_i(x,y,z)$ describes the probability that a positron emitted at location (x,y,z) is detected in detector pair i. Thus the PET reconstruction problem is to estimate the continuous object $f(x,y,z)$ given a measured set of data g_i. The conventional approach to formulating this problem is to approximate $f(x,y,z)$ by the linear combination of J cubic voxel basis functions, denoted here by $c_j(x, y, z)$ where the subscript j refers to the j^{th} basis function. With these voxel basis functions, the object can be approximated by:

$$\tilde{f}(x, y, z) = \sum_{j=1}^{J} \tilde{f}_j c_j(x, y, z), \tag{7.2}$$

where $\tilde{f}_j$ are coefficients that weight each object voxel. In this formulation, $\tilde{f}(x, y, z)$ is substituted in Eq. 7.1 for $f(x, y, z)$ and the reconstruction problem becomes finding the estimate of the cubic voxel weighting coefficients$\tilde{f}_j$. The PET data measurement process can then be expressed as:

$$\tilde{g}_i = \sum_{j=1}^{J} a_{i,j} \tilde{f}_j, \tag{7.3}$$

where

$$a_{i,j} = \int_{FOV} h_i(x, y, z) c_j(x, y, z) dxdydz \tag{7.4}$$

is the contribution of the j^{th} voxel to the i^{th} detector pair. Eq. 7.3 can be written in matrix-vector form as:

$$\tilde{g} = A\tilde{f}. \tag{7.5}$$

The tomographic problem can also be described using a reconstruction model with natural pixel image basis functions [7,19,54,59]. These natural pixels are formed using the detector sensitivity functions naturally provided by the PET scanner. In this approach, the estimated reconstruction is constrained to be a linear combination of basis functions $h_j(x, y, z); j = 1 \ \ldots \ J$, which are the probability density functions of the detector pairs:

$$\tilde{f}(x, y, z) = \sum_{j=1}^{J} q_j h_j(x, y, z). \tag{7.6}$$

Substituting $\tilde{f}(x, y, z)$ into Eq. 7.1 for $f(x, y, z)$ gives:

$$\begin{aligned} g_i &= \sum_{j=1}^{J} q_j \int_{FOV} h_j(x, y, z) h_i(x, y, z) dxdydz, \\ g_i &= \sum_{j=1}^{J} M_{ij} q_j, \end{aligned} \tag{7.7}$$

where

$$M_{ij} \quad = \quad \int_{FOV} h_j(x,y,z)h_i(x,y,z)dxdydz. \tag{7.8}$$

M_{ij} is refered to as a natural pixel matrix. Note that because the final estimate of the object has to be represented in terms of voxels, Eq. 7.6 can be written in matrix-vector form as $\tilde{f} = A^T q$. Instead of solving for $\tilde{f}$ using the inverse problem of Eq. 7.5, one can also solve the inverse problem of Eq. 7.7 which can be expressed in matrix-vector form as:

$$g \quad = \quad Mq. \tag{7.9}$$

The solution of this inverse problem $\tilde{q}$ is a representation of the object in projection space. The backprojection of $\tilde{q}$ ($= A^T q$) then results in the estimate of the object $\tilde{f}$. By using this approach with natural pixels, one avoids the discretization of the object into a predefined voxelized grid until the final step $(A^T q)$. The object is represented by a sum of natural basis functions and the elements of the matrix M are the natural pixel values. An element at row i and column j in the matrix M represents the natural pixel formed by the intersection of LORs i and j. For a perfect imaging system this would be the intersection of two parallel strips and the natural pixel value would be the area of the intersection. However, it is well known that PET scanners do not measure strip integrals. For example we have shown in chapter 6 that for continuous detector PET these strips are better modeled as Gaussian weighted tubes with distance-dependent width. Figure 7.6(a) shows the response (in 2D) from two detector pairs in a 2D PET ring scanner. This hypothetical scanner only has 20 detector pairs and only geometrical effects are considered (the physics of the photon transport: light spread, Anger logic, crystal scatter, crystal penetration are not modeled). The integral over the product of these two response functions gives the natural pixel value, which is one element in the matrix M. The resulting matrix M for this hypothetical design is shown in Figure 7.6(b). It is important to note that the matrix M is block-circulant. A block-circulant matrix is one in which all block columns are simply shifted versions of the first block column. The block-circulant property arises due to the rotational symmetry of the basis functions and the ring detector geometry. Accordingly, the block-circulant feature obtained by a natural pixel basis implies that the system matrix for ring PET scanners can be stored with substantially less memory requirements than with conventional voxel basis functions.

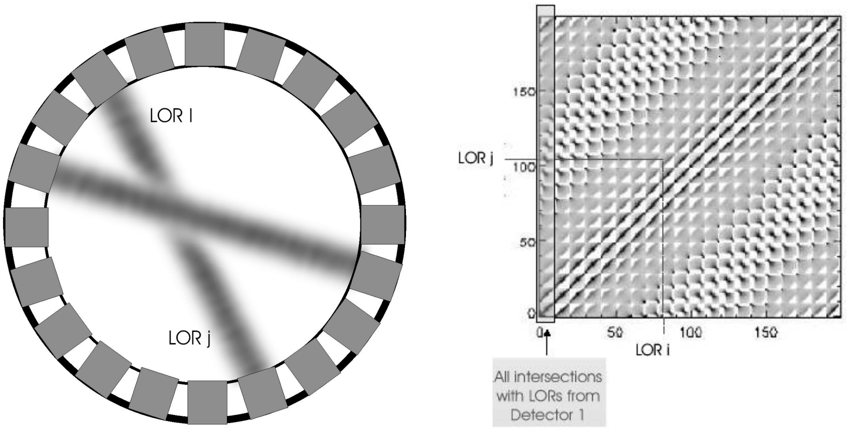

(a) (b)

Figure 7.6: (a) calculation of the natural pixel value formed by LOR i and LOR j. The gray value of the non-uniform strips is the probability that a detection in a LOR originated at a certain point in the FOV, (b) matrix M containing the natural pixel values for a PET ring with 20 detectors. Each detector combines with 10 detectors on the opposite side of the ring. This results in 200 possible LORs.

Generalized natural pixels

The largest computational burden with the natural pixel reconstruction discussed above, is the final backprojection operation: $A^T q$. Therefore we propose to use a generalized natural pixel basis, which is formed by the combination of a different projection and backprojection operator. A fast and efficient backprojector that we propose is a parallel geometry strip backprojector in 2D or a square tube in 3D. The desired solution is now constrained to be a sum of these parallel square tubes at different angles:

$$\tilde{f}(x,y,z) \quad = \quad \sum_{j=1}^{J} q_j b_j(x,y,z). \tag{7.10}$$

Substitution of Eq. 7.10 into Eq. 7.1 gives another expression for the matrix M'_{ij}:

$$\begin{aligned} g_i &= \sum_{j=1}^{J} q_j \int_{FOV} b_j(x,y,z) h_i(x,y,z) dxdydz, \\ g_i &= \sum_{j=1}^{J} M'_{ij} q_j, \end{aligned} \tag{7.11}$$

where

$$M'_{ij} = \int_{FOV} b_j(x,y,z)h_i(x,y,z)dxdydz. \tag{7.12}$$

M'_{ij} is referred to as the generalized natural pixel matrix. Once this matrix is determined, the estimate of the object can be computed by solving the inverse problem of Eq. 7.11 with ART (section 2.1.6) which has fast convergence, and then backprojecting q using the fast inverse Radon transform (Radon transform=R_{2D}) in this case since $M' = AR^T_{2D}$ and $\tilde{f} = A^T\tilde{g} = A^T M' q = R^T_{2D} q$. The parallel sinogram q can be compared to a ramp filtered sinogram which is well known from FBP (2.1.6). It does however take into account the discrete nature of the detection process and the detector sensitivity functions. This is not the case for FBP which is derived from a continuous detection model and is based on a line integral approximation. M'_{ij} was simulated by using a cylinder filled with a uniform distribution of ^{18}F introduced into the FOV of a simulated PET scanner. A Monte Carlo method is then used and a randomly located annihilation is detected at a certain detector pair i. A second LOR is then projected from the same emission location towards the detectors oriented in a parallel geometry (figure 7.7). This second step is simply the Radon transform of a point object at the emission location and a random angle in the parallel projection geometry. To increase computational efficiency, the Radon transform of this point object for all discrete angles can be computed at once. Thus a value of one is added to the elements in M'_{ij} for LOR i and all locations j for which the point location projects into the parallel geometry (figure 7.7). Using Monte Carlo simulations to obtain this matrix M'_{ij} allows to incorporate all image degrading effects and avoids having to analytically model the detector sensitivity functions. Another possibility to estimate the system matrix is to measure it on a real PET system by moving a source throughout the field of view using computer driven motion control. A number of problems arise in this approach; the major ones being the prohibitively large memory required to store the response and the long measurement time to move the voxel throughout the FOV which can possibly be overcome by using filled squared tubes with the same shape and dimensions as the parallel geometry square tubes described in Eq. 7.10.

7.2.2 Enhancements by using GATE

The possibilities of this new reconstruction method were explored by generating M'_{ij} using a Monte Carlo simulator incorporating only geometrical effects (sampling). Recent work by our group [125, 126, 131] showed that there was a

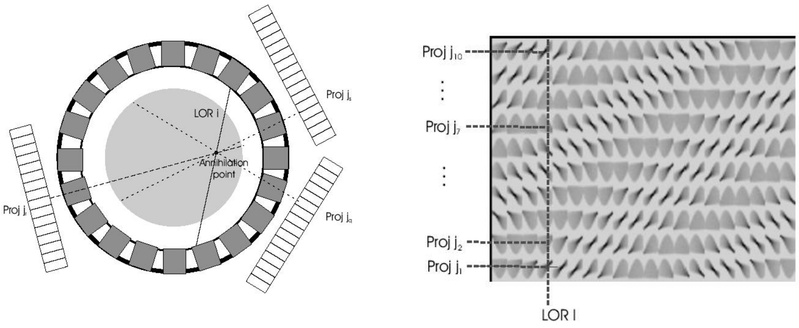

(a) (b)

Figure 7.7: (a)Monte Carlo generation of matrix $M^{'}$ for a PET ring with 20 detectors and a virtual parallel projection system: FOV is filled with uniform activity, (b) an element at each projection angle is updated with one. The matrix is only square if the number of projections equals the number of LORs.

resolution improvement by the generalized natural pixel reconstruction, compared to a standard list-mode MLEM-algorithm. This appeared to be valid both for centered and off-center point sources. The average resolution improvement was about 1 mm. The only point where MLEM outperformed generalized natural pixel reconstruction was at the edge of the FOV where there is no longer complete data available. Also, the variance on 10 different natural pixel based reconstructions is shown to be clearly lower than for 10 MLEM reconstructions. The noise evaluation was performed at equal resolution using a Gaussian postfilter. Finally, the generalized natural pixel based reconstruction also outperformed MLEM on hot spot detectability for a signal known exactly task as higher areas under the ROC-curve were obtained for natural pixel reconstruction. These results were obtained using a simple Monte Carlo simulator only incorporating geometric effects. More powerful resolution recovery can be obtained by generating $M_{ij}^{'}$ using GATE. That will allow to incorporate effects as : positron range, gamma-gamma non-collinearity, Anger logic, and optical photon spread. Moreover, we showed in chapter 4 and in chapter 6 that crystal scatter and crystal penetration respectively, are the determining contributions in detector sensitivity functions, especially for low stopping power detector materials. This is demonstrated with GATE in figure 7.8 which accounts for geometrical effects, crystal scatter and crystal penetration. All other degradations were ignored. Already at first sight, a clear broadening for oblique incidences can be noted. We believe this proves that Monte Carlo based (generalized) natural pixel reconstruction is one of the most elegant and powerful

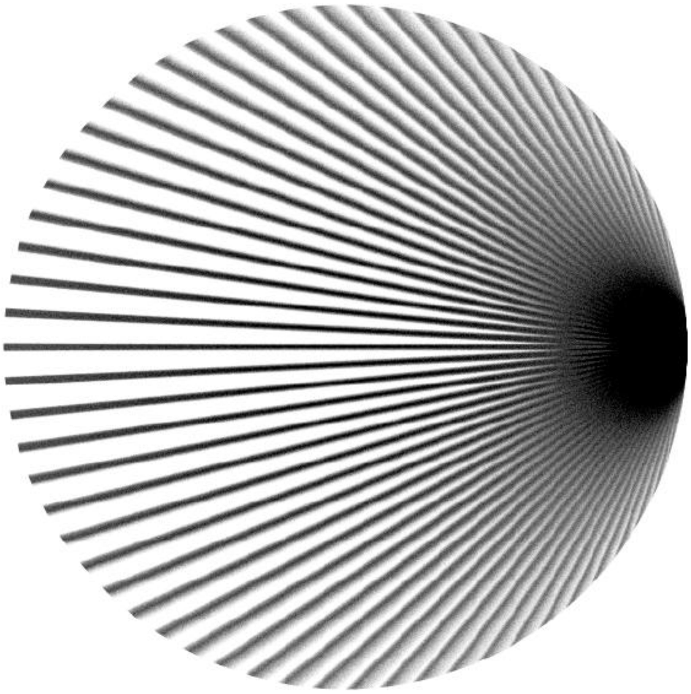

(a)

Figure 7.8: Simulated responses for BGO 2D PET scanner (7 mm large): no position blurring, only crystal scatter and crystal penetration.

ways to incorporate image degrading effects into the reconstruction using only a limited storage size by exploiting the intrinsic symmetries.

7.3 Conclusion + original contributions

Chapter 4 showed that a Beacon attenuation image is often degraded near the center of large patients in a medium energy emission study and that it would be recommendable to replace the MEGP collimators by the LEHR variants if a recovery for the increased photon spread is implemented.

We described an approach that derives the detector response from a fully 3D simulated system matrix, for medium energy studies on low energy collimators in order to replace the MEGP collimators by the LEHR variants. We incorporated this detector response in a dedicated Monte Carlo based reconstruction that accurately recovers the medium energy isotope photon spread on a LEHR. This recovery performance is inferior for the MEGP collimator where the individual hole positions become important given their size, since this is not accounted for in the averaged system response. In all cases the reconstruction of medium energy isotopes on LEHR gives the best result, provided that the detector response is fully simulated and incorporated. Since the market of miniclusters is rapidly gaining importance in the scientific community and is becoming affordable we believe this approach to be useful in protocol optimization, and reconstruction technique examination for the medium energy studies discussed above. We believe to have derived a very important guideline for transmission imaging in a medium energy emission study. This work resulted in a peer reviewed journal publication [106]. The influence of the resolution recovery on noise magnification for realistic images still has to be investigated in more detail.

A multiyear project has been filed in which the potential benefits of natural pixel reconstruction are described and in which we highlight future research work. Investigating Monte Carlo based generalized natural pixel reconstruction will be one of our main research topics for the next 5 years. The implementation discussed in section 7.2.1 describes how we were able to gain 1 mm reconstructed resolution by using a generalized natural pixel reconstruction in which the system matrix was simulated using a geometric Monte Carlo simulator. The geometric simulator only accounts for the geometric sampling and does not include Anger logic and light spread. Moreover, the main degradation factors are crystal scatter (chapter 4) and crystal penetration (chapter 6) which were also not accounted for by the geometric simulator. Future work will investigate what additional resolution recovery can be achieved by simulating the generalized natural pixel representation of the system matrix with

GATE, incorporating crystal scatter and crystal penetration for several detector materials as was described in section 7.2.2.

Chapter 8

General Conclusion

This finalizing chapter will give an overview of the research discussed in this manuscript and will delineate the envisioned future research projects that originated from this work.

In chapter 2 a short overview of nuclear medicine, including reconstruction, was given in order to frame the underlying dissertation. Furthermore, the GATE simulation package was introduced as an upper layer of the general-purpose high energy physics code, Geant4. GATE is a Monte Carlo code capable of accomodating complex scanner geometry and imaging configurations in a user-friendly way, accounting for timing information while retaining the comprehensive physics modeling abilities of Geant4. A thorough literature study was presented in chapter 2 about the applications of Monte Carlo methods in nuclear medicine which highlighted four main fields in which GATE could be of significant relevance: attenuation and scatter correction techniques, imaging systems and collimator design, intrinsic detector modeling and Monte Carlo based reconstruction. Specific research on these four topics is presented in this dissertation.

Chapter 3 starts with reporting the SPECT validation study that was performed to verify the accuracy of GATE simulations versus measurements on a commercial SPECT acquisition system. For this purpose we have modeled all aspects of a scintillation camera, including different collimators. The most important aspects for SPECT imaging were validated and it was demonstrated that GATE needs very little assumptions to accurately describe real camera designs, making it in that way very flexible. This leads to the possibility of using GATE for simulating existing camera setups in different acquisition modes with different parameters, different isotopes and different collimators. Ongoing work is being performed on the validation of GATE for dosimetric applications. The latter is one of the most important future research aspects of the

OpenGATE collaboration next to gridification and cluster distribution.

Chapter 4 deals with attenuation and scatter correction on Beacon (gamma camera) PET and Beacon-SPECT. It is the first simulation study using the virtual GATE clock synchronisation to such a large extent. Suggestions for protocol optimization studies in Beacon PET on a hybrid gamma camera were made. The important detector parts for contamination of the attenuation image by the 511 keV emission isotope were pinpointed: entrance sheets and end parts. Design work should focus on those aspects to further reduce cross-contamination if one wants to keep using gamma camera PET without the time-consuming mock scan before switching to PET or PET/CT. We showed that the interwindow contamination of the emission energy window in the case of simultaneous emission/transmission imaging for Beacon-SPECT is smallest in the LEHR collimator, thick crystal setup. Moreover we found that the Beacon attenuation image is often degraded near the center of large patients when a transmission acquisition is performed simultaneously or sequentially with the medium energy emission study. In this particular case, it would be recommendable to replace the MEGP collimators by the LEHR variants if one uses the Monte Carlo based reconstruction method, discussed in chapter 7, that accounts for the increased photon spread.

Chapter 4 also discusses a qualitative interpretation for the importance of multiple order scatter in 3D PET. Various crystal types, including innovative materials as $LaBr_3$ and LuI_3, were examined. It became clear that only first order patient scatter is significantly degrading the photopeak acquisitions for all crystal types. The importance of multiple order scatter is less than 10%. It was also shown that BGO and LSO give rise to higher NEC's. This will not be the case for BGO in higher count rate studies since dead time effects will become predominant due to the slow scintillation time of the crystal material. Incorporation of the effect of crystal scatter in reconstruction appeared to be mandatory. Two approaches were suggested, of which one was further discussed in chapter 7.

In chapter 5 we investigated a new acquisition system design with a strip solid state detector and with a slat collimator by comparison with parallel beam setups on a pixelated solid state detector and on a single crystal NaI detector. Solid state devices have a better energy resolution making them more appropriate for dual isotope imaging. The rotating slat collimator results in a better resolution and in a higher sensitivity. As far as the contrast and hot spot detectability is concerned, the classical collimator setup on a CZT and on a NaI detector outperforms the rotating slat equivalent. However when we increased the strip width behind the slats, the rotating slat performance closed in on the parallel beam setup performances. This is promising since the active detector area in the rotating slat design is, in this case, still only half of the two other acquisition models. The solid state setups have the disadvantage of economic cost however as the CZT material is far more expensive than a NaI crystal. Observer studies should be extended on a data set generated using a dedicated 3D reconstruction algorithm as was very recently derived by Zeng [147] and by Wang [135]. In those implementations the additional distance-dependent sensitivity information for the rotating slat design could result in an improved performance on reconstructions and could cancel out the performance deficit in the aforementioned projection study. This will be subject to further research. We also extended the work of Metz (parallel hole), and Tsui (fanbeam and conebeam) for the geometric transfer function of a slat collimator on a strip detector. For sensitivity and resolution as well as for transaxial profiles of line spread functions we could calculate closed analytical behavior formulations, derived from the analytical expression for the geometric transfer function in the Fourier domain. We found that the sensitivity depends on the angle of incidence and on the distance to the detector, while the spatial resolution of this particular imaging system is constant in a plane at a fixed distance from the collimator. We also concluded that the line spread functions were triangular. The presented formulation of the geometric transfer function will be useful in iterative reconstruction algorithms in order to incorporate distance dependent effects. It will be applied in combination with additional simulation study results which account for collimator scatter and septal penetration of the slats, a contribution that only gains importance with higher energy isotopes.

In chapter 6 we have derived a theoretical model for incorporation of the detection location uncertainty in continuous detector PET. The resulting detector sensitivity function could not be analytically expressed in a closed form and was thus calculated each time by means of numerical integration. We found that the transversal profiles could be approximated by Gaussians, for perpendicular incidences with an error of 0.1%, while an error of 1% resulted for oblique incidences on a thin crystal detector. We incorporated the depth of interaction of a photon into our theoretical model for oblique incidences on thicker crystals and reached an analytical expression for the function that should replace the traditional Gaussian for the detection uncertainty. We also confirmed the statement that the interaction probability of a 511 keV photon through the PET-crystal is almost uniform. After verification it became clear that this model is valid for incorporation in a reconstruction algorithm in order to more accurately model the acquisition process and to improve the spatial resolution of the tomographic images. This model can also be used to calculate the spatial resolution of systems that are still in design which proves its multiple usefulness. To our knowledge this is the first theoretical LOR model for a continuous detector PET system accurately incorporating the detection uncertainty of the annihilation photons as a function of distance to the detector heads.

In chapter 7 we described a reconstruction implementation that derives the detector response from a fully 3D Monte Carlo simulated system matrix, for medium energy studies on low energy collimators. We incorporated this detector response in a dedicated Monte Carlo based reconstruction that accurately recovers the medium energy isotope photon spread on a LEHR. In all cases the reconstruction of medium energy isotopes on LEHR gives the best result, provided that the detector response is fully simulated and incorporated. In this way we solved the issue, raised by chapter 4, which showed that a Beacon attenuation image is often degraded near the center of large patients in a medium energy emission study and that it would be recommendable to replace the MEGP collimators by the LEHR variants if a recovery for the increased photon spread is incorporated. We believe to have derived in that way a very important guideline for transmission imaging in a medium energy emission study. Since the market of miniclusters is rapidly gaining importance in the scientific community and is becoming affordable, the approach of Monte Carlo based reconstruction will be useful in protocol optimization, and reconstruction technique examination for the medium energy studies discussed above.

Apart from this dedicated Monte Carlo based reconstruction, a multiyear project has been filed in which the potential benefits of natural pixel reconstruction are described and in which we highlight future research work. Investigating Monte Carlo based generalized natural pixel reconstruction will be one of our main research topics for the next years. The implementation discussed in chapter 7 describes how we were able to gain 1 mm reconstructed resolution by using a generalized natural pixel reconstruction in which the system matrix was simulated using a geometric Monte Carlo simulator. The geometric simulator only accounts for the geometric sampling and does not include Anger logic and light spread. Moreover, the main degradation factors are crystal scatter which was extensively analyzed in chapter 4 and crystal penetration which showed to be determining in chapter 6. The latter two effects were also not accounted for by the geometric simulator. Future work will investigate what additional resolution recovery can be achieved by simulating the generalized natural pixel representation of the system matrix with GATE, incorporating crystal scatter and crystal penetration for several detector materials. A Gaussian blurring can be added to account for the Anger logic and for the light spread although a realistic optical model will be derived using dedicated software to achieve a more accurate representation of the intrinsic crystal resolution. Extension of the generalized natural pixel reconstruction to 3D will be of future interest by using a Fourier transformation for the block diagonalization of the block circulant system matrix. Since GATE is one of the most accurate simulation tools for SPECT and PET, and given the promising preliminary results of the generalized natural pixel reconstruction, we believe this method can evolve to one of the most powerful resolution recovery techniques available in nuclear medicine research.

Bibliography

[1] S. Agnostelli et al., "Geant4: a simulation toolkit," *Nuclear Instruments and Methods A*, vol. 506, pp. 250–303, 2003.

[2] P. Andreo, "Monte Carlo techniques in medical radiation physics," *Physics in Medicine and Biology*, vol. 36, pp. 861–920, 1991.

[3] H. Anger, "Gamma ray efficiency and image resolution in sodium iodide," *Review of Scientific Instruments*, vol. 35, pp. 693–697, 1964.

[4] K. Assie, V. Breton, I. Buvat, C. Comtat, S. Jan, M. Krieguer, D. Lazaro, C. Morel, M. Rey, G. Santin, L. Simon, S. Staelens, D. Strul, J. Vieira, and R. Van de Walle, "Monte Carlo simulation in PET and SPET instrumentation using GATE," *Nuclear Instruments and Methods A*, vol. 527/1-2, pp. 180–189, 2004.

[5] K. Assie, I. Gardin, P. Vera, and I. Buvat, "Validation of Monte Carlo simulations of Indium11 SPECT using GATE," *Journal of Nuclear Medicine*, vol. 45, no. 5, p. 1298, 2004.

[6] C. Bai, G. Zeng, and G. Gullberg, "A slice by slice blurring model and kernel evaluation using the Klein-Nishina formula for 3D scatter compensation in parallel and converging beam SPECT," *Physics in Medicine and Biology*, vol. 45, pp. 1275–1307, 2000.

[7] J. Baker, T. Budinger, and R. Huesman, "Generalized approach to inverse problems in tomography: image reconstruction for spatially variant systems using natural pixels," *Critical Reviews in Biomedical Engineering*, vol. 20, pp. 47–71, 1992.

[8] F. Beekman, H. de Jong, and E. Slijpen, "Efficient SPECT scatter calculation in non-uniform media using correlated Monte Carlo simulation," *Physics in Medicine and Biology*, vol. 44, pp. 183–192, 1999.

[9] F. Beekman, J. den Harder, M. Viergever, and P. van Rijk, “SPECT scatter modeling in non-uniform attenuating objects,” *Physics in Medicine and Biology*, vol. 42, pp. 1133–1142, 1997.

[10] F. Beekman, C. Kamphuis, B. Hutton, and P. van Rijk, “Half-fanbeam collimators combined with scanning point sources for simultaneous emission-transmission imaging,” *Journal of Nuclear Medicine*, vol. 39, pp. 1996–2002, 1998.

[11] F. Beekman, C. Kamphuis, and M. Viergever, “Improved SPECT quantitation using fully three-dimensional iterative spatially variant scatter response compensation,” *IEEE Transactions on Medical Imaging*, vol. 15, pp. 491–499, 1996.

[12] F. Beekman, B. Vastenhouw, and F. Van der Have, “Towards 3D nuclear microscopy using locally focussing many pinhole small animal SPECT,” in *Proceedings of the Fully 3D Conference*, Saint Malo, France, 2003, pp. Th PM 1–6.

[13] F. Beekman, H. W. de Jong, and S. van Geloven, “Efficient fully 3D iterative SPECT reconstruction with Monte Carlo based scatter correction,” *IEEE Transactions on Medical Imaging*, vol. 21, pp. 867–877, August 2002.

[14] H. Benveniste and S. Blackband, “MR microscopy and high resolution’small animal MRI: applications in neuroscience research,” *Progress in Neurobiology*, vol. 67, no. 5, pp. 393–420, 2002.

[15] A. Bice, T. Lewellen, R. Miyaoka, R. Harrison, D. Haynor, K. Pollard, C. Hanson, and S. Gillispie, “Monte Carlo simulations of BaF_2 detectors used in time of flight positron emission tomography,” *IEEE Transactions on Nuclear Science*, vol. 37, pp. 696–701, 1990.

[16] A. Bielajew, H. Hirayama, W. Nelson, and D. Rogers, “History, overview and recent improvements of EGS4,” National Research Council, Ottawa, Canada, Tech. Rep., 1994.

[17] J. Briesmeister, “MCNP - A general Monte Carlo N-particle transport code,” Los Alamos National Laboratory, Los Alamos, NM, USA, Tech. Rep., 1993.

[18] R. Brun and F. Rademakers, “ROOT, an object oriented data analysis framework,” *Nuclear Instruments and Methods A*, vol. 389, pp. 81–86, 1997.

[19] H. Buonocore, W. Brody, and A. Macowski, “A natural pixel decomposition for twodimensional image reconstruction,” *IEEE Transactions on Biomedical Engineering*, vol. 2, pp. 69–78, 1981.

[20] I. Buvat, “A non-parametric bootstrap approach for analysing the statistical properties of SPET and PET images,” *Physics in Medicine and Biology*, vol. 47, pp. 1761–1775, 2002.

[21] I. Buvat and I. Castiglioni, “Monte Carlo simulations in SPET and PET,” *Quarterly Journal of Nuclear Medicine*, vol. 46, pp. 48–61, 2002.

[22] I. Buvat, D. Lazaro, and V. Breton, “Fully 3D Monte Carlo reconstruction in SPECT: Proof of concept and is it worthwile?” in *Proceedings of the Fully 3D Conference*, Saint Malo, France, 2003, pp. We AM1–1.

[23] I. Buvat, M. Rodriguezvillafuerte, A. Toddpokropek, H. Benali, and R. Dipaolo, “Comparative assessment of 9 scatter correction methods based on spectral-analysis using Monte Carlo simulations,” *Journal of Nuclear Medicine*, vol. 36, no. 8, pp. 1476–1488, 1995.

[24] S. Cherry, Y. Shao, R. Silverman, K. Meadors, S. Siegel, A. Chatziioannou, J. Young, W. Jones, J. Moyers, D. Newport, A. Boutefnouchet, T. Farquhar, M. Andreaco, M. Paulus, D. Binkley, R. Nutt, and M. Phelps, “MicroPET: A high resolution PET scanner for imaging small animals,” *IEEE Transactions on Nuclear Science*, vol. 44, no. 3, pp. 1161–1166, 1997.

[25] O. Chibani and X. Li, “Monte Carlo dose calculations in homogeneous media and at interfaces: A comparison between GEPTS, EGSnrc, MCNP, and measurements,” *Medical Physics*, vol. 29, no. 5, pp. 835–847, 2003.

[26] Z. Cho, J. Jones, and M. Singh, *Foundations of medical imaging*. John Wiley & sons Inc., 1993.

[27] Y. Chung, Y. Choi, G. Cho, Y. Choe, K. Lee, and B. Kim, “Optimization of dual layer phoswich detector consisting of LSO and LuYAP for small animal PET,” in *Proceedings of the IEEE Medical Imaging Conference*, Portland, USA, 2003, pp. M7–12.

[28] K. Comanor, P. Virador, and W. Moses, “Algorithms to identify detector Compton scatter in PET modules,” *IEEE Transactions on Nuclear Science*, vol. 43, pp. 2213–2218, 1996.

[29] C. Contag and B. Ross, "It's not just about anatomy: In vivo bioluminescence imaging as an eyepiece into biology," *Journal of Magnetic Resonance Imaging*, vol. 16, no. 4, pp. 378–387, 2002.

[30] A. Cot, J. Sempau, D. Pareto, S. Bullich, J. Pavia, F. Calvino, and D. Ros, "Evaluation of the geometric, scatter, and septal penetration components in fan-beam collimators using Monte Carlo simulation," *IEEE Transactions on Nuclear Science*, vol. 49, no. 1, pp. 12–16, 2002.

[31] Y. D'Asseler, C. Croiselle, H. Gifford, S. Vandenberghe, R. Van de Walle, I. Lemahieu, and S. Glick, "Calculating numerical observer performance for list mode PET using the bootstrap method," in *Proceedings of the Fully 3D Conference*, Saint Malo, France, 2003, pp. Th PM2–4.

[32] Y. D'Asseler, C. Croiselle, H. Gifford, S. Vandenberghe, R. Van de Walle, I. Lemahieu, and S. Glick, "Evaluating human observer performance for list mode pet using the bootstrap method," in *Proceedings of the IEEE Medical Imaging Conference*, Portland, USA, 2003, pp. M14–207.

[33] Y. D'Asseler, C. Groiselle, H. Gifford, S. Vandenberghe, S. Staelens, R. Van de Walle, I. Lemahieu, and S. Glick, "Evaluating human observer performance for list mode PET using the bootstrap method," august 2004, submitted for IEEE Transactions on Nuclear Science.

[34] J. De Beenhouwer, S. Staelens, Y. D'Asseler, S. Vandenberghe, I. Lemahieu, and R. Van de Walle, "Geomterical importance sampling and pulse height tallies in GATE," April 2004, accepted for the EMBS Conference, San Fransisco, USA.

[35] M. Defrise, "A factorization method for the 3D X-ray transform," *Inverse Problems*, vol. 11, pp. 983–994, 1997.

[36] B. Efron, *The jackknife, bootstrap and other resampling plans*. Siam, 1982.

[37] K. Erlandsson, M. Ivanovic, S. Strand, K. Sjorgen, and D. Weber, "High resolution pinhole SPECT for small animal imaging," *Journal of Nuclear Medicine*, vol. 34, no. 5, p. 9, 1993.

[38] J. Feng and B. Penney, "Determination of attenuation maps using a Ba-133 source and medium energy collimators in SPECT," in *Proceedings of the IEEE Medical Imaging Conference*, vol. 2, 2002, pp. 1264 – 1266.

[39] C. Floyd, R. Jaszczak, and R. Coleman, "Inverse Monte Carlo: a unified reconstruction algorithm for SPECT," *IEEE Transactions on Nuclear Science*, vol. 32, pp. 779–785, 1985.

[40] C. Floyd, R. Jaszczak, K. Greer, and R. Coleman, "Inverse Monte Carlo: a unified reconstruction algorithm for ECT," *Journal of Nuclear Medicine*, vol. 27, pp. 1577–1585, 1996.

[41] B. Fraass, J. Smathers, and J. Deye, "Summary and recommendations of a national cancer institute workshop on issues limiting the clinical use of Monte Carlo dose calculation algorithms for megavoltage external beam radiation therapy," *Medical Physics*, vol. 30, no. 12, pp. 3206–3216, 2003.

[42] D. Gagnon, C. Tung, L. Zeng, and W. Hawkins, "Design and early testing of a new medium-energy transmission device for attenuation correction in SPECT and PET," in *Proceedings of the IEEE Medical Imaging Conference*, vol. 3, 1999, pp. 1349 – 1353.

[43] D. Gagnon, G. Zeng, M. Links, J. Griesmer, and C. Valentino, "Design considerations for a new solid state gammacamera: SOLSTICE," in *Nuclear Science Symposium Conference Record*, vol. 2, 2001, pp. 1156–1160.

[44] S. Garelli, S. Giordano, G. Piemontese, and S. Squaricia, "Interactive FLUKA: a World Wide Web version for a simulation code in protontherapy," *Journal de Chimie Physique et de Physico-Chimie Biologique*, vol. 95, no. 4, pp. 767–771, 1998.

[45] GATE, http://www-lphe.epfl.ch/GATE/.

[46] Geant4, http://wwwasd.web.cern.ch/wwwasd/geant4/geant4.html.

[47] H. Gifford and M. King, "Comparison of human- and model-observer LROC studies," in *Proceedings of the SPIE Medical Imaging conference*, vol. 5034, San Diego, USA, 2003, pp. 16–24.

[48] G. Gindi, M. Lee, A. Rangarajan, and I. Zubal, *Bayesian Reconstruction of Functional Images using Anatomical Information as Priors*. Colchester, A.C.F. and Hawkes, D.J.Springer, New York, 1991, pp. 121–131.

[49] G. Gindi, M. Lee, A. Rangarajan, and I. Zubal, "Bayesian reconstruction of functional images using anatomical information as priors," *IEEE Transactions on Medical Imaging*, vol. 12, pp. 351–359, 1993.

[50] S. Glick, “The effect of intrinsic spatial resolution on the quantitative accuracy of SPECT imaging,” *IEEE Transactions on Nuclear Science*, vol. 46, pp. 1009–1015, 1999.

[51] E. Graves, R. Weissleder, and V. Ntziachristos, “Fluorescence molecular imaging of small animal tumor models,” *Current Molecular Medicine*, vol. 4, no. 4, pp. 419–430, 2004.

[52] J. Griesmer, B. Kline, J. Grosholz, K. Parnham, and D. Gagnon, “Performance evaluation of a new CZT detector for nuclear medicine:SOLSTICE,” in *Nuclear Science Symposium Conference Record*, vol. 2, 2001, pp. 1050–1054.

[53] C. Groiselle, Y. D’Asseler, J. Kolthammer, C. Matthews, and S. Glick, “A Monte Carlo simulation study to evaluate septal spacing using triple-head hybrid PET imaging,” *IEEE Transactions on Nuclear Science*, vol. 50, no. 5, pp. 1339–1346, 2003.

[54] G. Gullberg, Y. Hsieh, and G. Zeng, “An SVD reconstruction algorithm using the natural pixel representation of the attenuated radon transform,” *IEEE Transactions on Nuclear Science*, vol. 43, pp. 295–303, 1996.

[55] R. Harrison, S. Vannoy, D. Haynor, S. Gillipsie, M. Kaplan, and T. Lewellen, “Preliminary experience with the photon generator module of a public-domain simulation system for emission tomography,” in *Proceedings of the IEEE Medical Imaging Conference*, San Fransico, USA, 1993, pp. 1154–1158.

[56] U. Heinrichs, U. Pietrzyk, and K. Ziemons, “Design optimization of the PMT-ClearPET prototypes based on simulation studies with GEANT3,” *IEEE Transactions on Nuclear Science*, vol. 50, no. 5, pp. 1428–1432, 2003.

[57] E. Hoffman, S. Huang, M. Phelps, and D. Kuhl, “Quantitation in positron emission computed tomography: 4 effects of accidental coincidences,” *Journal of Computer Assisted Tomography*, vol. 5, pp. 391–440, 1981.

[58] C. Holdsworth, C. Levin, M. Janecek, M. Dahlbom, and E. Hoffman, “Performance analysis of an improved 3-D PET Monte Carlo simulation and scatter correction,” *IEEE Transactions on Nuclear Science*, vol. 49, no. 1, pp. 83–89, 2002.

[59] Y. Hsieh, G. Zeng, and G. Gullberg, "Projection space image reconstruction using strip functions to calculate pixels more natural for modeling the geometric response of the SPECT collimator," *IEEE Transactions on Medical Imaging*, vol. 17, pp. 24–44, 1998.

[60] H. Huesman, E. Salmeron, and J. Baker, "Compensation for crystal penetration in high resolution positron tomography," *IEEE Transactions on Nuclear Science*, vol. 36, pp. 1100–1107, 1989.

[61] Images courtesy of GE Healthcare, "SPECT/CT case study."

[62] Images courtesy of Philips Medical Systems, "Mosaic small animal PET."

[63] Interfile, "http://gamma.wustl.edu/interfile33."

[64] S. Jan, "Simulateur Monte Carlo et caméra à xénon liquide pour la Tomographie à Emission de Positons," Ph.D. dissertation, Université Joseph Fourier, Grenoble, France, 2002.

[65] S. Jan, A. Chatziioannou, C. Comtat, D. Strul, G. Santin, and R. Trebossen, "Monte Carlo simulation for the microPET P4 system using GATE," in *Proceedings of the HiRes Conference*, vol. 5, Academy of Molecular Imaging, Madrid, 2003, p. 138.

[66] S. Jan, C. Comtat, D. Strul, and R. Trebossen, "Monte Carlo Simulation for the ECAT EXACT HR+ system using GATE," in *Proceedings of the IEEE Medical Imaging Conference*, Portland, USA, 2003, pp. M10–178.

[67] S. Jan, C. Comtat, R. Trebossen, and A. Syrota, "Monte Carlo simulation of the MicroPET Focus for small animal," *Journal of Nuclear Medicine*, vol. 45, no. 5, p. 1313, 2004.

[68] S. Jan, G. Santin, D. Strul, S. Staelens, K. Assié, D. Autret, D. Avner, R. Barbier, M. Bardiès, P. Bloomfield, D. Brasse, V. Breton, P. Bruyndonckx, I. Buvat, A. Chatziioannou, Y. Choi, Y. Chung, C. Comtat, D. Donnarieix, L. Ferrer, S. Glick, C. Groiselle, S. Kerhoas-Cavata, A. Kirov, V. Kohli, M. Koole, M. Krieguer, J. van der Laan, F. Lamare, G. Largeron, C. Lartizien, D. Lazaro, M. Maas, L. Maigne, F. Mayet, F. Melot, S. Nehmeh, E. Pennacchio, J. Perez, U. Pietrzyk, F. Rannou, M. Rey, D. Schaart, R. Schmidtlein, L. Simon, T. Song, J. Vieira,

D. Visvikis, R. Van de Walle, E. Wieers, and C. Morel, “GATE: a simulation toolkit for PET and SPECT,” *Physics in Medicine and Biology*, vol. 49, no. 19, pp. 4543–4561, 2004.

[69] P. Kinahan, “Analytic 3D image reconstruction using all detected events,” *IEEE Transactions on Nuclear Science*, vol. 36, no. 1, pp. 964–968, 1989.

[70] M. Koole, S. Staelens, S. Vandenberghe, Y. D’Asseler, R. Van de Walle, and I. Lemahieu, “Analytical model for Solstice detector response,” in *Proceedings of the IEEE Medical Imaging Conference*, Portland, USA, 2003, pp. M14–270.

[71] F. Lamare, A. Turzo, Y. Bizais, and D. Visvikis, “Simulation of the Allegro PET system using GATE,” in *Proceedings of the SPIE Medical Imaging conference*, vol. 5368, San Diego, USA, 2004, pp. 890–897.

[72] C. Lartizien, A. Reilhac, N. Costes, M. Janier, and D. Sappey-Marinier, “Monte Carlo simulation-based design study of a LSO-LuAP small animal pet system,” *IEEE Transactions on Nuclear Science*, vol. 50, no. 5, pp. 1433–1438, 2003.

[73] D. Lazaro, I. Buvat, G. Loudos, D. Strul, G. Santin, N. Giokaris, D. Donnarieix, L. Maigne, V. Spanoudaki, S. Styliaris, S. Staelens, and V. Breton, “Monte Carlo simulation of a CsI(Tl) gamma camera dedicated to small animal imaging using GATE,” *Physics in Medicine and Biology*, vol. 49, no. 2, pp. 271–286, 2004.

[74] R. Leahy and X. Yan, *Incorporation of Anatomical MR data for Improved Functional Imaging with PET.* Colchester, A.C.F. and Hawkes, D.J.Springer, New York, 1991, pp. 121–131.

[75] M. Ljungberg and S. Strand, “A Monte Carlo program for the simulation of scintillation camera characteristics,” *Computer Methods and Programs in Biomedicine*, vol. 29, pp. 257–272, 1989.

[76] M. Ljungberg, S. Strand, and M. King, *Monte Carlo simulations in nuclear medicine: applications in Diagnostic imaging*. Institute of Physics, 1998.

[77] F. Maes, A. Collignin, D. Vandermeulen, G. Marchal, and P. Suetens, “Multimodality image registration by maximization of mutual information,” *IEEE Transactions on Medical Imaging*, vol. 16, pp. 187–198, 1997.

[78] D. McCracken, “The Monte Carlo method,” *Scientific American*, vol. 192, pp. 90–96, 1955.

[79] C. Metz, F. Atkins, and R. Beck, “The geometric transfer function component for scintillation camera collimators with straight parallel holes,” *Physics in Medicine and Biology*, vol. 25, no. 6, pp. 1059–1070, 1980.

[80] W. Moses, “Time of flight in PET revisited,” *IEEE Transactions on Nuclear Science*, vol. 50, no. 5, pp. 1325–1330, 2003.

[81] W. Moses and S. Derenzo, “Design studies for a PET detector module using a PIN photodiode to measure depth of interaction,” *IEEE Transactions on Nuclear Science*, vol. 41, pp. 1441–1445, 1994.

[82] G. Muehllehner and J. Karp, “Positron emission tomography-technical considerations,” *Seminars on Nuclear Medicine*, vol. 14, pp. 35–50, 1986.

[83] *NEMA standars publication NU 2-2001 : Performance measurements of positron emission tomographs*, National electric manufacturers association, Rosslyn, VA, 2001.

[84] D. Pareto, A. Cot, J. Pavia, C. Falcon, I. Juvells, F. Lomena, and D. Ros, “Iterative reconstruction with correction of the spatially variant fanbeam collimator response in neurotransmission SPET imaging,” *European Journal of Nuclear Medicine*, vol. 30, no. 10, pp. 1322–1329, 2003.

[85] M. Paulus, S. Gleason, S. Kennel, P. Hunsicker, and D. Johnson, “High resolution X-ray computed tomography: An emerging tool for small animal cancer research,” *Neoplasia*, vol. 2, no. 1-2, pp. 62–70, 2000.

[86] D. Raeside, “Monte Carlo principles and applications,” *Physics in Medicine and Biology*, vol. 21, pp. 181–197, 1976.

[87] F. Rannou, V. Kohli, D. Prout, and A. Chatziioannou, “Investigation of OPET performance using GATE, a Geant4-based simulation software,” in *Proceedings of the IEEE Medical Imaging Conference*, Norfolk, USA, 2002, pp. M6–8.

[88] A. Reader, “Image reconstruction and correction techniques for positron volume imaging with rotating planar detectors,” Ph.D. dissertation, University of London, 1999.

[89] B. Reniers, F. Verhaegen, and S. Vynckier, “The radial dose function of low-energy brachytherapy seeds in different solid phantoms: comparison between calculations with the EGSnrc and MCNP4C Monte Carlo codes and measurements,” *Physics in Medicine and Biology*, vol. 49, no. 8, pp. 1569–1582, 2004.

[90] M. Rey, “Rapport de TP 4ieme,” Lausanne University, Tech. Rep., 2002.

[91] M. Rey, L. Simon, D. Strul, J. Vieira, and C. Morel, “Design study of the ClearPET LSO/LuYAP phoswich detector head using GATE,” in *Proceedings of the HiRes Conference*, vol. 5, Academy of Molecular Imaging, Madrid, 2003, p. 119.

[92] G. Santin, D. Strul, D. Lazaro, L. Simon, M. Krieguer, M. Vieira Martins, V. Breton, and C. Morel, “GATE, a Geant4-based simulation platform for PET and SPECT integrating movement and time management,” *IEEE Transactions on Nuclear Science*, vol. 50, pp. 1516–1521, 2003.

[93] C. Schmidtlein, S. Nehmeh, L. Bidaut, Y. Erdi, J. Humm, H. Amols, and A. Kirov, “Validation of GATE Monte Carlo simulations for the GE Advance PET scanner,” *Journal of Nuclear Medicine*, vol. 45, no. 5, p. 1283, 2004.

[94] Y. Shao, S. Cherry, S. Siegel, and W. Silverman, “A study of inter-crystal scatter in small scintillator arrays designed for high resolution PET imaging,” *IEEE Transactions on Nuclear Science*, vol. 43, pp. 1938–1944, 1996.

[95] L. A. Shepp and Y. Vardi, “Maximum likelihood reconstruction for emission tomography,” *IEEE Transactions on Medical Imaging*, vol. 1, no. 2, pp. 113–122, October 1982.

[96] L. A. Shepp, Y. Vardi, J. B. Ra, S. K. Hilal, and Z. H. Cho, “Maximum likelihood PET with real data,” *IEEE Transactions on Nuclear Science*, vol. 31, pp. 910–912, April 1984.

[97] L. Simon, D. Strul, G. Santin, M. Krieguer, and C. Morel, “Simulation of time curves in small animal PET using GATE,” *Nuclear Instruments and Methods A*, vol. 527, pp. 190–194, 2004.

[98] T. Song, Y. Choi, Y. Chung, J. Jung, Y. Choe, K. Lee, S. Kim, and B. Kim, “Optimization of pinhole collimator for small animal SPECT using Monte Carlo simulation,” *IEEE Transactions on Nuclear Science*, vol. 50, no. 3, pp. 327–332, 2003.

[99] J. Sorenson and M. Phelps, *Physics in Nuclear Medicine*. W.B. Saunders Company, 1987.

[100] S. Staelens, Y. D'Asseler, S. Vandenberghe, M. Koole, I. Lemahieu, and R. Van de Walle, "A 3D model incorporating spatial detection uncertainty in continuous detector PET: Monte Carlo evaluation of a theoretical study," in *Proceedings of the Fully 3D Conference*, Saint Malo, France, 2003, pp. We AM1–3.

[101] S. Staelens, Y. D'Asseler, S. Vandenberghe, M. Koole, I. Lemahieu, and R. Van de Walle, "A theoretical lor model incorporating spatial uncertainty in continuous detector pet," in *Proceedings of the SPIE Medical Imaging conference*, vol. 5030, San Diego, USA, 2003, pp. 667–676.

[102] S. Staelens, Y. D'Asseler, S. Vandenberghe, M. Koole, I. Lemahieu, and R. Van de Walle, "A simulation study comparing the imaging performance of a solid state detector with a rotating slat collimator versus a traditional scintillation camera," in *Proceedings of the SPIE Medical Imaging conference*, vol. 5372-36, San Diego, USA, 2004, pp. 301–310.

[103] S. Staelens, Y. D'Asseler, S. Vandenberghe, M. Koole, I. Lemahieu, and R. Van de Walle, "A threedimensional theoretical model incorporating spatial detection uncertainty in continuous detector PET," *Physics in Medicine and Biology*, vol. 49, no. 11, pp. 2337–2351, 2004.

[104] S. Staelens, M. Koole, S. Vandenberghe, Y. D'Asseler, I. Lemahieu, and R. Van de Walle, "The geometric transfer function for a slat collimator mounted on a strip detector," november 2004, in press and to appear in IEEE Transactions on Nuclear Science.

[105] S. Staelens, G. Santin, D. Strul, M. Koole, S. Vandenberghe, Y. D'Asseler, V. Breton, C. Morel, I. Lemahieu, and R. Van de Walle, "Monte Carlo simulations of Interfile based emission and attenuation maps for clinical applications," *Journal of Nuclear Medicine*, vol. 44, no. 5, p. 1048, 2003.

[106] S. Staelens, G. Santin, S. Vandenberghe, D. Strul, M. Koole, Y. D'Asseler, I. Lemahieu, and R. Van de Walle, "Transmission imaging with a moving point source: influence of crystal thickness and collimator type," november 2004, in press and to appear in IEEE Transactions on Nuclear Science.

[107] S. Staelens, D. Strul, S. Vandenberghe, G. Santin, M. Koole, Y. D'Asseler, I. Lemahieu, and R. Van de Walle, "Monte Carlo simulations of a scintillation camera using GATE: validation and application modeling," *Physics in Medicine and Biology*, vol. 48, no. 18, pp. 3021–3042, 2003.

[108] S. Staelens, S. Vandenberghe, S. Glick, Y. D'Asseler, I. Lemahieu, and R. Van de Walle, "Simulation of patient and crystal scatter in 3D PET for various crystals," October 2004, accepted for the IEEE Medical Imaging Conference, Roma, Italy.

[109] S. Staelens, S. Vandenberghe, M. Koole, D. Strul, G. Santin, H. Van Steendam, Y. D'Asseler, R. Dierckx, I. Lemahieu, and R. Van de Walle, "Monte Carlo simulations of transmission measurements with a medium energy moving point source," *European Journal of Nuclear Medicine*, vol. 30, p. 223, 8 2003.

[110] D. Strul, "Specification of a Geant4-based nuclear medicine simulation framework," UNIL, Lausanne, Switzerland, Tech. Rep., 2001, clearPET.

[111] D. Strul, G. Santin, D. Lazaro, V. Breton, and C. Morel, "GATE (Geant4 Application for Tomographic Emission): a PET/SPECT general-purpose simulation platform," *Nuclear Physics B*, vol. 125C, pp. 75–79, 2003.

[112] S. Surti, J. Karp, G. Muehllehner, and P. Raby, "Investigation of lanthanum scintillators for 3-D PET," *IEEE Transactions on Nuclear Science*, vol. 50, no. 3, pp. 348–354, 2003.

[113] J. Svedberg, "On the intrinsic resolution of a gamma camera system," *Physics in Medicine and Biology*, vol. 17, pp. 514–524, 1972.

[114] J. Svedberg, "Computed intrinsic efficiencies and modulation transfer functions for gamma cameras," *Physics in Medicine and Biology*, vol. 18, pp. 658–664, 1973.

[115] R. Swensson, "Unified measurement of observer performance in detecting and localizing target objects on images," *Medical Physics*, vol. 23, pp. 1709–1725, 1996.

[116] A. Syme, C. Kirkby, T. Riauka, B. Fallone, and S. McQuarrie, "Monte Carlo investigation of single cell beta dosimetry for intraperitoneal ra-

dionuclide therapy," *Physics in Medicine and Biology*, vol. 49, no. 10, pp. 1959–1972, 2004.

[117] P. Tan, D. Bailey, S. Meikle, S. Eberl, R. Fulton, and B. Hutton, "A scanning line source for simultaneous emission and transmission measurements in SPECT," *Journal of Nuclear Medicine*, vol. 34, pp. 1752–1760, 1993.

[118] C. Thompson, "The effect of collimation on singles rates in multi-slice PET," *IEEE Transactions on Nuclear Science*, vol. 35, pp. 598–602, 1988.

[119] C. Thomson, J. Cantu, and Y. Picard, "PETSIM: Monte Carlo program simulation of all sensitivity and resolution parameters of cylindrical positron imaging systems," *Physics in Medicine and Biology*, vol. 37, pp. 731–749, 1992.

[120] D. Townsend and T. Beyer, "A combined PET/CT scanner: the path to true image fusion," *British Journal of Nuclear Medicine*, vol. Special Issue, pp. S24–S30, 2002.

[121] B. Tsui and G. Gullberg, "The geometric transfer function for cone and fan beam collimators," *Physics in Medicine and Biology*, vol. 35, pp. 81–93, 1990.

[122] T. Turkington and C. Laymon, "Imaging properties of a half-inch Sodium Iodide gamma camera," *IEEE Transactions on Nuclear Science*, vol. 44, pp. 1262–1265, 1997.

[123] F. van der Have and F. Beekman, "Photon penetration and scatter in micro-pinhole imaging: a Monte Carlo investigation," *Physics in Medicine and Biology*, vol. 49, no. 8, pp. 1369–1386, 2004.

[124] S. Vandenberghe, "Iteratieve lijstmode reconstructie voor coïncidentiebeeldvorming," Ph.D. dissertation, Ghent university, 2002.

[125] S. Vandenberghe, C. Byrne, E. Soares, I. Lemahieu, and S. Glick, "Reconstruction of 2D PET data with Monte Carlo generated natural pixels," in *Proceedings of the IEEE ISBI (Biomedical imaging) Conference*, Arlington, USA, 2004, pp. 356–359.

[126] S. Vandenberghe, C. Byrne, E. Soares, I. Lemahieu, and S. Glick, "Reconstruction of 2D PET data with monte carlo generated natural pixels," June 2004, submitted to the IEEE Transactions on Medical Imaging.

[127] S. Vandenberghe, Y. D'Asseler, J. Kolthammer, R. Van de Walle, I. Lemahieu, and R. Dierckx, "Influence of the angle of incidence on the sensitivity of gamma gamera based PET," *Physics in Medicine and Biology*, vol. 47, pp. 289–303, 2002.

[128] S. Vandenberghe, Y. D'Asseler, M. Koole, L. Bouwens, R. V. Walle, R. A. Dierckx, and I. Lemahieu, "Iterative list mode reconstruction for coincidence data of gamma camera," in *Proceedings of the SPIE Medical Imaging*, vol. 3977, San Diego, USA, 2000, pp. 1538–1546.

[129] S. Vandenberghe, S. Staelens, M. Koole, R. Van de Walle, and I. Lemahieu, "Sensitivity of SPECT with rotating slat collimators," in *Proceedings of the IEEE Medical Imaging Conference*, Portland, USA, 2003, pp. M11–269.

[130] S. Vandenberghe, S. Staelens, M. Koole, R. Van de Walle, and I. Lemahieu, "Sensitivity of SPECT with rotating slat collimators," november 2003, accepted for publication in IEEE Transactions on Nuclear Science.

[131] S. Vandenberghe, S. Staelens, E. Soares, C. Byrne, and S. Glick, "Natural pixel reconstruction of 3D PET data," May 2004, submitted to the Medical Imaging Conference, Roma, Italy.

[132] Y. Vardi, L. A. Shepp, and L. Kaufman, "A statistical model for positron emission tomography," *Journal of the American Statistical Association*, vol. 80, no. 389, pp. 8–20, March 1985.

[133] J. von Neumann, "Various techniques in connection with random digits-Monte Carlo methods," National Bureau Standards, Tech. Rep. AMS 12, 1951.

[134] J. Wallis and T. Miller, "An optimal rotator for iterative reconstruction," *IEEE Transactions on Medical Imaging*, vol. 16, no. 1, pp. 118–123, 1997.

[135] W. Wang, W. Hawkins, and D. Gagnon, "3D RBI-EM reconstruction with spherically-symmetric basis function for SPECT rotating slat collimator," *Physics in Medicine and Biology*, vol. 49, no. 11, pp. 2273–2292, 2004.

[136] Z. Wang, T. Li, G. Han, and Z. Liang, "Pc graphics card-based accelaeration for OSEM image reconstruction of quantitative SPECT with vary-

ing focal-length fan-beam collimators," *Journal of Nuclear Medicine*, vol. 45, no. 5, p. 1295, 2004.

[137] S. Webb, D. Binnie, M. Flower, and R. Ott, "Monte Carlo modeling of the performace of a rotating slit collimator for improved planar gamma camera imaging," *Physics in Medicine and Biology*, vol. 37, pp. 1095–1108, 1992.

[138] F. Xu and K. Mueller, "Towards a unified framework for rapid computed tomography on commodity GPUs," in *Proceedings of the IEEE Medical Imaging Conference*, Portland, USA, 2003, pp. M10–331.

[139] F. Xu and K. Mueller, "Ultra-fast 3d filtered backprojection on commodity graphics hardware," in *Proceedings of the IEEE ISBI (Biomedical imaging) Conference*, Arlington, USA, 2004, pp. 571–574.

[140] J. Yanch, A. Dobrzeniecki, C. Ramanathan, and R. Behrman, "Physically realistic Monte Carlo simulation of source, collimator and tomographic data acquisition for emission computed tomography," *Physics in Medicine and Biology*, vol. 37, pp. 853–870, 1992.

[141] H. Zaidi, "Relevance of accurate Monte Carlo modeling in nuclear medical imaging," *Medical Physics*, vol. 26, pp. 574–608, 1999.

[142] H. Zaidi, "Addendum to Relevance of accurate Monte Carlo modeling in nuclear medical imaging [Med. Phys. 26, 574-608 (1999)]," *Medical Physics*, vol. 27, pp. 816–817, 2000.

[143] H. Zaidi, A. Hermann Scheurer, and C. Morel, "An Object-Oriented Monte-Carlo simulator for 3D cylindrical positron tomographs," *Computer Methods and Programs in Biomedicine*, vol. 58, pp. 133–145, 1999.

[144] H. Zaidi and K. Koral, "Scatter modeling and compensation in emission tomography," *European Journal of Nuclear Medicine*, vol. 31, no. 5, pp. 761–782, 2004.

[145] G. Zeng and D. Gagnon, "CdZnTe strip detector SPECT imaging with a slit collimator," *Physics in Medicine and Biology*, vol. 49, no. 11, pp. 2257–2271, 2004.

[146] G. Zeng and D. Gagnon, "Image reconstruction algorithm for a SPECT system with a convergent rotating slat collimator," *IEEE Transactions on Nuclear Science*, vol. 51, no. 1, pp. 142–148, 2004.

[147] G. Zeng, D. Gagnon, C. Matthews, J. Kolthammer, J. Radachy, and W. Hawkins, “Image reconstruction algorithm for a rotating slat collimator,” *Medical Physics*, vol. 29, no. 7, pp. 1406–1412, 2002.

[148] G. Zeng, G. Gullberg, P. Christian, D. Gagnon, and C.-H. Tung, “Asymmetric cone-beam transmission tomography,” *IEEE Transactions on Nuclear Science*, vol. 48, pp. 117 – 124, 2001.

Publications author: Journal Papers

[1] K. Assie, V. Breton, I. Buvat, C. Comtat, S. Jan, M. Krieguer, D. Lazaro, C. Morel, M. Rey, G. Santin, L. Simon, S. Staelens, D. Strul, J. Vieira, and R. Van de Walle. Monte Carlo simulation in PET and SPET instrumentation using GATE. *Nuclear Instruments and Methods A*, 527/1-2:180–189, 2004.

[2] Y. D'Asseler, C. Groiselle, H. Gifford, S. Vandenberghe, S. Staelens, R. Van de Walle, I. Lemahieu, and S. Glick. Evaluating human observer performance for list mode PET using the bootstrap method. submitted for IEEE Transactions on Nuclear Science, august 2004.

[3] S. Jan, G. Santin, D. Strul, S. Staelens, K. Assié, D. Autret, D. Avner, R. Barbier, M. Bardiès, P. Bloomfield, D. Brasse, V. Breton, P. Bruyndonckx, I. Buvat, A. Chatziioannou, Y. Choi, Y. Chung, C. Comtat, D. Donnarieix, L. Ferrer, S. Glick, C. Groiselle, S. Kerhoas-Cavata, A. Kirov, V. Kohli, M. Koole, M. Krieguer, J. van der Laan, F. Lamare, G. Largeron, C. Lartizien, D. Lazaro, M. Maas, L. Maigne, F. Mayet, F. Melot, S. Nehmeh, E. Pennacchio, J. Perez, U. Pietrzyk, F. Rannou, M. Rey, D. Schaart, R. Schmidtlein, L. Simon, T. Song, J. Vieira, D. Visvikis, R. Van de Walle, E. Wieers, and C. Morel. GATE: a simulation toolkit for PET and SPECT. *Physics in Medicine and Biology*, 49(19):4543–4561, 2004.

[4] D. Lazaro, I. Buvat, G. Loudos, D. Strul, G. Santin, N. Giokaris, D. Donnarieix, L. Maigne, V. Spanoudaki, S. Styliaris, S. Staelens, and V. Breton. Monte Carlo simulation of a CsI(Tl) gamma camera dedicated to small animal imaging using GATE. *Physics in Medicine and Biology*, 49(2):271–286, 2004.

[5] S. Staelens, Y. D'Asseler, S. Vandenberghe, M. Koole, I. Lemahieu, and R. Van de Walle. A threedimensional theoretical model incorporating spatial detection uncertainty in continuous detector PET. *Physics in Medicine and Biology*, 49(11):2337–2351, 2004.

[6] S. Staelens, M. Koole, S. Vandenberghe, Y. D'Asseler, I. Lemahieu, and R. Van de Walle. The geometric transfer function for a slat collimator mounted on a strip detector. in press and to appear in IEEE Transactions on Nuclear Science, september 2004.

[7] S. Staelens, G. Santin, S. Vandenberghe, D. Strul, M. Koole, Y. D'Asseler, I. Lemahieu, and R. Van de Walle. Transmission imaging with a moving point source: influence of crystal thickness and collimator type. in press and to appear in IEEE Transactions on Nuclear Science, september 2004.

[8] S. Staelens, D. Strul, S. Vandenberghe, G. Santin, M. Koole, Y. D'Asseler, I. Lemahieu, and R. Van de Walle. Monte Carlo simulations of a scintillation camera using GATE: validation and application modeling. *Physics in Medicine and Biology*, 48(18):3021–3042, 2003.

[9] S. Vandenberghe, S. Staelens, M. Koole, R. Van de Walle, and I. Lemahieu. Sensitivity of SPECT with rotating slat collimators. accepted for IEEE Transactions on Nuclear Science, november 2003.

Publications author: Conference Proceedings

[1] Y. D'Asseler, S. Staelens, S. Vandenberghe, S. Glick, and I. Lemahieu. Patient-specific optimization of iterative reconstruction for a search-detection task using the bootstrap method. accepted for the EANM Conference, Helsinki, Finland, August 2004.

[2] J. De Beenhouwer, S. Staelens, Y. D'Asseler, I. Lemahieu, and R. Van de Walle. Variance reduction techniques for Monte Carlo simulations in nuclear medicine. In *Book of abstracts of the 4th Phd Symposium of Ghent University*, page 96, Gent, Belgium, 2003.

[3] J. De Beenhouwer, S. Staelens, Y. D'Asseler, S. Vandenberghe, I. Lemahieu, and R. Van de Walle. Geometrical importance sampling and pulse height tallies in GATE. accepted for the EMBS Conference, San Fransisco, USA, April 2004.

[4] P. De Bondt, S. Vandenberghe, O. De Winter, J. De Sutter, S. Staelens, P. Segers, C. Vandewiele, P. Verdonck, and R. Dierckx. Development and validation of a dynamic ventricle phantom for planar and tomographic radionuclide ventriculography studies. *Eur. J. Nucl. Med.*, 29:367, August 2002.

[5] M. Koole, Y. D'Asseler, S. Staelens, S. Vandenberghe, K. Van Laere, I. Lemahieu, and R. Van de Walle. Influence of rebinning on the reconstructed resolution of fanbeam SPECT. In *Proceedings of the World Conference on Nuclear Medicine*, volume 1, page 160, Santiago de Chile, Chile, 2002.

[6] M. Koole, S. Staelens, Y. D'‘Asseler, S. Vandenberghe, K. Van Laere, I. Lemahieu, and R. Van de Walle. Influence of rebinning on the reconstructed resolution of fan-beam SPECT. In C. Veraart and P. Verdonck,

editors, *Book of abstracts of the 2nd National Day on Biomedical Engineering*, page 33, Brussel, 10 2002.

[7] M. Koole, S. Staelens, I. Lemahieu, R. Van de Walle, and R. Dierckx. Iterative reconstruction of grey matter activity in perfusion brain spet imaging. *Eur. J. Nucl. Med.*, 30:208, 8 2003.

[8] M. Koole, S. Staelens, R. Van de Walle, and I. Lemahieu. Correction for partial volume effects in brain perfusion ect imaging. In *Proceedings of the SPIE Medical Imaging Conference*, volume 5032, pages 986–994, San Diego, 2003.

[9] M. Koole, S. Staelens, K. Van Laere, I. Lemahieu, and R. Van de Walle. Modelling the senstivity of fan beam collimation in SPECT imaging. In C. Veraart and P. Verdonck, editors, *Book of abstracts of the 1st National Day on Biomedical Engineering*, volume 4, page 10, Brussel, 2001.

[10] M. Koole, S. Staelens, S. Vandenberghe, Y. D'Asseler, R. Van de Walle, and I. Lemahieu. Analytical model for Solstice detector response. In *Proceedings of the IEEE Medical Imaging Conference*, pages M14–270, Portland, USA, 2003.

[11] D. Lazaro, I. Buvat, D. Donnarieix, G. Loudos, D. Strul, G. Santin, N. Giokaris, L. Maigne, V. Spanoudaki, S. Styliaris, S. Staelens, and V. Breton. Monte Carlo simulation of a CsI(Tl) gamma camera dedicated to small animal imaging using GATE. *J. Nucl. Med.*, 44(5):1032, 1 2003.

[12] S. Staelens. Quantitative reconstruction of brain SPECT images. In *Book of abstracts of the 2nd Phd Symposium of Ghent University*, page 59, Gent, Belgium, 2001.

[13] S. Staelens. Spatial uncertainty in continuous detector PET : a theoretical approach. In *Book of abstracts of the 3rd Phd Symposium of Ghent University*, page 87, Gent, Belgium, 2002.

[14] S. Staelens, Y. D'Asseler, S. Vandenberghe, M. Koole, I. Lemahieu, and R. Van de Walle. Characteristics of a theoretical LOR model for PET representing spatial uncertainty in detection. In C. Veraart and P. Verdonck, editors, *Book of abstracts of the 2nd National Day on Biomedical Engineering*, page 37, Brussel, 10 2002.

[15] S. Staelens, Y. D’Asseler, S. Vandenberghe, M. Koole, I. Lemahieu, and R. Van de Walle. A 3D model incorporating spatial detection uncertainty in continuous detector PET: Monte Carlo evaluation of a theoretical study. In *Proceedings of the Fully 3D Conference*, pages We AM1–3, Saint Malo, France, 2003.

[16] S. Staelens, Y. D‘Asseler, S. Vandenberghe, M. Koole, I. Lemahieu, and R. Van de Walle. A theoretical lor model incorporating spatial uncertainty in continuous detector pet. In *Proceedings of the SPIE Medical Imaging conference*, volume 5030, pages 667–676, San Diego, 2003.

[17] S. Staelens, Y. D’Asseler, S. Vandenberghe, M. Koole, I. Lemahieu, and R. Van de Walle. A simulation study comparing the imaging performance of a solid state detector with a rotating slat collimator versus a traditional scintillation camera. In *Proceedings of the SPIE Medical Imaging conference*, volume 5372-36, pages 301–310, San Diego, 2004.

[18] S. Staelens, J. de Beenhouwer, M. Koole, Y. D’Asseler, S. Vandenberghe, I. Lemahieu, and R. Van de Walle. Monte Carlo simulations for SPECT: object-oriented flexibility benchmark. In C. Veraart and P. Verdonck, editors, *Book of abstracts of the 3rd National Day on Biomedical Engineering*, Brussel, 10 2003.

[19] S. Staelens, I. Lemahieu, and R. Van de Walle. GATE, a Geant4 based simulation platform for nuclear medicine : development, validation and application modeling. In *Book of abstracts of the 4th Phd Symposium of Ghent University*, page 99, Gent, Belgium, 2003.

[20] S. Staelens, G. Santin, D. Strul, M. Koole, S. Vandenberghe, Y. D‘Asseler, V. Breton, C. Morel, I. Lemahieu, and R. Van de Walle. Monte carlo simulations of interfile based emission and attenuation maps for clinical applications. *J. Nucl. Med.*, 44(5):1048, 5 2003.

[21] S. Staelens, S. Vandenberghe, S. Glick, Y. D’Asseler, I. Lemahieu, and R. Van de Walle. Patient and crystal scatter analysis in 3D PET. *J. Nucl. Med.*, 45(5):123, 2004.

[22] S. Staelens, S. Vandenberghe, S. Glick, Y. D’Asseler, I. Lemahieu, and R. Van de Walle. Simulation of patient and crystal scatter in 3D PET for various crystals. accepted for the IEEE Medical Imaging Conference, Roma, Italy, October 2004.

[23] S. Staelens, S. Vandenberghe, M. Koole, Y. D‘Asseler, P. Debondt, I. Van den Eede, I. Lemahieu, and R. Van de Walle. Comparison of FBP

and OSEM for volume determination in SPECT imaging. In *Proceedings of the 2nd joint EMBS/BMES conference*, pages 973–974, Houston, 2002.

[24] S. Staelens, S. Vandenberghe, M. Koole, D. Strul, G. Santin, H. Van Steendam, Y. D‘Asseler, R. Dierckx, I. Lemahieu, and R. Van de Walle. Monte carlo simulations of transmission measurements with a medium energy moving point source. *Eur. J. Nucl. Med.*, 30:223, 8 2003.

[25] S. Staelens, S. Vandenberghe, M. Koole, H. Van Steendam, Y. D’Asseler, I. Lemahieu, and R. Van de Walle. Transmission imaging with a moving point source: influence of crystal thickness and collimator type. In *Proceedings of the IEEE Medical Imaging Conference*, pages M10–274, Portland, USA, 2003.

[26] S. Vandenberghe, S. Staelens, S. Glick, and I. Lemahieu. Methods for generating system matrices for natural pixel reconstruction. *J. Nucl. Med.*, 45(5):291, 2004.

[27] S. Vandenberghe, S. Staelens, M. Koole, R. Van de Walle, and I. Lemahieu. Sensitivity of SPECT with rotating slat collimators. In *Proceedings of the IEEE Medical Imaging Conference*, pages M11–269, Portland, USA, 2003.

[28] S. Vandenberghe, S. Staelens, E. Soares, C. Byrne, and S. Glick. Natural pixel reconstruction of 3d pet data. submitted to the IEEE Medical Imaging Conference, Roma, Italy, May 2004.

[29] J. Verhaeghe, Y. D’Asseler, S. Vandenberghe, S. Staelens, and I. Lemahieu. Ml reconstruction from dynamic list-mode PET data using temporal splines. accepted for the IEEE Medical Imaging Conference, Roma, Italy, October 2004.

-